UNIVERSITÉ DE TOURS

ÉCOLE DOCTORALE EMSTU

GREMAN

THÈSE présentée par :

Priyadarshini SHANMUGAM

soutenue le : **03 Décembre 2021**

pour obtenir le grade de : **Docteur de l'université de Tours**

Discipline/ Spécialité : Électronique

Design, fabrication and characterization of micro resonant systems for hydrogen detection in a radioactive environment

THÈSE dirigée par :

M. ALQUIER Daniel	Professeur, Université de Tours

RAPPORTEURS :

Mme. BANO Edwige	Professeur, Grenoble Institute of Technology
M. THOMSEN Erik Vilain	Professeur, Technical University of Denmark

---

JURY :

M. ALQUIER Daniel	Professeur, Université de Tours
Mme. BANO Edwige	Professeur, INP Grenoble
M. THOMSEN Erik Vilain	Professeur, Technical University of Denmark
Mme. DUFOUR Isabelle	Professeur, Université de Bordeaux
M. CERTON Dominique	Professeur, Université de Tours
M. MICHAUD Jean-François	Maître de conférences, Université de Tours

Membre invité :

M. BERTRAND Johan	Ingénieur R&D, ANDRA

Abstract

A gas sensor is a device that can detect gases in our surroundings, especially dangerous ones in extreme environments. Our goal is to develop a microsystem for hydrogen surveillance in a radioactive environment. Moreover, hydrogen is highly flammable in air when mixed to a level of 4 to 70 %. Given the risky nature of the gas, the proposed sensor should be highly reliable and effective to protect our lives from an unexpected accident. We can accomplish this with a gas sensor that has better-related attributes, such as sensitivity, selectivity, material property, etc. Until now, the commercially available gas sensors are mostly coated with sensitive material, which causes various device failures, like ageing, low reliability and high response time. In contrast, there are few physical sensors based on Lidar and thermal conductivity detection, but these are either huge in size or have higher limits of detection. To overcome these disadvantages, we present two types of physical sensors without sensitive coating.

The first system is capacitive micromachined ultrasonic transducers (CMUTs) made of silicon nitride. This detects changes in gas mixture due to shifts in gas mass density and ultrasound velocity. The second system is an uncoated microcantilever made of cubic silicon carbide (3C-SiC). This material was chosen for its excellent mechanical properties and its ability to withstand harsh/radioactive environments. Both the microsystems are developed to detect the presence of hydrogen gas below lower explosion limit (LEL), i.e. <4 %, in a radioactive environment. The obtained outcomes proved the hypothesis and detected concentration of hydrogen lower than 1 %.

Keywords: hydrogen gas sensors, CMUTs, 3C-SiC, microcantilevers, mass density, ultrasound velocity, gas sensing.

Résumé

Un détecteur de gaz est un dispositif capable de détecter des gaz dans notre environnement, notamment des gaz dangereux dans des environnements sévères. Notre objectif est de développer un microsystème pour la surveillance de l'hydrogène dans un environnement radioactif. En effet, l'hydrogène est hautement inflammable dans l'air lorsqu'il est présent à des concentrations allant de 4 à 70 %. Compte tenu de la nature dangereuse de ce gaz, le capteur proposé doit être fiable et efficace afin de protéger nos vies lors d'un accident inattendu. Nous pouvons y parvenir avec un capteur de gaz qui possède des caractéristiques, telles que bonne sensibilité et sélectivité, propriété du matériau adéquate, etc. Jusqu'à présent, les capteurs de gaz disponibles dans le commerce sont pour la plupart recouverts d'un matériau dit sensible, ce qui entraîne des défaillances du dispositif, comme son vieillissement, une fiabilité moindre et un temps de réponse plus long. En revanche, il existe quelques capteurs physiques basés sur le Lidar et la détection de la conductivité thermique, mais ils sont soit de taille importante, soit ont des limites de détection trop élevées. Pour surmonter ces inconvénients, nous présentons deux types de capteurs physiques sans couche sensible.

Le premier système est constitué de transducteurs ultrasonores capacitifs micro-usinés (CMUTs: Capacitive Micromachined Ultrasonic Transducers) en nitrure de silicium. Ils détectent les changements dans le mélange gazeux en raison des variations de la densité massique du gaz et de la vitesse de propagation des ultrasons. Le deuxième système est un microcantilever en carbure de silicium du type cubique (3C-SiC). Le choix de ce matériau est basé sur ses propriétés mécaniques exceptionnelles et sa résistance aux environnements sévères. Les deux microsystèmes sont développés pour détecter la présence d'hydrogène gazeux en dessous de la limite inférieure d'explosivité, c'est-à-dire <4 %, dans un environnement radioactif. Les résultats obtenus ont prouvé cette hypothèse et ont permis de détecter une concentration d'hydrogène inférieure à 1 %.

Mots clés: capteurs d'hydrogène gazeux, CMUTs, 3C-SiC, microcantilevers, densité massique, vitesse ultrasonore, détection de gaz.

எப்பொருள் யார்யார்வாய்க் கேட்பினும் அப்பொருள்
மெய்ப்பொருள் காண்ப தறிவு.
(திருக்குறள்-423)

The mark of wisdom is to discern the truth, from whatever source it is heard.
(Thirukkural-423)

De quelque bouche qu'on entende quoi que ce soit, en saisir le véritable sens est l'entendement.
(Tiroukoural-423)

Dedicated to:

My parents, who always believed in me.

&

My dear husband, for his unconditional love and trust.

Acknowledgement

First, I extend my sincere gratitude to my supervisor **Daniel Alquier** for giving me the wonderful opportunity to be involved in Project H2MEMS. During these four years, he expressed his support and enthusiasm on both professional and personal level. He was always available, when his presence was needed the most and gave comments from a broad perspective. Moreover, he encouraged me to keep going whenever I encountered obstacles along the way.

I am grateful to **ANDRA** for funding this project, as well as to our **H2MEMS team** for their significant support and contribution to the results presented here. The insights and knowledge sharing of our multifaceted team helped to broaden my reasoning capacity. I also acknowledge that this research work is benefited from **CERTeM's** technological platforms.

My special thanks goes to **Dominique Certon**, a good human and curious person I have ever seen. I acknowledge his timely responses, support, and advice throughout the project. I enjoyed working with him in the lab when we were trying to discover something new. Every time we fail or succeed, we learn something new.

My heartfelt thanks to **Jean François Michaud** for allowing me to stand on my own feet. During these four years, he trusted and supported me. The journey would not have been smooth without his encouragement and patience.

I would like to thank my crisis management team, **Virginie Grimal**, **David Chouteau**, **Beatrice Negulescu**, **Micka Bah** and **Damien Valente**. Having their timely assistance helped me move forward in the various stages of cleanroom processes. I would also like to acknowledge Laurent Colin, Marie Perroteau and Flavien Barcella for their technical assistance.

My warmest gratitude to **Clément** (PZ), **Jaweb**, **Hugo**, **Taoufik**, **Igor**, **Camille**, **Maxime**, **Clément**, **Romain**, **Sylvain** and **Thomas**, for their friendship. You people made living in Tours more enjoyable.

I now thank my parents, **Shanmugam** and **Jayalakshmi**, who have been living models of hard work and perseverance, and never failed to pour their unconditional love during hard times. My lovely brothers **Hari**, **Santhosh** and **Dharun**, who never fails to put a smile on my face. I would also like to thank my sweet heart friends **Revathy** and **Priya** for being my therapists.

Last but not least, my very special thanks to my best friend and husband, **Deepak**. It will take me my whole life to thank you for all your trust in me, even when I doubted myself. You are the best thing that has ever happened to me. Thank you for tolerating me and helping me stay positive during hard times.

All of these people deserve my sincere thanks and appreciation for their support. This experience will remain one of my best memories as well as my motivation to pursue my future dreams. Un trés **GRAND MERCI** à tous.

Priyadarshini SHANMUGAM

Tours, 03/12/2021

Table of Contents

Abstract **3**

Résumé **5**

General introduction **15**

1. Background, motivation and previous studies on gas detection **23**

1.1 General introduction on hydrogen detection 25

1.2 Background and project H2MEMS 26

1.3 Hydrogen detection based on chemical properties 28

1.3.1 Catalytic hydrogen sensors 28

1.3.2 Electrochemical hydrogen sensors 30

1.3.3 Fiber optic hydrogen sensors 32

1.4 Hydrogen detection based on physical properties 36

1.4.1. Thermal conductivity hydrogen sensors 36

1.4.2 Lidar hydrogen sensors 37

1.5 Comparison between chemical and physical sensors 40

1.6 MEMS sensors with/without sensitive coating 42

1.6.1 Gas sensing with cantilevers 42

1.6.2 Gas sensing with capacitive micromachined ultrasonic transducers 44

1.7 Our approach for hydrogen gas sensing 45

1.7.1 3C-SiC microcantilever based gas sensor 46

1.7.2 CMUT based gas sensor 48

Conclusion 52

References 53

2. Design, fabrication and characterization of 3C-SiC microcantilevers without functionalized coating **67**

2.1 General introduction of silicon carbide and its properties 69

2.1.1 Motivation to choose cubic crystallographic orientation 69

2.1.2 Brief history of pioneering researches on 3C-SiC epilayer growth, etching and characterization processes by our associated groups 72

2.1.3 The growth process of 3C-SiC epilayer on Si substrate used in our study . 76

2.2 Background for design validations 79
2.3 Fabrication of 3C-SiC-microcantilevers (µCs) 83
2.3.1 Sample preparation 84
2.3.2 Defining the geometries of 3C-SiC-µCs 86
2.3.3 Optimization of the isolation layer 87
2.3.4 Deposition of metals for piezoresistive detection 91
2.3.5 Deposition of metals for electromagnetic actuation 96
2.3.6 Turning sample into device 99
2.3.7 Packaging of fabricated 3C-SiC-µCs 104
2.4 Electrical characterizations of 3C-SiC-µCs in air 106
2.4.1 Laser Doppler vibrometry measurements 106
2.4.2 Electrical measurements 110
2.5 Testing of fabricated 3C-SiC-µCs in binary gas mixture environments 113
Conclusion and perspectives 116
References 117
3. Design, fabrication and characterization of air-coupled CMUT gas sensor without functionalized coating 127
3.1 CMUT technology 129
3.1.1 State-of-the-art 129
3.1.2 Brief history on CMUTs fabrication advancement from labs associated with University of Tours 130
3.2 Topology of CMUTs array 133
3.2.1 Cell level representation 133
3.2.2 Element level representation 135
3.2.3 Chip level representation 137
3.3 Fundamentals of CMUTs 138
3.3.1 Static analysis with 1-D model 140
3.3.2 1-D dynamic analysis without acoustic loading 143
3.3.3 Dynamic analysis in gas medium and CMUTs design 148
3.4 Fabrication and packaging of CMUTs 153
3.5 Characterizations of fabricated CMUTs 156
3.5.1 Digital holographic microscopy (DHM) measurements 156

3.5.2 Electrical impedance measurements 160
3.6 Electroacoustic characterizations of CMUTs in air 164
3.6.1 Design and fabrication of the measuring cell 164
3.6.2 Experimental setup and preliminary results 166
3.6.3 Impact of V_{bias} and V_{ac} on time of flight performances 170
3.6.4 Comparison between different emission frequencies 173
3.6.5 Detection of maximum working distances 174
3.7 Binary gas mixture analyses 176
3.7.1 Time of flight model validation in gas mixture environments 176
3.7.2 Gas mixture analysis for CMUTs working at resonance mode 179
Conclusion and perspectives 181
References 183
General conclusion and perspectives 189
Scientific contributions 193
Extended Summary 195

General introduction

Globally, hydrogen detection/monitoring is not that something we think about very often, but might be in the future. This can be attributed to several factors, including the use of hydrogen in energy production, hydrogen as a fuel source, and the creation of hydrogen as a byproduct during certain industrial processes or in radioactive storage sites. Since hydrogen is colorless, odorless, tasteless, lightest of all other elements in the periodic table, and easily flammable at a concentration of 4-70 % in the volume of air, it is essential to monitor hydrogen regularly for safety reasons. Firstly, energy production uses hydrogen for several refining processes, such as lowering the sulfur content in fuels and reducing heavy gases and oils with lower molecular weight. These industries are continuously in need of hydrogen due to the demand for clean and safe fuels, as well as the constantly changing standards of environmental protection. Moreover, hydrogen is described as a potentially effective alternative fuel. Therefore, it is more important to monitor hydrogen leakage during storage, transportation, and refueling stations.

It is worth mentioning that hydrogen may also lead to difficulties. As an example, abundant release of hydrogen during coal mining can also cause unanticipated accidents. Further, hydrogen can be produced as a byproduct in certain environments, namely in facilities that store radioactive wastes. It may have originated either as the result of plutonium reprocessing over radiolysis of water or as a result of reactions between metallic materials among wastes, which results in hydrogen production due to corrosion in an anoxic environment (corrosion by water in absence of oxygen). In our study, we will be focusing on this aspect of hydrogen detection. Because, nuclear energy is the primary source of electricity in many countries today. According to 2020 data, nuclear power plants produced 67 % of France's electricity [1]. Despite a 50 % reduction in nuclear energy production in France by 2035, the presently generated nuclear wastes must be handled carefully. In order to store these nuclear wastes indefinitely, the French national agency for radioactive waste management (ANDRA: Agence nationale pour la gestion des déchets radioactifs) has constructed an underground facility for storing those wastes for a long time. Moreover, they announced a call for R&D projects devoted to the theme “Nucléaire de Demain” under Programme d’Investissements d’Avenir, in which our project, H2MEMS, is one of them. The purpose of this project is to develop a micro resonant system for hydrogen detection in the deep geological nuclear waste disposal facility built by ANDRA. Therefore,

the fabricated sensors will be installed in the facility's ventilation system. This is to reduce the risk of gas accumulation and improve safety. Particularly in the case of hydrogen, which is explosive in nature.

Presently, the need for hydrogen gas detectors is increasing due to safety reasons. Depending on the application, one's requirement differs. In our case, the sensor will be placed in a radioactive environment. Hence, it requires a faster response time and an adequate choice of materials that will survive in this kind of environment. A majority of commercially available hydrogen sensors contain sensitive coatings that absorb the analyte of interest. Usually, hydrogen sensors are coated with metals like palladium or platinum. These coated sensors have extremely high detection limits of parts per billion, but are more susceptible to cross-sensitivity to other reducing gases as well as fast aging. As an alternative to these chemical detection sensors, we proposed to develop gas sensors based on the physical properties detection, in the frame of H2MEMS project. Although this family of sensors offers less selectivity, it will have better performances in terms of durability. The aim of H2MEMS project is not only to show gas detection by means of physical sensors but also make them a "selective" sensor. The physical quantities on which we focused are mass, viscosity and acoustic properties. To meet this demand, this PhD work aimed to develop new generation of MEMS-based (MicroElectroMechanicalSystems) sensors with different approaches in term of detection methods.

The first microsystem is a microcantilever (µC) based physical hydrogen detector. The detection mechanism will be based on resonance frequency monitoring method, which will detect changes in gas concentration to the shift in the cantilever's mechanical resonance according to gas viscosity variations. This work follows from M. T. Boudjiet's PhD [3], in which he used silicon based µCs. In this PhD, to meet safety and durability requirements, it was targeted to develop similar devices where silicon is replaced by silicon carbide material (and more specifically 3C-SiC). 3C-SiC has excellent electrical and mechanical properties to survive in harsh environments and is probably one of the most suitable materials for the monitoring of nuclear waste storing sites. To monitor the change of the mechanical resonance frequency, two approaches were implemented :

- One, as used in M. T. Boudjiet's PhD [3] where actuation is electromagnetic and detection is based on change in piezo resistance (method I).

- The second also uses electromagnetic actuation and detection is based on change in induction (method II).

Then, the second microsystem will be capacitive micromachined ultrasonic transducers (CMUTs). These devices are arrays of suspended micro-plates (with circular or square shapes) actuated by electrostatic forces. These devices are mostly used in medical imaging. Hence, the use of CMUT as a physical gas sensor is one of the novelties of this PhD. Based on CMUTs working, we proposed two types of detection mechanisms:

- The first is resonance mode approach (method III), where the mechanical resonance of the plate is monitored according to change of gas properties. It is worth mentioning that the working frequency is in the MHz range while for the cantilever, it is in the kHz range.
- In the second method, the gas detection will be based on a change in ultrasound velocity using time of flight (ToF) measurement technique (method IV). Here, the CMUT is used as an air-coupled ultrasonic transducer, for working frequency in the MHz range (typically 1 MHz).

The CMUT based device can be operated using method III and IV detection at the same time. This is also the novelty of our approach. In one case, it will work at higher frequency range, i.e. several MHz, for resonance mode detection, and around 1 MHz for time of flight measurement. Hence, this approach paves the way to the development of multi-modal sensors that could address the issue of gas discrimination.

Both microsystems (3C-SiC-µCs and CMUTs) would be new concept gas sensors without sensitive coatings. It is expected that these microsystems will detect very low concentration of hydrogen in nitrogen, i.e. less than 1 %. The presented work will focus on design, fabrication and validation of cantilever type and CMUTs hydrogen gas sensors for the targeted application. This thesis comprises three chapters.

- Chapter 1 begins by explaining the importance of hydrogen detection in various industries, then the background and motivation for our study emphasizing the project H2MEMS, as well as describing existing solutions for hydrogen detection. Essentially, the existing solutions can be divided into two categories: chemical and physical sensors based on their detection mechanism, which will be briefly discussed and compared. Further, cantilever and CMUT based MEMS gas sensors will also be reviewed in the

study, since they correspond to the proposed microsystems. At the end of this chapter, the need for the proposed microsystems and their detection mechanisms will be elaborated.

- Chapter 2 deals with the fabrication and characterization of 3C-SiC-µCs. The chapter starts by giving an overview of SiC material properties and reasons for choosing cubic silicon carbide. After, the systematic fabrication process will be discussed in detail, in which the issues encountered during different stages of fabrication will be addressed with suitable solutions. As stated previously, Boudjiet has validated the design of these cantilevers, and the same design was selected here for the chosen material. Afterward, the electrical characterizations of 3C-SiC-µCs in air will be discussed, in which the major parameters like resonance frequency, quality factor, etc. are evaluated. Lastly, the performance of newly developed 3C-SiC-µCs under gas mixture environments will be disclosed.
- Chapter 3 is devoted to CMUTs-based gas sensors. Firstly, an overview of state-of-the-art CMUT technology will be presented, followed by a description of multi-element CMUT topologies. After, the fundamentals of dynamic analysis in gas medium and CMUT design optimization will be explained. Next, this chapter is focused on the fabrication, characterization and test of several CMUT prototypes with different geometrical configurations. For each detection method, we will demonstrate that CMUT technology meets the need in terms of detection threshold and their intrinsic limits will be discussed. Particular attention will be paid to show that a unique CMUT prototype is enough to address the two detection methods.

Throughout this work, different methods for measuring hydrogen concentration in nitrogen by examining changes in different physical properties of the gas mixture will be presented. In conclusion, we summarize the most important findings presented in this work. In addition, an outlook and new perspectives beyond this work are provided.

References

[1] Hortense Goulard, “L’éolien, troisième source d’électricité en France en 2020,” *Les Echos,* Mar. 2021. [Online]. Available: https://www.lesechos.fr/industrie-services/energie-environnement/leolien-troisieme-source-delectricite-en-france-en-2020-1295128.

[2] A. Boulmé, “Conception et caractérisation de sondes cmut large bande pour l’imagerie conventionnelle et l’évaluation du tissu osseux,” PhD dissertation, University of Tours, 2013.

[3] M.-T. Boudjiet, “Microsystèmes durables de mesures de concentration d’hydrogène utilisant des micropoutres sans couche sensible,” PhD dissertation, University of Bordeaux, 2015.

1. Background, motivation and previous studies on gas detection

1.1 General introduction on hydrogen detection 25
1.2 Background and project H2MEMS 26
1.3 Hydrogen detection based on chemical properties 28
1.3.1 Catalytic hydrogen sensors 28
1.3.2 Electrochemical hydrogen sensors 30
1.3.3 Fiber optic hydrogen sensors 32
1.4 Hydrogen detection based on physical properties 36
1.4.1. Thermal conductivity hydrogen sensors 36
1.4.2 Lidar hydrogen sensors 37
1.5 Comparison between chemical and physical sensors 40
1.6 MEMS sensors with/without sensitive coating 42
1.6.1 Gas sensing with cantilevers 42
1.6.2 Gas sensing with capacitive micromachined ultrasonic transducers 44
1.7 Our approach for hydrogen gas sensing 45
1.7.1 3C-SiC microcantilever based gas sensor 46
1.7.2 CMUT based gas sensor 48
Conclusion 52
References 53

Chapter 1

Background, motivation and previous studies on gas detection

The main objective of our work is to develop a suitable microsystem to monitor the presence of hydrogen gas in a radioactive environment. Therefore, this chapter explains the need for proposed microsystems for the targeted application. This chapter has been divided into seven subsections. The first section presents the general introduction on risk of safety, due to hydrogen's flammable nature and need for gas surveillance. Secondly, the background and motivation of this project, "H2MEMS" is elaborated. The third and the fourth sections enumerate several types of hydrogen detectors. The presented sensors detect the existence of hydrogen gas using change in chemical or physical properties. These chemical-based sensors commonly have sensitive coatings to detect the molecule of interest, whereas the physical sensors monitor change in physical properties such as heat, light intensity, etc.

Subsequently, in section five, the advantages and the disadvantages of existing chemical and physical hydrogen gas sensors are summarized. This part highlights the core reason for choosing the hydrogen gas sensor based on physical property monitoring for the aimed application. Thereafter, in the sixth section, gas sensors made of cantilever and capacitive micromachined ultrasonic transducer (CMUT) types are discussed. These micro electro mechanical systems (MEMS) based gas sensors are particularly illustrated, because the proposed microsystems are of the described types, i.e. cantilevers and CMUTs. This part is more interesting due to huge advancements in MEMS technology during the last two decades and more relevant to the current studies. Later, in the final section, the bottom line of this thesis is interpreted. This last section discloses our approach of using physical MEMS sensors for hydrogen detection.

1.1 General introduction on hydrogen detection

Hydrogen (H_2) is a unique gas, which is highly flammable when it is mixed at a concentration of 4-75% in air. This colorless, odourless and tasteless gas makes it indistinguishable for human sensory organs. In addition, it is the lightest chemical element that tends to leak easily. Hence, it is important to monitor the concentration of H_2 in air, given the dangerous and risky nature of this gas. As hydrogen is widely used in metallurgical industries and in many space related applications, a fast and precise monitoring becomes essential to improve the level of safety and to avoid the risk of explosion. Detection of hydrogen concentration has a history of over a century [1]. Nevertheless, there are continuing demands for rapid, accurate and more sensitive hydrogen gas sensors to monitor and control the gas concentration, which is requisite to many industrial applications. In addition, while speaking about their applications, one cannot proceed without mentioning numerous ongoing researches on hydrogen energy generation. Indeed in the near future, there will be a huge need for hydrogen monitoring in production, transportation and storages, whether in pipelines, at refueling stations or in automotive vehicles [2].

As mentioned previously, the need for hydrogen generation is increasing. This makes it essential to monitor the outgrowth of hydrogen during storage or reprocessing of nuclear wastes. For example, in coal mines, sudden emission of abundant levels of hydrogen sulfide (H_2S) present inside coals and rock layers cause unanticipated disasters. This kind of H_2S emission is crucial to monitor because it ignites the spark during an accident and causes a serious impact on the human health system [3], [4]. Likewise, in nuclear power plants, hydrogen can be formed due to the radioactive waste storage. This could have originated either while reprocessing plutonium over radiolysis of water or through reaction with metallic materials among these wastes, which produce hydrogen by corrosion in an anoxic environment (corrosion by water in absence of oxygen) leading to an explosion. To give examples, three accidents caused by failure in surveillance have been referred: Three Mile Island (1979), Chernobyl (1986) and Fukushima Daiichi (2011) [5]–[7]. For this reason, one can easily understand that fast and precise gas monitoring of these types of harsh environments are mandatory.

1.2 Background and project H2MEMS

Presently, nuclear energy is the vital source of electricity in many countries; especially in France, where 67 % of the electricity is being produced by nuclear power plants, as of 2020's data [8], [9]. Even though the nuclear energy proportion in France is expected to be lowering to/by 50 % in 2035, it is essential to preserve the currently produced medium active with long life (MA-LL) and highly radioactive (HA) wastes with great care to avoid catastrophes, as explained in the introduction. Hence, in France, a national agency for radioactive waste management, ANDRA (Agence nationale pour la gestion des déchets radioactifs) has been created in 1979 by CEA (Commissariat à l'énergie atomique et aux énergies alternatives) to manage these long-term radioactive wastes within the French territory.

ANDRA was made an autonomous public agency in 1991 under the supervision of French Ministries for Energy, Environment and Research. Since then, a set of research activities have been undergoing, to safely manage the hazardous radioactive wastes. As a result, in 2006, ANDRA came up with an idea of building an industrial center for geological disposals, so called "project Cigéo" (Centre industriel de stockage géologique). This deep geological disposal facility located in Meuse/Haute-Marne, France, is constructed below earth's surface (app. ≈500 m), to handle and store the radioactive wastes properly, as shown in figure 1.1. The waste disposal will take place for 100 years and then the facility will be sealed to contain the radioactive wastes for a long time without human involvement.



Figure 1.1: Schematic diagram of deep geological radioactive disposal facility constructed by ANDRA, as part of project Cigéo [10].

Subsequently, ANDRA has endowed nearly 47 billion euros under the investments for a program called "Investissements d'Avenir" in 2010. The main aim of this program was to provide funding in the regions of French states for innovative and promising projects related to radioactive waste management. Following this, ANDRA has allocated 75 million euros beneath "Nucléaire de Demain" and launched calls for R&D projects devoted to this theme. Overall, 90 projects were submitted, of which only 29 have been selected and "project H2MEMS" is one among them.

The main goal of project H2MEMS is to develop hydrogen gas sensors, for long-term monitoring, of its deep geological disposal facility. In this kind of underground storage unit, release of hydrogen is expected due to corrosion of metals in an anoxic environment. The structural components like metal frames of reinforced concentrate, waste containers or presence of large quantities of metallic materials among these wastes can be a major issue. However, hydrogen is flammable at concentrations of 4-75% in the air. Hydrogen can also lead to explosions in presence of trigger element called activation energy, like ultrasound, static electricity, shock, etc. As a result, it is important to monitor this environment regularly. In addition, to avoid the accumulation of gases, the underground and the surface facilities will be vented during the operating period. Hence, our specially developed hydrogen sensor will be placed at the ventilation system for gas detection. This is to avoid the risk of explosion and improve safety measurement.

Project H2MEMS is a five-year project involving four laboratories within France. They are: i) CRHEA laboratory (Centre de Recherche sur l'Hétéro-Epitaxie et ses Applications) at Valbonne; ii) GREMAN laboratory (Groupe de Recherche en Matériaux, Microélectronique, Acoustique et Nanotechnologies) at Tours; iii) IMS laboratory (Intégration du Matériau au Système) at Bordeaux and iv) LAAS-CNRS (Laboratoire d'analyse et d'architecture des systèmes) at Toulouse. Each laboratory performs a key step in device creation. CRHEA provides epi-wafers for fabrication of 3C-SiC microcantilevers, which will be detailed in chapter 2 (refer §2.1.3). Then, GREMAN fabricates the hydrogen sensors with the electronics provided by LAAS and characterizes them in an air environment before handing it to gas testing. Lastly, IMS tests and validates the final prototypes under a gas mixture environment. To mention, Isabelle Dufour, from IMS, is the project coordinator.

1.3 Hydrogen detection based on chemical properties

1.3.1 Catalytic hydrogen sensors

Catalytic gas sensors are broadly used for monitoring the concentration of combustible gases. This is one of the classical techniques used in many industries to prevent gas explosions. The operating principle is based on detecting heat released on the sensor surface due to oxidation of combustible gases and then this change in temperature is converted into an electrical signal that activates the alarm. Such sensors are divided into pellistor type and thermoelectric type catalytic gas sensors.

The first catalytic gas sensor was proposed by Jonson in 1923 and firstly used for methane (CH_4) detection in mines [11], [12]. The classic pellistor sensor is composed of active and passive elements connected to a Wheatstone bridge. Both the elements are made of platinum (Pt) covered with a ceramic bead. The passive element acts as a reference that balances the external temperature, pressure and humidity. Unlike, the active element is responsible for catalytic combustion reaction, which senses the temperature difference and causes resistance imbalance in the bridge. This active element is coated with sensitive material (mostly palladium (Pd)), it serves as catalyst to sorb change in the environment [13].

Recently, due to huge development in micromachining technology, the scale of devices has decreased from centimeters to a few micrometers, which lowers the power consumption. Thanks to scaling law, it helps in the reduction of thermal response time because of its size. Furthermore, it enables reduced duty cycle operation and power consumption. Harley *et al.* presented a catalytic hydrogen sensor that has sensitivity and limit of detection (LOD) of 17 $mV/10^4$ ppm and 65 ppm with low power consumption of 2.2 mW. This sensor has remarkably fast response and recovery time of 0.97 s and 0.72 s respectively [14]. Jang *et al.* compared the properties of catalytic combustion gas sensors of different heater plate thicknesses i.e. 150 nm and 450 nm. From this study, they identified that sensitivity of the plate is proportional to its thickness. This effect is more notable in methane detection than in hydrogen gas detection. The sensitivity corresponding to H_2 in air for 150 nm and 450 nm thick heaters are 3.65 $mV/10^3$ ppm and 3.81 $mV/10^3$ ppm respectively. In case of CH_4 in air, it is 0.6 $mV/10^4$ ppm and 3.51 $mV/10^4$ ppm [15].

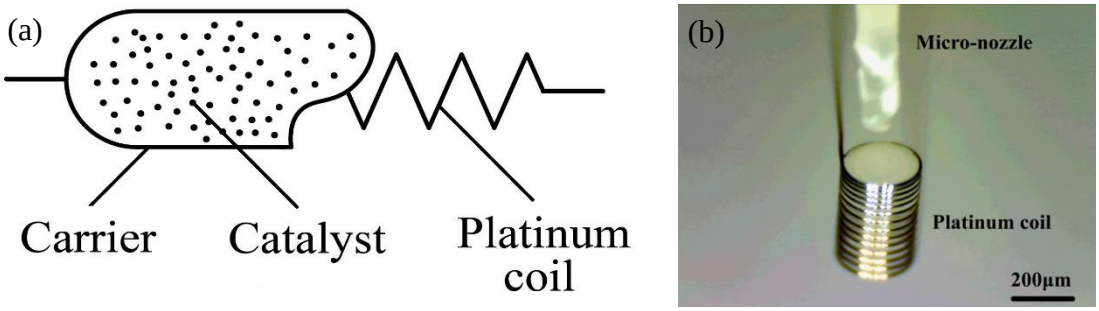


Figure 1.2: (a) Schematic of micropellistor type catalytic gas sensor and (b) placement of Pt coil and the micro nozzle position for Al_2O_3 suspension [16].

Wu *et al.* have further enhanced and developed a novel droplet generating fabrication technique, where they can control the size of the micropellistor by controlling the Al_2O_3 fine dispersion and Pt-Pd catalyst (see figure 1.2). The sensitivity and power consumption of CH_4 in air are 32 mV/10^4 ppm and 120 mW respectively [16].

The second type is a thermoelectric catalytic sensor. This type also generates electrical response because of temperature rise in the active part due to oxidation of the gas molecules. In this technology, it uses thermoelectric effect (Seebeck effect) to generate the electrical signal. The Seebeck effect occurs when there is a change in voltage between two points of the conductors/semiconductors caused by the temperature difference between those two points. McAleer *et al.* reported the first use of Seebeck effect in 1985 for combustible gas sensing [17].

Due to advancement in MEMS, new generations of micro-thermoelectric hydrogen sensors (µ-THS) are being fabricated. Tajima *et al.* focused on preparing low power µ-THS with Pt catalyst and micro heater on a suspended thermal isolation structure. This sensor has a faster response time T_{90}, which consumes less power (0.34 W) and detects between 0.1 and 30*10^3 ppm of H_2 in air [18], whose preliminary work is shown in [19]. Their recent works follow gas sensing for medical diagnosis to detect ppm levels of breath gases, as referred in figure 1.3.a. This includes monitoring of hydrogen concentration (0 to 200 ppm) [20].

Brauns *et al.* have firstly examined the new concept of using highly porous catalyst to achieve high sensitivity with their novel material (tiny Pt nanoparticle linked by phenylenediamine) [21], whose previous study is mentioned in [22]. This sensor has a shorter response time and sensitivity of <150 ms and 220 mV/10^4 ppm for H_2 in air with low power consumption of 30 mW [21]. In recent times, they enhanced the design criteria to achieve better

performances, as shown in figure 1.3.b. With this, the improved sensitivity of 395 mV/10^4 ppm H_2 in air is measured [23].

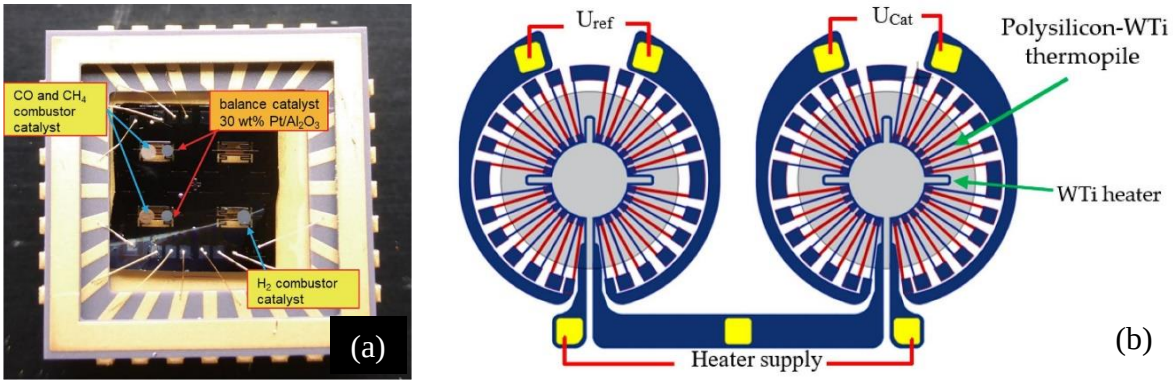


Figure 1.3: (a) µ-THS used in medical breath sensing for hydrogen detection [20] and (b) hydrogen sensor design that uses novel catalyst material (highly sensitive to hydrogen) [23].

1.3.2 Electrochemical hydrogen sensors

The electrochemical sensor detects differences in charge transfer or electrical property due to the electrochemical reaction that takes place at sensing electrodes. The first quantitative hydrogen detection using electrochemical cell was suggested by LaConti and Maget in the early 1970's [24]. Subsequently, Korotcenkov *et al.* reviewed the performances of these types of sensors in hydrogen monitoring for various applications [25]. These sensors are broadly classified into two categories based on their working principle: amperometric and potentiometric.

The amperometric sensor operates at constant applied voltage and measures signal of the diffused current [26]. For any amperometric sensor, there are three important elements: i) electrode, ii) electrolyte and iii) gas permeable layer. Typically, they consist of two electrodes, one acts as a sensing electrode and the other is a counter electrode. These electrodes are made of noble metals (acting as catalyst) for hydrogen oxidation. Sometimes, a third electrode is added for reference that is shielded from the chemical reactions to maintain the constant thermodynamic potential during sensing. Then, these electrodes are immersed in the liquid/solid electrolyte to facilitate the charge transfer. Thus, the electrons flowing from anode to cathode are directly proportional to the H_2 concentration, following the Faraday's law [26]:

$$I = nFQ \qquad \text{Eq. 1.1}$$

where I is the diffused current (C/s), n the number of exchanged electrons per molecule, F the Faraday constant (9.648x10^4 C/mol) and Q the hydrogen conversion rate (m^3/s).

Lastly, a gas permeable layer was added to cover the inlet of the sensing electrode and to prevent leakage. Several advancements were made in terms of sensor size and electrolyte material. Ramesh *et al.* developed a sensor that operates at room temperature using solid electrolyte Nafion, as shown in figure 1.4.a. This sensor has an exceptional selectivity to H_2 of 5 ppm in argon [27], [28]. More recently, Tang *et al.* have demonstrated a continuous amperometric H_2 sensor, as displayed in figure 1.4.b. This sensor uses the unique property and redox reaction of hydrogen in the ionic liquids (ILs) to address the signal drift and cross sensitivity issues [29].

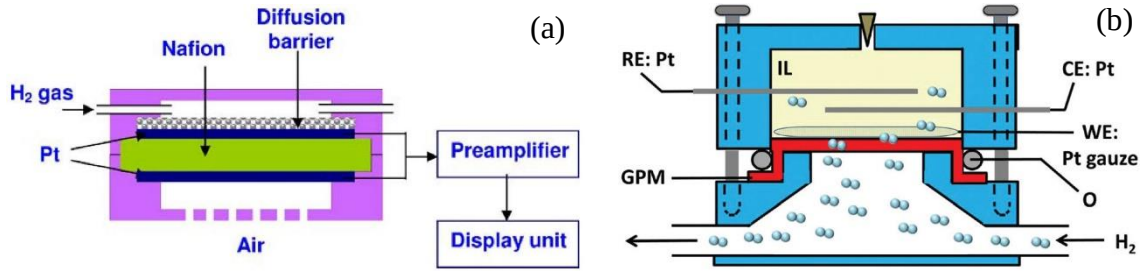


Figure 1.4: (a) Schematic of Nafion based amperometric H_2 sensor [27] and (b) continuous amperometric H_2 sensor with ILs [29].

The potentiometer sensors operate at zero current and measure the potential difference or electromotive force between the working/sensing electrode and the reference electrode. Therefore, hydrogen concentration is given by the electrode potential and can be simply expressed by Nernst equation [25]:

$$E = E^0 + \left[\frac{RT}{zF}\right] \ln\left(\frac{a}{a_0}\right) \qquad \text{Eq. 1.2}$$

where E is the electrode potential, E^0 the standard electrode potential, R the universal gas constant, T the absolute temperature, F the Faraday constant, z the number of transferred electrons, a the analyte chemical activity responsible for detecting H_2 concentration and a_0 the activity of the reference.

The structure of this sensor is similar to an amperometric sensor. They consist of two electrodes made of noble elements and they are both in contact with electrolyte. Recently, Ahmad Fauzi *et al.* have realized a sensor with proton conducting graphene oxide membrane fitted with tungsten trioxide (WO_3), as shown in figure 1.5. This gas sensor has a sensitivity of 50 mV/10^2 ppm for H_2 in air at room temperature and LOD of 11 ppm [30]. On the contrary, Zhu *et al.* have proposed a novel idea of using three-electrode solid electrolyte for hydrogen detection. This system has a maximal detecting range of 12*10^4 ppm of H_2 with corresponding output voltage of 0.65 V, whereas in the two electrode configurations, they encountered a maximal range of 10^4 ppm with output voltage of 0.25 V at room temperature [31]. Li *et al.* developed YSZ based $CdWO_4$|YSZ|Pt sensor that works at high temperature, i.e. 500 °C. It has an exceptional response for hydrogen concentrations ranging between 0.5 and 3*10^4 ppm and sensitivity of 182 mV/10 ppm [32]. Likewise, Yi *et al.* designed the hydrogen sensor based on hierarchical porous hollow SnO_2 nanofiber sensing electrode that has short response time and sensitivity of 5 s and 289.1 mV/10^3 ppm for H_2 in air at 450 °C [33].

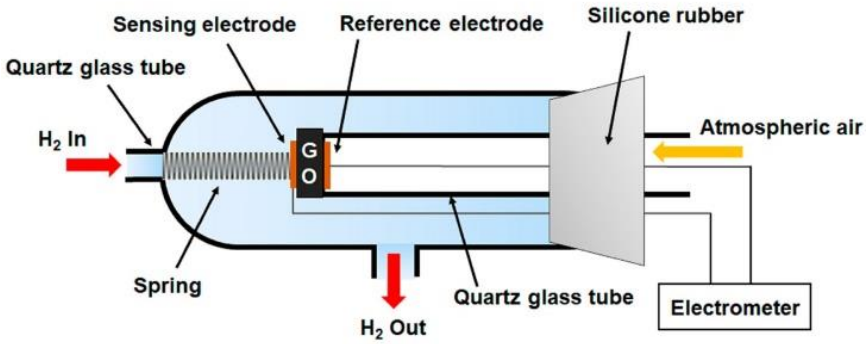


Figure 1.5: Structure of carbon based potentiometric hydrogen sensor with proton conducting graphene oxide membrane fitted with WO_3 for sensing very low concentration of H_2 at room temperature [30].

1.3.3 Fiber optic hydrogen sensors

Optical fiber gas sensors detect change in gas concentrations depending on the variations of optical properties in the coated sensitive materials on adsorbing the gas molecules. This sensitive layer is composed of metal or chemochromic oxide and coated along the fiber length or only on its tip. On exposing the sensor to a hydrogen environment, the physiochemical characteristics of the sensitive film will change, thereby causing variation in optical signal which is transmitted in the fiber optic with reference to wavelength, intensity and phase [34].

Based on this sensing principle, the fiber optical sensors could be classified into five types depending on their measurement techniques: i) micromirror type, ii) evanescent type, iii) interference type, iv) surface plasmon resonance (SPR) type and v) fiber Bragg grating (FBG) type.

The micromirror type fiber optic hydrogen sensor was firstly proposed by Butler in 1991 [35]. A change in gas concentration is observed, due to variation in intensity or reflective index of the sensitive film on exposing it to the gas mixture environment. These sensitive films are of 10 nm to 50 nm thick and coated at the cleaved end of the fiber optics. Xu *et al.* recently developed a reflective hydrogen sensor composed of polarization maintaining fiber (PMF) coated with Pt loaded WO_3 [36]. This sensor has high sensitivity of 18.04 nm/10^4 ppm for 0 to 4*10^4 ppm H_2 in air with a short response time around ≈5 s.

Similar to micromirrors, evanescent type sensors are also intensity based hydrogen sensors but the sensing mechanism depends on the evanescent field. This field occurs at the junction of the fiber core exposed to the optic and the sensitive film. Unlike micromirror, the sensitive film in this sensor is coated on the etched, tapered or side polished fiber core. Tabib-Azar *et al.* proposed the first evanescent field fiber optic hydrogen sensor, as shown in figure 1.6. It is coated with 10 nm of Pd that detects hydrogen concentration from 0.2 to 0.6*10^4 ppm with response time of 20-30 s at room temperature [37]. More recently, Yahya *et al.* have developed a novel evanescent tapered fiber optic hydrogen sensor coated with Pd/ZnO nanostructure that operates at 180 °C [38]. Sensors with ZnO layer thicknesses, such as 150 nm, 200 nm, 280 nm and 550 nm are compared. Out of all, the device with 280 nm thick possesses maximum absorbance response and it shows 64 % higher absorbance after annealing compared to as-prepared samples upon exposure to 1 % of H_2 in synthetic air.

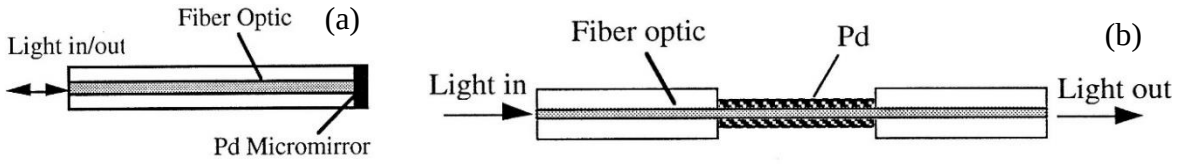


Figure 1.6: (a) Schematic of micromirror type fiber optic hydrogen sensor and (b) schematic of evanescent field type fiber optic hydrogen sensor [37].

The fiber optic surface plasmon resonance (SPR) and fiber optic evanescent field sensors have similar structures. SPR sensors have the sensitive coating on an unclad fiber core generating SPR effect, which is a phenomenon involving electromagnetic surface waves generated at the

interface of metal and dielectric material. Later, variation in gas concentration is identified due to the change in refractive index of the sensitive film caused by change in the wavelength and the intensity in SPR. Chadwick *et al.* disclosed the first fiber optical SPR hydrogen sensor with Pd/Ni alloy film [39]. This sensor operates between 0.1 and $10*10^4$ ppm range of H_2 concentrations in air and shows a large reflected light intensity of 6.6 % for $1*10^4$ ppm of H_2 in air. More recently, Aray *et al.* have reported an experimental investigation of fiber optic H_2 sensor using an oxygen defect-induced plasmonic that uses nanostructured α-MoO_3 thin film as sensitive material for the first time [40]. This sensor has a sensitivity of 38.1 pm/ppm and detects low concentration between 0.15 and $2*10^3$ ppm of hydrogen in air.

The interference type sensor detects the variation in the gas concentration due to the change in dimension or refractive index of the sensitive film. The schematic of this sensor is shown in figure 1.7. The interference type hydrogen sensor was first reported by Butler in 1984, which used a sensitive coating of Pd (10 µm) [41]. On exposing the device to H_2 environment, it resulted in formation of hydride PdH_x with *x* dependent on partial pressure of hydrogen that was larger than pure Pd. Lately, Zhang *et al.* demonstrated a high-birefringence fiber loop mirror (HBFLM) coated with Pd/WO_3 film on PMF [42]. The variation in gas concentration is identified by the shift in interference spectrum of HBFLM caused by change of strain in PMF. This sensor has sensitivity of ≈2.18 nm/10^4 ppm from 0 to $1*10^4$ ppm of H_2 concentration in air.

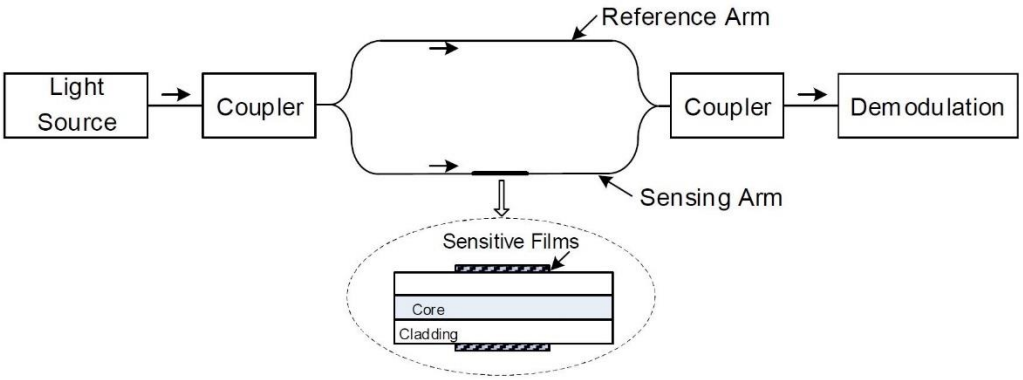


Figure 1.7: Schematic of interference type fiber optic sensor [43].

Finally, the FBG is an intrinsic device, which controls the light property propagated inside the fiber. It consists of a periodic structure that has refractive index modulation with the constant modulation period in the core of an optical fiber. The FBG has a short modulation period of less than 1 µm. Sutapun *et al.* proposed the first FBG based hydrogen sensor with a sensitive

coating of Pd (560 nm) in 1999 [44]. This sensor showed a linear sensitivity of 0.3-1.8*10^4 ppm H_2 in nitrogen (N_2) at room temperature. Almost after a decade, Caucheteur *et al.* developed a hybrid fiber grating consisting of long period fiber grating (LPG) and superimposed uniform FBG [45]. This LPG has a modulation period ranging between 10 µm and 100 µm. Both gratings were coated with Pt/WO_3 sensitive film and this hybrid configuration has detection threshold of 1.5*10^4 ppm H_2 in air at -50 °C.

More recently, Yang *et al.* have proposed a novel and highly sensitive WO_3-Pd_2Pt-Pt coated FBG hydrogen sensor based on intensity modulation that uses a self-referenced demodulating method (see figure 1.8). This sensor has excellent LOD for H_2 concentration <10 ppm in air at room temperature [46].

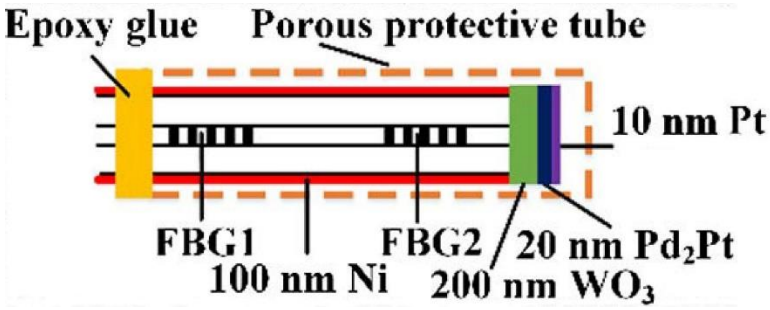


Figure 1.8: Schematic of high sensitive WO3-Pd2Pt-Pt coated FBG type hydrogen sensor [46].

To summarize, Wang *et al.* briefed all the types of previously mentioned optical sensors [43]. From this review, it is clear that the FBG hydrogen sensors are one of the most favorable fiber optic sensors with potential applications, as they are capable of multipoint detection on having different wavelengths on single fiber. However, the main difficulty lies in the miniaturization. The size reduction helps to improve sensor's accuracy but weakens the strength of fiber at the same time. In case of interference types, they have high sensitivity, accuracy and good repeatability whereas micromirrors have relatively simple design and low cost. Although the evanescent field sensors have high sensitivity, the device length could not be reduced, as it is directly proportional to the sensitivity. The SPR type hydrogen sensors are extremely sensitive as interference type sensors and have fast response on exposure but they lack multipoint detections. Currently, a number of researches are being conducted to identify nanomaterials that produce a strong SPR effect.

1.4 Hydrogen detection based on physical properties

1.4.1. Thermal conductivity hydrogen sensors

Thermal conductivity sensors detect the variation of heat losses measured from the hot body to the surrounding gas. These types of sensors are mostly suitable for hydrogen detection as the thermal conductivity of H_2 is seven times higher than that of normal air, i.e. 0.18 W/mK and 0.026 W/mK at room temperature [47]. Thermal conductivity experiments for gas mixture analyses have been taking place since many years [48]. The first hydrogen sensor based on thermal conductivity principle was used in 1913 for monitoring the variation of gas mixture while filling the airships [1].

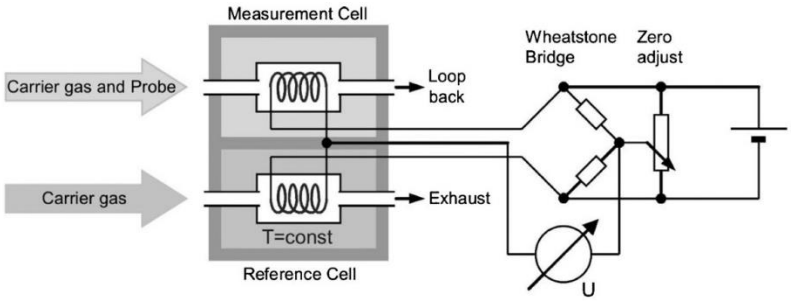


Figure 1.9: Schematic diagram of the resistors connected to the Wheatstone bridge for thermal conductivity measurement [2].

The classical sensors have two resistors, one acts as the reference and the other is exposed to the target gas. Both the resistors are connected to the Wheatstone bridge as referred in figure 1.9. The schematic looks similar to a catalytic pellistor type sensor but the detection principle is completely different. In case of hydrogen detection, the reference resistor is exposed to normal air and the measuring resistor to the gas mixture environment, thereby increasing the heat loss. This causes an imbalance in the Wheatstone bridge and, hence, the change in gas concentration is measured using the overall resistance.

Simon *et al.* have designed and characterized micromachined thermal conductivity sensors for hydrogen detection in automotive fuel cell systems. The measuring resistor was made of platinum on a thin silicon-nitride membrane and the reference resistor on bulk silicon (see figure 1.10.a). This sensor has a LOD of $0.2*10^4$ ppm hydrogen in air and it withstands a wide range of temperature from -40 to 130 °C [49]. Tardy *et al.* proposed a dynamic thermal conductivity gas sensor based on transient thermal response. The sensitive microplates are made

of silicon carbide due to the fact that they have high thermal diffusivity [50]. This gas was specifically designed for determining carbon monoxide (CO) in H_2 for fuel cells and has a resolution of 150 ppm of CO in H_2.

With the recent advancements in MEMS technology, Graaf *et al.* have miniaturized the sensor design and fabricated micrometer sized thermopiles of 300x300x0.7 μm^3 [51]. This sensor has a sensitivity of 6 $\mu V/10^4$ ppm H_2 in air at 1 mW heat dissipation without amplification. More recently, Berndt *et al.* reported MEMS based nm-thick hotplate on thin silicon-nitride membrane for hydrogen sensing in automotive applications, as shown in figure 1.10.b. This sensor exhibits LOD of 2000 ppm H_2 in air and has a low power consumption of 90 µW [52].

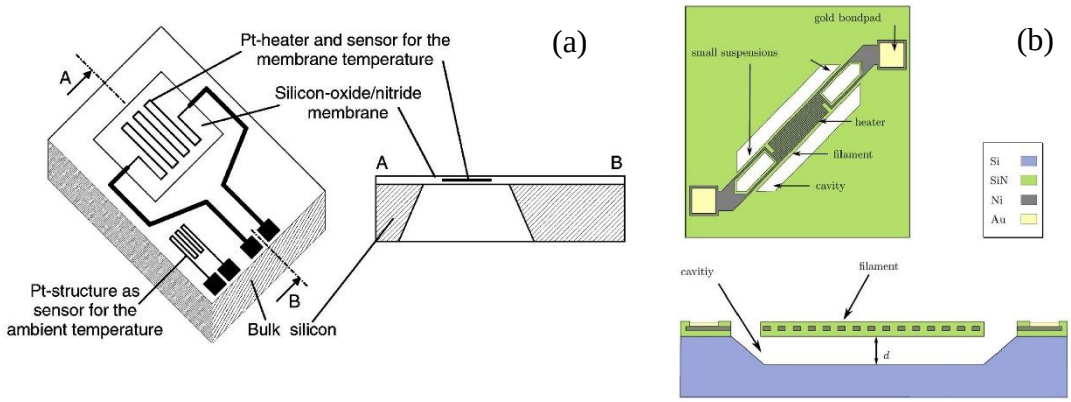


Figure 1.10: Schematic view of the sensor element in thermal conductivity measurement used for automotive application (a) Simon *et al.* (2002) [49], (b) Berndt *et al.* (2020) [52].

1.4.2 Lidar hydrogen sensors

Light detection and ranging (Lidar) is an ideal technique to monitor large distances remotely and safely. Commonly, lidars are used in high-resolution mapping for applications like surveying, geography, atmospheric physics, etc. Lidar has a similar operation principle as Radar (Radiometry detection and ranging). The main difference is self-explanatory: lidar uses a high-pulsed laser whereas radar uses radio waves to detect the target. Smullin and Fiocco firstly conducted definite measurement using lidar in 1962, just after the invention of the functional laser by T.H. Maiman in 1960 [53]. The experiment is to focus the optical pulse on

the surface of the moon and detect the echoes [54], [55]. The lidar technique is presently used in a wide range of applications, as referred in [56], [57].

Lidar techniques use different types of scattering, such as Raman scattering, Mie scattering, Rayleigh scattering, etc. Raman scattering is an inelastic scattering of photons when a molecule is excited by an intense light source, as shown in figure 1.11. This small fraction of light is scattered at different frequencies from the original frequency of the incident light. When frequency shifts with creation of photons, resulting in longer wavelengths, it is called Stokes and if the shift happens due to absorption of photons, then it is called anti-Stokes (shorter wavelength). In general, Stokes scattering intensity is higher than anti-Stokes scattering and exceptionally strong when the Raman shift is huge. Due to the fact that hydrogen gas has a strong Raman effect, the Raman lidar is the most appropriate technique for hydrogen remote sensing [58].

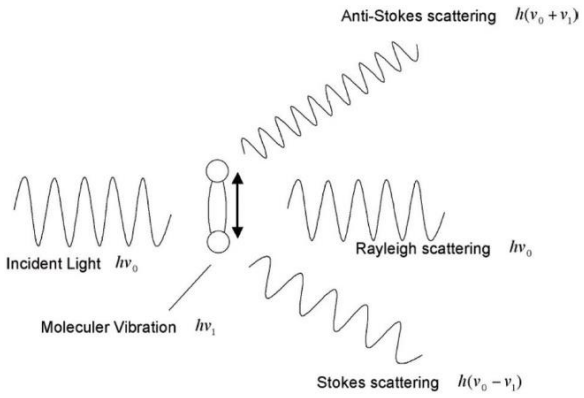


Figure 1.11: Raman scattering [58].

Miya *et al.* have proposed a compact Raman lidar for hydrogen leakage detection. These in-lined Raman lidars use laser-induced fluorescence echoes to detect targets from long distances (i.e. 70 m). The sensitivity of the developed system is not adequate because it could not sense H_2 concentration below $4*10^4$ ppm at 50 m distance. In spite of that, it could detect a thin smoke at the same distance [59]. Later, Asahi *et al.* optimized the setup by using Nd:YAG laser of wavelength 354.7 nm and Galilean telescope of aperture 170 mm. This system detected the lowest concentration of $0.6*10^4$ ppm of H_2 in air at a distance of 13 m [60]. Shiina reported the compact and the mini-Raman lidar used for quantitative measurement of hydrogen. The developed diode pumped solid state (DPSS) laser-based Raman lidar detects H_2 of $1*10^4$ ppm in air within 50 m distance with accumulation time of 30 s (refer figure 1.12.a). The other LED based mini-Raman lidar could detect the same at 0-20 m distance in 3.5 mins [58] (see

figure 1.12.b). From the same group, Sugimoto *et al.* measured 100 ppm of H_2 in a small area (<1 cm^2) using the developed Raman lidar [61].



Figure 1.12: (a) Outlook of compact Raman lidar, (b) experimental setup of LED mini-Raman lidar, (c) Hydrogen nozzle of LED mini-Raman lidar [58].

Concurrently, Liméry *et al.* have developed multi-channel Raman lidar to monitor hydrogen concentration in the radioactive environment (shown in figure 1.13). This sensor performs high resolution profiling of hydrogen gas and water vapor simultaneously. This system has a LOD of 500 ppm for H_2 in dry air at 500 m distance in 11 mins [62].

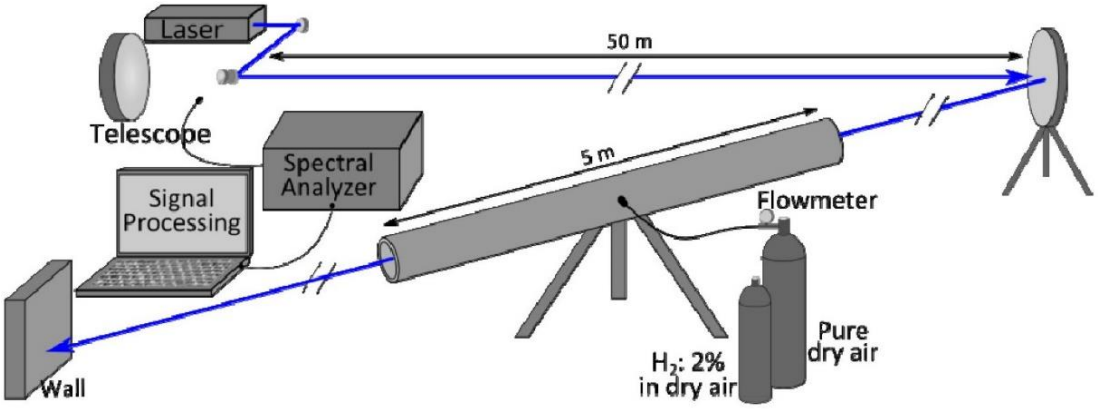


Figure 1.13: Experimental setup of multi-channel Raman lidar developed by Liméry *et al.* [62].

1.5 Comparison between chemical and physical sensors

Hydrogen sensors are broadly used in many industries for safety reasons. Based on the applications, one's requirement varies. From the literature, it is clear that the history of hydrogen gas sensors were discussed over a century [1]. There were numerous technologies developed and demonstrated, in which few of them were discussed previously.

To begin with, the chemical sensors are very stable and highly sensitive but have longer response time. This is due to the chemical absorption and desorption process. Until now, many types of hydrogen sensors have been manufactured and sold commercially, including electrochemical, catalytic and fiber-optic sensors. Nevertheless, none of them meets the expectation to survive in a harsh environment. From table 1, the catalytic type sensors need at least 5 to $10*10^4$ ppm of oxygen to operate and have no selectivity towards hydroge [23]. In addition, there is a risk of poisoning due to catalyst contamination. On the contrary, they have a long lifetime and are more stable [16], [20].

In terms of cost, electrochemical sensors need expensive electrical equipment to perform amperometric or potentiometric measurements [2]. Both catalytic and electrochemical sensors are cross sensitive to other reducing gases and these make those unreliable [25], [26], [63]. In the case of fiber optic based sensors, they use sensitive coatings and light signals for gas monitoring [37], [39], [40], [42]. The problem lies in the cost, size of the structure and LOD. If the precision is better, then it has no multi point detection and vice versa [43].

The physical sensors are those that do not use any sensitive coatings like chemical sensors. This means it has a short response time [2]. Thermal conductive sensors are more stable, robust, less expensive and have a wide measuring range yet they suffer due to cross-sensitivity issues and have high LOD [51], [52]. Raman lidar based sensors have high selectivity towards hydrogen and could monitor over long distances (several meters). For instance, to monitor daily air quality, gas or dust in construction sites [62]. These kinds of sensors are huge and expensive due to the cost of laser and spectrum analyzer and consume high power [60]. Finally, the overall advantages and disadvantages of different techniques have been briefly summarized in table 1.1.

Table 1.1: Advantages and disadvantages of chemical and physical sensors [1], [2], [16], [20], [23], [25], [26], [37], [39], [40], [42], [43], [51], [52], [60], [62], [63].

Type	Technique		Advantages	Disadvantages
Chemical	Catalytic	Pellistor	Robust	No selectivity
		Thermoelectric	Easy to operate Wide operating temperature Stable Durable	Requires oxygen for detection Long response time Temperature sensitive High power requirement Catalyst can be inactive (or) poisoned due to contamination
	Electro-chemical	Amperometric	Sensitive	Non-durable
		Potentiometric	Low power consumption Do not require element heating High operating temperature	Expensive Cross sensitive to CO Needs periodic calibration
	Fiber optic	Micromirror	High sensitivity	Complexity in miniaturization
		Evanescent field	Simple structure Less expensive Long distance monitoring Low response time	Only suitable for point measurement Low mechanical stability
		SPR	High precision Sensitive and responsive	No multipoint detection Expensive Complex structure
		Interference	High accuracy Good repeatability Sensitive	Big structure No temperature compensation Cannot work in unstable environment
		FBG	Multi point detection Wide measurement range Favorable to remote sensing Immune to intensity fluctuations	Low sensitivity High LOD
Physical	Thermal conductivity		Short response time Less expensive Stable Robust Wide measuring range	No selectivity Cross sensitive to Helium High LOD Heating element reacts with gas
	LIDAR		Long distance measurement High selectivity	High energy consumption Large structure High LOD Expensive

1.6 MEMS sensors with/without sensitive coating

1.6.1 Gas sensing with cantilevers

Cantilever-based gas sensing has a long history after the breakthrough of the first real time cantilever application for atomic force microscopy (AFM) in 1986 by Binnig *et al.* [64]. The shift in resonance frequency due to cantilever bending during chemical adsorption was well described by Wilfinger *et al.* [65]. They detected the mechanical deflection of a large cantilever beam (50x30x8 mm^3) by electrically induced thermal expansion. The mechanical excitation was performed by temperature gradient in the cantilever, causing deflection and localized thermal expansion that produces desired gradient in a diffused resistor situated near the cantilever support. Gimzewski *et al.* have reported the first silicon-based microcantilever for chemical sensing application in 1994, as shown in figure 1.14.a [66]. This sensor has LOD and sensitivity of $\approx 10^{-5}$ K and 1 pJ at 300 K respectively. Similarly, Thundat *et al.* observed shift in resonance frequency due to vapor adsorption caused by the thermal and ambient induced deflection [67], [68].

Later, in 2000, the first surface-micromachined MEMS cantilever for hydrogen sensing was proposed by Britton *et al.*, presented in figure 1.14.b [69]. This sensor was selectively coated with gold and palladium for mercury and hydrogen sensing. The experiments were done at room temperature. The Pd coated H_2 sensor has better sensitivity for increasing thickness of palladium but possesses longer response time than thinner ones, due to the fact it attains equilibrium slowly. The sensor has a LOD of 100 ppm of H_2 in N_2.

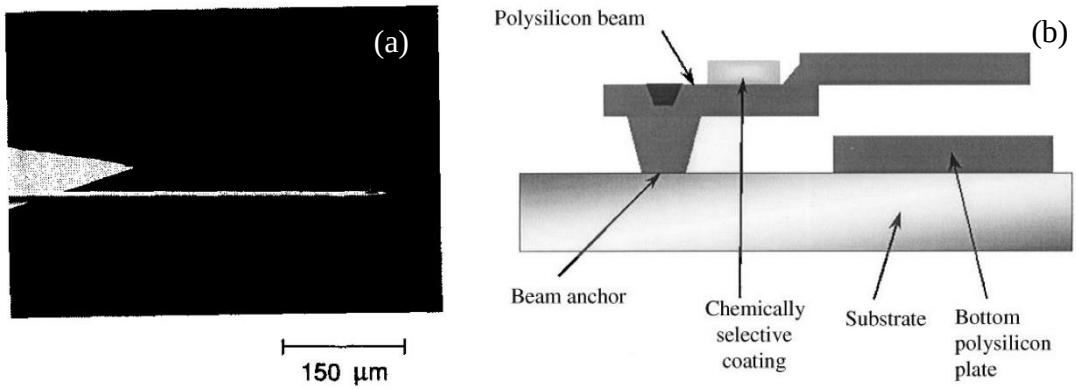


Figure 1.14: (a) SEM image of first silicon based cantilever used in chemical sensing by Gimzewski *et al.* [66] and (b) cross-section schematic of first surface micromachined MEMS cantilever used for H_2 detection by Britton *et al.* [69].

The same group has further optimized the parameters and decreased the power consumption (84 mW), to detect H_2 between 0.1 and $100*10^4$ ppm with improved response time, less than one minute [70], [71]. Likewise, interesting works were done by other groups, which are worth mentioning in the field of gas sensing [72]–[76].

When most of the research was based on gas sensors with functionalized coatings, Tétin *et al.* have proposed alternative ways of using silicon cantilevers as chemical sensors without sensitive coatings (see figure 1.15.a) [77]. This sensor produces shifts in two basic parameters associated with resonance frequency, i.e. density and viscosity under a gas mixture environment. The results prove that the cantilever geometries with higher width/height ratio have best sensitivity. Their LOD for He/N_2 and CO_2/N_2 are 70 and 106 ppm respectively. Then, Dufour *et al.* summarized the new idea of using uncoated microsystems for gas sensing applications, by stating the drawbacks of using sensitive coatings (higher response time and lower reliability) [78]. Therefore, these uncoated microsystems are more reliable and reversible, yet do not have intrinsic selectivity that limits the applications. In addition, it can sense single gas concentration only, like in environmental monitoring applications.

Boudjiet *et al.* have developed a hydrogen sensor without sensitive coating and have proposed a strategy to improve its sensitivity by optimizing cantilever's geometry [79]. Therefore, they compared cantilevers with different shapes (rectangular, U- and T-shaped). From their analyses, it is clear that the short rectangular shaped cantilevers are the most sensitive for the change in gas density. However, the variation in thicknesses only changes the resonance frequency without affecting the sensitivity [80]. The LOD for H_2 in N_2 is 100 ppm, corresponding to the density variation of 0.11 mg/L, which is very low compared to state of art piezoelectric gas density sensors (88 mg/L) [81].

Even though the work mentioned in [78], [79], [81], [82] were concerning uncoated gas sensors, they either belong to silicon or piezoelectric based cantilevers working in a few kilohertz's frequency range. Therefore, in our study we propose cantilevers based hydrogen sensors with chosen material that is capable of working in harsh environments. The outline of this work will be explained elaborately in §1.7.1. In addition, capacitive ultrasonic micromachined transducers (CMUTs) based sensors can also be suitable for high frequency applications.

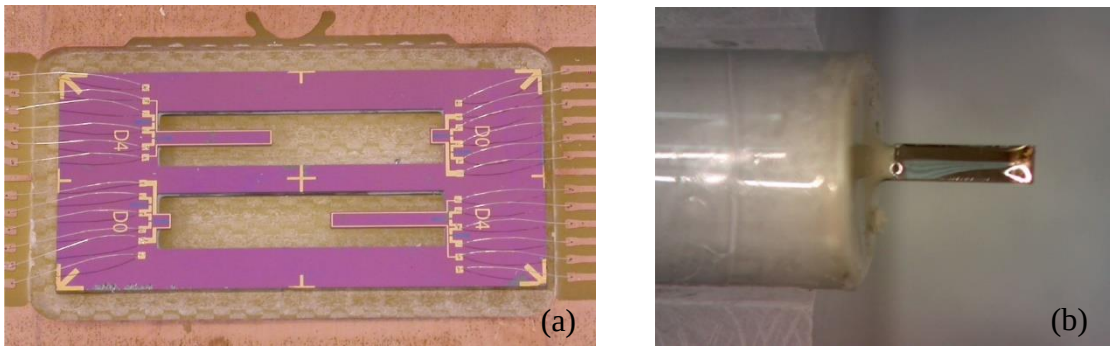


Figure 1.15: (a) Uncoated silicon microcantilever with electromagnetic actuation and piezoresistive detection [77]. (b) Millimeter sized state of art piezoelectric cantilever for gas density monitoring [81].

1.6.2 Gas sensing with capacitive micromachined ultrasonic transducers

The interest for capacitive micromachined ultrasonic transducers based gas sensors is growing in recent years. Unlike cantilevers, CMUTs were predominantly used in medical imaging and therapeutic applications [83], [84]. The first publication based on CMUT gas sensing was published in 2007 by Park *et al.* [85]. The detection of change in chemical was identified by a shift in the oscillating frequency due to the mass-loading effect. The schematic of gas measurement setup is shown in figure 1.16.a. They have used CMUTs with a resonant frequency of 6 MHz, originally developed for medical and underwater ultrasonic imaging by Stanford group [86]. These CMUTs were drop coated with three different polymers polyallylamine hydrochloride (PMMA), polyethylene glycol (PEG) and polyvinyl alcohol (PVA) to detect analytes such as water, isopropanol, acetone and methanol. In all, PMMA showed better sensitivity and LOD of $41.6*10^{-3}$ ppm/Hz and $16.6*10^{-3}$ ppm for water respectively [85].

Subsequently, Lee *et al.* and Park *et al.* continued working on CMUTs with higher resonance frequency than previous ones, i.e. 18 MHz (with 1000 individual cells in parallel) for detection of dimethyl methylphosphonate (DMMP) in air. These transducers were functionalized with 50 nm of polyisobutylene (PIB), which possesses sensitivity and LOD of $37.8*10^{-3}$ ppm/Hz and $21*10^{-3}$ ppm [87]–[89]. Thereafter, Lee *et al.* further optimized the CMUT design by reducing the diameter of circular plates from 9 µm to 5.3 µm, which produced CMUTs with higher resonance frequency, i.e. 47.7 MHz (consisting of 1027 cells). Henceforth, their hypothesis made a huge impact on mass sensitivity from 130 zg/Hz/µm² to 48.8 zg/Hz/µm².

Also, the sensitivity and LOD are remarkable for DMMP in air, which are $30.6*10^{-6}$ ppm/Hz and $16.8*10^{-6}$ ppm respectively [90], [91].

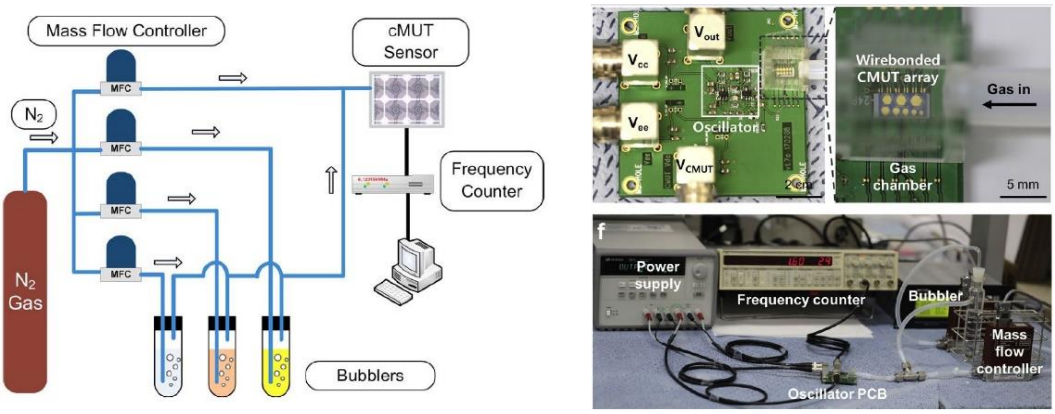


Figure 1.16: (a) Schematic of first CMUT gas sensor setup used for chemical detection in nitrogen [85] and (b) CMUT gas sensor setup for VOC detection with low operating voltage [92].

Later, Mahmud *et al.* have explored low power consuming gas sensors for environmental monitoring. These anodic-bonded functionalized CMUTs operate at 4.33 MHz and consume 0.77 mW with average sensitivity of 270 Hz/ppm for 10-20 ppm concentration of toluene. Early works have been conducted on a transducer with 50 MHz working frequency that consumes 70 mW [93]. There are other potential gas sensors based on CMUTs technology, which are still under research for various chemical/bio/gas sensing applications [92], [94], [95].

1.7 Our approach for hydrogen gas sensing

The aim of this project is to develop a microsystem to monitor the presence of hydrogen in radioactive environments. As explained in §1.2, ANDRA has constructed a deep geological disposal facility to store radioactive wastes. This underground facility will be vented during the operating period and surveilled after closure, for safety reasons. In spite of the high sensitive chemical sensors, they suffer from certain drawbacks, such as high response time (due to chemical adsorption and desorption), low reliability and irreversibility, which are mainly related to their sensitive coatings. On the other hand, the physical sensors have comparetively less aging due to absence of sensitive coating and short response time but the limit of detection are high than chemical sensors. In addition, most of them are not designed to work in hostile environments (refer §1.5). The targeted application needs a small size, robust, durable and

highly responsive sensor that could detect less than 4% of hydrogen in the environment. Since hydrogen is explosive when it is 4-70 % in the volume of air.

In our study, we propose two microsystems for hydrogen monitoring, as explained below. Both detect change in binary gas mixture based on variation in physical properties, such as mass density and acoustic velocity. These sensors are not coated with any sensitive materials to absorb the gas of interest. This makes it highly responsive and durable.

1.7.1 3C-SiC microcantilever based gas sensor

Conventional gas sensors are made of silicon or piezoelectric ceramics, as presented in §1.6.1. Classical systems suffer from aging, low reliability, and inability to survive harsh environments. Therefore, our first microsystem is made from silicon carbide (SiC). This work is a continuation of Boudjiet's PhD thesis [96], but the present study uses a better and more suitable choice of material that fits the targeted application. Here, SiC is advantageous over conventional materials due to the following reasons:

- Robust and durable – due to their impressive mechanical and physical properties, it is a suitable material to work in hostile environment;
- Chemical stability – SiC is inert to most of the chemicals and resistant against all commonly used acids and solvents during microfabrication. This makes it almost universally corrosion-resistant;
- Threshold energy – generally semiconductors generate defects on exposure to extreme radiation and these defects are directly proportional to the threshold energy of the material. In the case of SiC, the threshold energy is higher than silicon, which makes it more adaptable for radiation-exposed environments.

More than 250 polytypes of SiC are present based on their crystalline structures [97]. Out of all, in our study, we chose to work with cubic polytype, i.e. 3C-SiC. This allows us to grow 3C-SiC (100) thin films epitaxially on inexpensive Si (100) substrates.

The 3C-SiC microcantilever works on electromagnetic actuation. This cantilever-type gas sensor does not use any sensitive coating and has two detection techniques for binary gas mixture analyses, namely: i) induction and ii) piezoresistive. In both cases, to generate vibrations, an AC current $\left(\vec{I}(t)\right)$ is passed through the conductive wire placed at the cantilever

periphery. In the presence of a magnetic field $(\vec{B})$ collinear to the longitudinal axis of the beam, an AC Lorenz force $(\vec{F}(t))$ is created at the microcantilever free-end and induces out-of-plane vibrations as shown in Figures 1.17 and 1.18. Here, the 3C-SiC microcantilevers work in low frequency range, i.e. few kHz, at resonance mode.

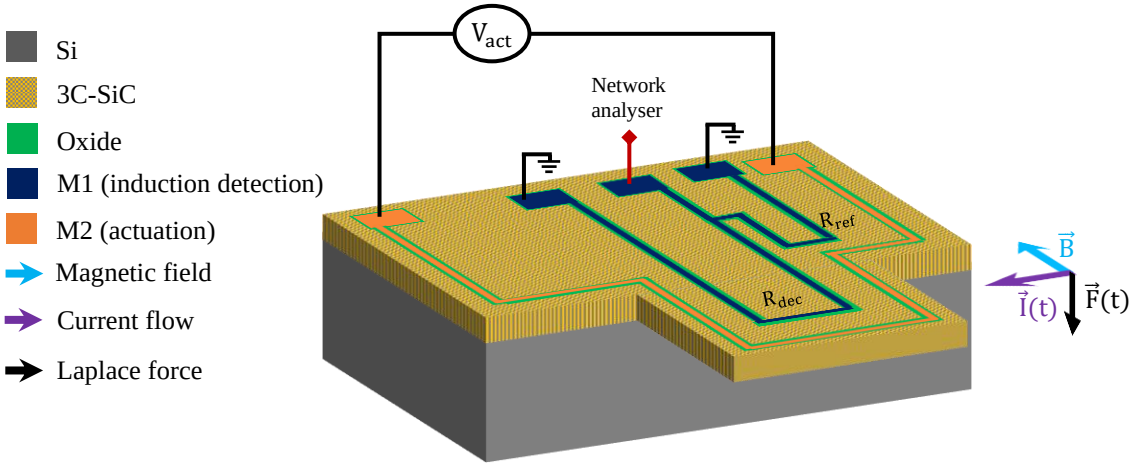


Figure 1.17: 3C-SiC based microcantilever that works on electromagnetic actuation and induction detection (method I).

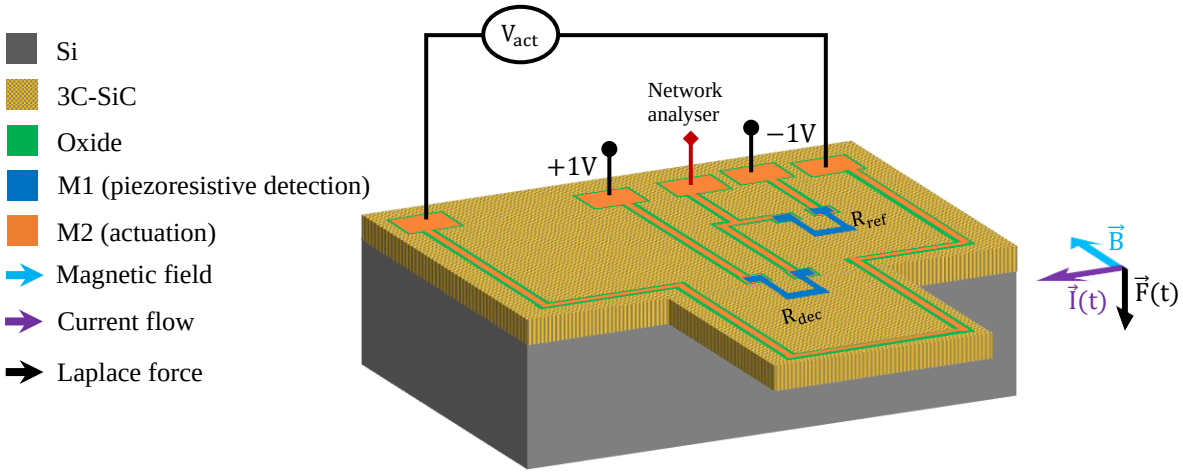


Figure 1.18: 3C-SiC based microcantilever that works on electromagnetic actuation and piezoresistive detection (method II).

Both induction and piezoresistive detection consist of two resistors, where one is on the stable part that acts as reference (R_{ref}) and the other one on cantilever for detecting the change in motion (R_{dec}). These resistors are composed of metal 1 (M1) and the conducting wires are of metal 2 (M2). The schematic of gas measurement setup for this method is shown in figure 1.19 and has been clearly explained in section 2.5. Here, the cantilever is actuated using electromagnetic actuation and the detection is based on change in gas mixture by identifying

the shift in resonance frequency (Δf_r). The background of choosing material, their complex fabrication processes, characterization results in air to verify the device functionality and detection of hydrogen in nitrogen will be detailed in chapter 2.

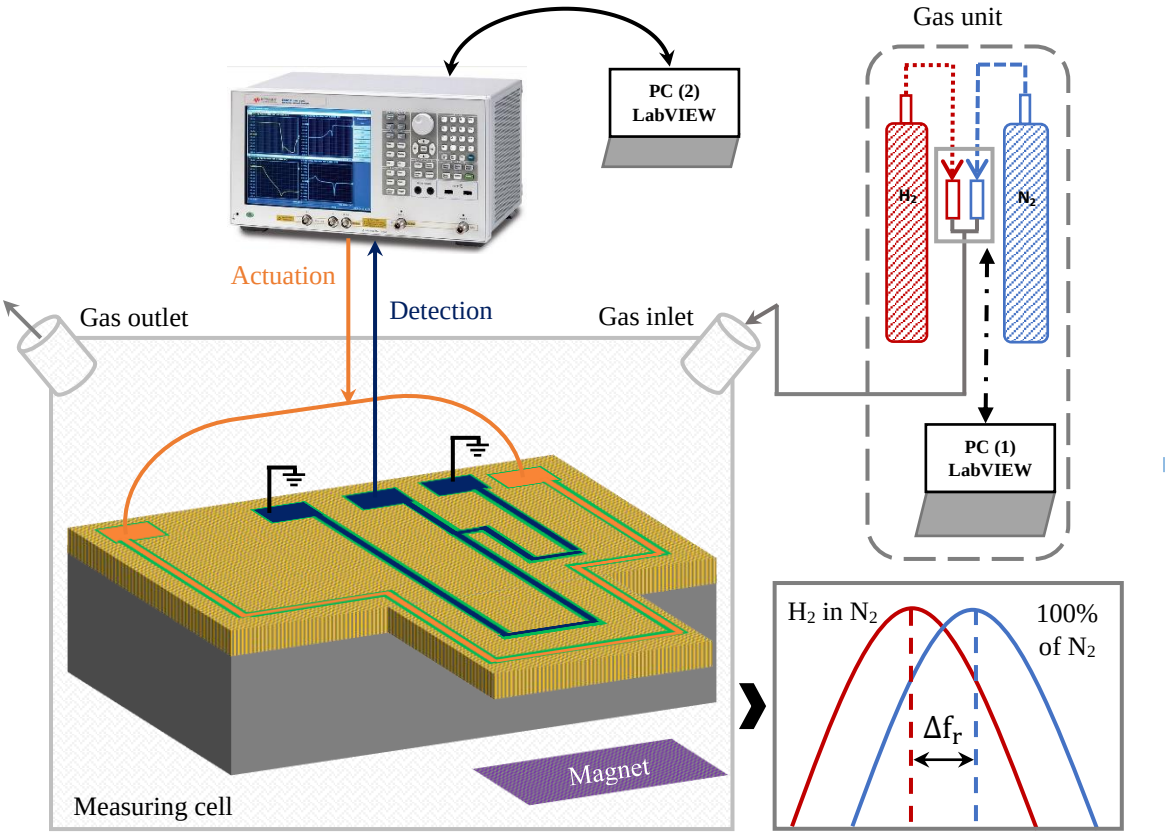


Figure 1.19: Schematic of experimental protocol to measure change in binary gas mixture due to shift in resonance frequency using 3C-SiC microcantilever, which works on electromagnetic actuation and induction detection (method I).

1.7.2 CMUT based gas sensor

The second system is surface micromachined CMUT that works on electrostatic mechanism. Unlike cantilevers, CMUTs are membrane based resonant systems, as depicted in Figure 1.20 and 1.21. This silicon nitride (SiN) membrane helps us quantify certain physical quantities, like acoustic impedance and acoustic velocity while exposed to various gas environments. It is notable that CMUTs were manufactured for ultrasound imaging applications as mentioned in [98]. Later, they have been used in chemical/gas sensing applications due to the following reasons:

- Versatility – can be used for range of applications on modifying few design parameters;
- Scalability – the size of the device can be modified based on application need and CMUTs do not need huge external power supply units;
- Advanced manufacturing techniques – surface micromachining and wafer bonding processes are made simpler due to growth in microelectronics industries;
- Parallelism – enhances the resolution by controlling frequency noise on adding multiple homogenous micro resonators in parallel. Also, reduces the risk of false alarm for any chemical/gas sensors and no risk of device failure.

The objective of using CMUTs is to address gas detection using other physical quantities, such as acoustic impedance and acoustic velocity. Firstly, the variation of acoustic impedance is identified by monitoring variation in CMUT resonance frequency due to change in gas mixture (method III). This detection mechanism is classically used in most of the gas sensing applications with CMUTs. Figure 1.20 shows a schematic of electrostatically actuated CMUT, which has been placed in a gas chamber for binary gas mixture analysis. In addition, the graph represents the detection technique, i.e. shift of resonance frequency (Δf_r) in the admittance for change in gas concentration. This shift is due to change in a physical property of gas, i.e. mass density. Here the CMUTs work in high frequency range, at resonance mode.

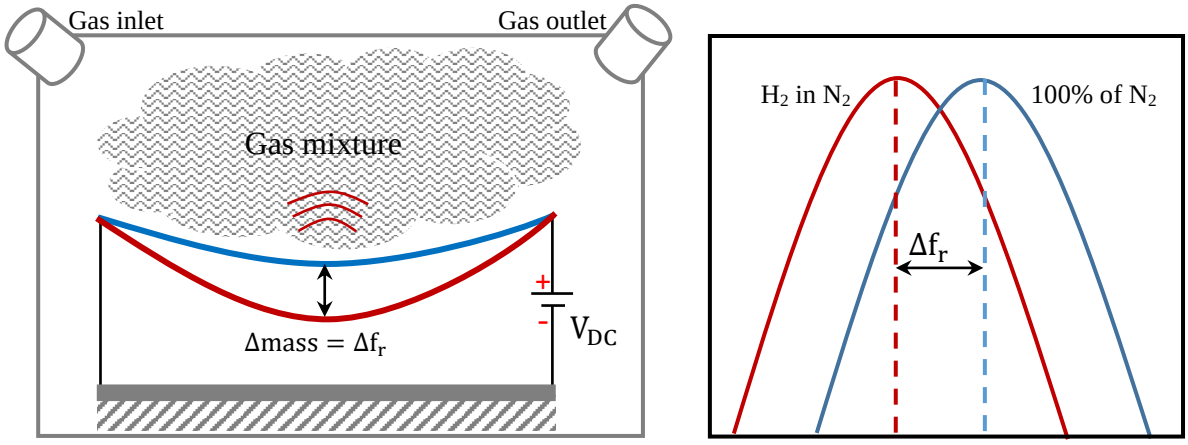


Figure 1.20: Schematic of gas detection with CMUTs using resonance mode approach (method III) [99].

Secondly, the variations in gas concentration by change in acoustic velocity is detected using time of flight (ToF) technique [100]. In both methods III and IV, the CMUTs are actuated electrostatically. This detection mechanism is represented as method IV in this study. The main reason for using this technique for hydrogen sensing is that the ultrasound velocity of hydrogen is 3.8 times higher than the velocity of air at room temperature. Hence, it is natural to try gas

discrimination using this physical quantity. To mention, the ultrasound velocity of hydrogen and air are 1320 m/s and 343 m/s respectively at room temperature [47]. Using this principle of detection, one can monitor variation in gas acoustic property, i.e. ultrasound velocity. Unlike the previous method, this technique needs two sets of CMUTs, where one acts as ultrasonic emitter and the other as ultrasonic receiver, to emit and receive ultrasound in air (see figure 1.21). Transducer fabrication for air application is very challenging and many approaches exist [93], [101]–[105]. One of the main issues is acoustic mismatching in transducers that work in air, which often leads to design sensors with high sensitivity but low frequency bandwidth, i.e. <50 %, while in water, frequency bandwidth higher than 80 % are easy to achieve an optimization. This aspect will be explained in chapter 3. Here, we have chosen a very different approach from the usual one, in order to produce air-coupled CMUT ultrasonic sensors with the highest possible bandwidth.

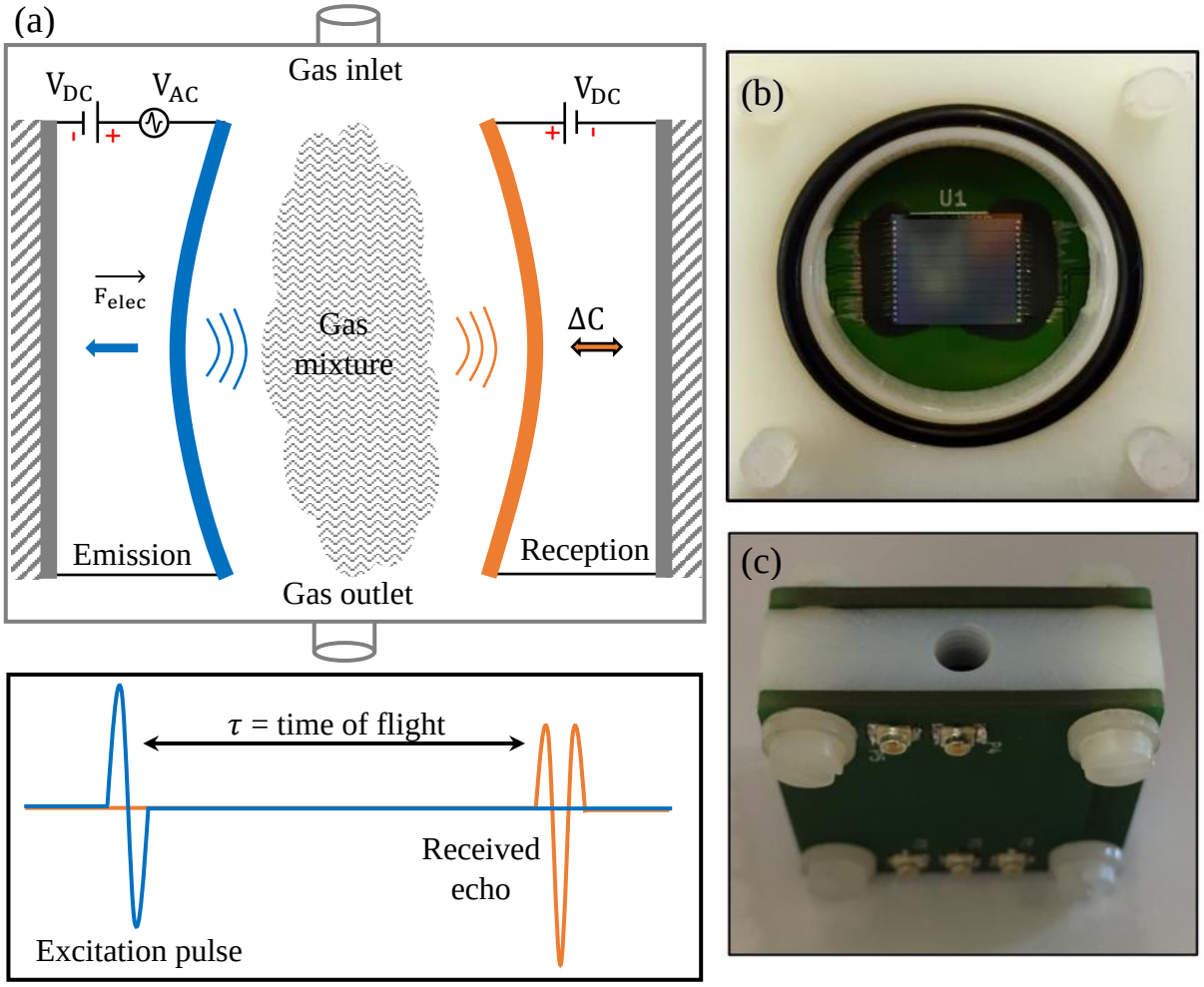


Figure 1.21: (a) Schematic of gas detection with CMUTs using time of flight detection (method IV) [100], (b) Inner view of the fabricated measuring cell with emitter/receiver prototype and (c) completely packed gas sensor unit to perform time of flight measurement in air.

With the chosen CMUT technology, the two approaches can be addressed in the same device. In previous works from GREMAN, i.e. in PhD thesis of Senegond, he has shown that a CMUT with resonance frequency in the MHz range (typically from 5 to 10 MHz) could able to emit ultrasound in air at 1 MHz, when it is forced to work in quasi-static regime [106]. So in the framework of project H2MEMS, it is shown that CMUT can work as a "bimodal sensor" and it is able to detect two different acoustic properties without changing its design. Therefore, for the first time we will show the shift of resonance in air by small change in acoustic impedance even if acoustic coupling between CMUT and gas medium is very low. Finally, we will also demonstrate the working of CMUT in a "quasi-static" regime, as an acoustic emitter in air with an innovative and relevant application in chapter 3.

Conclusion

To summarize, this first chapter is solely dedicated to illustrate the need for the project H2MEMS and distinguish existing hydrogen sensors based on chemical and physical detection. The chemical sensors disclosed in §1.3 show best sensitivity and limit of detection for very low hydrogen concentrations. Despite their great performances, they still suffer from certain drawbacks mainly associated with sensitive coated layers, such as fast ageing, longer response time, cross sensitivity to other gases, etc. The currently available physical sensors have overcome the disadvantages of chemical sensors but they still have high limits of detection and low selectivity.

The traditionally and commercially used chemical and physical hydrogen sensors until date have their own advantages and disadvantages. In addition, most of them are not designed to work in hostile environments, as explained in §1.5. Therefore, we proposed two kinds of physical gas sensors based on MEMS cantilever and capacitive micromachined ultrasonic transducer (CMUT) types.

The proposed cantilever type gas sensor is novel due to the choice of material, i.e. 3C-SiC, which is suitable for harsh environments. In addition, the addressed CMUT type physical gas sensor is also innovative, because it could detect two acoustic properties (acoustic impedance and acoustic velocity) at the same time. The ability of using CMUT, as a bimodal gas sensor makes it unique compared to other existing gas detectors. This aspect of using CMUT as multi-modal sensor paves the way for potential future applications, like “eNose” for gas discrimination in different mixtures. Both the sensors do not use sensitive coatings and have better limits of detection for targeted application.

The 3C-SiC microcantilever works on an electromagnetic actuation mechanism. Also, these cantilevers perform gas detection in two ways based on their design: i) induction (method I) and ii) piezoresistive (method II), as said in §1.7.1. Next, the silicon nitride CMUTs work on electrostatic mechanism. In this technology, we proposed two kinds of detection based on their working frequency: i) at resonance mode (method III) and ii) low frequency mode (method IV), as explained in §1.7.2. The two aspects of using microcantilevers and CMUTs, as physical gas detectors, will be discussed in chapter 2 and 3 individually.

References

[1] MAN Company, "Vorrichtung zur fortlaufenden Bestimmung des Wasserstoffgehaltes in Gasgemischen," Patent DRP 165 349, 1904

[2] T. Hübert *et al.*, "Hydrogen sensors – A review," *Sensors and Actuators B: Chemical*, vol. 157, no. 2, pp. 329–352, Oct. 2011, doi: 10.1016/j.snb.2011.04.070.

[3] S. K. Chaulya and G. M. Prasad, "Gas Sensors for Underground Mines and Hazardous Areas," in *Sensing and Monitoring Technologies for Mines and Hazardous Areas*, Elsevier, 2016, pp. 161–212. doi: 10.1016/B978-0-12-803194-0.00003-9.

[4] Q. Deng *et al.*, "Research Advances of Prevention and Control of Hydrogen Sulfide in Coal Mines," *The Scientific World Journal*, vol. 2019, pp. 1–15, Apr. 2019, doi: 10.1155/2019/8719260.

[5] "Three Mile Island Accident (1979)." https://www.world-nuclear.org/information-library/safety-and-security/safety-of-plants/three-mile-island-accident.aspx.

[6] "Chernobyl Accident (1986)." https://www.world-nuclear.org/information-library/safety-and-security/safety-of-plants/chernobyl-accident.aspx.

[7] "Fukushima Daiichi Accident (2011)." https://www.world-nuclear.org/information-library/safety-and-security/safety-of-plants/fukushima-daiichi-accident.aspx.

[8] Hortense Goulard, "L'éolien, troisième source d'électricité en France en 2020," *Les Echos*, Mar. 2021. [Online]. Available: https://www.lesechos.fr/industrie-services/energie-environnement/leolien-troisieme-source-delectricite-en-france-en-2020-1295128.

[9] "World Nuclear Power Reactors & Uranium Requirements," Jan. 2021. https://www.world-nuclear.org/information-library/facts-and-figures/world-nuclear-power-reactors-and-uranium-requireme.aspx.

[10] "Project Cigéo." https://www.andra.fr/cigeo.

[11] J. G. Firth *et al.*, "The principles of the detection of flammable atmospheres by catalytic devices," *Combustion and Flame*, vol. 20, no. 3, pp. 303–311, Jun. 1973, doi: 10.1016/0010-2180(73)90021-7.

[12] D. W. Dabill *et al.*, "A fast-response catalytic sensor for flammable gases," *Sensors and Actuators*, vol. 11, no. 2, pp. 135–143, Mar. 1987, doi: 10.1016/0250-6874(87)80012-4.

[13] M. Krawczyk and J. Namiesnik, "Application of a catalytic combustion sensor (Pellistor) for the monitoring of the explosiveness of a hydrogen-air mixture in the upper explosive limit range," *Journal of Automated Methods and Management in Chemistry*, vol. 25, no. 5, pp. 115–122, 2003, doi: 10.1155/S1463924603000208.

[14] A. Harley-Trochimczyk *et al.*, "Catalytic hydrogen sensing using microheated platinum nanoparticle-loaded graphene aerogel," *Sensors and Actuators B: Chemical*, vol. 206, pp. 399–406, Jan. 2015, doi: 10.1016/j.snb.2014.09.057.

[15] W. Jang *et al.*, "Methane and hydrogen sensing properties of catalytic combustion type single-chip micro gas sensors with two different Pt film thicknesses for heaters," *Micro and Nano Syst Lett*, vol. 6, no. 1, p. 7, Dec. 2018, doi: 10.1186/s40486-018-0069-y.

[16] L. Wu *et al.*, "A Novel Fabricating Process of Catalytic Gas Sensor Based on Droplet Generating Technology," *Micromachines*, vol. 10, no. 1, p. 71, Jan. 2019, doi: 10.3390/mi10010071.

[17] J. F. McAleer *et al.*, "Tin dioxide gas sensors: use of the seebeck effect," *Sensors and Actuators*, vol. 8, no. 3, pp. 251–257, Nov. 1985, doi: 10.1016/0250-6874(85)85008-3.

[18] K. Tajima *et al.*, "Micromechanical fabrication of low-power thermoelectric hydrogen sensor," *Sensors and Actuators B: Chemical*, vol. 108, no. 1–2, pp. 973–978, Jul. 2005, doi: 10.1016/j.snb.2004.11.025.

[19] W. Shin *et al.*, "Thermoelectric gas sensor for detection of high hydrogen concentration," *Sensors and Actuators B: Chemical*, vol. 97, no. 2–3, pp. 344–347, Feb. 2004, doi: 10.1016/j.snb.2003.08.029.

[20] W. Shin *et al.*, "Thermoelectric gas sensors with selective combustion catalysts," *J. Ceram. Soc. Japan*, vol. 127, no. 2, pp. 57–66, Feb. 2019, doi: 10.2109/jcersj2.18098.

[21] E. Brauns *et al.*, "A fast and sensitive catalytic gas sensors for hydrogen detection based on stabilized nanoparticles as catalytic layer," *Sensors and Actuators B: Chemical*, vol. 193, pp. 895–903, Mar. 2014, doi: 10.1016/j.snb.2013.11.048.

[22] H. Sturm *et al.*, "A highly sensitive catalytic gas sensor for hydrogen detection based on sputtered nanoporous platinum," *Procedia Engineering*, vol. 5, pp. 123–126, 2010, doi: 10.1016/j.proeng.2010.09.063.

[23] A. S. Pranti *et al.*, "Design and Fabrication Challenges of a Highly Sensitive Thermoelectric-Based Hydrogen Gas Sensor," *Micromachines*, vol. 10, no. 10, p. 650, Sep. 2019, doi: 10.3390/mi10100650.

[24] A. B. LaConti and H. J. R. Maget, "Electrochemical Detection of H2, CO, and Hydrocarbons in Inert or Oxygen Atmospheres," *J. Electrochem. Soc.*, vol. 118, no. 3, p. 506, 1971, doi: 10.1149/1.2408093.

[25] G. Korotcenkov *et al.*, "Review of Electrochemical Hydrogen Sensors," *Chem. Rev.*, vol. 109, no. 3, pp. 1402–1433, Mar. 2009, doi: 10.1021/cr800339k.

[26] J. R. Stetter and J. Li, "Amperometric Gas SensorsA Review," *Chem. Rev.*, vol. 108, no. 2, pp. 352–366, Feb. 2008, doi: 10.1021/cr0681039.

[27] C. Ramesh *et al.*, "Improved Nafion-based amperometric sensor for hydrogen in argon," *J Solid State Electrochem*, vol. 12, no. 9, pp. 1109–1116, Sep. 2008, doi: 10.1007/s10008-007-0448-4.

[28] E. Jayanthi *et al.*, "Sensing Behavior of Room Temperature Amperometric H_2 Sensor with Pd Electrodeposited from Ionic Liquid Electrolyte as Sensing Electrode," *J. Electrochem. Soc.*, vol. 164, no. 8, pp. H5210–H5217, 2017, doi: 10.1149/2.0331708jes.

[29] Y. Tang *et al.*, "Continuous amperometric hydrogen gas sensing in ionic liquids," *Analyst*, vol. 143, no. 17, pp. 4136–4146, 2018, doi: 10.1039/C8AN00577J.

[30] A. S. Ahmad Fauzi *et al.*, "Carbon-based potentiometric hydrogen sensor using a proton conducting graphene oxide membrane coupled with a WO3 sensing electrode," *Sensors and Actuators B: Chemical*, vol. 323, p. 128678, Nov. 2020, doi: 10.1016/j.snb.2020.128678.

[31] M. Zhu *et al.*, "A Novel Three-Electrode Solid Electrolyte Hydrogen Gas Sensor," in *Intelligent Computing for Sustainable Energy and Environment*, vol. 355, K. Li, S. Li, D. Li, and Q. Niu, Eds. Berlin, Heidelberg: Springer Berlin Heidelberg, 2013, pp. 37–45. doi: 10.1007/978-3-642-37105-9_5.

[32] Y. Li *et al.*, "Potentiometric hydrogen sensors based on yttria-stabilized zirconia electrolyte (YSZ) and CdWO 4 interface," *Sensors and Actuators B: Chemical*, vol. 223, pp. 365–371, Feb. 2016, doi: 10.1016/j.snb.2015.09.110.

[33] J. Yi *et al.*, "Hierarchical porous hollow SnO2 nanofiber sensing electrode for high performance potentiometric H2 sensor," *Sensors and Actuators B: Chemical*, vol. 268, pp. 456–464, Sep. 2018, doi: 10.1016/j.snb.2018.04.086.

[34] Y. Zhang *et al.*, "Recent advancements in optical fiber hydrogen sensors," *Sensors and Actuators B: Chemical*, vol. 244, pp. 393–416, Jun. 2017, doi: 10.1016/j.snb.2017.01.004.

[35] M. A. Butler, "Fiber Optic Sensor for Hydrogen Concentrations near the Explosive Limit," *J. Electrochem. Soc.*, vol. 138, no. 9, pp. L46–L47, Sep. 1991, doi: 10.1149/1.2086073.

[36] B. Xu *et al.*, "Reflective optical fiber sensor based on light polarization modulation for hydrogen sensing," *J. Opt. Soc. Am. B*, vol. 36, no. 12, p. 3471, Dec. 2019, doi: 10.1364/JOSAB.36.003471.

[37] M. Tabib-Azar *et al.*, "Highly sensitive hydrogen sensors using palladium coated fiber optics with exposed cores and evanescent field interactions," *Sensors and Actuators B: Chemical*, vol. 56, no. 1–2, pp. 158–163, Jul. 1999, doi: 10.1016/S0925-4005(99)00177-X.

[38] N. A. M. Yahya *et al.*, "H $_2$ Gas Sensor Based on Pd/ZnO Nanostructures Deposited on Tapered Optical Fiber," *IEEE Sensors J.*, vol. 20, no. 6, pp. 2982–2990, Mar. 2020, doi: 10.1109/JSEN.2019.2957838.

[39] B. Chadwick *et al.*, "A hydrogen sensor based on the optical generation of surface plasmons in a palladium alloy," *Sensors and Actuators B: Chemical*, vol. 17, no. 3, pp. 215–220, Feb. 1994, doi: 10.1016/0925-4005(93)00875-Y.

[40] A. Aray *et al.*, "Plasmonic fiber optic hydrogen sensor using oxygen defects in nanostructured molybdenum trioxide film," *Opt. Lett.*, vol. 44, no. 19, p. 4773, Oct. 2019, doi: 10.1364/OL.44.004773.

[41] M. A. Butler, "Optical fiber hydrogen sensor," *Appl. Phys. Lett.*, vol. 45, no. 10, pp. 1007–1009, Nov. 1984, doi: 10.1063/1.95060.

[42] Y. Zhang *et al.*, "Hydrogen sensor based on high-birefringence fiber loop mirror with sol-gel Pd/WO3 coating," *Sensors and Actuators B: Chemical*, vol. 248, pp. 71–76, Sep. 2017, doi: 10.1016/j.snb.2017.03.155.

[43] G. Wang *et al.*, "Fiber-Optic Hydrogen Sensors: A Review," *IEEE Sensors J.*, pp. 1–1, 2020, doi: 10.1109/JSEN.2020.3029519.

[44] B. Sutapun, "Pd-coated elastooptic fiber optic Bragg grating sensors for multiplexed hydrogen sensing," *Sensors and Actuators B: Chemical*, vol. 60, no. 1, pp. 27–34, Nov. 1999, doi: 10.1016/S0925-4005(99)00240-3.

[45] C. Caucheteu *et al.*, "Hybrid fiber gratings coated with a catalytic sensitive layer for hydrogen sensing in air," *Opt. Express*, vol. 16, no. 21, p. 16854, Oct. 2008, doi: 10.1364/OE.16.016854.

[46] M. Yang *et al.*, "High-sensitivity fiber optic hydrogen sensor in air by optimizing a self-referenced demodulating method," *Appl. Opt.*, vol. 57, no. 27, p. 8011, Sep. 2018, doi: 10.1364/AO.57.008011.

[47] "Engineering ToolBox." https://www.engineeringtoolbox.com/.

[48] H. A. Daynes, "Gas Analysis by Measurement of Thermal Conductivity," *Cambridge University Press, London*, 1933, doi: 10.1002/zamm.19330130419.

[49] I. Simon and M. Arndt, "Thermal and gas-sensing properties of a micromachined thermal conductivity sensor for the detection of hydrogen in automotive applications," *Sensors and Actuators A: Physical*, vol. 97–98, pp. 104–108, Apr. 2002, doi: 10.1016/S0924-4247(01)00825-1.

[50] P. Tardy *et al.*, "Dynamic thermal conductivity sensor for gas detection," *Sensors and Actuators B: Chemical*, vol. 98, no. 1, pp. 63–68, Mar. 2004, doi: 10.1016/j.snb.2003.09.019.

[51] G. de Graaf and R. F. Wolffenbuttel, "Surface-micromachined thermal conductivity detectors for gas sensing," in *2012 IEEE International Instrumentation and Measurement Technology Conference Proceedings*, Graz, Austria, May 2012, pp. 1861–1864. doi: 10.1109/I2MTC.2012.6229412.

[52] D. Berndt *et al.*, "MEMS-based thermal conductivity sensor for hydrogen gas detection in automotive applications," *Sensors and Actuators A: Physical*, vol. 305, p. 111670, Apr. 2020, doi: 10.1016/j.sna.2019.111670.

[53] T. H. Maiman, "Stimulated Optical Radiation in Ruby," *Nature*, vol. 187, no. 4736, pp. 493–494, Aug. 1960, doi: 10.1038/187493a0.

[54] L. D. Smullin and G. Fiocco, "Optical Echoes from the Moon," *Nature*, vol. 194, no. 4835, pp. 1267–1267, Jun. 1962, doi: 10.1038/1941267a0.

[55] G. Fiocco and L. D. Smullin, "Detection of Scattering Layers in the Upper Atmosphere (60–140 km) by Optical Radar," *Nature*, vol. 199, no. 4900, pp. 1275–1276, Sep. 1963, doi: 10.1038/1991275a0.

[56] D. Bruneau and J. Pelon, "A new lidar design for operational atmospheric wind and cloud/aerosol survey from space," Others (Wind, Precipitation, Temperature, etc.)/Remote Sensing/Instruments and Platforms, preprint, Dec. 2020. doi: 10.5194/amt-2020-487.

[57] J. Barrientos Barria *et al.*, "Progress on high energy optical parametric transmitter for multiple greenhouse gases dial," in *International Conference on Space Optics — ICSO 2014*, Tenerife, Canary Islands, Spain, Nov. 2017, p. 97. doi: 10.1117/12.2304157.

[58] T. Shiina, "Hydrogen Gas Detection by Mini-Raman Lidar," in *Ionizing Radiation Effects and Applications*, B. Djezzar, Ed. InTech, 2018. doi: 10.5772/intechopen.74630.

[59] H. Miya *et al.*, "Compact Raman lidar for hydrogen gas leak detection," in *2009 Conference on Lasers & Electro Optics & The Pacific Rim Conference on Lasers and Electro-Optics*, Shanghai, China, Aug. 2009, pp. 1–2. doi: 10.1109/CLEOPR.2009.5292527.

[60] I. Asahi *et al.*, "Remote sensing of hydrogen gas concentration distribution by Raman lidar," Kyoto, Japan, Nov. 2012, p. 85260X. doi: 10.1117/12.977348.

[61] S. Sugimoto *et al.*, "Hydrogen gas concentration measurement in small area using raman lidar measurement technnology," *EPJ Web Conf.*, vol. 176, p. 01019, 2018, doi: 10.1051/epjconf/201817601019.

[62] A. Liméry *et al.*, "Raman lidar for hydrogen gas concentration monitoring and future radioactive waste management," *Opt. Express*, vol. 25, no. 24, p. 30636, Nov. 2017, doi: 10.1364/OE.25.030636.

[63] W. J. Buttner *et al.* "An overview of hydrogen safety sensors and requirements," *International Journal of Hydrogen Energy*, vol. 36, no. 3, pp. 2462–2470, Feb. 2011, doi: 10.1016/j.ijhydene.2010.04.176.

[64] G. Binnig *et al.*, "Atomic Force Microscope," *Phys. Rev. Lett.*, vol. 56, no. 9, pp. 930–933, Mar. 1986, doi: 10.1103/PhysRevLett.56.930.

[65] R. J. Wilfinger *et al.*, "The Resonistor: A Frequency Selective Device Utilizing the Mechanical Resonance of a Silicon Substrate," *IBM J. Res. & Dev.*, vol. 12, no. 1, pp. 113–118, Jan. 1968, doi: 10.1147/rd.121.0113.

[66] J. K. Gimzewski *et al.*, "Observation of a chemical reaction using a micromechanical sensor," *Chemical Physics Letters*, vol. 217, no. 5–6, pp. 589–594, Jan. 1994, doi: 10.1016/0009-2614(93)E1419-H.

[67] T. Thundat *et al.*, "Thermal and ambient-induced deflections of scanning force microscope cantilevers," *Appl. Phys. Lett.*, vol. 64, no. 21, pp. 2894–2896, May 1994, doi: 10.1063/1.111407.

[68] T. Thundat *et al.*, "Vapor Detection Using Resonating Microcantilevers," *Anal. Chem.*, vol. 67, no. 3, pp. 519–521, Feb. 1995, doi: 10.1021/ac00099a006.

[69] C. L. Britton *et al.*, "Multiple-input microcantilever sensors," *Ultramicroscopy*, vol. 82, no. 1–4, pp. 17–21, Feb. 2000, doi: 10.1016/S0304-3991(99)00155-2.

[70] Z. Hu *et al.*, "Investigation of adsorption and absorption-induced stresses using microcantilever sensors," *Journal of Applied Physics*, vol. 90, no. 1, pp. 427–431, Jul. 2001, doi: 10.1063/1.1378333.

[71] D. R. Baselt *et al.*, "Design and performance of a microcantilever-based hydrogen sensor," *Sensors and Actuators B: Chemical*, vol. 88, no. 2, pp. 120–131, Jan. 2003, doi: 10.1016/S0925-4005(02)00315-5.

[72] A. Fabre *et al.*, "Monitoring the chemical changes in Pd induced by hydrogen absorption using microcantilevers," *Ultramicroscopy*, vol. 97, no. 1–4, pp. 425–432, Oct. 2003, doi: 10.1016/S0304-3991(03)00070-6.

[73] T. Ono *et al.*, "Mass sensing of adsorbed molecules in sub-picogram sample with ultrathin silicon resonator," *Review of Scientific Instruments*, vol. 74, no. 3, pp. 1240–1243, Mar. 2003, doi: 10.1063/1.1536262.

[74] J. Zhou *et al.*, "Self-excited piezoelectric microcantilever for gas detection," *Microelectronic Engineering*, vol. 69, no. 1, pp. 37–46, Aug. 2003, doi: 10.1016/S0167-9317(03)00227-2.

[75] I. Dufour and L. Fadel, "Resonant microcantilever type chemical sensors: analytical modeling in view of optimization," *Sensors and Actuators B: Chemical*, vol. 91, no. 1–3, pp. 353–361, Jun. 2003, doi: 10.1016/S0925-4005(03)00110-2.

[76] C. Vančura *et al.*, "Magnetically Actuated Complementary Metal Oxide Semiconductor Resonant Cantilever Gas Sensor Systems," *Anal. Chem.*, vol. 77, no. 9, pp. 2690–2699, May 2005, doi: 10.1021/ac048378t.

[77] S. Tétin *et al.*, "Modeling and performance of uncoated microcantilever-based chemical sensors," *Sensors and Actuators B: Chemical*, vol. 143, no. 2, pp. 555–560, Jan. 2010, doi: 10.1016/j.snb.2009.09.062.

[78] I. Dufour *et al.*, "Unconventional uses of microcantilevers as chemical sensors in gas and liquid media," *Sensors and Actuators B: Chemical*, vol. 170, pp. 115–121, Jul. 2012, doi: 10.1016/j.snb.2011.02.050.

[79] M. T. Boudjiet *et al.*, "New characterization methods for monitoring small resonant frequency variation: Experimental tests in the case of hydrogen detection with uncoated silicon microcantilever-based sensors," *Sensors and Actuators B: Chemical*, vol. 199, pp. 269–276, Aug. 2014, doi: 10.1016/j.snb.2014.03.098.

[80] M. T. Boudjiet *et al.*, "Geometry optimization of uncoated silicon microcantilever-based gas density sensors," *Sensors and Actuators B: Chemical*, vol. 208, pp. 600–607, Mar. 2015, doi: 10.1016/j.snb.2014.11.067.

[81] R. Rosario and R. Mutharasan, "Piezoelectric excited millimeter sized cantilever sensors for measuring gas density changes," *Sensors and Actuators B: Chemical*, vol. 192, pp. 99–104, Mar. 2014, doi: 10.1016/j.snb.2013.10.017.

[82] L. Iglesias *et al.*, "Discrimination and concentration measurement of different binary gas mixtures with a simple resonator through viscosity and mass density measurements," *Sensors and Actuators B: Chemical*, vol. 285, pp. 487–494, Apr. 2019, doi: 10.1016/j.snb.2019.01.070.

[83] Haller and Khuri-Yakub, "A surface micromachined electrostatic ultrasonic air transducer," in *Proceedings of IEEE Ultrasonics Symposium ULTSYM-94*, Cannes, France, 1994, pp. 1241–1244 vol.2. doi: 10.1109/ULTSYM.1994.401810.

[84] D. Gross *et al.*, "Evaluation of an Ultrasound-Guided Focused Ultrasound CMUT Probe for Targeted Therapy Applications," *OJAppS*, vol. 08, no. 01, pp. 25–45, 2018, doi: 10.4236/ojapps.2018.81003.

[85] K. K. Park *et al.*, "Capacitive micromachined ultrasonic transducers for chemical detection in nitrogen," *Appl. Phys. Lett.*, vol. 91, no. 9, p. 094102, Aug. 2007, doi: 10.1063/1.2776348.

[86] O. Oralkan *et al.*, "Capacitive micromachined ultrasonic transducers: next-generation arrays for acoustic imaging?," *IEEE Trans. Ultrason., Ferroelect., Freq. Contr.*, vol. 49, no. 11, pp. 1596–1610, Nov. 2002, doi: 10.1109/TUFFC.2002.1049742.

[87] Kwan Kyu Park *et al.*, "Capacitive micromachined ultrasonic transducer as a chemical sensor," in *2008 IEEE Sensors*, Lecce, Italy, Oct. 2008, pp. 5–8. doi: 10.1109/ICSENS.2008.4716369.

[88] H. J. Lee *et al.*, "CMUT as a chemical sensor for DMMP detection," in *2008 IEEE International Frequency Control Symposium*, Honolulu, HI, May 2008, pp. 434–439. doi: 10.1109/FREQ.2008.4623034.

[89] K. K. Park *et al.*, "Capacitive micromachined ultrasonic transducer (CMUT) as a chemical sensor for DMMP detection," *Sensors and Actuators B: Chemical*, vol. 160, no. 1, pp. 1120–1127, Dec. 2011, doi: 10.1016/j.snb.2011.09.036.

[90] H. J. Lee *et al.*, "Highly sensitive detection of DMMP using a CMUT-based chemical sensor," in *2010 IEEE Sensors*, Kona, HI, Nov. 2010, pp. 2122–2126. doi: 10.1109/ICSENS.2010.5690493.

[91] H. J. Lee *et al.*, "Chemical Vapor Detection Using a Capacitive Micromachined Ultrasonic Transducer," *Anal. Chem.*, vol. 83, no. 24, pp. 9314–9320, Dec. 2011, doi: 10.1021/ac201626b.

[92] S. Park *et al.*, "CMUT-based resonant gas sensor array for VOC detection with low operating voltage," *Sensors and Actuators B: Chemical*, vol. 273, pp. 1556–1563, Nov. 2018, doi: 10.1016/j.snb.2018.07.043.

[93] M. M. Mahmud *et al.*, "A low-power gas sensor for environmental monitoring using a capacitive micromachined ultrasonic transducer," Nov. 2014, pp. 677–680. doi: 10.1109/ICSENS.2014.6985089.

[94] M. M. Mahmud *et al.*, "Gravimetric biosensor based on a capacitive micromachined ultrasonic transducer functionalized with peptide ligands," in *2017 IEEE SENSORS*, Glasgow, Oct. 2017, pp. 1–3. doi: 10.1109/ICSENS.2017.8234352.

[95] D. Barauskas *et al.*, "Greenhouse gas molecule CO2 detection using a capacitive micromachined ultrasound transducer (CMUT)," *Anal. Chem.*, vol. 88, no. 13, pp. 6662–6665, Jul. 2016, doi: 10.1021/acs.analchem.6b02085.

[96] M.-T. Boudjiet, "Microsystèmes durables de mesures de concentration d'hydrogène utilisant des micropoutres sans couche sensible," PhD dissertation, University of Bordeaux, 2015.

[97] T. L. Daulton, "Polytype Distribution in Circumstellar Silicon Carbide," *Science*, vol. 296, no. 5574, pp. 1852–1855, Jun. 2002, doi: 10.1126/science.1071136.

[98] A. Boulmé *et al.*, "A capacitive micromachined ultrasonic transducer probe for assessment of cortical bone," *IEEE Transactions on Ultrasonics, Ferroelectrics, and Frequency Control*, vol. 61, no. 4, pp. 710–723, Apr. 2014, doi: 10.1109/TUFFC.2014.2959.

[99] L. Iglesias *et al.*, "Proof of Concept and Preliminary Results of Gas Detection by Measuring the Admittance at the Resonance and Anti-resonance of an Uncoated CMUT," *Front. Mech. Eng.*, vol. 6, p. 14, Mar. 2020, doi: 10.3389/fmech.2020.00014.

[100] P. Shanmugam *et al.*, "Broad bandwidth air-coupled micromachined ultrasonic transducers for gas sensing," *Ultrasonics*, vol. 114, p. 106410, Jul. 2021, doi: 10.1016/j.ultras.2021.106410.

[101] K. K. Park and B. T. Khuri-Yakub, "3-D airborne ultrasound synthetic aperture imaging based on capacitive micromachined ultrasonic transducers," *Ultrasonics*, vol. 53, no. 7, pp. 1355–1362, Sep. 2013, doi: 10.1016/j.ultras.2013.04.003.

[102] G. Bui *et al.*, "Two Capacitive Micro-Machined Ultrasonic Transducers for Wind Speed Measurement," *Sensors*, vol. 16, no. 6, p. 814, Jun. 2016, doi: 10.3390/s16060814.

[103] S. Na *et al.*, "An Optimization and Comparative Study of Air-Coupled CMUT Cells With Circular and Annular Geometries," *IEEE Trans. Ultrason., Ferroelect., Freq. Contr.*, vol. 64, no. 11, pp. 1723–1734, Nov. 2017, doi: 10.1109/TUFFC.2017.2739692.

[104] B. Ma *et al.*, "Wide Bandwidth and Low Driving Voltage Vented CMUTs for Airborne Applications," *IEEE Trans. Ultrason., Ferroelect., Freq. Contr.*, vol. 66, no. 11, pp. 1777–1785, Nov. 2019, doi: 10.1109/TUFFC.2019.2928170.

[105] T. M. Khan *et al.*, "High-Intensity Airborne CMUT Transmitter Array With Beam Steering," *J. Microelectromech. Syst.*, vol. 29, no. 6, pp. 1537–1546, Dec. 2020, doi: 10.1109/JMEMS.2020.3026094.

[106] N. Sénégond, "Approche temporelle de le simulation et de la caractérisation des transducteurs ultrasonores capacitifs micro-usinés," PhD dissertation, University of Tours, Tours, 2010.

2. Design, fabrication and characterization of 3C-SiC microcantilevers without functionalized coating

2.1 General introduction of silicon carbide and its properties 69

2.1.1 Motivation to choose cubic crystallographic orientation 69

2.1.2 Brief history of pioneering researches on 3C-SiC epilayer growth, etching and characterization processes by our associated groups 72

2.1.3 The growth process of 3C-SiC epilayer on Si substrate used in our study 76

2.2 Background for design validations 79

2.3 Fabrication of 3C-SiC-microcantilevers (µCs) 83

2.3.1 Sample preparation 84

2.3.2 Defining the geometries of 3C-SiC-µCs 86

2.3.3 Optimization of the isolation layer 87

2.3.4 Deposition of metals for piezoresistive detection 91

2.3.5 Deposition of metals for electromagnetic actuation 96

2.3.6 Turning sample into device 99

2.3.7 Packaging of fabricated 3C-SiC-µCs 104

2.4 Electrical characterizations of 3C-SiC-µCs in air 106

2.4.1 Laser Doppler vibrometry measurements 106

2.4.2 Electrical measurements 110

2.5 Testing of fabricated 3C-SiC-µCs in binary gas mixture environments 113

Conclusion and perspectives 116

References 117

Chapter 2

Design, fabrication and characterization of 3C-SiC microcantilevers without functionalized coating

This chapter is mainly involved in the development of silicon carbide (SiC) based micro resonant system for hydrogen detection in radioactive environments. As explained in chapter 1, the goal is to fabricate 3C-SiC microcantilevers (µCs) using the design validated by M. T. Boudjiet on silicon, which works on electromagnetic actuation and piezoresistive detection mechanism [1]. Additionally, a second set of cantilevers have been produced with the same actuation but with a different detection mechanism (i.e. induction). In both cases, the change in gas mixture is identified by a shift in the resonance frequency induced by the mass density of the gas.

In terms of microcantilever fabrication, processing the 2-inch 3C-SiC epi-wafer is more challenging than a silicon based system, but it is possible. In the case of Boudjiet *et al.*, they worked on well-known silicon material [2]. In our work, we present the process optimization made to manufacture successful hydrogen sensors with predetermined design validation on chosen material.

This chapter is divided into five parts. Firstly, the general introduction on material of choice, i.e. silicon carbide, is elaborated. This section highlights the best properties of SiC that made it a potential candidate to work in a harsh environment. Followed by explaining the reasons behind choosing cubic structure with specific growth orientation and growth process used in our study. The second part briefly explains the reason behind the choice of geometry and their dimensions based on previous studies carried out on silicon based microcantilevers, as mentioned earlier. Besides, the geometries used in our study have been summarized. Then, the third part is the heart of this chapter, which extensively describes different subprocesses used in microcantilever fabrication. Next, the characterizations of different 3C-SiC-µCs geometries using optical and electrical measurements in the air environment are presented. These experiments aid to derive basic parameters, such as resonance frequency, quality factor and

resistance across the actuation and detection circuits for various geometries. Finally, the devices are tested in the gas mixture environment to validate the fabricated sensor. In our case, we use two binary gas mixtures, i.e. hydrogen in nitrogen and carbon dioxide in nitrogen.

2.1 General introduction of silicon carbide and its properties

Silicon carbide (SiC) is a wide bandgap material (2.3-3.2 eV). It was first produced by Edward G. Acheson in 1892, while he was attempting to fabricate artificial diamonds [3]. However, from history, the Swedish scientist Jöns Jacob Berzelius first proposed the idea of silicon-carbon bond in 1824. Formerly, SiC was used as cutting and polishing tools, due to its material hardness. In the beginning of 20th century, Henry H. C. Dunwoody has used SiC, as a detector in first radios [4] and then Henry J. Round produced a light emitting diode by applying a voltage on a SiC crystal [5]. Since then, there are a large number of researches ongoing due to its excellent electrical, thermal and mechanical properties. Silicon carbide can be a leading alternative material to any applications that work under extreme conditions [6].

SiC have more than 250 polytypes based on their crystalline structures [7]. Nevertheless, among all, only 4H-SiC, 6H-SiC (hexagonal structures) and 3C-SiC (cubic structure) are commercially available [8], [9]. The current SiC based electronic devices are largely made of bulk 4H-SiC polytypes for various present and future applications [10]–[13]. On the other hand, 3C-SiC has a significant progress in producing device-grade hetero epilayers, which can be used to produce potential devices in near future. Silicon carbide has higher breakdown field (2-4 MV/cm), higher thermal expansion coefficient (3.16-3.33*10^{-6} K^{-1}), higher Young's modulus (300-700 GPa), higher density (3.2 g/cm^3) and higher sublimation temperature (2700 °C) than silicon [14]. These electromechanical properties are firmly related to their crystalline structures. Hence, they vary slightly from one polytype to another without change in their tendencies. As mentioned in §1.7.1, SiC can withstand high levels of radiation, high-temperature oxidative environments and corrosion (i.e. highly resistive to a wide range of chemicals). Therefore, these remarkable properties make SiC a potential candidate to operate in hostile and radioactive environments, which is presently not served by silicon technologies.

2.1.1 Motivation to choose cubic crystallographic orientation

In comparison with other polytypes, 3C-SiC is more attractive due to its cubic crystalline structure. It can be epitaxially grown on classical, cheap and largely available silicon (Si) substrates. As of now, silicon is dominant in microfabrication platforms, it leverages the highly-parallel batch fabrication paradigm [15]. Moreover, one can take advantage of a large

amount of expertise on silicon masking and etching techniques to remove them entirely or to pattern complicated geometries in any heteroepitaxial structures with Si substrates. From literature, Nishino *et al.* have laid the groundwork of growing 3C-SiC epilayers on Si substrates for the first time, as shown in figure 2.1.a. In addition, they have suggested the introduction of a carbonization step to create a buffer layer before growing the epilayer on the substrate (see figure 2.1.b) [16]. This novel idea accommodates the lattice mismatch between 3C-SiC and Si, which is 20 % at room temperature.

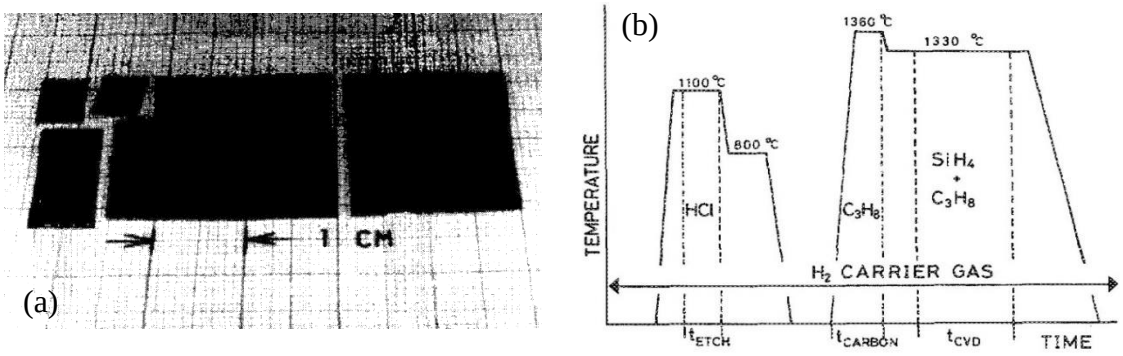


Figure 2.1: (a) An example of 3C-SiC single crystal grown by Nishino *et al.*, where the wafer has broken into several pieces [16]. (b) The optimized growth program with a carbonization step created by the same team [17].

Successively, Liaw *et al.* experimented developing monocrystalline crack-free 3C-SiC epilayers on Si (001) and Si (111) substrates and also reported the impacts of *off-axis* orientation during epilayer growth with their morphologies [18]. Afterwards, Pirouz *et al.* have made an extensive work on growth mechanism; exploited the origin of planar defects and the role of buffer layer by comparing one-step and two-step growth processes [19]. In one-step growth process, the reactor is maintained at final temperature throughout the growth that results in polycrystalline aggregate. It is experimentally proven that the polycrystalline 3C-SiC possesses lower Young's modulus [20], [21] and higher surface roughness [22] than single crystal 3C-SiC epilayer.

Therefore, by performing a two-step growth process, one can carry out the carbonization step at low temperature to form a continuous buffer layer. Later, the initial epitaxial growth begins on a clean and homogenous buffer layer, which has been performed at final growth temperature. Over years, the growth strategies have been advanced by several research groups, where few results are tabulated in table 2.1. Mostly all the groups worked on 2-4 inch substrates except Severino *et al.*, who managed to grow high quality 3C-SiC (111) epilayer on 6-inch Si (111) substrate [23].

Table 2.1: Research works based on various growth conditions for the specified growth orientations.

Growth orientation	Cleaning/ etching	Carbonization (buffer layer)	Growth temperature	Growth technique	Growth pressure	Ref.
Si (001)	*HCI + H_2 at 1200 °C	RT	1400 °C	CVD	ATM	[16]
Si (001) Si (111)	*HCl + H_2 at 1100 °C	1360 °C	1330 °C	CVD	ATM	[17]
Si (001)	*HCl + H_2 at 1150 °C	1300 °C	1200 °C	RTCVD	ATM	[24]
Si (001) Si (111)	*H_2 at 1000 °C	200 °C	1250-1350 °C	VPE reactor	250 mbar-ATM	[25]
Si (001) Si (111)	*H_2 at 850-1100 °C	RT - -	700 °C, 850 °C, 850 °C	APCVD, RMS, SS	ATM, 0.003 mbar, 0.005 mbar	[26]
Si (001)	-	600-1200 °C	1400 °C	LPE-CVD	50 mbar	[27]
Undulant Si(001)	**HF at RT	1350 °C	1350 °C	LPCVD	0.13 mbar	[28]
Si (001)	-	1190 °C	1380 °C	LPCVD	100-400 mbar	[29]
Si (001)	**HF at RT	1150 °C	1350 °C	APCVD	ATM	[30]
Si (001)	-	1100 °C	1300-1400 °C	LPCVD	200 mbar	[31]
Si (001) Si (111)	-	1100 °C	1350 °C	LPCVD	200 mbar	[32]
Si (001) Si (110) Si (111)	**Piranha (110 °C) + HF at RT	1120 °C	1350 °C	LPCVD	100 mbar	[33]
Si (111)	**Piranha (110 °C) + HF at RT	1120 °C	1350 °C	LPCVD	100 mbar	[23]

**in-situ* cleaning/etching to remove native oxide layer on Si and ***ex-situ* cleaning/etching for the same reason.

From table 2.1, RT refers to room temperature, HCl – hydrogen chloride, H_2 – hydrogen gas. Similarly, CVD – chemical vapor deposition, RTCVD – rapid thermal CVD, VPE – vapor phase epitaxy, APCVD – atmospheric pressure CVD, RMS – reactive magnetron sputtering, SS – sequential sputtering, LPE-CVD – liquid phase epitaxy CVD, LPCVD – low pressure CVD. Lastly, ATM indicates the atmospheric pressure.

Subsequently, two-step growth process paved the way for increasing interest of 3C-SiC hetero-epitaxies on Si substrates. In addition, they helped in reducing the defect densities and molded 3C-SiC epilayers suitable for electronic devices. With a wide range of fundamental research on epitaxial growth of 3C-SiC on Si, several potential applications are proposed. They can be used for midinfrared index sensing [34], novel atomic force microscopy (AFM) cantilevers [35], bio-compatible devices [36], [37], surface wave accelerators [38], in photovoltaic applications [39], tandem solar cells (with proven high energy efficiency) [40], in power electronics applications [41]–[43] and can be used in device operating in harsh environments [44]–[46].

2.1.2 Brief history of pioneering researches on 3C-SiC epilayer growth, etching and characterization processes by our associated groups

Over two decades, CRHEA (Centre de Recherche sur l'Hétéro-Epitaxie et ses Applications) and GREMAN (Groupe de Recherche en Matériaux, Microélectronique, Acoustique et Nanotechnologies) are working closely to produce high quality 3C-SiC epilayers with very less defects, thereby enlightening the interest on the material as well as for promising future MEMS/NEMS applications. In the early 2000's, Leycuras from CRHEA lab had built a special hot wall internal furnace reactor to perform 3C-SiC epitaxy that adapts 2-inch substrates [27]. The designed reactor was capable of withstanding temperatures more than 2000 °C, but in practical, it has been used less than 1500 °C (∵ melting point of silicon is 1414 °C), which was enough according to the growth process specifications. The obtained preliminary result illustrates an excellent surface morphology and uniform thickness of the 3C-SiC epilayer (refer figure 2.2.a). With these encouraging outcomes, the growth process has been further optimized in terms of crystal orientation, silane flow during the carbonization process, growth temperature, growth pressure and growth rate [29]–[31], [47].

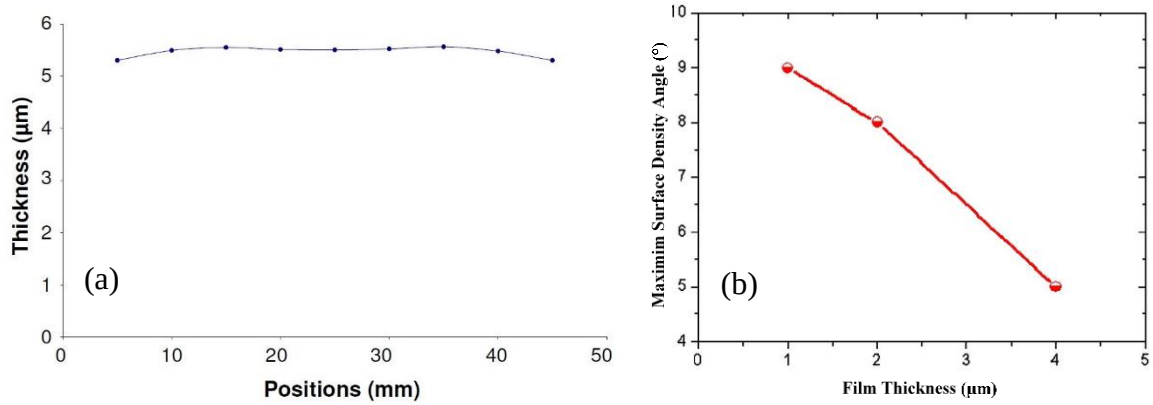


Figure 2.2: (a) Thickness uniformity of 3C-SiC epilayer for growth conditions defined by Chassagne *et al.* [29]. (b) Evolution of maximum surface density angle for varying thickness [48].

The most significant obstacle in the development of 3C-SiC/Si heteropitaxial structures are their structural defects, like Dislocations, Stacking Faults, Anti-Phase Domains (APDs) and Twins. Jiao *et al.* have investigated study on the APDs, which is more common in cubic zinc-blende crystal structures, like 3C-SiC [48]. From the obtained results, they found that the APDs decrease with increase in off-cut angle up to a certain value and this value depreciates on increasing the film thickness, as shown in figure 2.2.b. In addition, Michaud *et al.* explored the impacts of growth parameters in the mechanical properties of single crystalline 3C-SiC epilayers. This includes growth orientation, silane flow during carbonization temperature ramp-up and epilayer thickness [21]. According to the acquired results, the single crystalline 3C-SiC epilayers oriented in (001) direction have best trade-off in terms of FWHM (full width at half maximum) for thicker films, whereas the values were constant for (111) oriented epilayers.

After, they continued the material research in the aim of attaining 100 % monocrystalline 3C-SiC devices. To begin, they worked on optimizing layer by layer. From literature, contrary to the growth of 3C-SiC epilayer on Si substrate, the regrowth of Si epilayer on 3C-SiC/Si has not been thoroughly studied. These were mainly due to the defects attributed from the underlying 3C-SiC films. Björketun *et al.* were the first team to investigate the growth of Si epilayers on 3C-SiC/Si in 1998 [49]. The Si epilayer growth on 3C-SiC/Si heterostructure was performed using APCVD. The resulting structure was unfavorable because the achieved Si epilayer was not of high quality.

Just after, Ishida *et al.* accomplished the formation of single crystal Si islands on 3C-SiC films but unfortunately they did not form continuous layers [50]. Later, Jiao *et al.* have produced the first continuous single crystalline Si epilayer along (110) orientation on 3C-SiC(001)/Si(001) substrate. This deposition has been performed using conventional LPCVD reactor [51]. In their work, the significance of growth orientations and the temperatures have been studied and optimized. With the realized Si/3C-SiC/Si heterostructures, our group proposed an idea of using them as AFM probes (see figure 2.3), thereby opening a path in new MEMS devices [35]. To mention, the work specified in [35], is a continuation of their study in the influence of surface disorientations of APDs on the heteroepitaxial layers, as previously explained in the same section [48].

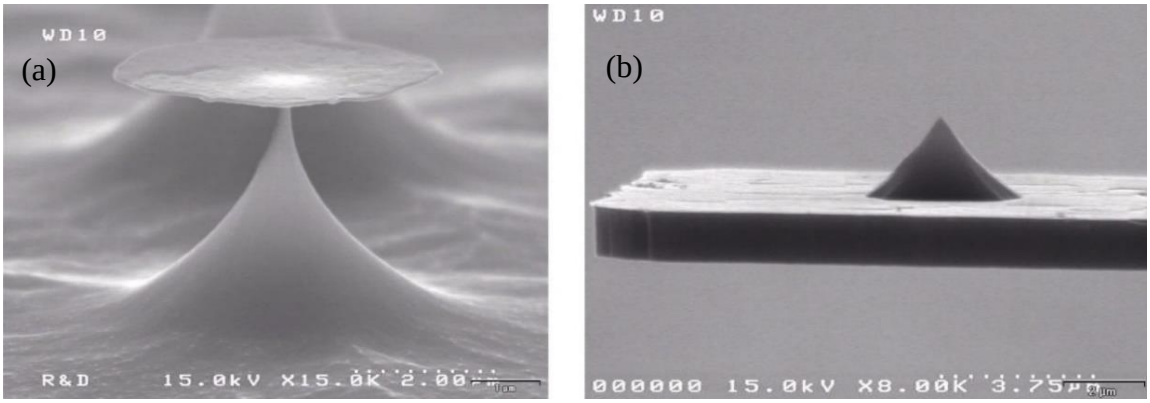


Figure 2.3: SEM image of monocrystalline Si tip (a) with nickel mask and (b) on 3C-SiC cantilever [35].

Afterwards, Michaud *et al.* have demonstrated the possibility of obtaining an innovative 3C-SiC microstructures on 3C-SiC pseudo-substrates (i.e. 3C-SiC(110)/Si(110)/3C-SiC(001)/ Si(001) heterostructure), as shown in figure 2.4. They managed to form novel and 100 % monocrystalline 3C-SiC (110) membranes on 3C-SiC (001) pseudo-substrate by using Si (110) epilayer, as a sacrificial layer [52]. These kinds of 3C-SiC membranes were promising for future MEMS applications.

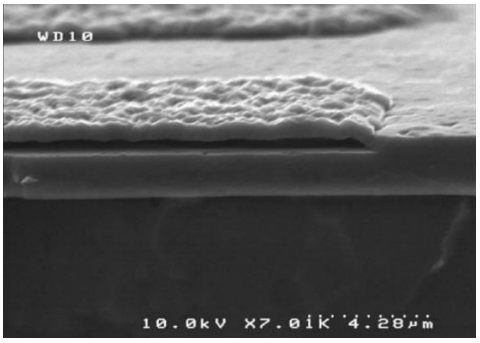


Figure 2.4: SEM cross-section view of 3C-SiC membrane on 3C-SiC monocrystalline epilayer [52].

Following the aforementioned pioneering works, Khazaka *et al.* have improved the crystalline quality of the membranes to enhance their mechanical properties [53]. Figure 2.5 shows the obtained results for different membrane growth directions. From the SEM cross-section, it is clear that the membranes grown in (111) direction were smoother than membranes attained in (110) direction. Additionally, few other factors have been adjusted in order to procure homogeneous membranes, as explained in [54].

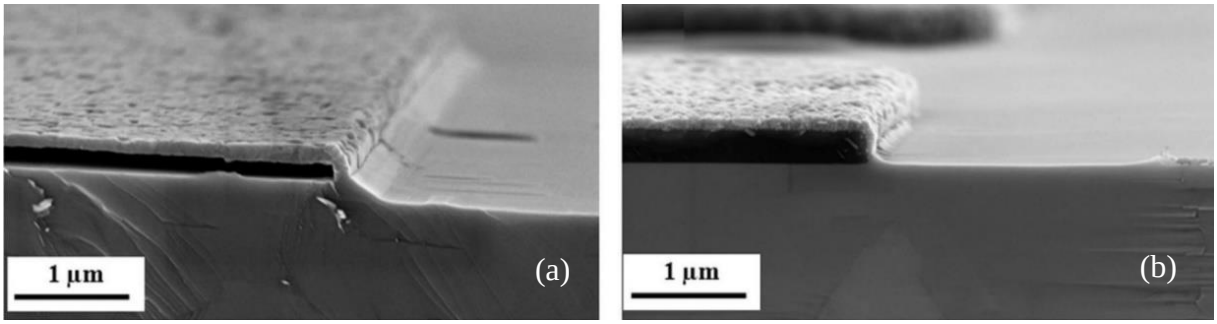


Figure 2.5: SEM cross-section view of 3C-SiC membrane on 3C-SiC pseudo substrate grown on (a) 111 orientation and (b) 110 orientation [53].

More recently, Khazaka *et al.* evidenced an ingenious method to construct 3C-SiC freestanding membranes on 3C-SiC pseudo substrate during *in-situ* growth of membrane layer [55]. This method has been elaborated in the PhD thesis of R. Khazaka referred in [54]. The proposed method forms the top membrane by consuming the patterned Si islands on the 3C-SiC/Si layer. This creates a breakthrough in NEMS/MEMS fabrications by eliminating various technological steps, such as dry etching (to create a hole in membrane), wet etching (to remove sacrificial layer) and membrane sealing. The membrane sealing is a very crucial step to be optimized, because it has the risk of producing non-functional devices (stiction), which will be briefly explained in chapter 3 (refer §3.3.1), as non-negligible curvature of CMUT membranes. This curvature modifies the gap height during sealing. However, with the proposed novel technique at *in-situ* condition, one can overcome these difficulties.

To summarize, along with SiC material properties and obtained 100 % monocrystalline 3C-SiC structures, one can use these wisely, over range of applications namely in medical field (as they are biocompatible), also fabricate any form of sensors that work in extreme environments. The final process to attain 3C-SiC membrane on 3C-SiC epilayer is shown in figure 2.6.

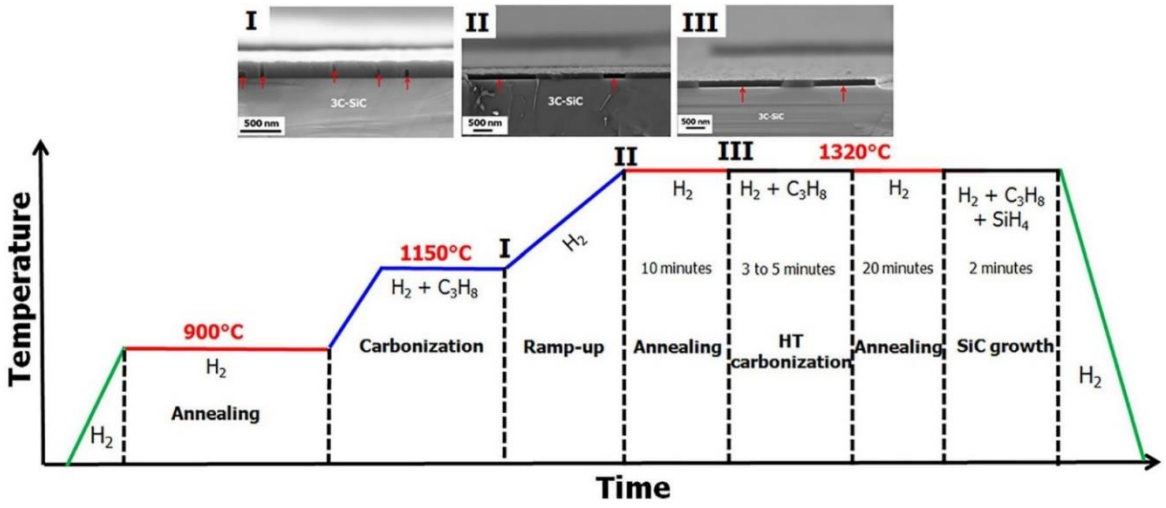


Figure 2.6: Schematic of novel growth technique proposed by Khazaka *et al.* [56].

2.1.3 The growth process of 3C-SiC epilayer on Si substrate used in our study

In this work, the standard growth process of 3C-SiC (001) epilayer on Si (001) will be presented. To mention, the 3C-SiC/Si wafers used in fabrication of the microcantilevers for hydrogen detection were provided by CRHEA, who is one of our collaborators in the project H2MEMS. As aforementioned, several stages of the growth process were optimized as referred in [27], [29], [31], [32]. With these optimizations, the seven-step growth process shown in figure 2.7, gives a satisfactory crystalline quality. The systematic process towards the growth of 3C-SiC epilayers are summarized below:

Step 1: the temperature was augmented to 1050 °C from room temperature under hydrogen (H_2) flux of 8 slm (standard liter per minute) at pressure of 600 mbar.

Step 2: involves Si nucleation process i.e. homo-epitaxial growth of thin film of Si on Si substrate. This process provides a clean and non-oxidized Si surface at *in-situ* condition, to grow subsequent layers. It takes place during 10 min with silane (SiH_4) flow of 1 sccm (standard cubic centimeter per minute) at constant temperature and pressure of 1050 °C and 600 mbar respectively.

Step 3: after Si nucleation, the temperature plunges to 870 °C and during this transition the pressure also declines to 200 mbar under H_2 environment.

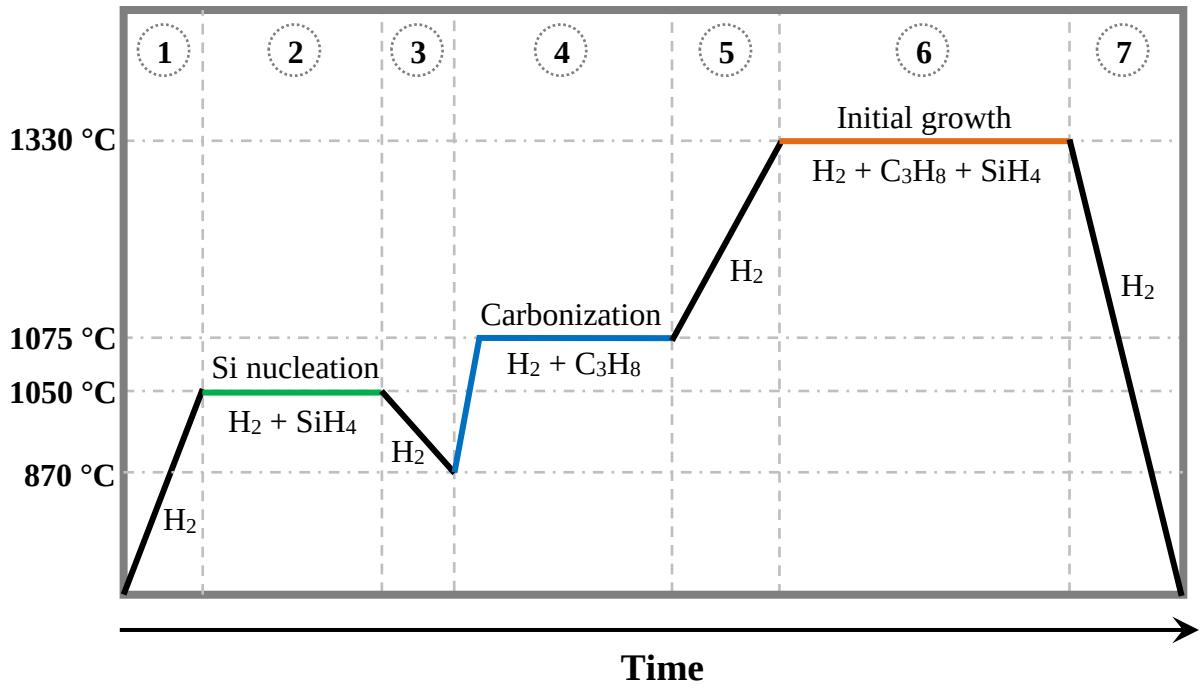


Figure 2.7: Standard growth process of 3C-SiC (001) epilayer on Si (001) substrate used in our study.

Step 4: the carbonization step leads to the formation of a so-called, "buffer layer". This step facilitates the growth of 3C-SiC on Si by reducing the large lattice mismatch. The temperature is then level off at an optimal value (here 1075 °C) from 870 °C, allowing to grow a thin layer of cubic silicon carbide on the Si homo-epitaxial layer. A propane (C_3H_8) flow of 20 sccm was introduced into the reactor preceding the temperature stabilization with fixed pressure of 200 mbar.

Step 5: following the formation of homogeneous 3C-SiC thin film, the temperature was ramped-up to the final value (here 1330 °C) with slight raise in H_2 flow of 15 slm to promote the epilayer growth in further. The transition occurs at steady pressure and C_3H_8 flow of 200 mbar and 20 sccm.

Step 6: the initial growth of the 3C-SiC epilayer takes place by introducing the C_3H_8 and SiH_4 simultaneously into the reaction chamber at balanced temperature (1330 °C) and pressure (200 mbar) under H_2 flux. The SiH_4 and C_3H_8 flow were maintained at 1.4 sccm and 0.8 sccm respectively.

Step 7: upon reaching the desired thickness of 3C-SiC epilayer, the temperature declined drastically to room temperature, in the presence of hydrogen.

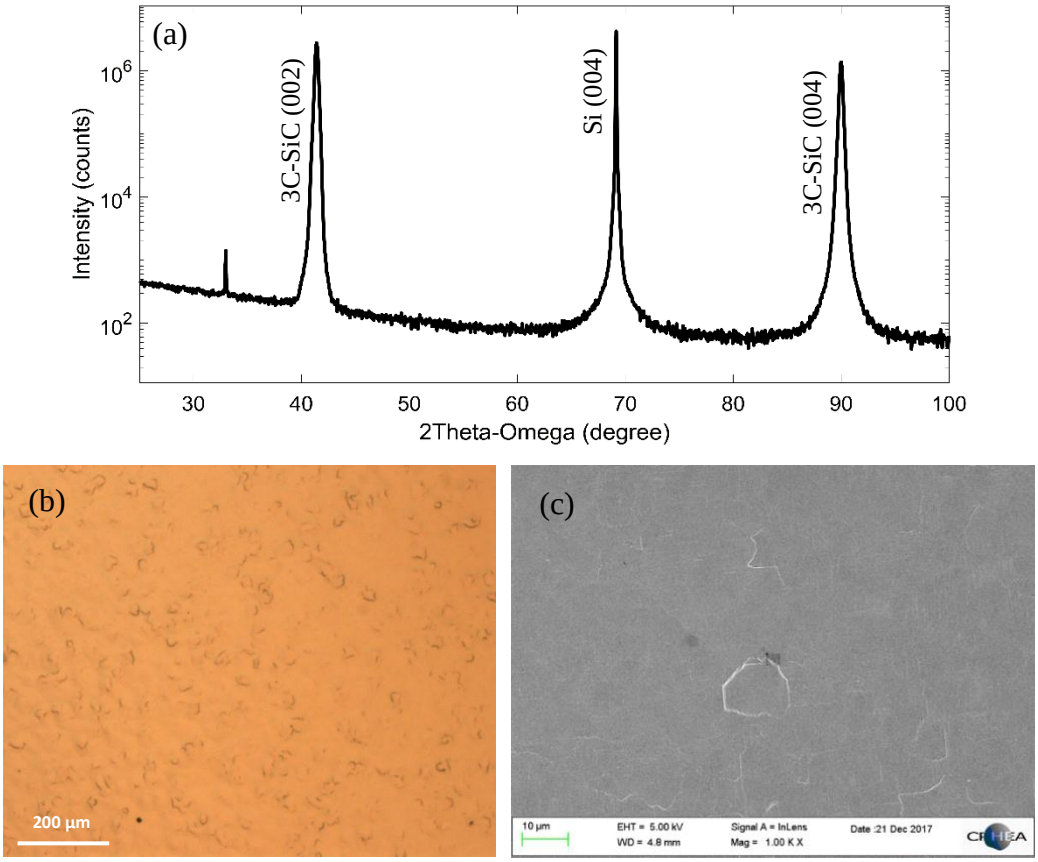


Figure 2.8: (a) 2Theta-Omega XRD scan of 3C-SiC/Si heterostructure, (b) optical microscopy view of the 3C-SiC epilayer surface and (c) plan view SEM image of the same.

The XRD measurement and the microscopic images are showing the surface morphology of the epiwafer presented in this study (see figure 2.8). The 3C-SiC (002) and 3C-SiC (004) diffraction peaks signify that the 3C-SiC epilayer has grown along (001) direction. Furthermore, the Si (004) indicates growth direction of silicon substrate along (001) direction. The more detailed explanation was presented in the PhD dissertation of R. Khazaka [54].

The epi-wafers used in our study have epilayer thicknesses ranging between 5 and 10 µm. Prior to fabrication, the epi-wafers have been polished by NOVASiC [57].

2.2 Background for design validations

Boudjiet *et al.* have done the groundwork on silicon-based systems to optimize several parameters, to obtain best sensitivity and limit of detection in binary gas mixture analysis. These micro-resonators work under the principle of electromagnetic actuation and piezoresistive detection [2]. More elaborate studies have been presented in the PhD thesis of M. T. Boudjiet [1]. Their research helps in understanding the influence of geometries and dimensions of microcantilevers in gas detection. They have also explained the advantages of using optimized electrical parameters, such as current and bias voltage. Followed by, explaining the influence of mechanical parameters, like working at higher resonance modes and the significance of operating in non-linear regime to achieve better sensitivity.

With all, we concentrated the studies based on geometries and dimensions. Because, these parameters play major roles in the device performances, as they have higher influence than others in terms of design strategies. To give an idea about the dimensions used by Boudjiet *et al.*, the values are listed in table 2.2.

Table 2.2: Dimensions of silicon microcantilevers for different geometries. The extension "_5µ" and "_10µ" indicates the thickness of the structure [1].

Geometry	L (µm)	b (µm)	h (µm)	L_{leg} (µm)	b_{leg} (µm)
A0_5µ	500	250	5	-	-
A1_5µ	500	500	5	-	-
A2_5µ	1000	1000	5	-	-
A2_10µ	1000	1000	10	-	-
A3_5µ	2000	1000	5	-	-
U1_5µ	1000	1000	5	666	250
U2_5µ	1000	1000	5	333	250
T1_5µ	1000	1000	5	500	200
T2_5µ	1000	1000	5	250	200

Firstly, to understand the influence of geometries, the cantilevers of various shapes have been examined under a gas mixture environment [58]. Boudjiet *et al.* have compared different shapes like rectangular, U- and T-shaped cantilevers with the same total length (L), width (b) and

thickness (*h*). Among all, the selected geometries were A2, U1, U2, T1, and T2, as referred in figure 2.9 and their corresponding results are shown in figure 2.10.

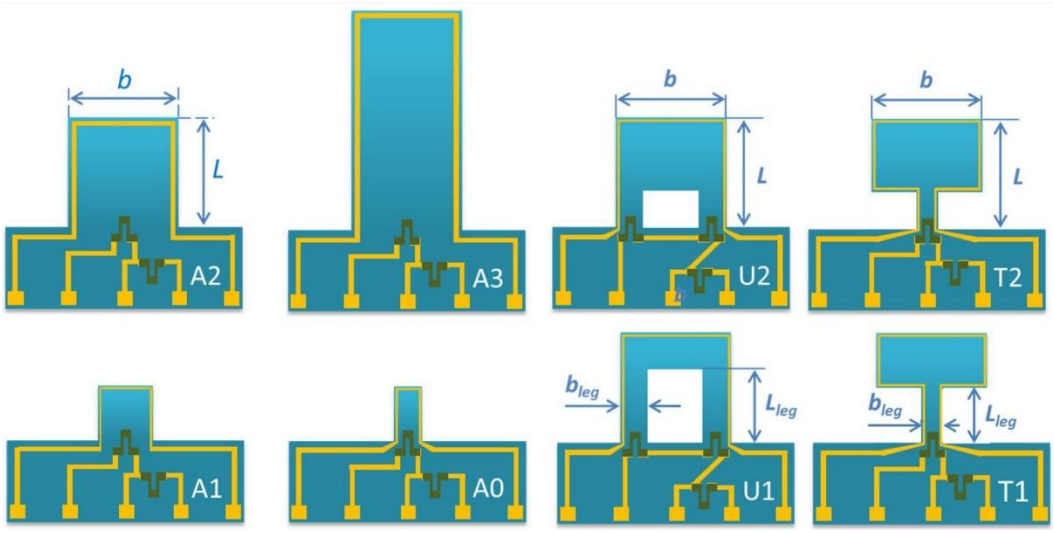


Figure 2.9: Silicon based microcantilevers with different geometries (rectangular, U-, T-shaped) [1].

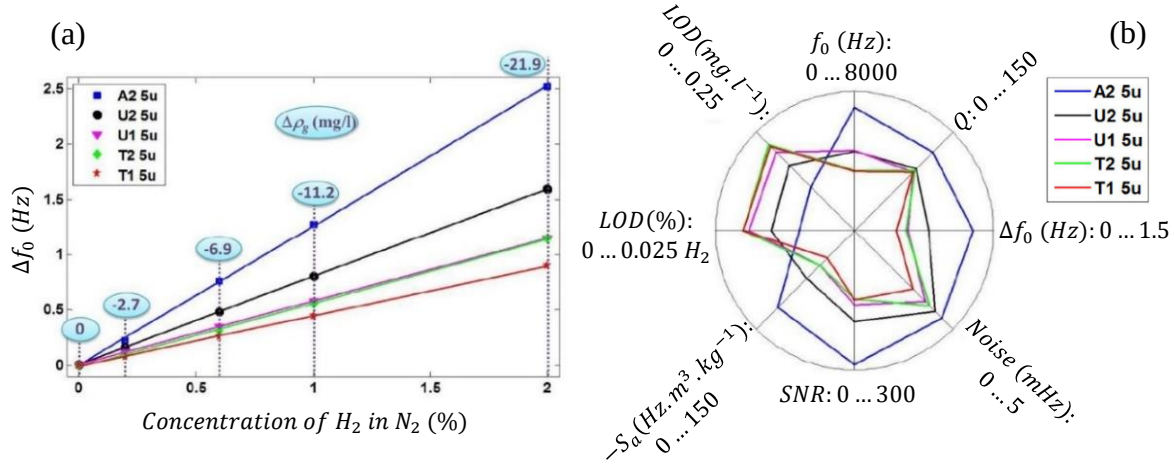


Figure 2.10: Preliminary results. (a) Resonance frequency variation of various geometries for different concentrations of H_2 in N_2. (b) Performance comparison of microcantilevers with different geometries (i.e. A2, U1, U2, T1 and T2) in terms of resonance frequency (f_0), quality factor (Q), variation of resonance frequency (Δf_0) at 1 % of H_2 in N_2, noise calculated by standard deviation, signal to noise ratio (SNR), absolute sensitivity (S_a) and limit of detection (LOD) [1].

These comparative analyses allow us to contrast the influence of cantilever geometries. From figure 2.10.a, it is evident that the rectangular shaped cantilever has higher sensitivity for gas density monitoring. One cannot decide with this simplistic conclusion, even though they have the same dimensions, the contact/active surface were not the same. Apart from this, geometry A2 (5µm) possesses better quality factor, high signal-to-noise ratio for 1 % of H_2 in N_2, best

limit of detection of 100 ppm or 0.11 mg.L^{-1} of H_2 in N_2 and remarkable absolute sensitivity of 117 Hz.kg^{-1}.m^3 (refer figure 2.10.b). Therefore, with these valid results, the rectangular geometry has been selected for further investigation.

Secondly, to retain the best dimension of the selected geometry, the cantilevers with various dimensions have been studied. Primarily, to examine the influence of thicknesses, the cantilevers with the same length, width and various thicknesses (5 µm and 10 µm) are taken. From figure 2.11, it is clear that the variation of gas densities and absolute sensitivities for A2_5µ and A2_10µ were independent of the cantilevers thicknesses. Next, the structures with various lengths and widths have been compared and the dimensions of these compared structures are mentioned in table 2.2. From the experimental results, they found that the sensitivity has increased by a factor of ≈2, when $L=L/2$ and $b=b/2$. Also, for fixed lengths, the widest cantilevers show higher absolute sensitivities [1], [58].

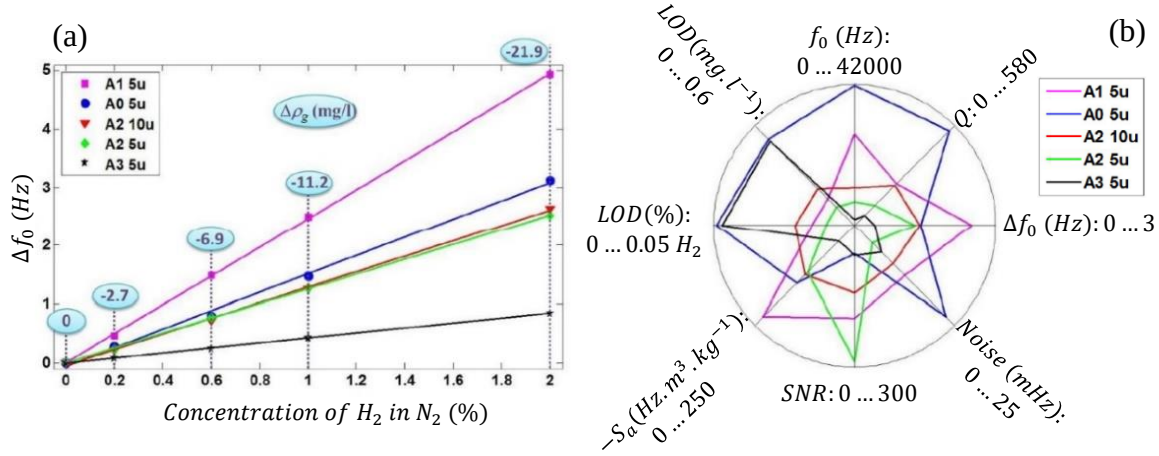


Figure 2.11: Preliminary results. (a) Resonance frequency variation of various dimensions for different concentrations of H_2 in N_2. (b) Performance comparison of microcantilevers with different dimensions in terms of f_0, Q, Δf_0 at 1 % of H_2 in N_2, SNR, S_a and LOD [1].

With these analyses, we choose to work in rectangular geometry of various dimensions. Therefore, the chosen models with their dimensions are mentioned in table 2.3. It is also noteworthy that all the models tabled respect Euler-Bernoulli's beam theory assumptions, i.e. $h \ll b \ll L$, except for A0-REC/iREC and A1-REC/iREC. These 'REC' models were created out of hypotheses proposed by early studies, which say, shorter and wider the cantilevers, higher the absolute sensitivities.

Table 2.3: Dimension for the retained geometries for future fabrications.

Geometry	*L* (µm)	*b* (µm)	*h* (µm)
A0-REC/A0-iREC	250	500	10
A0-SQR/A0-iSQR	500	500	
A1-REC/A1-iREC	500	1000	
A1-SQR/A1-iREC	1000	1000	
A3/A3-i	1000	200	
A4/A4-i	2000	400	

*i represents induction detection

The fabricated cantilevers will work under the same actuation (electromagnetic) and have different detection mechanisms, i.e. induction (method I) and piezoresistive (method II), as shown in figures 2.12 and 2.13 respectively. As explained before, the materials and metals are chosen with great care to work under harsh environments.

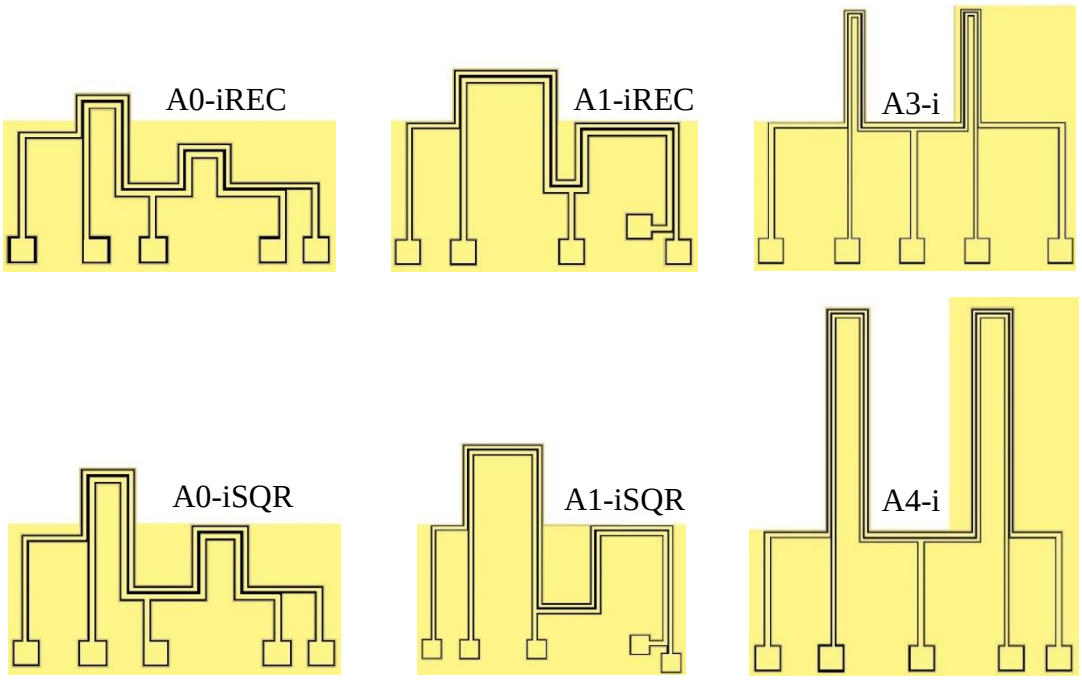


Figure 2.12: Schematic of 3C-SiC-µCs that works on electromagnetic actuation and induction detection (method I).

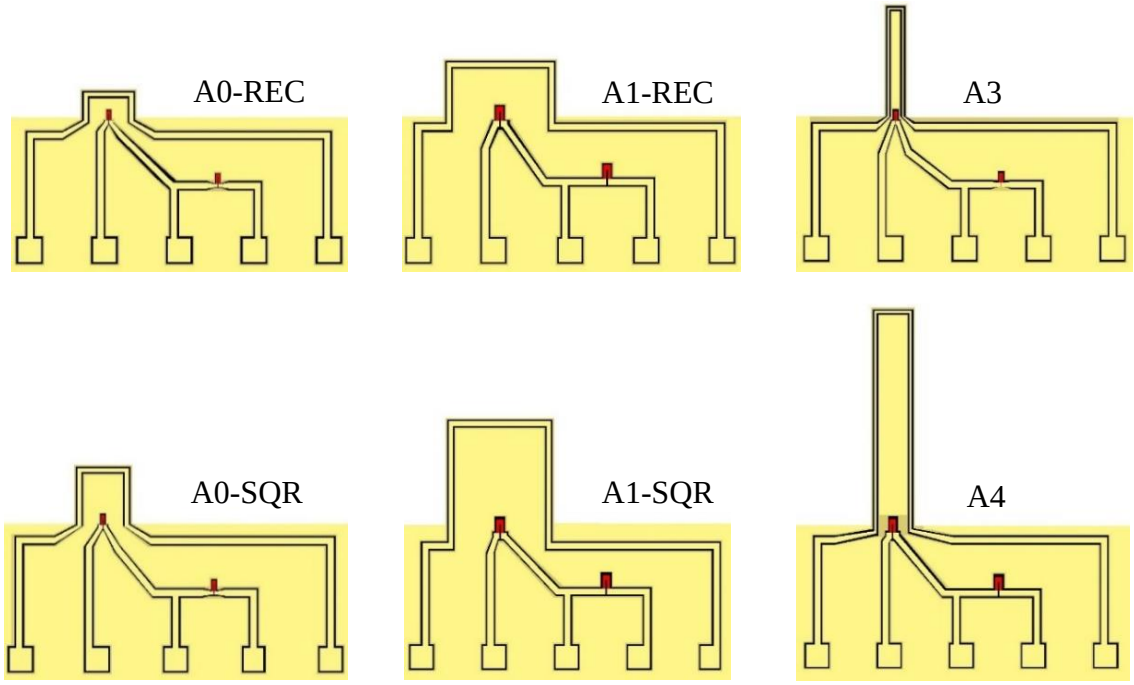


Figure 2.13: Schematic of 3C-SiC-µCs that works on electromagnetic actuation and piezoresistive detection (method II).

2.3 Fabrication of 3C-SiC-microcantilevers (µCs)

Unlike silicon, silicon carbide micromachining is more challenging due to its chemical inertness. As explained earlier, we use cubic SiC grown on Si substrate, in which the cantilever has to be released using wet etching of Si. In addition, SiC acts as an etch-stop layer during Si wet etching because it is inert to typical silicon isotropic etchants, like KOH and TMAH. The fabrication of 3C-SiC-µCs used in our study consists of six-stage processes, from creating the alignment patterns to releasing the cantilevers (refer figure 2.14). The systematic process and the hindrances of using 2-inch wafers at a certain level are surmounted. The epi-wafers of 3C-SiC(001)/Si(001) orientation, with 5-10 µm epilayer thicknesses were used for the microcantilever fabrication.

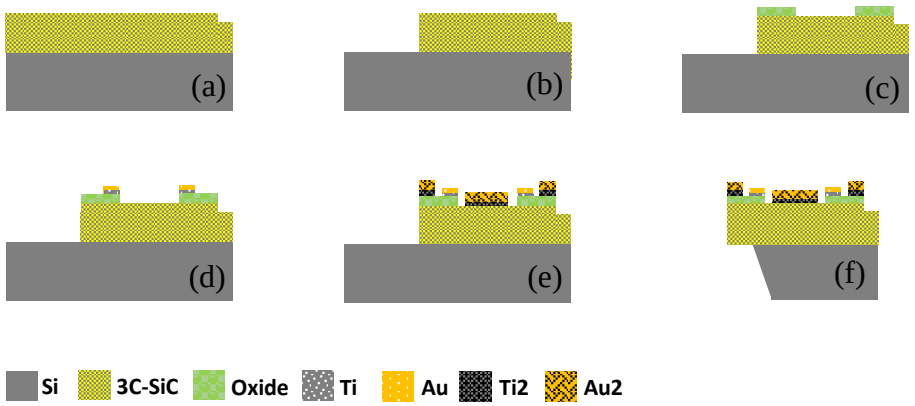


Figure 2.14: Systematic process flow of 3C-SiC-µCs fabrication. (a) Patterning alignment crosses, (b) defining cantilevers geometries, (c) introduction of isolation layer to separate 3C-SiC and metal contacts, (d) deposition of metals for piezoresistive detection, (e) deposition of metals for electromagnetic actuation and (f) releasing of cantilevers from rear side by etching the Si substrate.

2.3.1 Sample preparation

Primarily, before starting the fabrication, a two-step cleaning process was carried out to discard the surface impurities. Firstly, the 2-inch epi-wafers were immersed in Caro's acid (a.k.a. piranha bath). This solution is a mixture of one part of sulfuric acid (H_2SO_4-96 wt.%) and one part of hydrogen peroxide (H_2O_2-30 wt.%). Caro's acid naturally heats up between 100-130 °C on combining with each other at a 1:1 ratio. The aim of this step is to eliminate organic residues and this cleaning procedure takes place about 10-15 min. Next, the hydrofluoric acid (HF) dip, which removes a thin layer of native oxide present on the epi-wafer. The HF dip is made of one part of water (H_2O) and one part of HF (50 wt.%). The process occurs at room temperature about 1-3 min. Finally, the epi-wafers were thoroughly rinsed in deionized water for at least 5 min and then dried manually.

Consecutive to cleaning, the first photolithography step was performed to pattern the alignment crosses by etching a few nanometers of 3C-SiC layer, to position further layers. In order to protect the uninteresting areas, a thin layer of 100 nm nickel (Ni) was sputtered on the epilayer at room temperature under argon (Ar) flow and working pressure of 15 sccm and 5 mTorr respectively. This layer acts as a hard mask while etching 3C-SiC (see figure 2.15.a). Then to pattern Ni, OIR 906-12 photoresist (PR) has been used and etched through wet etching, by commercially available ANPE solution (acetic acid: nitric acid: phosphoric acid: water of

5:5:85:5 ratio) at 50 °C. The resulting structure is shown in figure 2.16.a. After defining Ni mask, PR was removed using oxygen (O_2) plasma, as referred in figure 2.15.d.

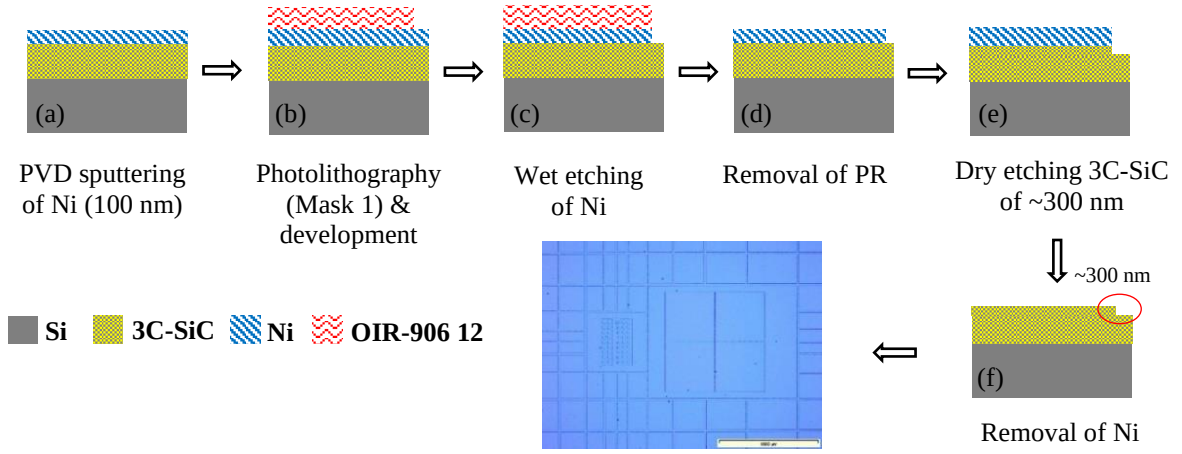


Figure 2.15: Process flow for defining the alignment crosses, step 1.

Later the silicon carbide layer was etched using an inductively coupled plasma (ICP) reactor by Corial (200 IL). The plasma etching was carried out under SF_6 (sulfur hexafluoride) and O_2 environment at working pressure and chiller temperature of 10 mTorr and 5 °C respectively. The addition of a small amount of O_2 during the reaction helps to form nickel oxide thereby making it a durable mask. The ICP and RF power of 1400 W and 250 W were maintained throughout the process. With these parameters, the epilayer was etched anisotropically for ≈300 nm, about 20 s. This process was optimized by our team and has been used for over a decade [21]. Lastly, after dry etching, the nickel mask was wet-etched using ANPE solution at 70 °C. Few process steps corresponding to figures 2.15.b, 15.d and 15.f are shown on the optical microscopic images in figures 2.16.a, 16.b and 16.c.

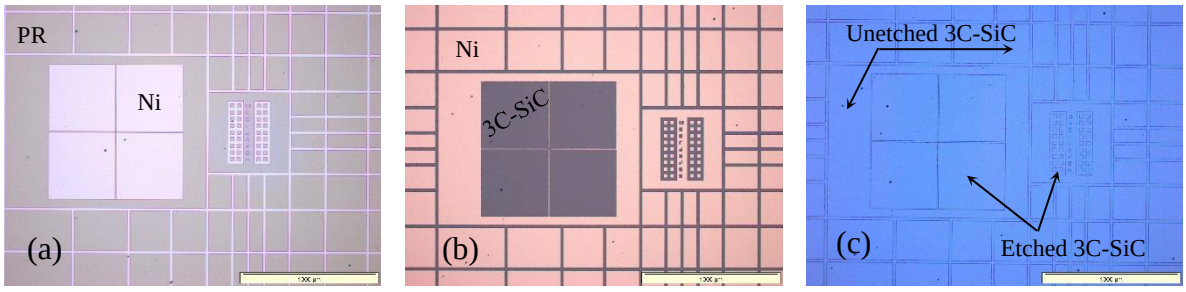


Figure 2.16: Top view of optical microscopic images showing (a) Photoresist as mask to pattern nickel, (b) nickel as hard mask for 3C-SiC plasma etching and (c) end of stage one with patterned alignment crosses.

2.3.2 Defining the geometries of 3C-SiC-µCs

The microcantilevers are entirely made of 3C-SiC material; the Si in the substrate only serves as a support and has no effect on electrical connections. Therefore, to achieve better cantilever geometries, it is essential to pattern the 3C-SiC epitaxial layer perfectly. Furthermore, the entire epilayer height must be etched in order to facilitate the cantilever release. We will discuss this in the sixth stage of fabrication (§2.3.6). To define the cantilever geometry, the second photolithography stage was conducted. From figure 2.17, one can notice that the process flow of stage one and two are almost the same except for the objectives. The first step entails etching ≈300 nm of the 3C-SiC to distinguish the alignment crosses in the epilayer, so that the upcoming stages can be positioned.

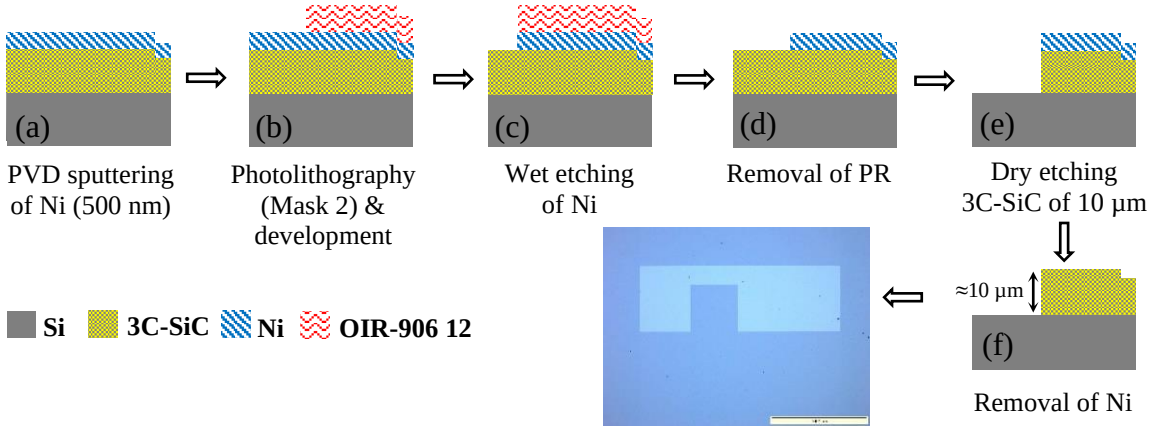


Figure 2.17: Process flow for defining the geometries of 3C-SiC-µCs, step 2.

However, here the whole height of the 3C-SiC epilayer has been removed except in cantilever areas, which were safely protected with a hard mask (i.e. nickel of 500 nm). In this step, a thicker layer of Ni was used, due to the thicker etching layer and longer etching time. The dry etching of 3C-SiC epilayer was carried out using ICP by Corial (200 IL). This device is equipped with a laser interferometer head and a CCD camera. With the help of laser interferometry, one can identify change in film thickness and/or refractive index while the layer of interest is being etched and the function is called end-point-detection (EPD). This interferometric information is provided by monitoring sudden change in signal intensity corresponding to the interference [59], [60]. The EPD helps to identify heterolayers and determine etch rates during *in-situ* dry etching process. To mention, the refractive index for SiC and Si are 2.65 and 3.88 respectively. This etching was done with great care, because if the

3C-SiC layer was not completely etched, it would complicate cantilever release in the final stage and has a high risk of obtaining ill-defined geometries.

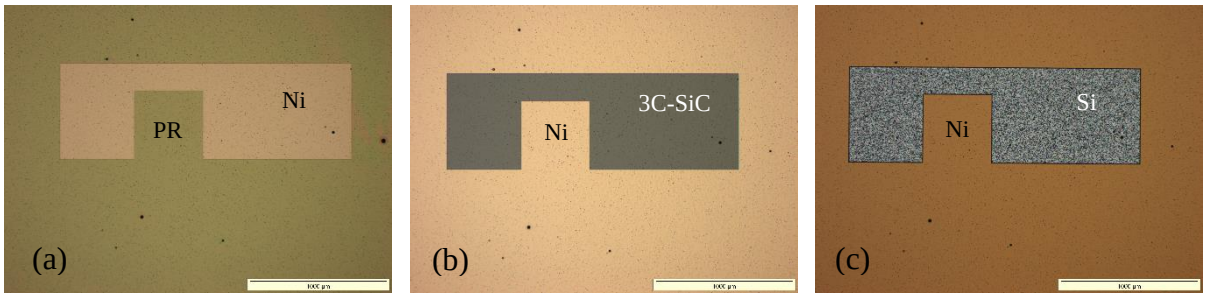


Figure 2.18: Top view of optical microscopic images showing (a) Geometry patterned using PR to shape Ni mask, (b) etched Ni motifs to define 3C-SiC-µC geometry and (c) after ICP etching of 3C-SiC with Ni mask.

From figures 2.18.b and 2.18.c, one can notice the color variation of Ni mask. This is due to oxide formation, which makes Ni a harder mask and more difficult to remove. To remove this tough layer, the ANPE etching temperature was increased to 70 °C.

2.3.3 Optimization of the isolation layer

The aim of having the isolation layer is to insulate the 3C-SiC epilayer from actuation and detection metals. As this layer is the base for forthcoming layers, the homogeneity and surface morphology are very important. In our study, we compared two types of oxide layers: i) silicon dioxide (SiO_2) deposited using sputtering at room temperature and ii) undoped silicon glass (USG) deposited at higher temperature, i.e. at 400 °C, by plasma-enhanced chemical vapor deposition (PECVD).

The process flow of this stage is shown in figure 2.19. Primarily, the oxide of interest was deposited. Subsequently, the third photolithography procedure has been performed to pattern the mask for the isolation layer. Here, the photoresist was deposited using a spray coater rather than spin coating, due to the difference of height between Si and 3C-SiC layers (5-10 µm).

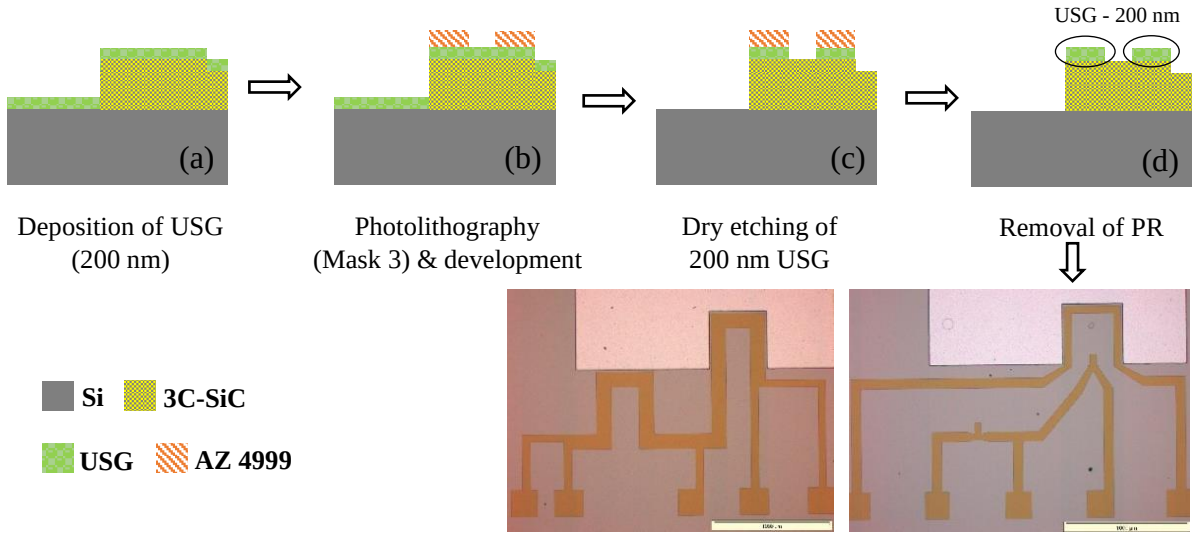


Figure 2.19: Process flow of patterning isolation layer on substrate to separate the future metal contacts, step 3.

The choice of PR coating technique is illustrated in figure 2.20. For spin coating, the photoresist OIR 908-35 and for spray coating AZ4999 were used. Both the PRs have the same thickness after development (i.e. ≈3 µm). Figures 2.20.a and 2.20.b show the spin coated resist layers. These optical microscopic images demonstrate the poorly defined layer and residues at the edges of the cantilever. The left-over photoresist in the edges of the cantilever can be removed during final release, but the poorly defined isolation layer will not retain functional cantilevers. Therefore, the spray coating technique was chosen due to its excellent patterning (refer to figure 2.20.c).

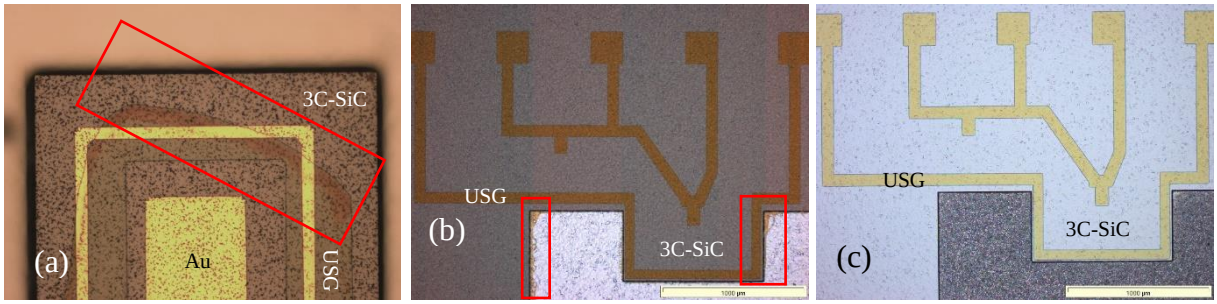


Figure 2.20: Top view of optical microscopic images showing patterned oxide layer using PR mask coated with (a), (b) spin coater and (c) spray coater.

Firstly, the oxide deposited using the sputtering technique was studied. This layer was deposited at 150 W under 20 sccm of Ar flow. An angle of 20 degrees was maintained with planetary rotation throughout the deposition to attain a homogeneous layer. During the photolithography process, the stack was baked, before and after UV exposure. After these bakings, the surface

morphology of the oxide layer has been changed. The optical microscopic images of oxide surfaces are shown in figure 2.21. They look rough and powdery while baked in a hot plate and formed lumps when exposed in a fusion furnace. In both cases the roughness was around 50-80 nm.

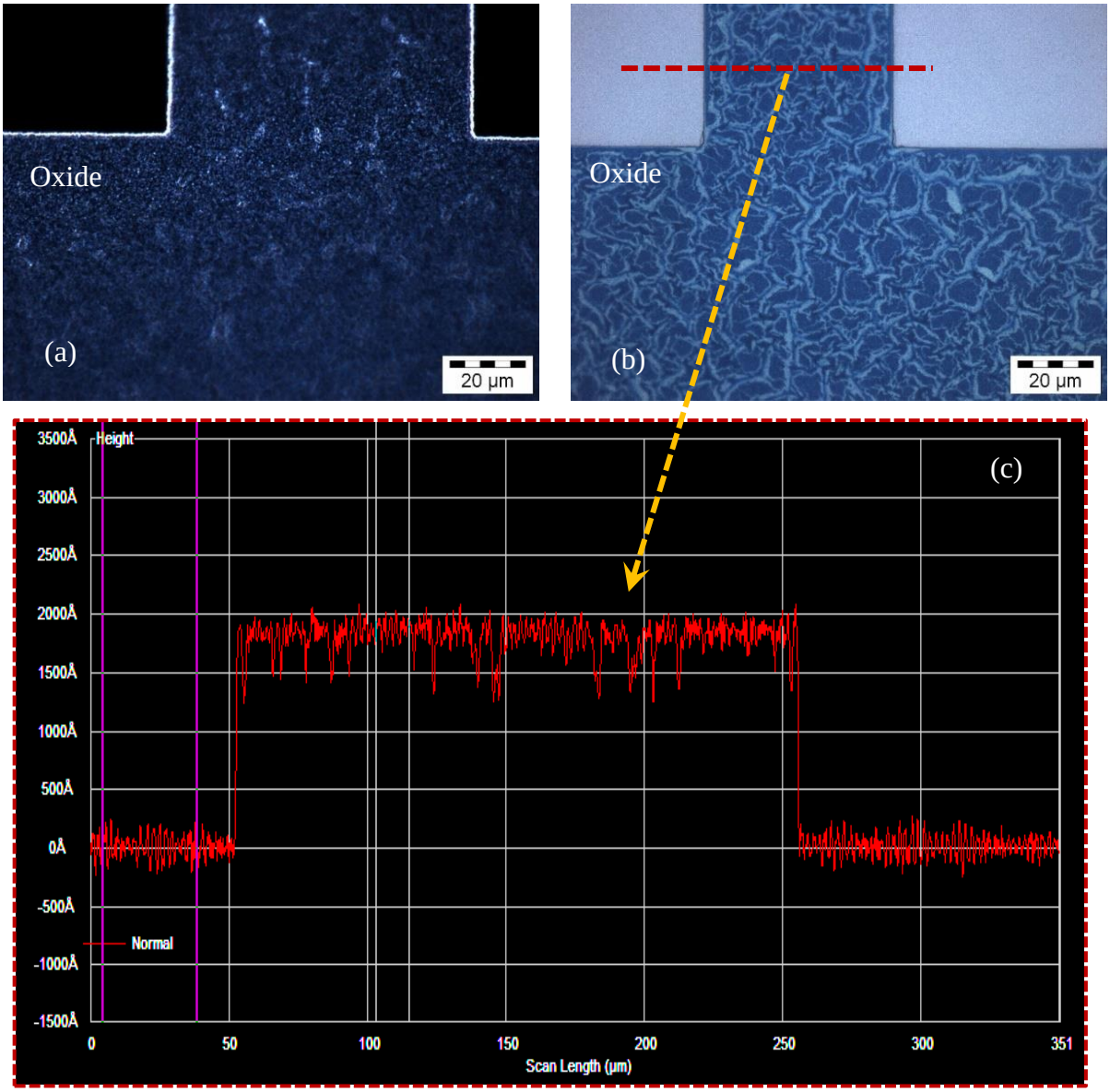


Figure 2.21: Optical microscopic images of sputtered oxide layer (a) baked in hotplate and (b) in fusion furnace during photolithography stage. (c) Profilometric graph showing the roughness on the oxide layer (baked using fusion furnace).

As mentioned earlier, the surface morphology of this layer is crucial because the contact metals for actuation and detection will be patterned on this layer. In both cases explained in figures 2.21.a and 2.21.b, the upcoming layers have favorable chances of open circuit due to cracks and/or small openings in metallic tracks, especially for very thin metal films. Therefore,

the oxide deposition has been performed by PECVD, as explained at the beginning of this section. This low stress USG was deposited at an optimal gas flow of 18 sccm (SiH_4), 710 sccm (N_2O) and 160 sccm (N_2) at 400 °C with RF power of 20 W. Unlike the preceding one, the oxide surface was smooth and the deposition was homogeneous. The microscopic view of the patterned oxide is presented in figure 2.22. The corresponding AFM scan shown in figure 2.23 demonstrates the uniformity of the layer. In this case, the overall roughness was less than 5 nm.

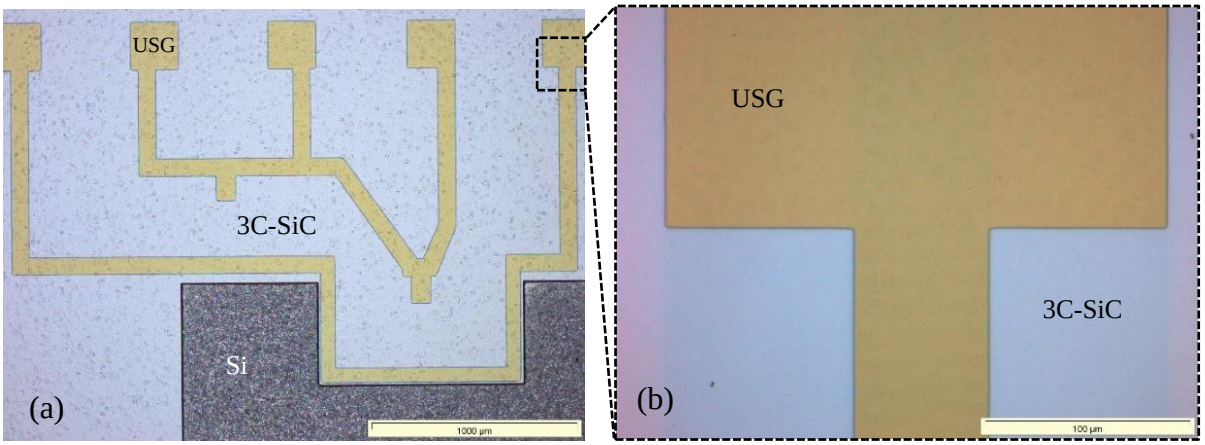


Figure 2.22: Patterned USG on 3C-SiC epilayer deposited using PECVD (a) Optical microscopy view (5x), (b) Optical microscopic image taken at 50x magnification (for the selected region).

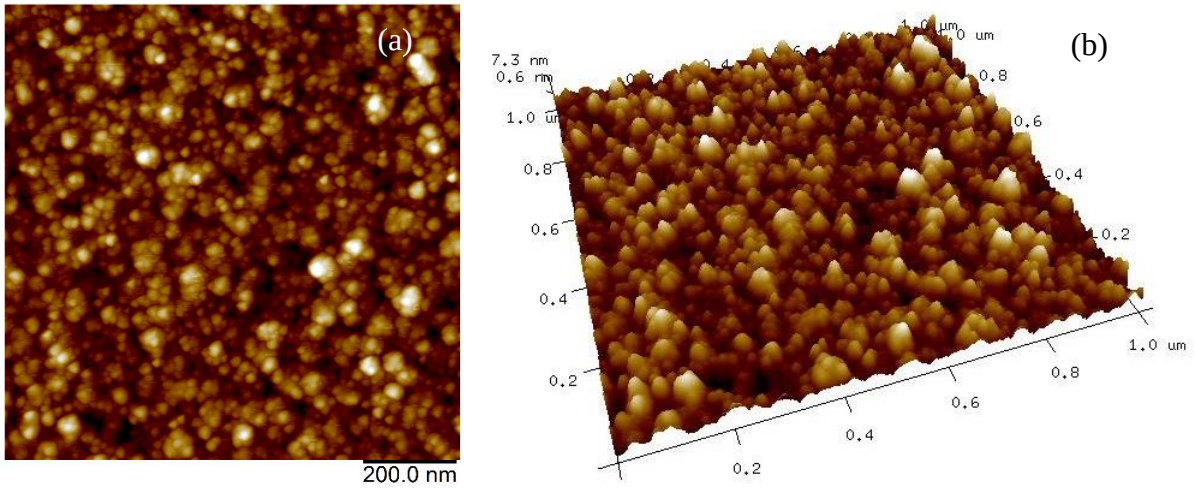


Figure 2.23: Patterned USG on 3C-SiC epilayer deposited using PECVD (a) AFM (1x1 µm²) scan on USG layer and (b) 3D image showing surface morphology of the same.

Finally, the dry etching process was carried out by ICP etching at 20 °C. Fluoroform (CHF_3) and ethylene (C_2H_4) of 30 sccm and 3 sccm respectively were employed simultaneously to perform anisotropic etching under 3 mTorr working pressure. The etching was controlled by

the EPD function in the Corial (200 IL) reactor. After etching, the PR mask has been removed using oxygen plasma.

2.3.4 Deposition of metals for piezoresistive detection

To define the detection metal layer, a simple lift-off technique has been used, as illustrated in figure 2.24. In contrast to classical surface micromachining, lift-off processes are relatively simple. Notably with metallic layer stacks like gold or platinum, the direct wet etching procedures are complex to perform. Besides, it not only involves patterning of metal layers but also safeguards the oxide layer underneath. In most cases, the chemical etchants used for patterning gold are more vigorous and difficult to control while etching. For this reason, a simple lift-off procedure was chosen.

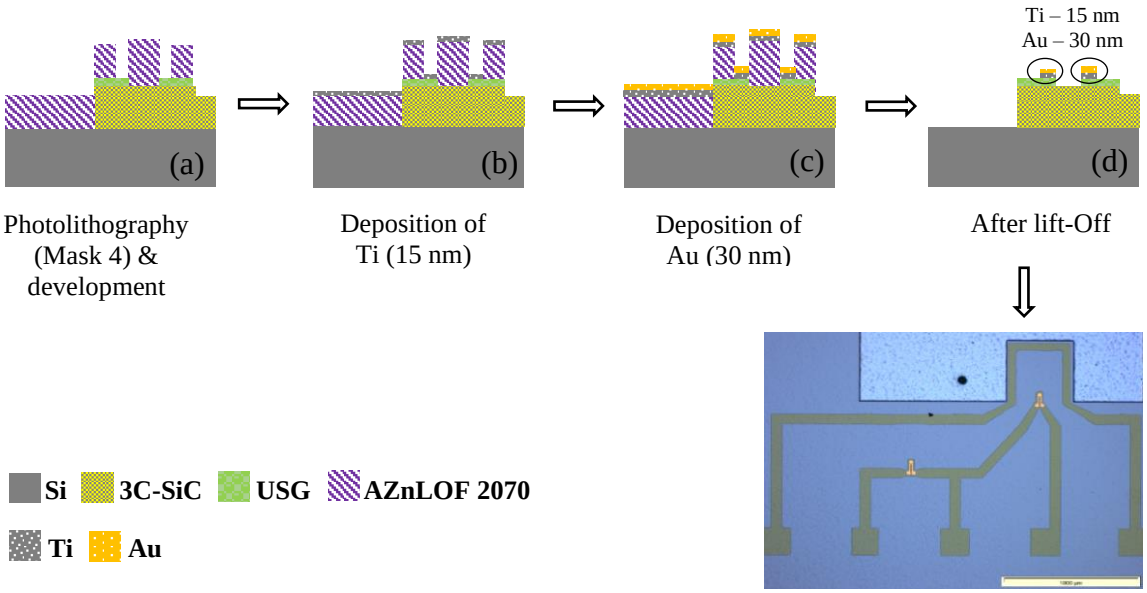


Figure 2.24: Process flow of patterning piezoresistive detection metal layer for method II technique, step 4.

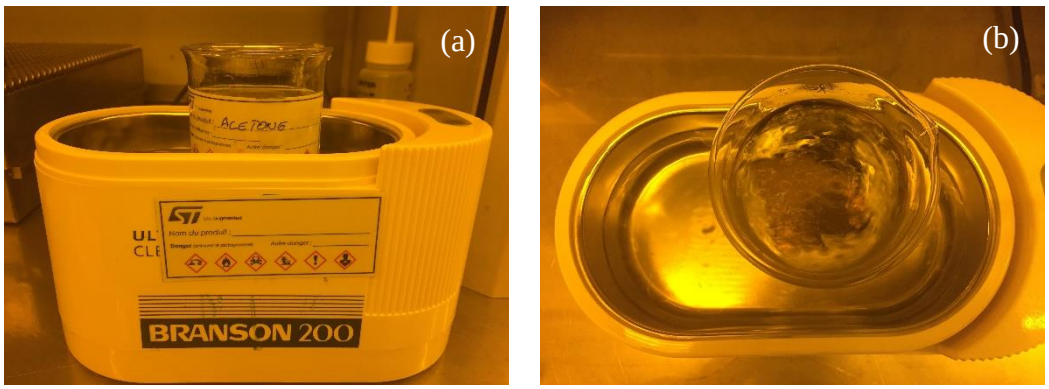


Figure 2.25: (a) Ultrasonic bath used for lift-off process and (b) sample placed in acetone undergoing ultrasonic vibrations at room temperature.

Therefore, this fourth photolithography stage was performed using photoresist dedicated to lift-off, i.e. AZnLOF 2070. The thickness of this PR is 7 µm. This thicker PR facilitates the lift-off by providing high sidewalls of opening and allows structuring without breaking the metallic films. Afterward, the metal of interest was deposited on the epi-wafer. Then, the lift-off procedure was carried out using ultrasonic treatment with suitable solvent, in our case acetone has been used, refer figure 2.25.

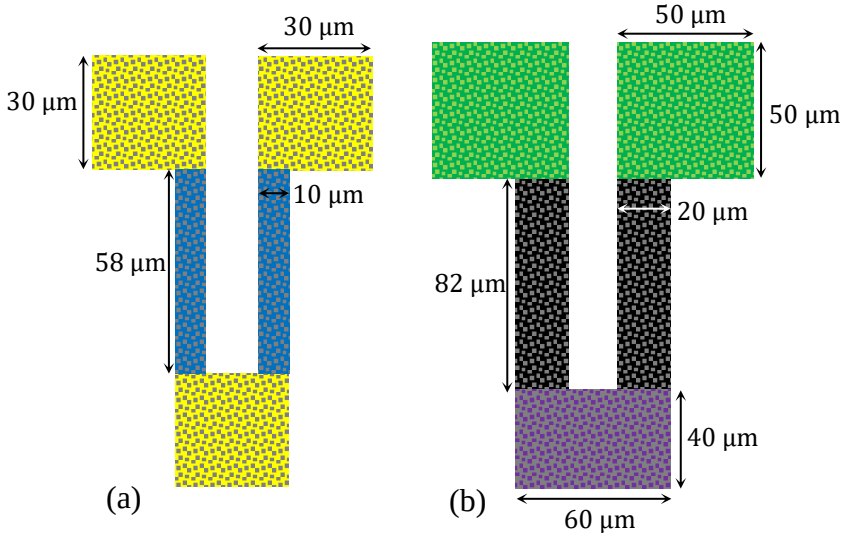


Figure 2.26: Dimensions of piezoresistors (a) used in A0-REC, A0-SQR, A3 geometries and (b) in A1-REC, A1-SQR, A4 geometries.

In our study, we analyzed two kinds of detections, as mentioned in §2.2. Out of which, method II uses piezoresistors as referred in figure 2.13. In the current study, we have two dimensions of resistors that vary according to the geometry. In case of A0-REC, A0-SQR and A3, the resistor dimensions are small due to the design complexity, as shown in figure 2.26.a. Moreover, the resistors of A1-REC, A1-SQR and A4 are a few micrometers higher than others (refer figure 2.26.b).

Ideally, the resistor must have a smaller thickness and width (b) than the conducting wires to provide maximum resistance, but the length (L) is kept optimum to detect the deformation of the structure during gas detection. Nonetheless, the thickness (t) of the detection metal layer also plays an important role in resistance calculation, since it is inversely proportional to it (refer eq. 2.1). The electrical resistance of conductor with uniform cross-section is given by:

$$R = \rho \frac{L}{A} = \rho \frac{L}{bt} \qquad \text{Eq. 2.1}$$

where, *R* is the resistance in ohm (Ω) with the resistivity of the metal ρ in (Ω.m) for given length of the conductor in meter (m), which having a cross-section area (*A*) in m². The cross-section area can also be expressed as a function of width and metal thickness. In this study, gold (Au) is chosen as a detection metal. Additionally, a thin layer of titanium (Ti) has been deposited for better adhesion between oxide and gold layer.

On substituting the known values in eq. 2.1, we obtain the values of resistances for Ti and Au. In our case, $R_{Ti} \gg R_{Au}$, this is because the resistivity of titanium (ρ_{Ti}) is higher than gold (ρ_{Au}). To mention, the resistivity of Au and Ti are 2.44*10^{-8} Ω.m and 4.20*10^{-7} Ω.m respectively at room temperature. Also, the thickness of the gold used in this layer is twice thicker than titanium. This is due to fabrication process complications, which will be explained later in this section. The bimetal layer with various resistances look like two resistors in parallel circuit, as shown in figure 2.27.

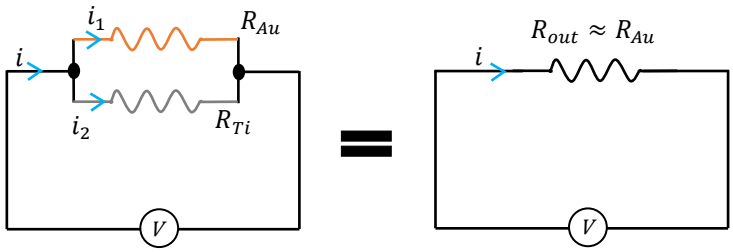


Figure 2.27: Equivalent circuit for the output resistance.

According to figure 2.27, the output resistance (R_{out}) is approximately equal to the resistance of gold (R_{Au}). In addition one can recall the ohm's law to understand this approximation with the help of the current flow in the circuit. It states that the current flow in an amount inversely proportional to the resistance ($\because I = V/R$). Therefore, higher the resistance, lower the current flow through the resistor. Hence the current flow is higher in gold layer rather than titanium as expected, i.e. $i_1 > i_2$.

This can be explained by the following relation corresponding to the output resistance in parallel circuit, written as:

$$\frac{1}{R_{out}} = \frac{1}{R_{Au}} + \frac{1}{R_{Ti}} \qquad \text{Eq. 2.2}$$

The above equation can be rewritten as:

$$R_{out} = \frac{R_{Au} * R_{Ti}}{R_{Au} + R_{Ti}} \approx R_{Au}; only\ if\ R_{Au} \ll R_{Ti} \quad \text{Eq. 2.3}$$

It is noted that the output resistance of the detection metal layer must be higher than the actuation metal layer. This is to distinguish between variations caused by piezoresistors due to their geometrical change during cantilever deflections. This could have been done by varying the thickness of the Au layer. The eq. 2.1 has made clear that lower the thickness, higher the resistance value. Based on this theoretical assumption and on substituting the known values of resistivity, length and width for Ti and Au in eq 2.3, we need ≈10 nm and ≈6 nm of Ti and Au respectively, to achieve ≈50 Ω resistors for presented geometrical structure in figure 2.26. Due to limitations in fabrication, these calculated thicknesses are practically impossible to achieve. Therefore, in the beginning, A 30 nm-thick Au layer was deposited on the 15 nm-thick Ti layer. Later, a Ti/Au stack of 15/15 nm was experimented. To specify, the thickness of Au layer is more crucial than Ti layer, because it is influential due to its lower value of resistance (refer to eq. 2.3).

Metals for detection can be deposited using a variety of techniques. In this work, the metals deposited by PVD sputtering and evaporation on polished and unpolished epi-wafers are compared. First, the trail was made using PVD sputtering at room temperature on polished and unpolished epi-wafers. The deposition takes place under 5 mTorr pressure with DC power and Ar flow of 500 W and 15 sccm respectively. The targeted thickness of 15 nm of Ti and 30 nm of Au were achieved.

Furthermore, after lift-off, the surface morphology of piezoresistors were compared using AFM scans for both the epi-wafers. After observing the optical microscopic images and AFM measurements, one can conclude that PVD sputtering works fairly well for thicker materials, but the resistors were poorly defined (refer figures 2.28.a and 2.28.c). Indeed, they were a few micrometres higher than expected, because the high sidewalls are slightly covered with deposited metals that made lift-off difficult. Moreover, the layer was porous, non-uniform and rough compared to the PVD evaporation. At the end of the first comparison, unpolished epi-wafers are eliminated. By comparing figures 2.28.c and 2.28.d, we can see that the grain sizes are smaller, and there are sharp peaks on the unpolished epi-wafer, which indicates differences in altitudes on the surface. The root mean square (RMS) value is between 10 and 15 nm for these AFM scans.

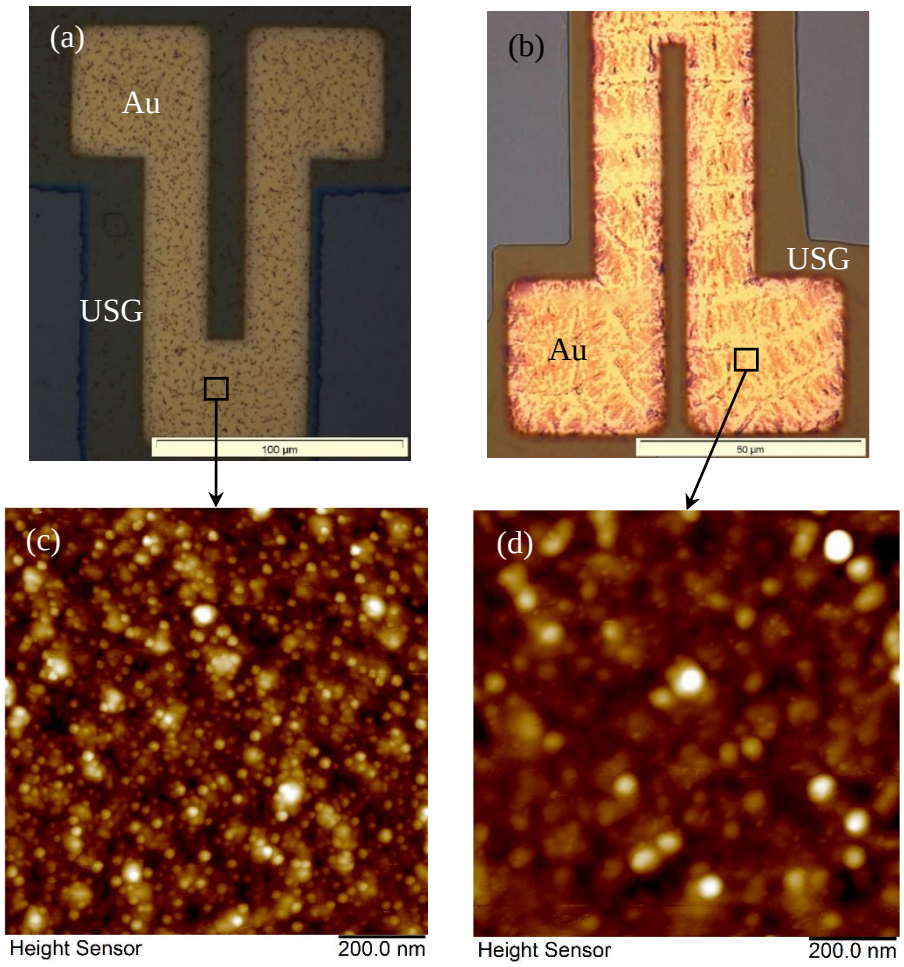


Figure 2.28: Top view of optical microscopic images showing patterned piezoresistors using PVD sputtering for Ti/Au thickness of 15/30 nm on (a) unpolished epi-wafer and (b) polished epi-wafer. Corresponding AFM (1x1 µm²) scan showing the surface morphology of the (c) unpolished epi-wafer and (d) polished epi-wafer.

Secondly, PVD evaporation technique was performed. Deposition occurs under vacuum, where hot source material evaporates and condenses on the substrate facing each other. The filament underneath the crucible heats up for increasing current. In our process, the current flow of 60 mA and 85 mA were maintained to evaporate Ti and Au at the rate of 0.2 nm/s for each. During deposition, the sample holder rotates in planetary motion with speed of 5 rpm, to maintain the layer uniformity. Here, the gold layer with two different thicknesses of 30 nm and 15 nm were tested. Considering figure 2.29.b, one can conclude that the process is limited to thicknesses greater than or equal to 30 nm. Therefore, Ti and Au thicknesses of 15 nm and 30 nm using PVD evaporation technique were finalized to conclude this stage.

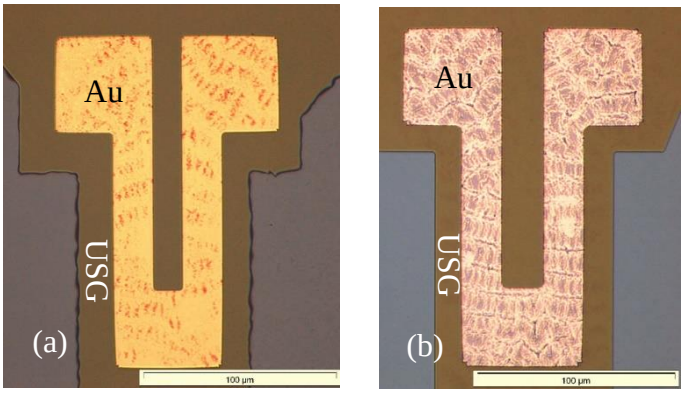


Figure 2.29: Top view of optical microscopic images showing metal deposition using PVD evaporation technique on polished epi-wafers for Ti/Au thickness of (a) 15/30 nm and (b) 15/15 nm.

The method II cantilever models consist of two piezoresistors, which were oriented accordingly to experience maximum mechanical strain. These resistors act as strain gauges, in which the detection gauge (R_{dec}) is placed on the surface of the cantilever beam, where there is maximum strain. Then, the reference gauge (R_{ref}) is situated on the stationary part, as referred in figure 2.30. The two gauges were mounted in a Wheatstone bridge configuration, in order to transform the variation of resistance into variation of voltage for applied current in the gas mixture environment.

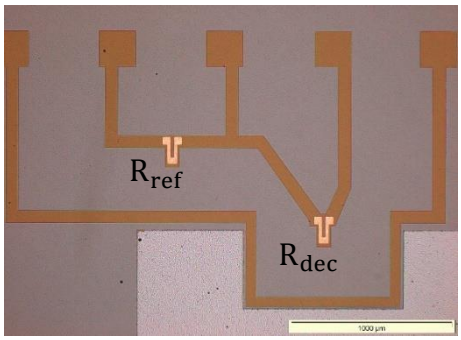


Figure 2.30: Top view of optical microscopic images showing 3C-SiC-µCs with patterned piezoresistors used in method II detection.

2.3.5 Deposition of metals for electromagnetic actuation

Actuation metals are as important as detection metals, without which, the cantilevers are non-functional. This patterning is the last step in front face processing of epi-wafer. The process flow is remarkably similar to that of the previous stage, which is shown in figure 2.31. A simple lift-off procedure was conducted, preceding the metal layer deposition using PVD evaporation

technique. Compared to piezoresistors, the connecting wires were longer and thicker. Moreover, the thickness of the Au layer was kept at least 10 times higher than the thickness of the piezoresistors. This is because, higher the metal thickness, lower the output resistance (refer to eq. 2.1 and eq. 2.3), which results in higher current flow while actuating the microcantilevers. Consequently, the resistance of Au contact wires were calculated for two different thicknesses of 300 nm and 500 nm with constant Ti thickness of 50 nm. The estimated sum discloses resistance values less than 1 Ω for both cases. As a result, we have chosen the ideal thickness of Ti/Au of 50/300 nm.

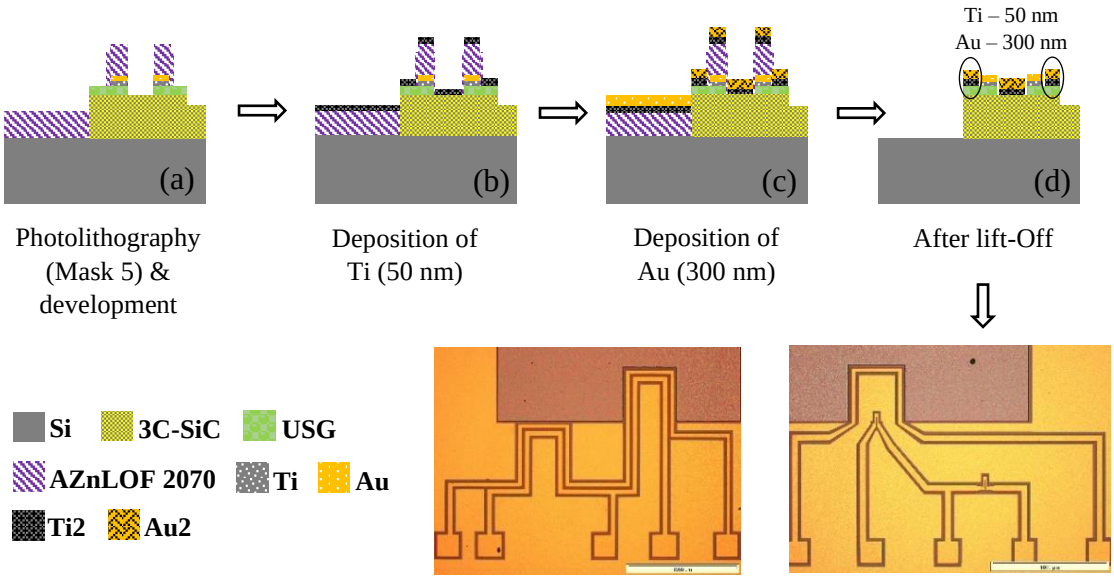


Figure 2.31: Process flow for patterning actuation metals, step 5.

Once again, the surface morphology for unpolished and polished epi-wafers were compared. Nevertheless, this time, the metal deposition was carried out using PVD evaporation technique. The AFM scans for both epi-wafers are shown in figure 2.32, which demonstrate the topographical features of the gold layer deposited for actuation. Certainly, the unpolished epi-wafer presented here has a larger grain size and is rougher than the polished epi-wafer.

To summarize, both surfaces were asymmetrical and smooth compared with PVD sputtering. However, the roughness present is purely determined by the morphologies of the bottom layers. Hence, it is recommended to use polished wafers in order to eliminate these problems. Also, to mention the RMS value was less than 5 nm for both cases.

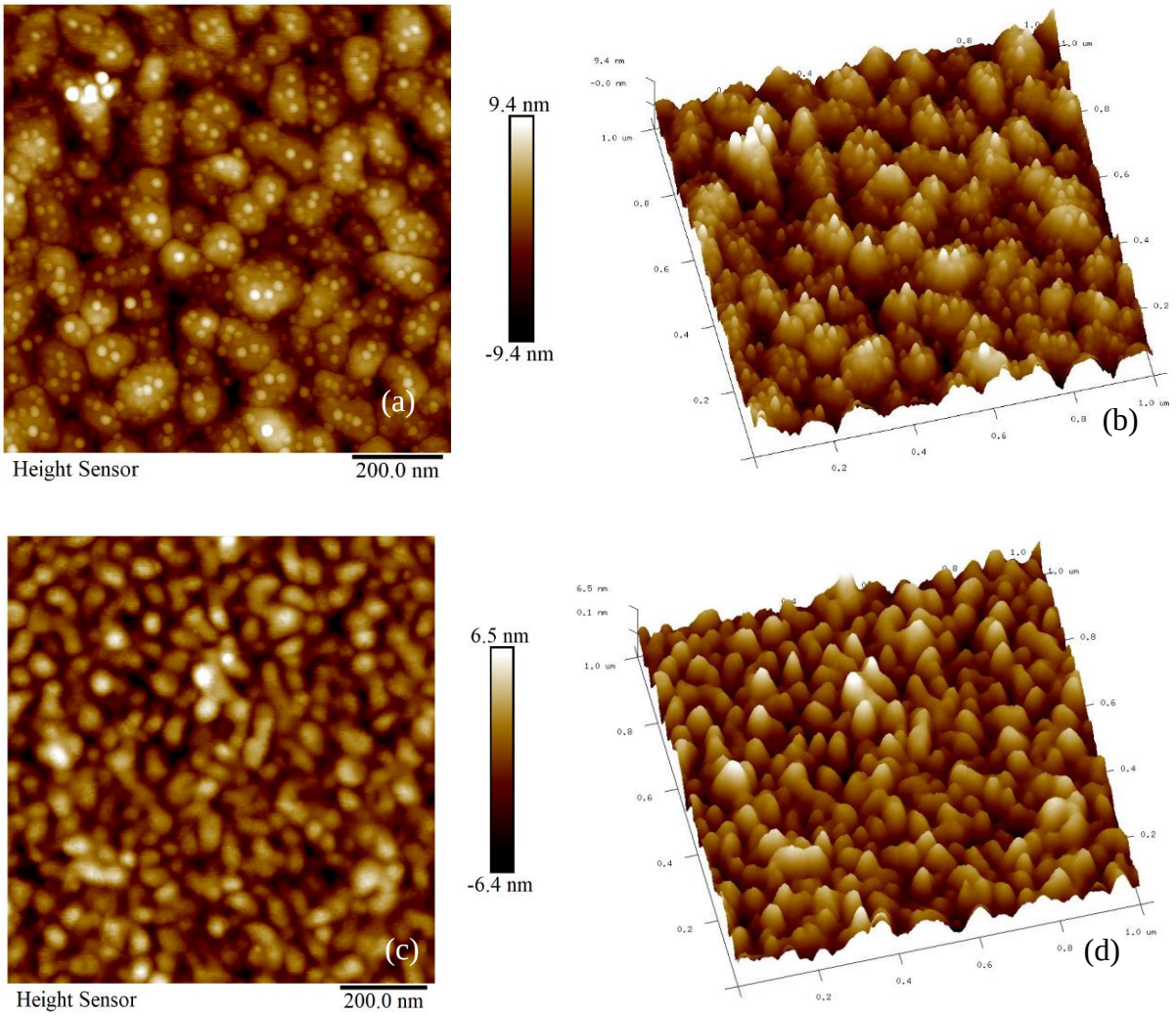


Figure 2.32: (a) AFM (1x1 µm²) scan showing the surface morphology of Au on the unpolished epi-wafer and (b) its corresponding 3D view. (c) AFM (1x1 µm²) scan showing the surface morphology of Au on the polished epi-wafer and (d) its corresponding 3D view.

In addition, focused ion beam (FIB) cross-sectional analysis was performed to examine the thicknesses of various layers on 3C-SiC microcantilever. This measurement was conducted at the end of the fabrication but discussed here to exhibit the certainty of the process. The FIB observation is almost similar to SEM from a topographical point of view. However, high-resolution cross-sectional images require FIB analyses. The area of analysis is mentioned in the optical microscopy image presented in figure 2.33.a. The figure 2.33.b presents the different thin layers, such as isolation layer (USG-200 nm), detection metal (Ti/Au-15/30 nm) and actuation metal (Ti2/Au2-50/300 nm). The top platinum layer was deposited by FIB during sample preparation, to protect the area of interest.

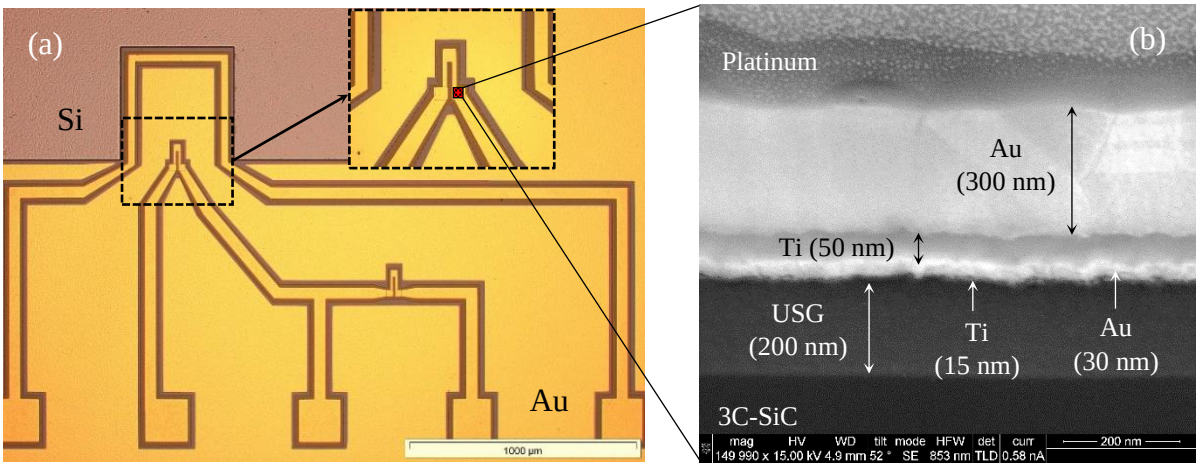


Figure 2.33: (a) Optical microscopy image of 3C-SiC-µC referring the area analyzed by FIB. (b) FIB cross-section showing various layers with their thicknesses.

2.3.6 Turning sample into device

The last stage of surface micromachining is the releasing of 3C-SiC-µC using classical potassium hydroxide (KOH) anisotropic etching along Si (111) direction, as shown in figure 2.34. In this final level, various steps have been enhanced, such as lithography settings and etching conditions due to the epi-wafer's size compatibility.

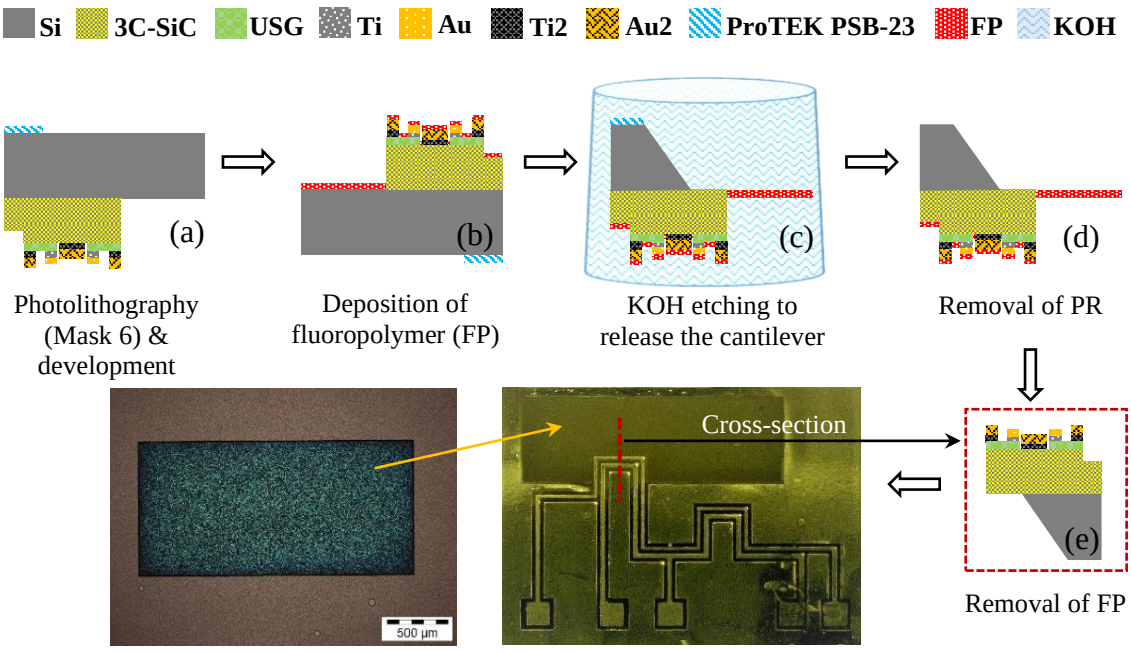


Figure 2.34: Process flow of releasing the cantilever from rear side, step 6.

The process begins with photolithography, to pattern the photoresist mask that protects the area of interest during wet etching. Firstly, the recipe for ProTEK PSB 23 photoresist was improved. The optimization includes spin coating time, rotation speed, UV exposure, temperature during soft bake (SB) and post exposure bake (PEB). To illustrate their importance, few optical microscopic images are shown in figure 2.35 with different UV exposures and spin coating times. Following a sequence of experiments, conditions such as 60 s of spin coating at 2500 rpm under 500 mJ/cm^2 of UV exposure, along with 3 min of SB and PEB at 120 °C and 220 °C have been chosen. The optical microscopic image for the selected recipe is shown in figure 2.35.b, in which it follows the same specifications as the recipe shown in figure 2.35.d, except for the spin coating time.

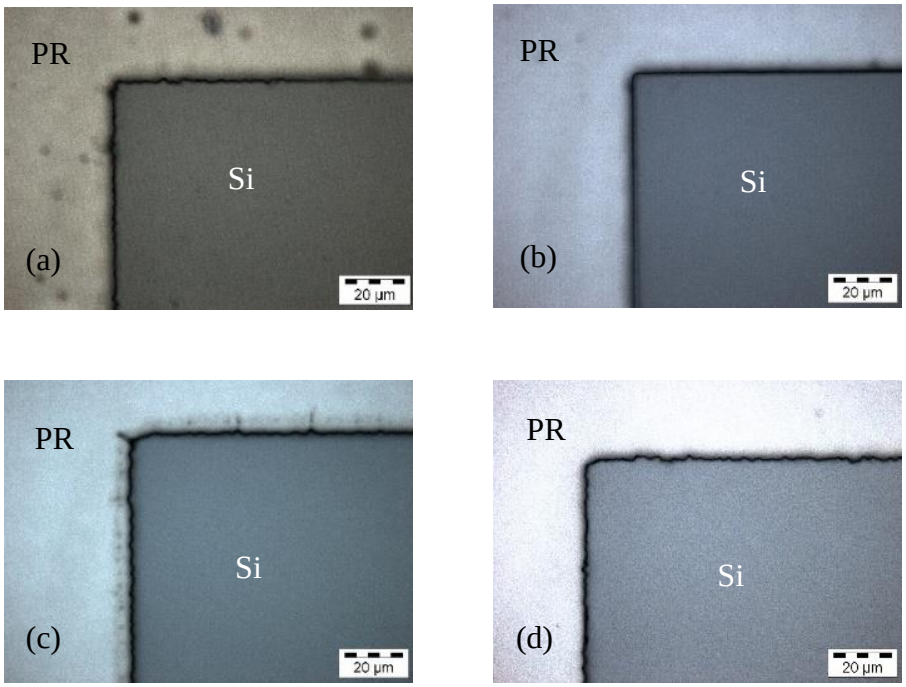


Figure 2.35: Optical microscopic images of patterned photoresist on rear side of substrate (i.e. on Si layer) during 60 s of spin coating (a) at UV dose of 470 mJ/cm², (b) 500 mJ/cm² and (c) 520 mJ/cm². (d) Spin coated for 30 s at 500 mJ/cm².

Subsequently, the sixth stage of photolithography was carried out using backside alignment (BSA) technique. The conventional lithographic tools for BSA work extensively on wafers over 4-inch diameter, as referred in figure 2.36, case (i). Since we use epi-wafers of 2-inch diameter in our study, the current system must be customized. This practical limitation can be overcome by changing our 5-inch mask into a 7-inch mask, so that both alignment crosses of 2-inch diameter can be seen from one side, as shown in figure 2.36, case (ii). With the semi-automated EVG6200 mask aligner, several optical positions can be saved while

alignment was being performed. Although the two crosses cannot be viewed simultaneously, the degree of misalignment can always be assessed with the saved optical positions.

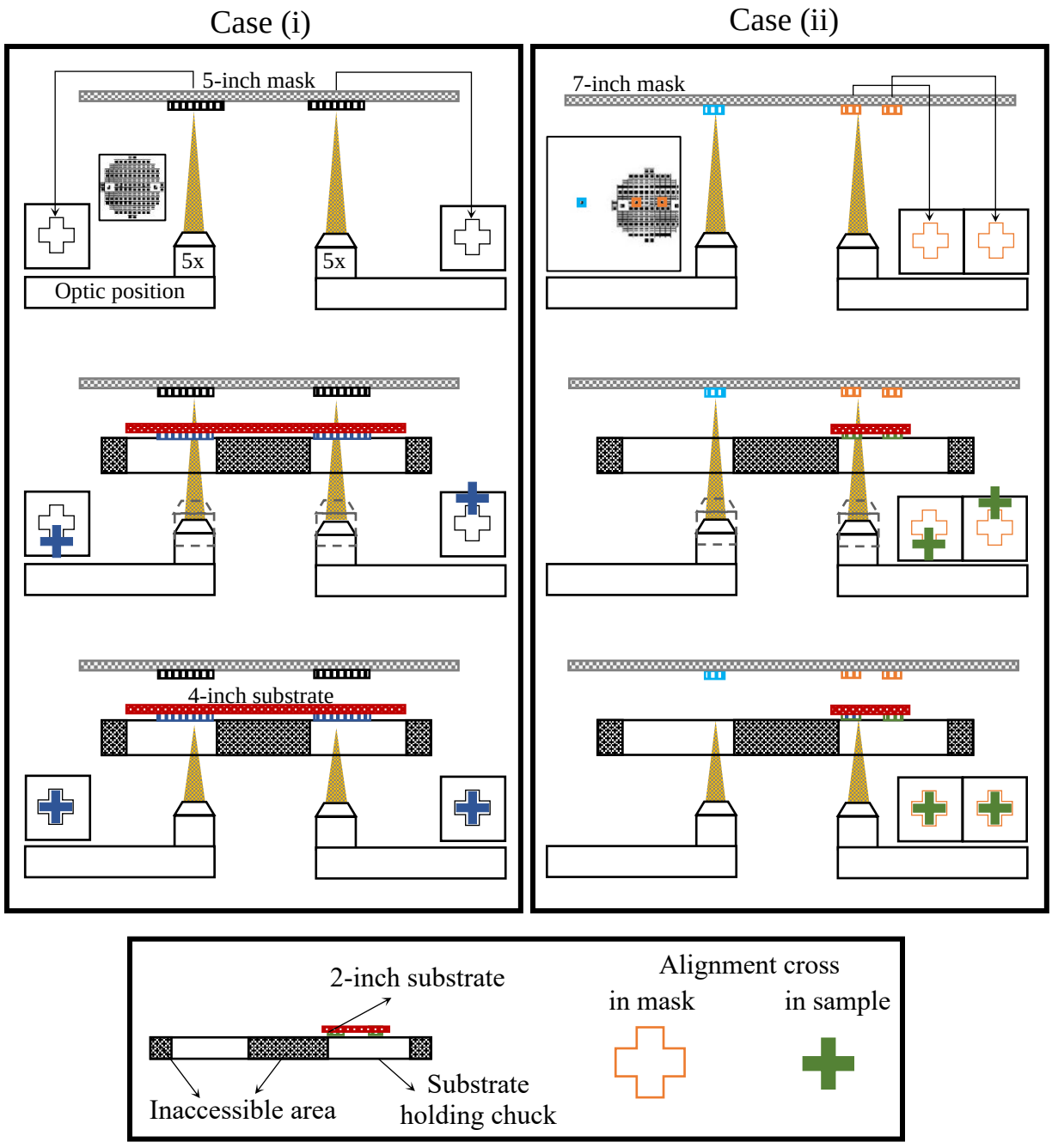


Figure 2.36: Lithography using BSA. (a) Performing regular case scenario with 5-inch mask for 4-inch substrate and (b) optimized process with altered 7-inch mask for 2-inch substrate.

An illustration of misaligned cantilevers can be seen in figures 2.37.a and 2.37.b. In this case, the USG oxide layer has been lifted due to KOH attack, as well as the deposited actuation and detection metals. By employing the above-mentioned solution, i.e. case (ii) lithography, the misalignment problem can be resolved. Further, a protection layer was added to preserve the

metal layer on the front face and to retain fully functional cantilever chips. This protective layer was a customized plasma-deposited fluoropolymer (FP) film that has been developed in GREMAN laboratory [61]. The FP was deposited on the front face of the epi-wafer, after patterning the rear side (see figure 2.37.c). The FP film was formed using C_2H_4 and CHF_3, and its thickness was 500 nm. This protective layer acts as an etch-stop layer and ensures the safety of metallic layers on the front face of epi-wafer in case of KOH outpouring during final release.

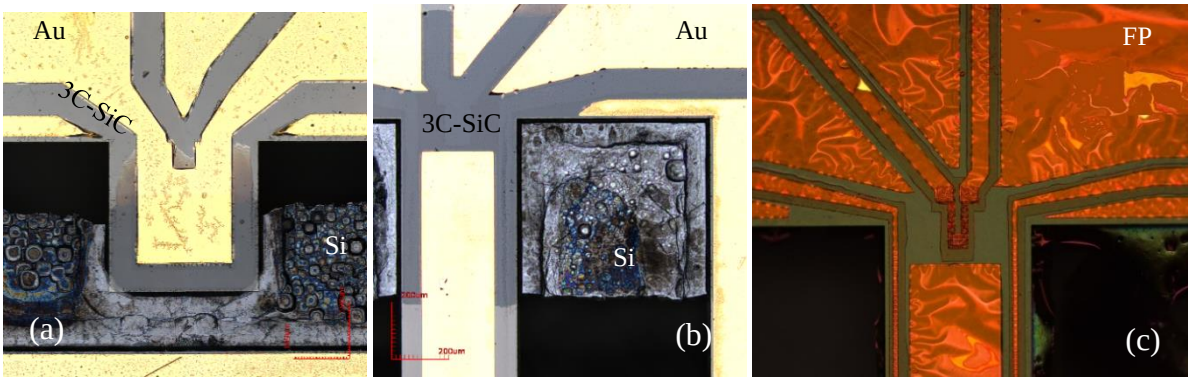


Figure 2.37: Confocal microscopic images of unreleased 3C-SiC-µCs for (a) A0-SQR and (b) A4 geometries. (c) Optical microscopy image of 500 nm fluoropolymer deposited on front face of the epi-wafer.

Consecutively, the KOH wet etching has been conducted. During etching, some parameters were optimized, such as KOH concentration, etching temperature, and wafer position. The literature clearly shows that etch rate and temperature were directly proportional [62]. In this case, with the available PR, the temperature should not exceed 80 °C. Furthermore, the etch rate for KOH etching is higher for lower concentrations. Due to these reasons, the initial test was conducted at 80 °C with a concentration of 20 % KOH. Besides, the volume of solution has to be determined. As the entire height of the Si substrate has to be etched to release the 3C-SiC-µCs, the volume of KOH has to be higher, respecting the beaker size, raise in volume on submersion of the wafer holder and evaporation during etching. In our case, we use a beaker with 2 L capacity, as shown in figure 2.38.a. With all due considerations, the optimum volume required for etching was 1200 mL. Subsequently, 300 grams of KOH salt required making 20 % KOH for 1200 mL of water. This was calculated using the following expression:

$$\%KOH = \frac{m_{KOH}}{m_{H_2O} + m_{KOH}} * 100 \qquad \text{Eq. 3.4}$$

where m_{KOH} and m_{H2O} are masses of KOH and water respectively.

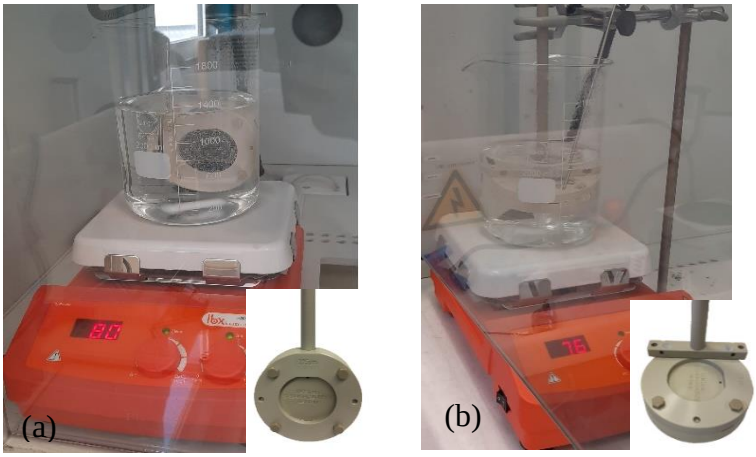


Figure 2.38: Releasing microcantilevers using KOH wet etching. (a) Performing etch at 80 °C with vertical sample holder position. (b) Etching under optimized temperature of 75 °C using a horizontal sample holder position.

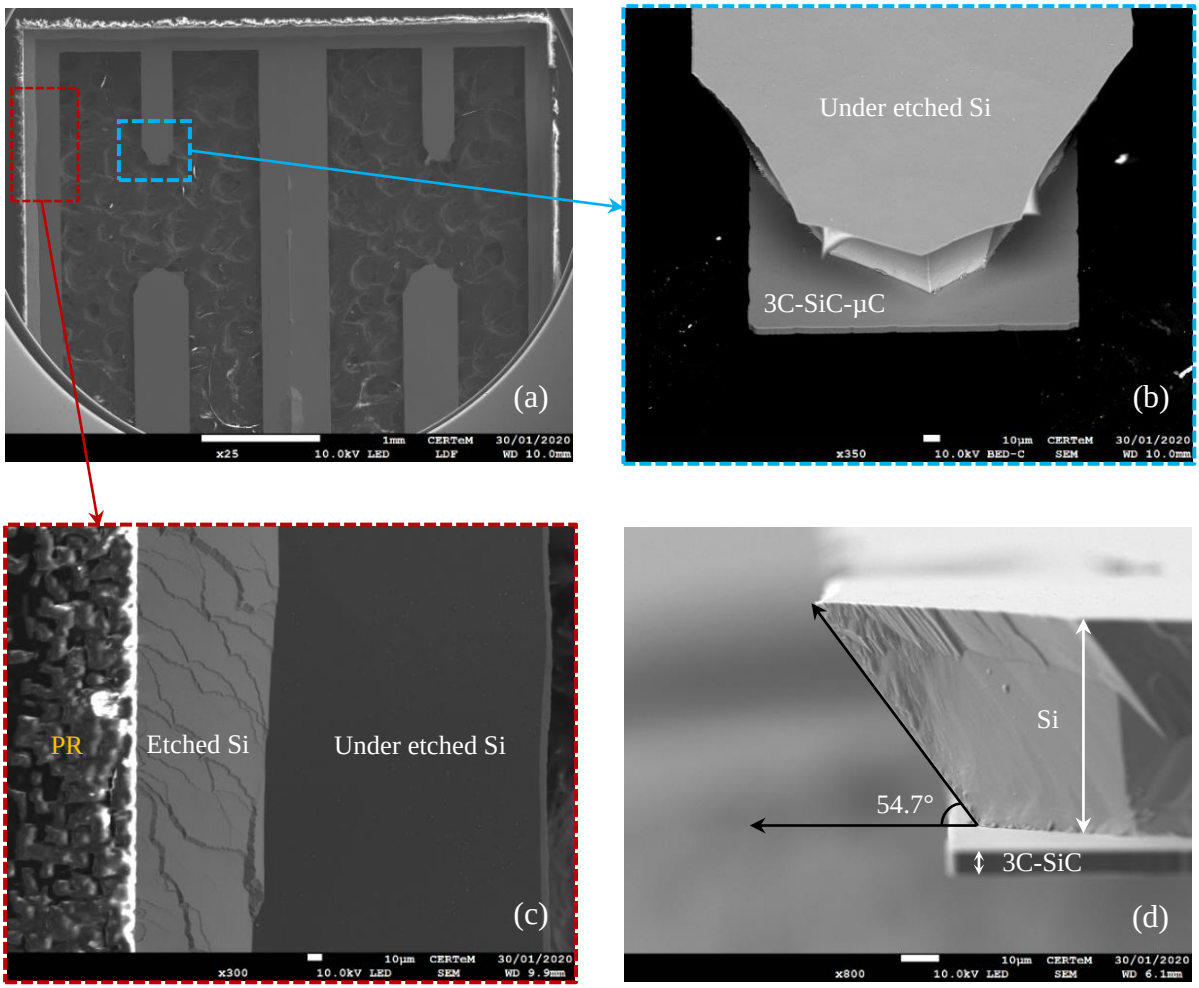


Figure 2.39: Plan view SEM images of rear side of cantilever chip (a) consisting of four available cantilevers, (b) focused view on the tip of cantilever showing the bulk under etched silicon on 3C-SiC epilayer and (c) shape of patterned PR on Si after 210 min of KOH etching at 80 °C. (d) Cross-section SEM image at the cantilever tip showing the etching angle of 54.7 degrees, i.e. along Si (111) direction.

Figure 2.39 shows the under etched Si on fully released 3C-SiC-µCs. The SEM image in figure 2.39.a shows that the epi-wafer was well aligned. The cantilevers were released, however, leaving a few micrometers of unetched Si, as shown in figure 2.39.b. It is caused by unsteady and vigorous KOH etching during final release. In order to resolve this, the etching temperature was lowered to 75 °C with a slight modification in the wafer holding position, as shown in figure 2.38.b, to maintain homogeneous solution throughout the etching area. To specify, although the etching was unsteady and vigorous at 80 °C, the etching angle of 54.7 degrees along the Si (111) direction is clearly visible in figure 2.39.d.

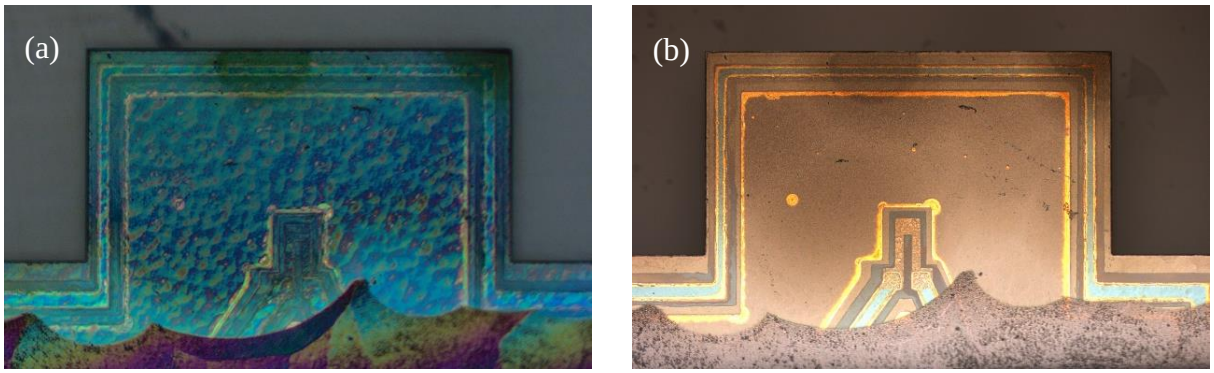


Figure 2.40: Optical microscopic view of 3C-SiC-µC on its rear side (a) before dry etching with few microns of Si on 3C-SiC epilayer and (b) complete 3C-SiC-µC after dry etching.

From figure 2.40, it is clear that the cantilever release was homogeneous with the chosen etching configuration and temperature. Nevertheless, there were very few micrometres of Si remaining under 3C-SiC-µCs, as shown in figure 2.40.a. Hence, these Si residues were removed using the ICP reactor. This dry etching follows the same recipe as 3C-SiC etching in stage 2, but without RF forward power. In addition, the etching process was controlled by EPD in Corial 200 IL. The microcantilevers are solely made of 3C-SiC epilayer, as evidenced in figure 2.40.b. The final step involves the removal of the PR and protection layer with oxygen plasma. After, these chips were packaged for further characterizations.

2.3.7 Packaging of fabricated 3C-SiC-µCs

Subsequent to the fabrication, the microcantilever chips were diced and prototyped to carry out further electrical characterization and gas mixture analysis. Each chip consists of four functional microcantilevers. Primarily, the chips were glued on specially designed printed

circuit boards (PCBs) using insulating epoxy adhesive from ALBEBOND 84-3J by Henkel. Afterwards, the glued chips were baked in a laboratory oven for one hour at 150 °C to improve the adhesion between the PCB and the chip. Consequently, the wedge bonding was performed using K&S 4523AD manual wedge bonder. The bonding wire was made of aluminum and it was 25 µm in diameter. The complete functional prototype is shown in figure 2.41.

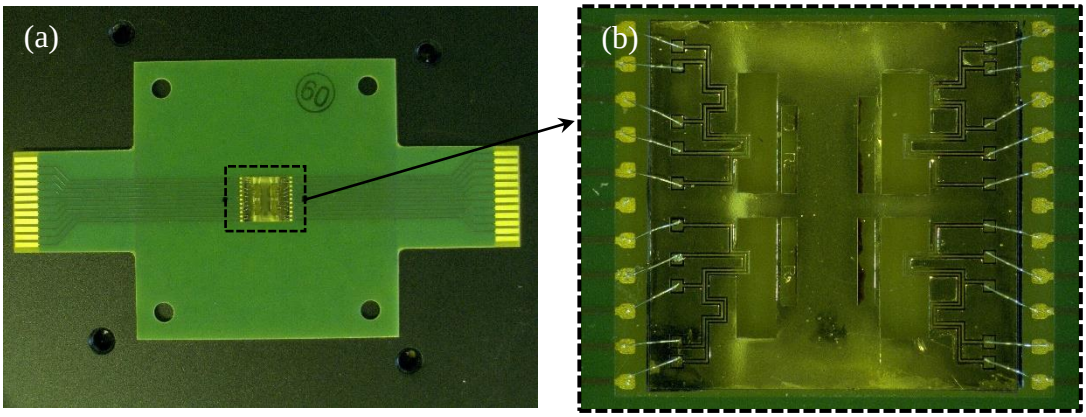


Figure 2.41: (a) Fully packaged prototype and (b) optical microscopic view of wedge bonded 3C-SiC microcantilevers on PCB.

Eventually, a sample holder was designed to provide support for the magnet used in electromagnetic actuation while performing gas mixture analysis, as shown in figure 2.42. This holder has been fabricated using laser engraving and laser cutter by Trotec.

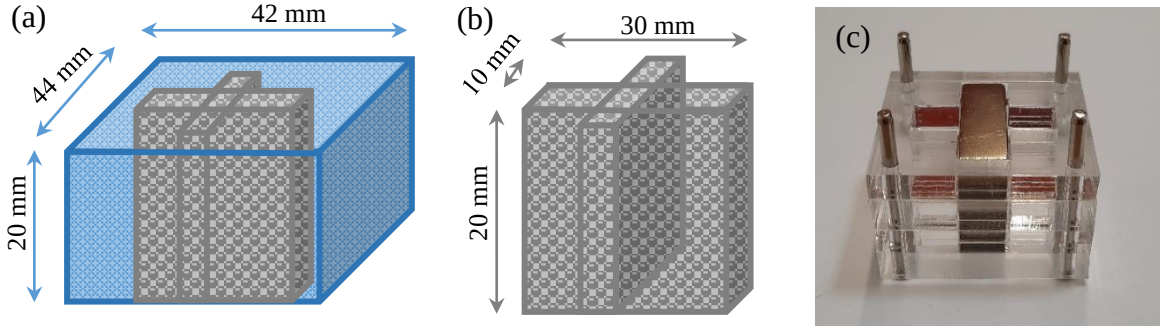


Figure 2.42: (a) Schematic of designed sample holder and (b) structure of the engraved cavity in the holder to mount the magnet. (c) Fabricated holder with affixed magnet.

After having the complete device, the electrical characterization in air was performed. These measurements help in retrieving basic parameters, such as resonance frequency, quality factor, etc., which is elaborately explained in the following section.

2.4 Electrical characterizations of 3C-SiC-µCs in air

The electrical characterization plays an important role in deriving the mechanical resonance frequency, quality factor and resistance of every single fabricated microcantilever. In general, optical measurement like laser Doppler vibrometry (LDV) is widely used to characterize the microbeams. Along with this, an electrical measurement is also performed here, to measure the resistance across various circuits in the cantilever. This observation is to verify the open/short circuit between different conducting wires. Moreover, we only discuss the characterization results for methods I cantilevers here. Later, the reason behind the non-functional method II cantilevers will be described.

2.4.1 Laser Doppler vibrometry measurements

LDV is a non-contact assessment of the surface that can measure vibrations up to few MHz and has a resolution in the pm range. The aim of this measurement is to extract the mechanical resonance frequency of manufactured 3C-SiC microcantilevers. The working principle of the vibrometer is based on the shift in Doppler frequency of a laser beam reflected from the target under motion. The on-board electronics convert the received signal into an analog voltage proportional to the absolute value of the target's velocity. Meanwhile, to generate vibrations, an AC current $\left(\vec{I}(t)\right)$ is passed through the conductive wire placed at the cantilever periphery. In the presence of a magnetic field $\left(\vec{B}\right)$ collinear to the longitudinal axis of the beam, an AC Lorenz force $\left(\vec{F}(t)\right)$ is created at the microcantilever free-end and induces out-of-plane vibrations as shown in Figure 2.43.

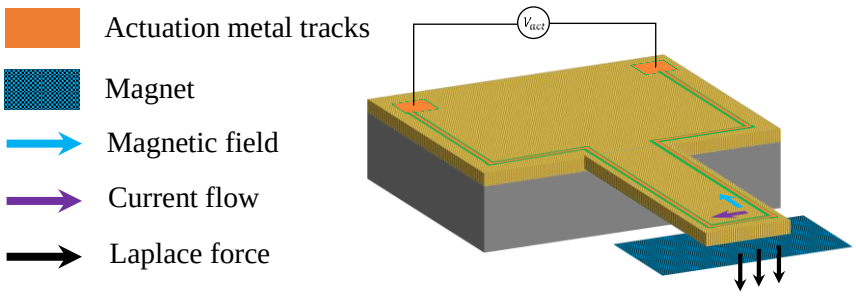


Figure 2.43: Electromagnetic actuation by Laplace force.

The complete real-time experimental setup is shown in figure 2.44. The cantilever beam of interest (specimen) was placed under the laser source and excited using built-in wave generator. The Polytec MSA500 vibrometer has two laser beams, one acts as a reference (white spot) that was always pointed on the stationary area. The second was a measurement beam (red spot), which was focused on the region of interest (on cantilever beam), to observe deflections. Upon actuating the cantilever, the velocities for the range of frequencies have been generated by the Doppler shift from the reflected laser beam due to the motion at the examining region. To elaborate, the resulting instantaneous velocity was constructed using the interference between the measurement and the reference beam. With these data, the displacement magnitude over a range of frequencies were derived.

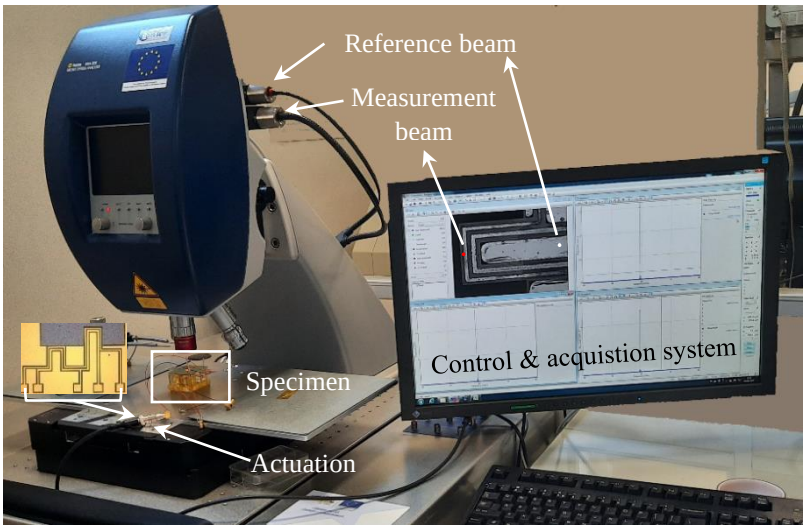


Figure 2.44: Experimental setup for laser Doppler vibrometry.

An example illustrating this is shown in figure 2.45 for A4-i geometry at 100 mV applied voltage. The graph presents the displacement amplitude and phase for a range of frequencies.

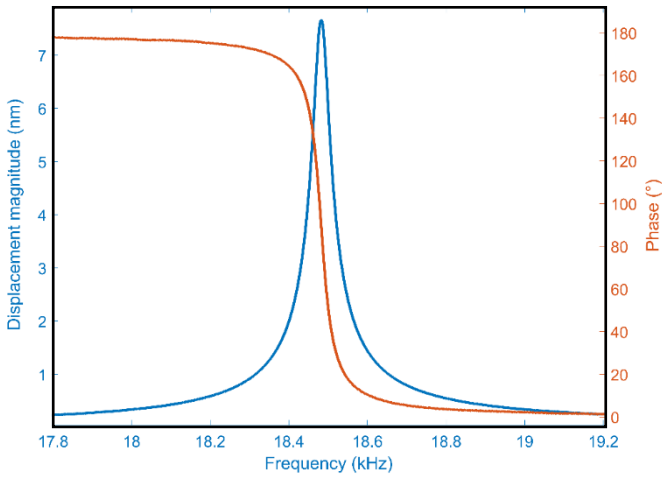


Figure 2.45: Measured displacement and phase for varying frequencies at 100 mV of A4-i geometry.

Preceding this, the cantilever was actuated at the aforementioned criteria, but over a wide frequency range, in order to witness succeeding modes. Figure 2.46 illustrates various modes of A4-i geometry. The different peaks corresponding to various modes of the cantilever and the images represent a fast scan with multiple scan points using LDV. The modes 1, 2 and 3 were witnessed at 18.48 kHz, 50.73 kHz and 97.51 kHz respectively. An unusual peak occurs at 28.38 kHz, corresponding to a torsion mode.

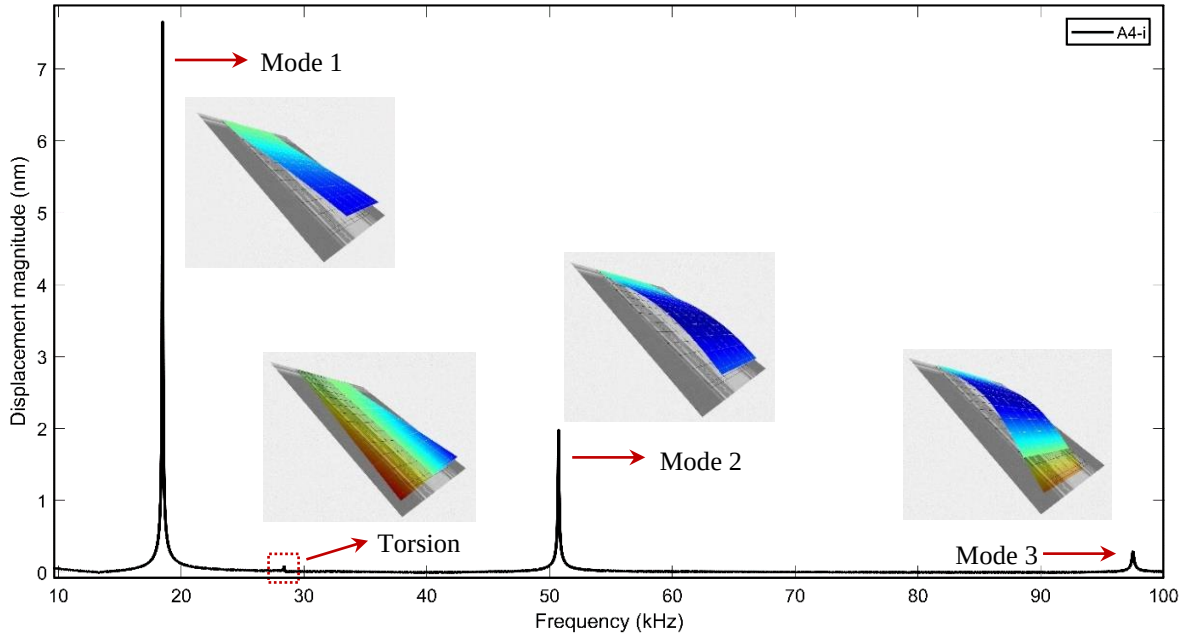


Figure 2.46: Measured cantilever displacement for A4-i geometry, over frequency range of 10 kHz to 100 kHz at 100 mV applied voltage.

Next, cantilever displacement for various applied voltages for different geometries with 10 µm thickness are shown in figure 2.48 and their resonance frequency (f_r) and calculated quality factor (Q) are listed in table 2.4. The quality factor was calculated using the following expression:

$$Q = \frac{f_r}{f_2 - f_1} \qquad \text{Eq. 2.6}$$

where frequency f_1 and f_2 are chosen at max/$\sqrt{2}$ position, as illustrated in figure 2.47.

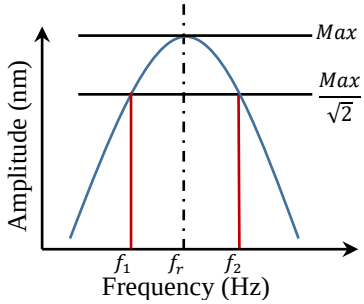


Figure 2.47: Schematic to explain various parameters used in quality factor calculation.

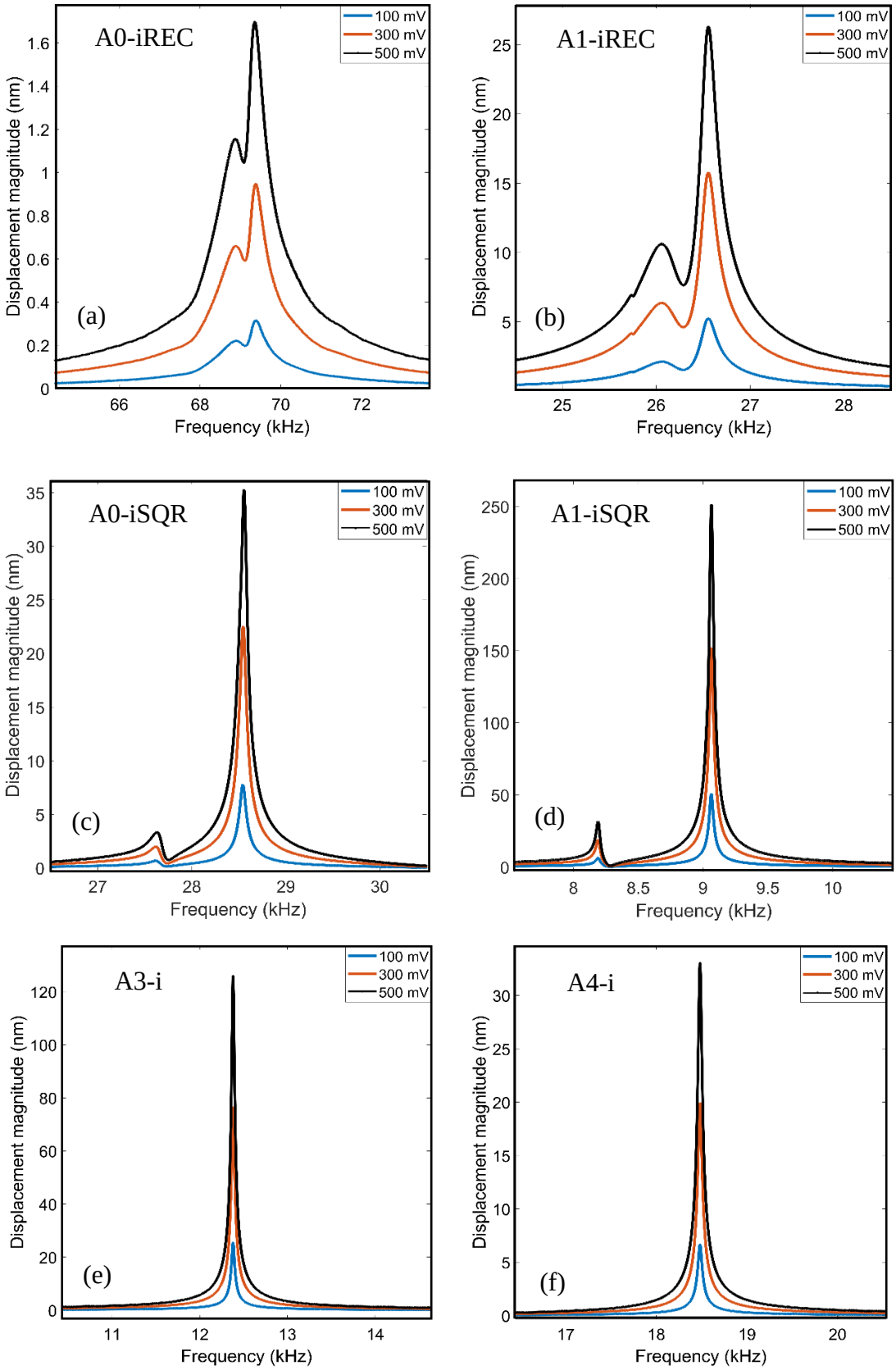


Figure 2.48: Measured displacement amplitude at different applied voltages for various geometries. (a) A0-iREC type, (b) A1-iREC type, (c) A0-iSQR type, (d) A1-iSQR type, (e) A3-i type and (f) A4-i type cantilever geometries.

Table 2.4: Measured resonance frequency and quality factor for different geometries at 500 mV for a 10 µm-thick (*h*) 3C-SiC-µCs.

Geometry	Length (*L*) (µm)	Width (*b*) (µm)	Resonance frequency (f_r) (kHz)	Quality factor (*Q*)
A0-iREC	250	500	69.36	157
A0-iSQR	500	500	28.55	357
A1-iREC	500	1000	26.56	156
A1-iSQR	1000	1000	9.06	302
A3-i	1000	200	12.38	412
A4-i	2000	400	18.48	370

The exhibited results are consistent, since smaller the dimension, higher the resonance frequency. The cantilever dimensions respecting the criteria of Euler-Bernoulli's beam theory have proper resonance mode. Predominantly, when $h \ll b \ll L$, there is a sharp resonance peak without any disturbance but in case of $h \ll L \ll b$, there is an auxillary mode very close to the resonance (refer to figures 2.48.a and 2.48.b). Because of this phenomenon, A0-iREC and A1-iREC have lower quality factors than other geometries. Moreover, at *L=b/2* condition, the quality factor is reduced by a factor of 2. Nevertheless, their performance under a gas environment should be studied in order to compare and contrast the absolute sensitivity, limit of detection, quality factor, signal-to-noise ratio, etc.

2.4.2 Electrical measurements

The electrical measurement is performed to determine the resistance across different current flowing circuits. This is to check the integrity of the metal contacts, as mentioned earlier. The experimental protocol followed here will be explained elaborately in chapter 3 (refer §3.5.2). The procedure is the same except no external power supply is used here. The specimen was connected to the HP4294A precision impedance analyzer probe. The frequency range for

observation was kept between 5 kHz to 100 kHz. The experimental setup and their electrical connections are shown in figure 2.49.a.

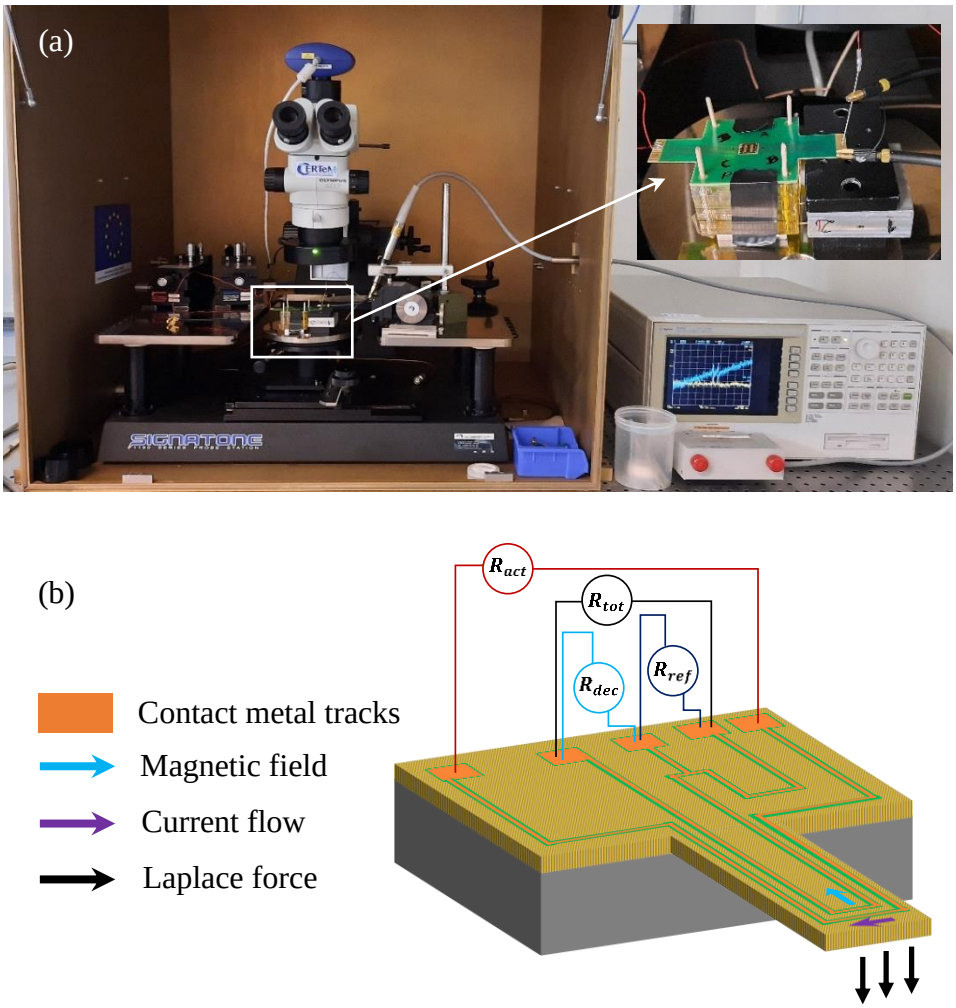


Figure 2.49: (a) Experimental setup for electrical analysis in air and (b) electrical connections to measure the resistance value of reference (R_{ref}), measurement (R_{dec}), total (R_{tot}) and actuation (R_{act}) resistors.

The measurement was carried out by connecting the circuit of interest namely R_{ref}, R_{dec}, R_{tot} or R_{act}, as shown in figure 2.49.b. This is to check its functionality and measure their resistance. As explained in §2.3.4, there are two resistors for method II detection. Similarly, there are two resistance in method I detection, where each circuit has its own resistance depending on its dimension.

Nevertheless, the measured resistance values of each geometry are summarized in table 2.5. The measured resistance values are such as $R_{act} > R_{tot} > R_{dec} > R_{ref}$, that is in accordance with the fact that each resistance is proportional to its length (eq. 2.1).

Table 2.5: Measured resistances for different geometries at 0 V for a 10 µm thick 3C-SiC-µCs.

Geometry	R_{dec} (Ω)	R_{ref} (Ω)	R_{tot} (Ω)	R_{act} (Ω)
A0-iREC	9.9	8.9	15.5	22.6
A0-iSQR	11.4	10.5	18.3	28.5
A1-iREC	12.8	9.5	18.6	27.0
A1-iSQR	16.8	14.0	27.7	40.2
A3-i	35	34.3	62.5	82.8
A4-i	40.7	38.8	72.6	89.8

As mentioned previously, the electrical characterizations of method II cantilevers are not discussed in this study. This is due to the open circuit in the piezoresistor, as referred in figure 2.50.

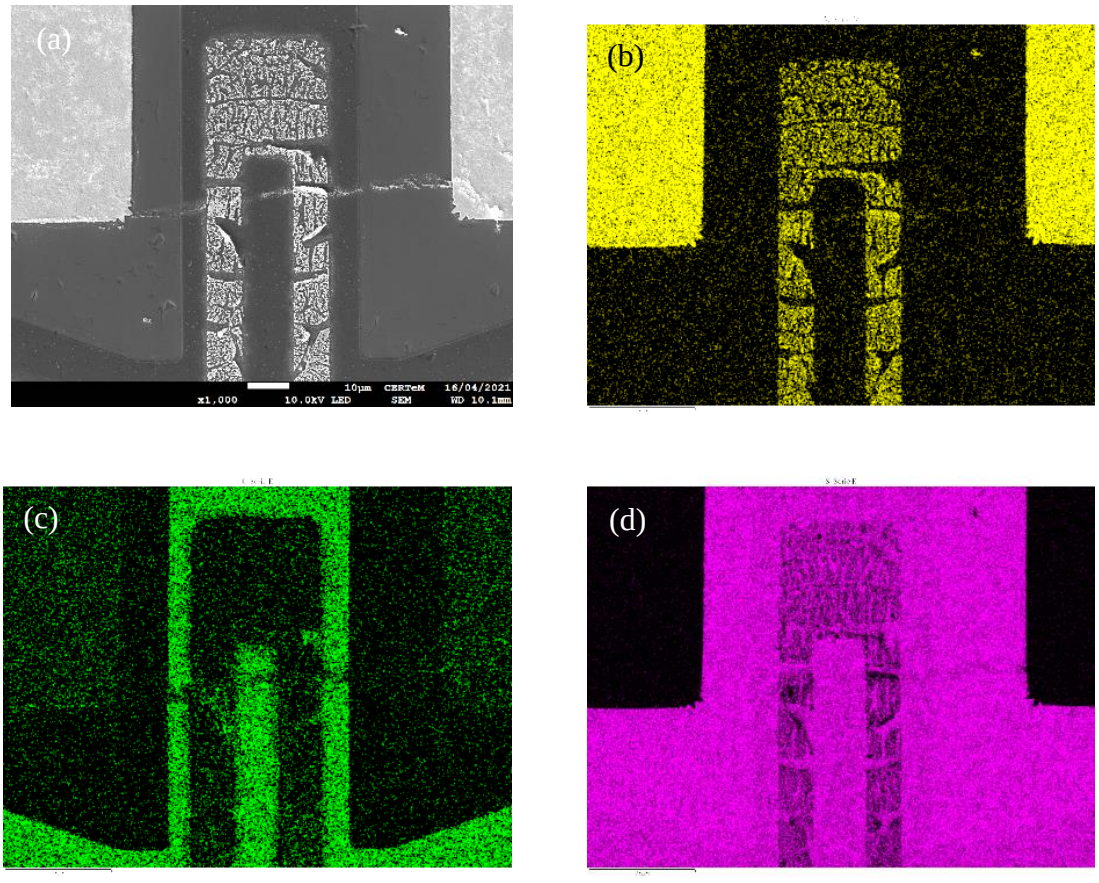


Figure 2.50: (a) Plan view SEM image of piezoresistor on 3C-SiC microcantilever and associated EDS images showing (b) gold (in yellow), (c) oxide (in neon green) and (d) silicon layers (in magenta).

The plan view SEM image and their corresponding energy dispersive spectroscopy (EDS) results show the cracked gold layer on the oxide layer. This phenomenon was caused by a poor adhesion between the oxide layer and the titanium layer, which was then lifted after final processing. Hence, in the future, thicker titanium films (>15 nm) are recommended for better adhesion. By increasing this thickness, the value of resistance remains almost unchanged, since Ti's resistivity is higher than Au's.

2.5 Testing of fabricated 3C-SiC-µCs in binary gas mixture environments

The binary gas mixture investigation of 3C-SiC-µCs has taken place with the parameters obtained through electrical characterization in air. The schematic view of the gas mixture analysis setup is shown in figure 2.51.

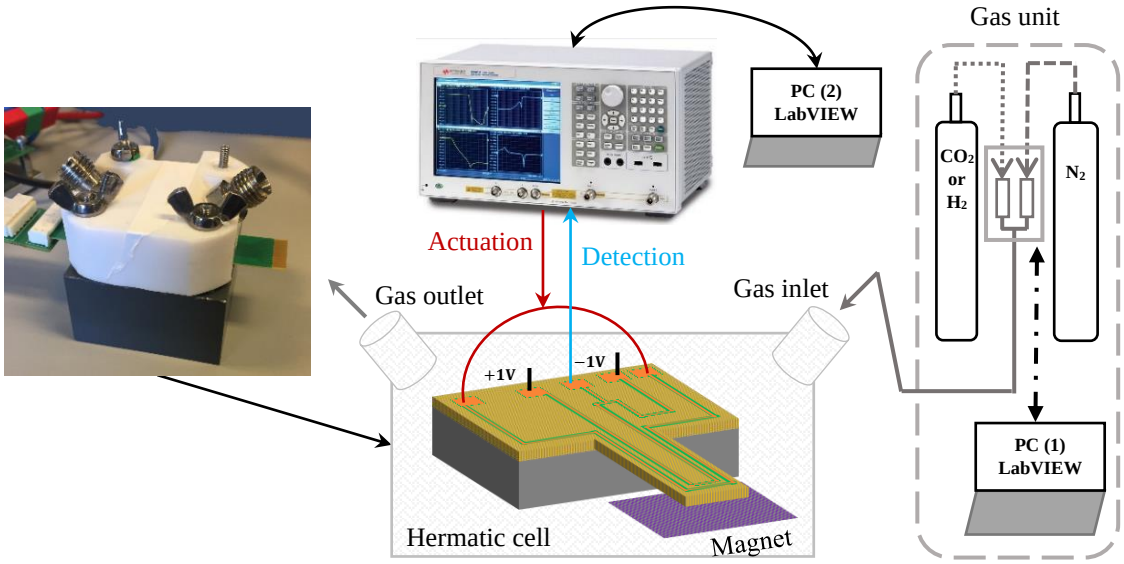


Figure 2.51: Schematic of experimental protocol to measure the shift in resonance frequency for various gas concentration present inside the hermetic cell under gas mixture environment, developed by IMS laboratory.

A geometry was arbitrarily chosen (here A0-iSQR) for performing the preliminary test. This geometry is square in shape and of dimension 500*500*10 µm^3. The resonance frequency and quality factor of this geometry are 28.55 kHz and 357 respectively. The selected cantilever was placed inside the hermetic cell, which allows the gas flow during measurement. This cell was tightly sealed using a gasket between the front face of PCB and top covering to avoid gas

leakage. The volume of the gas chamber was kept low, to reduce the filling time (here 500 µL). Then, the contacts on the PCB were connected for electrical connections, i.e. for electromagnetic actuation and induction detection, as referred in figure 2.51. The gas flow was controlled through a Labview program developed by IMS laboratory.

The first set of gas analysis was made with hydrogen (H_2) in nitrogen (N_2) for lower gas concentrations from 1 % to 4 %. Here, nitrogen was used as reference gas. The change in gas concentration was monitored for its relative shift in resonance frequency, as shown in figure 2.52. The gas concentration was varied for every 5 min with 100 % of nitrogen, to reset the measurement. The obtained result matches with the outcome of Boudjiet *et al.*, i.e. the resonance frequency increases, with increase of H_2 in N_2, due to the fact that hydrogen is lighter than nitrogen [63].

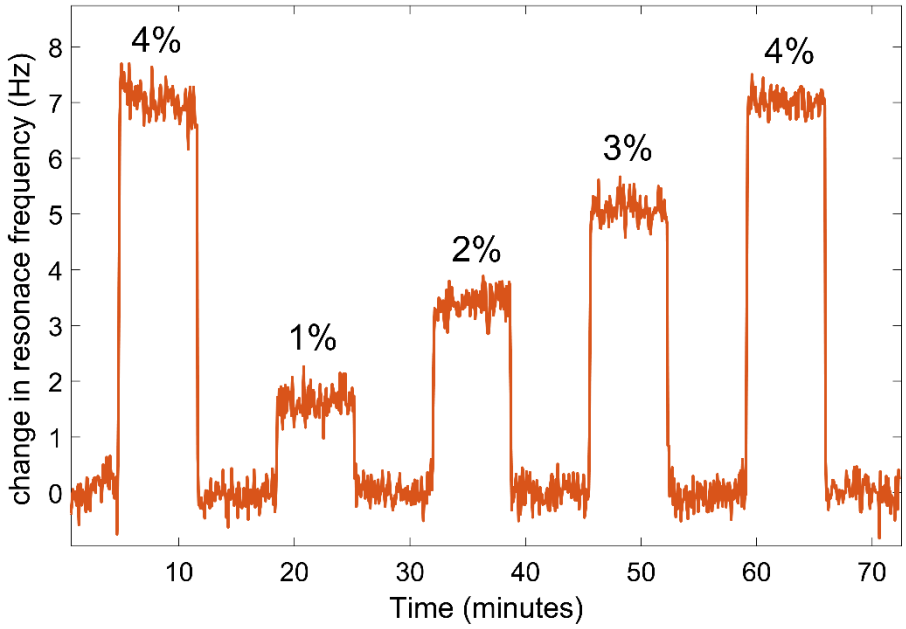


Figure 2.52: Measured relative shift in resonance frequency for H_2 in N_2 of A0-iSQR 3C-SiC-µC.

Consecutively, carbon dioxide (CO_2) in N_2 was also tested for the aforementioned gas concentration, in order to verify that the measurement was due to the modification of the gas mass density. From figure 2.53, the relative shift in frequency decreases with increase in gas concentration. This is due to the fact that CO_2 is heavier than N_2. Our results validate the principle of detection proposed by Boudjiet *et al.*, but by utilizing 3C-SiC-µCs, which can operate in harsh environments.

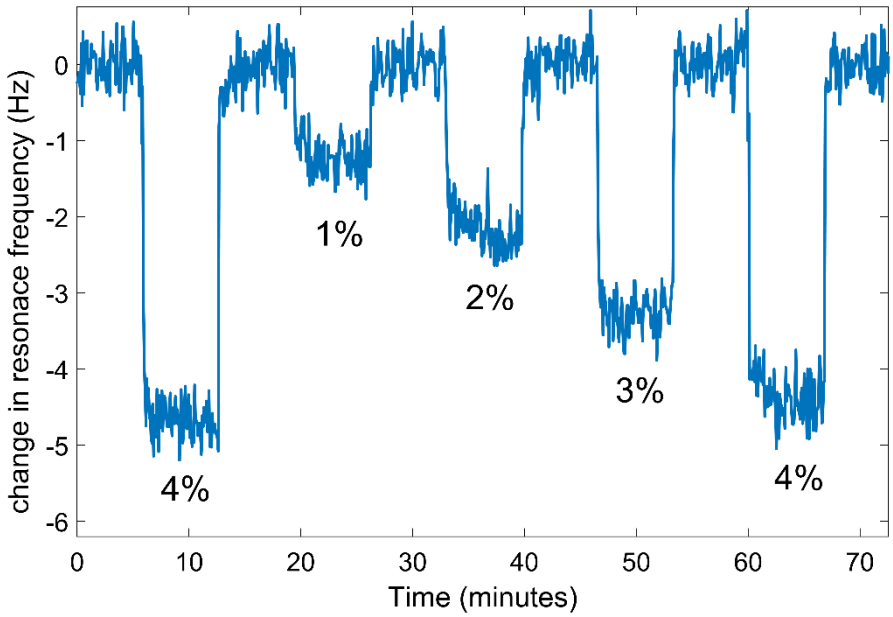


Figure 2.53: Measured relative shift in resonance frequency for CO_2 in N_2 of A0-iSQR 3C-SiC-µC.

Preceding the successful measurement of binary gas mixtures, the limit of detection (LOD) experiments were evaluated with very low gas concentrations, i.e. 0.2 % to 2 %. Based on figure 2.54, it is evident that the LOD for H_2 in N_2 and CO_2 in N_2 are 0.2 % and 0.25 % respectively.

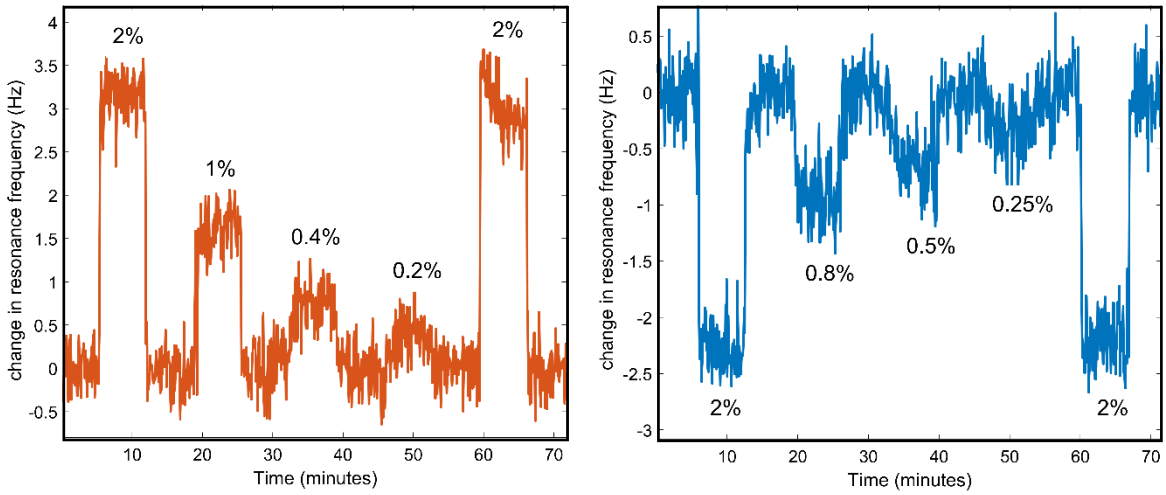


Figure 2.54: Limit of detection measurement for lowest concentration of H_2 in N_2 (in orange) and CO_2 in N_2 (in blue).

To mention, all the experimental results based on gas mixture analyses are provided by Luis Iglesias, researcher at IMS laboratory, Bordeaux.

Conclusion and perspectives

To summarize, the newly designed and fabricated 3C-SiC-µCs successfully detected the hydrogen in nitrogen below LEL (lower explosion limit), i.e. less than 4 %. These 3C-SiC-µCs detect change in gas mixture due to change in their physical property, i.e. shift in resonance frequency induced by variation in gas mass density. These microcantilevers work without any chemical/sensitive coatings. The optical measurement using LDV validates the electromagnetic actuation. Subsequently, the primary gas mixture analysis shown in §2.5 confirms the induction detection as well.

The limit of detection (LOD) for H_2 in N_2 and CO_2 in N_2 are 0.2 % and 0.25 % respectively, for A0-iSQR geometry. Nevertheless, lower LOD's could be probably achieved by means of further optimizations in future. Also, these promising results will help to compare and contrast various geometries, to retain the best configuration with good absolute sensitivity, limit of detection, signal-to-noise ratio, etc. in future.

Lastly, it is unfortunate that method II microcantilevers are ineffective, to conduct these first set of measurements. However, with the proposed new fabrication strategy, one could easily retain a new set of cantilever beams by slightly varying the process flow mentioned in §2.3.4, i.e. by increasing the thickness of titanium used in detection metal for better adhesion. Further, the process flow of step 4 can be slightly modified by adding an oxygen plasma etching for a few seconds after the photolithography step, in order to remove a thin layer of photoresist . During this step, we clean the small patterns of piezoresistors thoroughly, which facilitates the deposition of detection metals.

The last step of fabrication, i.e. step 6, can be further optimized by performing only dry etching using xenon difluoride (XeF_2) followed by photolithography. By doing this, we maintain a more durable microsystem than we currently have.

On a positive note, the currently working 3C-SiC-µCs based on electromagnetic actuation and induction detection give hope for next generation MEMS devices that are suitable for operation in extreme environments and can be applied to all kinds of medical devices, due to their material properties.

References

[1] M.-T. Boudjiet, "Microsystèmes durables de mesures de concentration d'hydrogène utilisant des micropoutres sans couche sensible," PhD dissertation, University of Bordeaux, 2015.

[2] M. T. Boudjiet *et al.*, "New characterization methods for monitoring small resonant frequency variation: Experimental tests in the case of hydrogen detection with uncoated silicon microcantilever-based sensors," *Sensors and Actuators B: Chemical*, vol. 199, pp. 269–276, Aug. 2014, doi: 10.1016/j.snb.2014.03.098.

[3] Edward G. Acheson, "Production of artificial crystalline carbonaceous materials," US492767A, Feb. 28, 1893 [Online]. Available: https://patents.google.com/patent/US492767A/en.

[4] Henry H. C. Dunwoody, "Wireless-telegram system," US837616A, Dec. 04, 1906 [Online]. Available: https://patents.google.com/patent/US837616

[5] Henry J. Round, "A note on carborundum," *Electrical World*, 1907.

[6] M. B. J. Wijesundara and R. G. Azevedo, *Silicon carbide microsystems for harsh environments*. New York: Springer, 2011.

[7] T. L. Daulton, "Polytype Distribution in Circumstellar Silicon Carbide," *Science*, vol. 296, no. 5574, pp. 1852–1855, Jun. 2002, doi: 10.1126/science.1071136.

[8] "Wolfspeed. A CREE company." https://www.wolfspeed.com/materials/products

[9] "NOVASiC." https://www.novasic.com/

[10] G. W. Hunter *et al.*, "An Overview of High-Temperature Electronics and Sensor Development at NASA Glenn Research Center," *Journal of Turbomachinery*, vol. 125, no. 4, pp. 658–664, Oct. 2003, doi: 10.1115/1.1579508.

[11] M. Shur *et al.*, Eds., *SiC materials and devices*. New Jersey ; London: World Scientific, 2006.

[12] Maurizio Di Paolo Emilio, "Insight of GaN and SiC Market," *EETimes*, Jul. 2020. https://www.eetimes.com/insight-of-gan-and-sic-market/

[13] Ezgi Dogmus *et al.*, "Power SiC 2020: Materials, Devices and Applications," *i-MicroNews*, Nov. 2020. https://s3.i-micronews.com/uploads/2020/11/YDR20119_Power_SiC_Materials_Devices_Applications_2020_Sample.pdf.

[14] W. J. Choyke *et al.*, Eds., *Silicon carbide: recent major advances ; with 82 tables*, Softcover repr. of the hardcover 1st ed. 2004. Berlin: Springer Berlin, 2013.

[15] T. Markku, Ed., *Handbook of silicon based MEMS materials and technologies*, Second edition. Amsterdam: William Anderew is an imprint of Elsevier, 2015.

[16] S. Nishino *et al.*, "Production of large-area single-crystal wafers of cubic SiC for semiconductor devices," *Appl. Phys. Lett.*, vol. 42, no. 5, pp. 460–462, Mar. 1983, doi: 10.1063/1.93970.

[17] S. Nishino *et al.*, "Epitaxial growth and electric characteristics of cubic SiC on silicon," *Journal of Applied Physics*, vol. 61, no. 10, pp. 4889–4893, May 1987, doi: 10.1063/1.338355.

[18] P. Liaw and R. F. Davis, "Epitaxial Growth and Characterization of β - SiC Thin Films," *J. Electrochem. Soc.*, vol. 132, no. 3, pp. 642–648, Mar. 1985, doi: 10.1149/1.2113921.

[19] P. Pirouz *et al.*, "Heteroepitaxy on (001) Silicon: Growth Mechanisms and Defect Formation.," *MRS Proc.*, vol. 116, p. 57, 1988, doi: 10.1557/PROC-116-57.

[20] M. Werner, "High-temperature Sensors Based in SiC and Diamond Technology.," *1999 Sensors Update*, vol. 5, no. 1, pp. 141–190, Sep. 2001, doi: 10.1002/1616-8984(199904)5:1<141::AID-SEUP141>3.0.CO;2-J.

[21] J.-F. Michaud *et al.*, "Micromachining of thin 3C-SiC films for mechanical properties investigation," *MRS Proc.*, vol. 1246, pp. 1246-B09-04, 2010, doi: 10.1557/PROC-1246-B09-04.

[22] R. Anzalone *et al.*, "Residual Stress Measurement and Simulation of 3C-SiC Single and Poly Crystal Cantilevers," *MSF*, vol. 645–648, pp. 865–868, Apr. 2010, doi: 10.4028/www.scientific.net/MSF.645-648.865.

[23] A. Severino *et al.*, "High-quality 6inch (111) 3C-SiC films grown on off-axis (111) Si substrates," *Thin Solid Films*, vol. 518, no. 6, pp. S165–S169, Jan. 2010, doi: 10.1016/j.tsf.2009.10.080.

[24] A. J. Steckl and J. P. Li, "Epitaxial growth of beta -SiC on Si by RTCVD with C/sub 3/H/sub 8/ and SiH/sub 4/," *IEEE Trans. Electron Devices*, vol. 39, no. 1, pp. 64–74, Jan. 1992, doi: 10.1109/16.108213.

[25] N. Nordell *et al.*, "Design and Performance of a New Reactor for Vapor Phase Epitaxy of 3C, 6H, and 4H SiC," *J. Electrochem. Soc.*, vol. 143, no. 9, pp. 2910–2919, Sep. 1996, doi: 10.1149/1.1837126.

[26] L.-O. Björketun *et al.*, "Interfacial void formation during vapor phase growth of 3C-SiC on Si(0 0 1) and Si(1 1 1) substrates. Characterization by transmission electron microscopy," *Journal of Crystal Growth*, vol. 182, no. 3–4, pp. 379–388, Dec. 1997, doi: 10.1016/S0022-0248(97)00346-1.

[27] A. Leycuras, "Growth of CVD Thin Films and Thick LPE 3C SiC in a Specially Designed Reactor," *MSF*, vol. 338–342, pp. 241–244, May 2000, doi: 10.4028/www.scientific.net/MSF.338-342.241.

[28] H. Nagasawa *et al.*, "3C-SiC hetero-epitaxial growth on undulant Si(001) substrate," *Journal of Crystal Growth*, vol. 237–239, pp. 1244–1249, Apr. 2002, doi: 10.1016/S0022-0248(01)02233-3.

[29] T. Chassagne *et al.*, "Investigation of 2 Inch SiC Layers Grown in a Resistively-Heated LP-CVD Reactor with Horizontal 'Hot-Walls,'" *MSF*, vol. 457–460, pp. 273–276, Jun. 2004, doi: 10.4028/www.scientific.net/MSF.457-460.273.

[30] T. Chassagne *et al.*, "Control of 3C-SiC/Si wafer bending by the 'checker-board' carbonization method," *phys. stat. sol. (a)*, vol. 202, no. 4, pp. 524–530, Mar. 2005, doi: 10.1002/pssa.200460415.

[31] M. Zielinski *et al.*, "Stress relaxation during the growth of 3C-SiC⁄Si thin films," *Appl. Phys. Lett.*, vol. 89, no. 13, p. 131906, Sep. 2006, doi: 10.1063/1.2357569.

[32] M. Portail *et al.*, "Comparative study of the role of the nucleation stage on the final crystalline quality of (111) and (100) silicon carbide films deposited on silicon substrates.," *Journal of Applied Physics*, vol. 105, no. 8, p. 083505, Apr. 2009, doi: 10.1063/1.3089215.

[33] R. Anzalone *et al.*, "Heteroepitaxy of 3C-SiC on different on-axis oriented silicon substrates," *Journal of Applied Physics*, vol. 105, no. 8, p. 084910, Apr. 2009, doi: 10.1063/1.3095462.

[34] B. Neuner *et al.*, "Midinfrared Index Sensing of pL-Scale Analytes Based on Surface Phonon Polaritons in Silicon Carbide," *J. Phys. Chem. C*, vol. 114, no. 16, pp. 7489–7491, Apr. 2010, doi: 10.1021/jp9114139.

[35] S. Jiao *et al.*, "A new approach for AFM cantilever elaboration with 3C-SiC," *Materials Letters*, vol. 77, pp. 54–56, Jun. 2012, doi: 10.1016/j.matlet.2012.02.128.

[36] S. E. Saddow *et al.*, "Single-Crystal Silicon Carbide: A Biocompatible and Hemocompatible Semiconductor for Advanced Biomedical Applications," *MSF*, vol. 679–680, pp. 824–830, Mar. 2011, doi: 10.4028/www.scientific.net/MSF.679-680.824.

[37] A. Oliveros *et al.*, "Protein immobilization on 3C-SiC (100) as a substrate for detecting the onset of acute myocardial infarction (AMI)," in *2012 Annual International Conference of the IEEE Engineering in Medicine and Biology Society*, San Diego, CA, Aug. 2012, pp. 1643–1646. doi: 10.1109/EMBC.2012.6346261.

[38] B. Neuner *et al.*, "Prism-coupled surface wave accelerator based on silicon carbide," *Phys. Rev. ST Accel. Beams*, vol. 15, no. 3, p. 031302, Mar. 2012, doi: 10.1103/PhysRevSTAB.15.031302.

[39] M. Syväjärvi *et al.*, "Cubic silicon carbide as a potential photovoltaic material," *Solar Energy Materials and Solar Cells*, vol. 145, pp. 104–108, Feb. 2016, doi: 10.1016/j.solmat.2015.08.029.

[40] H. Heidarzadeh *et al.*, "A new proposal for Si tandem solar cell: Significant efficiency enhancement in 3C–SiC/Si," *Optik*, vol. 125, no. 3, pp. 1292–1296, Feb. 2014, doi: 10.1016/j.ijleo.2013.08.018.

[41] A. E. Bazin *et al.*, "High Quality Ohmic Contacts on n-type 3C-SiC Obtained by High and Low Process Temperature," *AIP conference proceedings*, Strasbourg, (France), 2010, pp. 51–54. doi: 10.1063/1.3518309.

[42] X. Song *et al.*, "Dose Influence on Physical and Electrical Properties of Nitrogen Implantation in 3C-SiC on Si," *MSF*, vol. 711, pp. 154–158, Jan. 2012, doi: 10.4028/www.scientific.net/MSF.711.154.

[43] J. Biscarrat *et al.*, "Ti Thickness Influence for Ti/Ni Ohmic Contacts on N-Type 3C-SiC," *MSF*, vol. 711, pp. 179–183, Jan. 2012, doi: 10.4028/www.scientific.net/MSF.711.179.

[44] V. Cimalla *et al.*, "Group III nitride and SiC based MEMS and NEMS: materials properties, technology and applications," *J. Phys. D: Appl. Phys.*, vol. 40, no. 20, pp. 6386–6434, Oct. 2007, doi: 10.1088/0022-3727/40/20/S19.

[45] E. Mastropaolo *et al.*, "Piezo-electrically actuated and sensed silicon carbide ring resonators," *Microelectronic Engineering*, vol. 97, pp. 220–222, Sep. 2012, doi: 10.1016/j.mee.2012.03.008.

[46] R. Anzalone *et al.*, "Mechanical Proprieties and Residual Stress Evaluation on Heteroepitaxial 3C-SiC/Si for MEMS Application," *MSF*, vol. 711, pp. 51–54, Jan. 2012, doi: 10.4028/www.scientific.net/MSF.711.51.

[47] S. Roy *et al.*, "Transmission electron microscopy investigation of microtwins and double positioning domains in (111) 3C-SiC in relation with the carbonization conditions," *Appl. Phys. Lett.*, vol. 95, no. 8, p. 081903, Aug. 2009, doi: 10.1063/1.3202783.

[48] S. Jiao *et al.*, "Detailed study of the influence of surface misorientation on the density of Anti-Phase Boundaries in 3C-SiC layers grown on (001) silicon," Strasbourg, (France), 2010, pp. 15–18. doi: 10.1063/1.3518286.

[49] L.-O. Björketun *et al.*, "Texture Evolution in Si/SiC Layered Structures Deposited on Si(001) by Chemical Vapor Deposition," *J. Mater. Res.*, vol. 13, no. 9, pp. 2632–2642, Sep. 1998, doi: 10.1557/JMR.1998.0367.

[50] Y. Ishida *et al.*, "Elongated shaped Si Island Formation on 3C-SiC by Chemical Vapor Deposition and Its Application to Antiphase Domain Observation," *Jpn. J. Appl. Phys.*, vol. 38, no. Part 1, No. 6A, pp. 3470–3474, Jun. 1999, doi: 10.1143/JJAP.38.3470.

[51] S. Jiao *et al.*, "Elaboration of Monocrystalline Si Thin Film on 3C-SiC(100)/Si Epilayers by Low Pressure Chemical Vapor Deposition," *MSF*, vol. 711, pp. 61–65, Jan. 2012, doi: 10.4028/www.scientific.net/MSF.711.61.

[52] J. F. Michaud *et al.*, "Original 3C-SiC micro-structure on a 3C–SiC pseudo-substrate," *Microelectronic Engineering*, vol. 105, pp. 65–67, May 2013, doi: 10.1016/j.mee.2013.01.010.

[53] R. Khazaka *et al.*, "Toward high-quality 3C–SiC membrane on a 3C–SiC pseudo-substrate," *Materials Letters*, vol. 160, pp. 28–30, Dec. 2015, doi: 10.1016/j.matlet.2015.07.071.

[54] R. Khazaka, "From atomic level investigations to membrane architecture: An in-depth study of the innovative 3C-SiC/Si/3C-SiC/Si heterostructure," PhD dissertation, University of Tours, Tours, 2016.

[55] R. Khazaka *et al.*, "Procédé de fabrication d'une structure micromécanique en carbure de silicium comportant au moins une cavité," FR1653006, Dec. 10, 2017

[56] R. Khazaka *et al.*, "Turning the undesired voids in silicon into a tool: *In-situ* fabrication of free-standing 3C-SiC membranes," *Appl. Phys. Lett.*, vol. 110, no. 8, p. 081602, Feb. 2017, doi: 10.1063/1.4977033.

[57] "NOVASiC." https://www.novasic.com/services/polishing/polishing.php

[58] M. T. Boudjiet *et al.*, "Geometry optimization of uncoated silicon microcantilever-based gas density sensors," *Sensors and Actuators B: Chemical*, vol. 208, pp. 600–607, Mar. 2015, doi: 10.1016/j.snb.2014.11.067.

[59] W. Wei *et al.*, "Optical interferometry Endpoint Detection for Plasma Etching," in *2007 8th International Conference on Electronic Measurement and Instruments*, Xian, China, Aug. 2007, pp. 4-252-4–255. doi: 10.1109/ICEMI.2007.4351131.

[60] E. Aperathitis *et al.*, "Laser interferometry as a diagnostic tool for the fabrication of reactive ion etching-edge-emitting lasers," *J. Vac. Sci. Technol. B*, vol. 20, no. 5, p. 1994, 2002, doi: 10.1116/1.1505960.

[61] T. Defforge *et al.*, "Plasma-deposited fluoropolymer film mask for local porous silicon formation," *Nanoscale Res Lett*, vol. 7, no. 1, p. 344, Dec. 2012, doi: 10.1186/1556-276X-7-344.

[62] H. Seidel *et al.*, "Anisotropic Etching of Crystalline Silicon in Alkaline Solutions: I . Orientation Dependence and Behavior of Passivation Layers," *J. Electrochem. Soc.*, vol. 137, no. 11, pp. 3612–3626, Nov. 1990, doi: 10.1149/1.2086277.

[63] M. T. Boudjiet *et al.*, "Preliminary results of the feasibility of hydrogen detection by the use of uncoated silicon microcantilever-based sensors," *International Journal of Hydrogen Energy*, vol. 39, no. 35, pp. 20497–20502, Dec. 2014, doi: 10.1016/j.ijhydene.2014.03.228.

3. Design, fabrication and characterization of air-coupled CMUTs gas sensors without functionalized coating

3.1 CMUT technology 129

3.1.1 State-of-the-art 129

3.1.2 Brief history on CMUTs fabrication advancement from labs associated with University of Tours 130

3.2 Topology of CMUTs array 133

3.2.1 Cell level representation 133

3.2.2 Element level representation 135

3.2.3 Chip level representation 137

3.3 Fundamentals of CMUTs 138

3.3.1 Static analysis with 1-D model 140

3.3.2 1-D dynamic analysis without acoustic loading 143

3.3.3 Dynamic analysis in gas medium and CMUTs design 148

3.4 Fabrication and packaging of CMUTs 153

3.5 Characterizations of fabricated CMUTs 156

3.5.1 Digital holographic microscopy (DHM) measurements 156

3.5.2 Electrical impedance measurements 160

3.6 Electroacoustic characterizations of CMUTs in air 164

3.6.1 Design and fabrication of the measuring cell 164

3.6.2 Experimental setup and preliminary results 166

3.6.3 Impact of V_{bias} and V_{ac} on time of flight performances 170

3.6.4 Comparison between different emission frequencies 173

3.6.5 Detection of maximum working distances 174

3.7 Binary gas mixture analyses 176

3.7.1 Time of flight model validation in gas mixture environments 176

3.7.2 Gas mixture analysis for CMUTs working at resonance mode 179

Conclusion and perspectives 181
References 183

Chapter 3

Design, fabrication and characterization of air-coupled CMUT gas sensor without functionalized coating

This third chapter focuses on the second technology implemented for hydrogen detection, i.e. the use of capacitive micromachined ultrasonic transducers (CMUTs). As explained in chapter 1, the objective is to develop, characterize and test CMUTs-based airborne ultrasonic transducers, to meet the two proposed detection methods. In the third method, CMUT works at its resonance frequency and the physical properties of gases, such as acoustic impedance and viscosity are monitored [1]. This measurement is performed by detecting shifts in the resonance frequency due to change in gas concentration. The fourth method is based on the detection of the ultrasonic velocity variations using the time of flight (ToF) technique [2]. Unlike method III, here CMUTs work as an ultrasonic emitter and/or receiver at low frequency range; typically around 1 MHz, which is far lower from its resonance frequency. In concrete terms, the CMUT is used as a microphone in reception, and it is forced to work in pseudo-static mode in emission.

For ToF measurement, it is essential to state the constraints imposed by the measurement settings and the resulting specifications. Given the restrictions of measurement cell size for binary gas mixture analyses [3], the distance to perform ToF measurement is limited to a few millimeters. To measure an ultrasonic velocity between a transmitter and a receiver, over short propagation distances, the duration of the impulse response must be shorter than the time of flight itself. Given the ultrasonic frequencies currently used in air, typically between 200 kHz and 1.5 MHz, and the wavelengths involved (1.6 mm to 0.2 mm respectively) in relation with distance travelled, it was decided to emit ultrasonic pulse at 1 MHz central frequency with relative frequency bandwidth value of at least 50 %.

The strategy we adopted to build the CMUTs follows the thesis work carried out by N. Sénégond [4], and A. Boulmé [5]. One of the key points from the performed work was concerning the generation of low frequency (< 1.5 MHz) ultrasonic waves, for air or water, by

means of CMUTs. The manufacturing constraints of these devices led to the idea of using these technologies in an original way: to exploit them, in transmission as well as in reception, which is often characterized by high bandwidths. As said earlier, generally, an ultrasonic transducer is used at its resonance frequency, where the acoustic coupling between transducer and propagation medium is most efficient. In spite of it, we decided to use CMUTs below their resonance frequency, in order to meet specifications and to favor the frequency bandwidth.

This chapter consists of seven parts. The first part describe the state-of-the-art of CMUT technology and the research works carried out at GREMAN laboratory, which preceded this thesis. The CMUTs used and exploited were designed in the context of A. Boulmé's thesis work [5]. The second part is a general description on topology of CMUTs-based ultrasonic emitter/receiver, from unit scale to complete CMUT arrays. The device specification at chip level is described in this part. The third section describes the basic behavioral equations of a CMUT cell, both in static and dynamic mode. This part provides the basis for the design rules of CMUT for the two modes of operation: i) resonance mode and ii) air-coupled ultrasound transducer mode, i.e. microphone mode. The particularity and one of the original features of these devices, is that CMUTs can be used independently for these two modes. Part four presents the fabrication process of the CMUTs that were used in this study. The fifth and sixth sections present a set of characterization results of the fabricated CMUT devices. In section five, the optical and electrical characterizations in air are detailed. Part six demonstrates the design and fabrication of the measuring cell used in ToF measurements. Preceding that, the electroacoustic measurement in air is demonstrated, to explain the microphone operation mode. Then, different geometries with various combinations of input electrical parameters are compared. These experiments are performed to identify the device performance in terms of bandwidth for various geometries. Lastly, the demonstration of gas detections with chosen CMUT prototype are carried out for both operation modes.

3.1 CMUT technology

3.1.1 State-of-the-art

Capacitive micromachined ultrasonic transducers (CMUTs) technology is a new concept in the field of ultrasonic transducers. Traditionally, piezoelectric crystals and ceramics are broadly used, ever since the discovery of piezoelectricity in the 1880s for ultrasound generation and detection [6]. At the beginning, electrostatic or capacitive transducers were not prominent because they required a higher electric field than piezoelectric devices to achieve satisfactory efficiency. The early works on CMUTs have been recorded in late 1980s and early 1990s, as referred in [7]–[9], these transducers were neither fabricated efficiently nor characterized thoroughly. Later in 1993, M.I. Haller and B.T. Khuri-Yakub proclaimed first ever CMUTs with an advanced fabrication process that enables to understand the influence of gap size with respect to the breakdown voltage to achieve devices with higher operating points [10], [11].

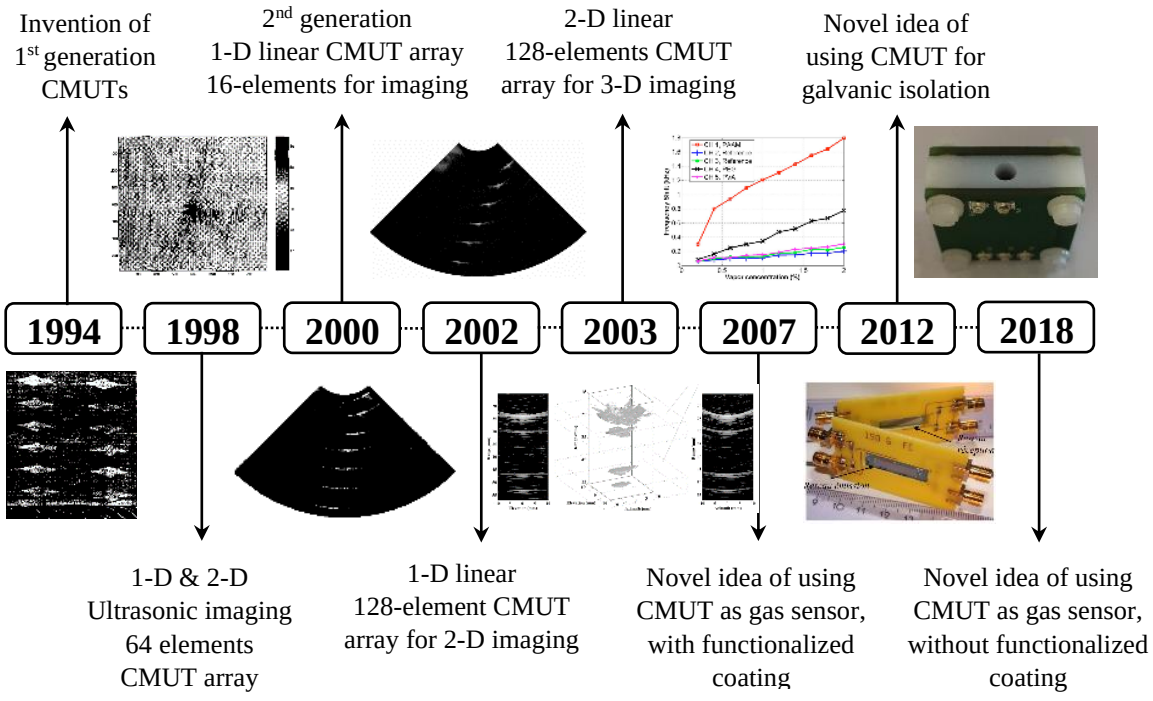


Figure 3.1: Major breakthrough of CMUTs in various fields [1], [10], [12]–[17].

Since the invention of first generation CMUTs, there is plenty of research carried out, all around the globe, for enhancing the transducer designs, fabrication processes and characterization techniques, as referred in [12], [18]–[24]. In which, few groundbreaking works are mentioned in figure 3.1. CMUTs established itself as a potential candidate in the field for medical

ultrasound imaging and therapeutic purposes [13]–[15], [25]–[28]. Moreover, they are being used as chemical/biosensors [16], [29], detection of human lung gas exchanges [30], monitoring of greenhouse gases [31] and wind speed measurements [32]. Their remarkable advancements in gas sensing were thoroughly discussed in chapter 1 (refer §1.6.2).

3.1.2 Brief history on CMUTs fabrication advancement from labs associated with University of Tours

In the end of 20th century, Pizarro *et al.* investigated electrostatic transducers for airborne applications. They worked with transducers made of metallic backplate, which were either grooved or de-polished and the membrane layer was of 2.5 µm-thick Mylar film. This study includes the design optimization in terms of groove widths and pitches, and resulted in producing membranes with different grooved surface ratios ranging from 33 % to 66 % as mentioned in [20]. These CMUTs have the same behavior, as the one fabricated by Carr *et al.* but the change in central frequencies were with respect to membrane width and driven voltages [33]. For devices developed by Pizarro *et al.*, the resonance frequency was fixed by the Helmholtz resonance of the air trapped in the cavity as explained by Hietanna *et al.* [34], [35]. After, Certon *et al.* further optimized the design with regard to gap height, choice of top electrode material, membrane thickness and shape to improve CMUTs sensitivity [36].

In parallel, Belgacem *et al.* made a distinctive difference in CMUTs fabrication process, by sealing the membranes, as shown in figure 3.2.a. This work includes choice of oxide (used for membrane sealing) and, selection of sacrificial layer material based on their sticking coefficient and integration. Also spotted the importance of non-negligible curvature of membrane while sealing, which can produce non-functional transducers [37]. Following this, Jeanne *et al.* improved the device of Belgacem *et al.* on the industrial platform (from STMicroelectronics) in terms of membrane sealing and control of the membrane layer (silicon nitride) during deposition. In addition, they have added a Parylene protection layer on their entire stack to avoid deterioration of the devices from the external environment, as shown in figure 3.2.b [38]. Both the CMUTs were dedicated to medical imaging.

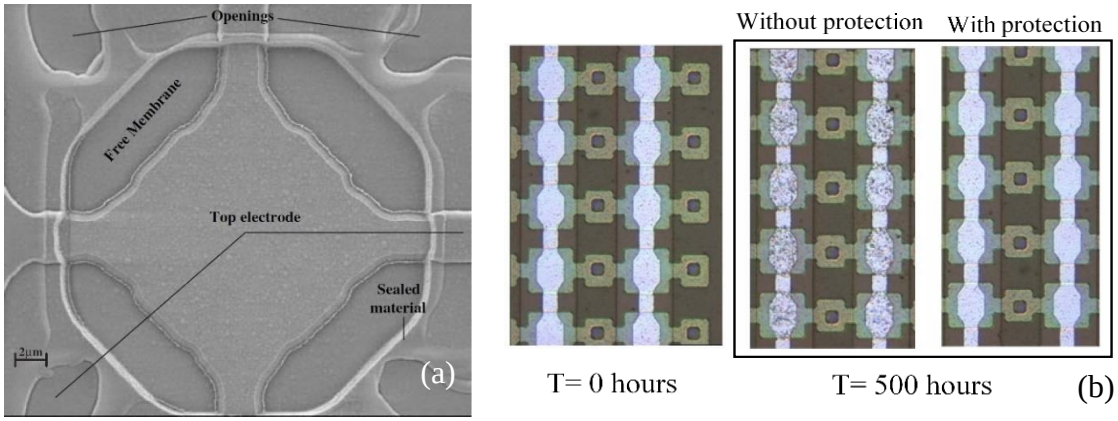


Figure 3.2: (a) SEM top view of the CMUT cell proposed by Belgacem *et al.* [37]. (b) Optical view of CMUTs demonstrated by Jeanne *et al.* with and without Parylene protection layer [38].

Then, Ngo *et al.* developed the idea of using double-faced wafer bonded CMUTs for acoustic transformer application, as shown in figure 3.3 [39]. Their work stabilized the fabrication process by enhancing the cavity sealing material, better control of membrane material deposition during surface micromachining and good repeatability. The other interesting key step is that they worked on a higher cavity gap compared to previous works, i.e. 400 nm. Ngo's work paved the way for our current devices for enlarging membrane sizes.

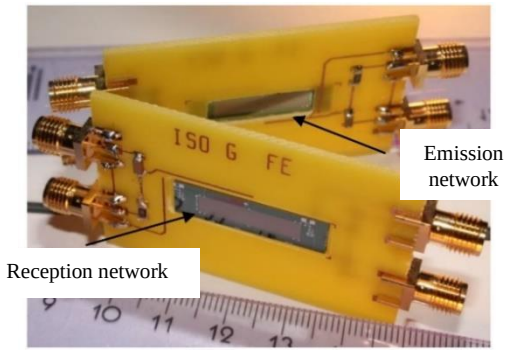


Figure 3.3: State-of-the-art double-faced wafer bonded CMUTs for galvanic isolation by Ngo *et al.* [39].

Concurrently, Sénégond *et al.* have developed a theoretical time-domain model, to use CMUTs in low frequency band for air-coupled applications [40]. They tested CMUT membrane behavior at high-voltage excitations for a range of frequencies, i.e. 250 kHz-10 MHz in air and fluid mediums [41]. This study explained the origin of membrane non-linearities. In addition, they demonstrated the ability of CMUTs to work in pseudo-static regime, below its resonance frequency. Eventually, electro mechanical characterizations of CMUTs using optical measurements such as digital holographic microscopy (DHM) and laser interferometry were implemented to help in deriving the basic parameters of CMUTs [41], [42].

Later, Boulmé *et al.* developed CMUTs for medical imaging [43] based on the key results from Sénégond *et al.* [44]. These CMUTs worked in a low frequency range, from 200 kHz to 2 MHz, arranged in linear arrays, as shown in figure 3.4.a. The designed probe was used for assessment of cortical bone with the axial transmission method, shown in figure 3.4.b. Boulmé *et al.* have compared the axial transmission measurement of CMUT probe with classical PZT probe. The obtained results prove that they have wider angular directivity patterns and higher frequency bandwidth than PZT probe [45].

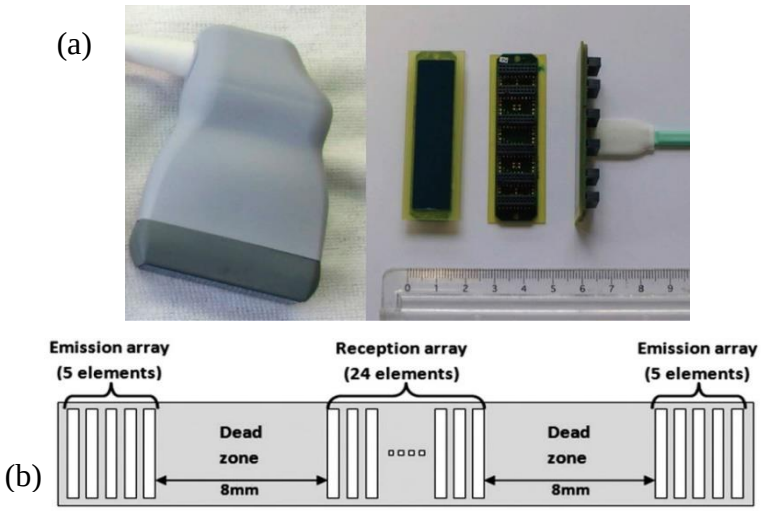


Figure 3.4: (a) CMUTs probe used for cortical bone assessment and (b) CMUTs arrangement for axial transmission measurement [45].

Gross *et al.* also proposed using CMUTs with the same emission principle as Boulmé *et al.* for preclinical evaluation of targeted therapy [26], [46]. The probe consists of CMUT arrays operating at low frequency range (1 MHz) that were arranged in a specific way, as shown in figure 3.5.

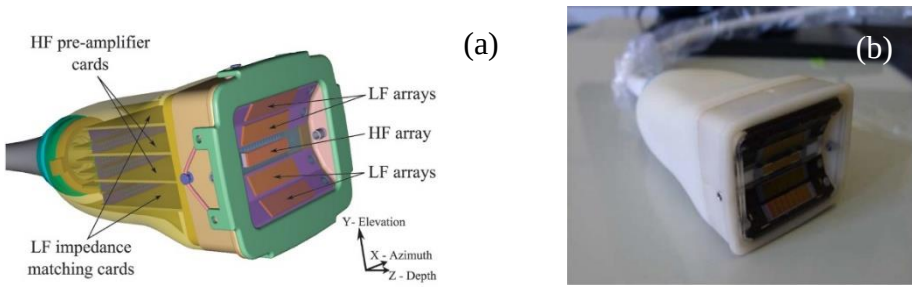


Figure 3.5: (a) Schematic of packaged probe and (b) fabricated ultrasound-guided focused ultrasound CMUTs probe used in targeted therapy applications [46].

To summarize, the previous research mentioned in this section helped the present study, in terms of design, material and method. In other words, it is a direct application of N. Sénégond

results, as mentioned in [4]. Those results are the proof of concept for CMUTs emission in air at low frequency range, working at pseudo-static mode, to benefit the ability of producing large displacement amplitudes. As well, the devices used in this research were developed in the context of A. Boulmé PhD thesis [5]. No devices have been fabricated in the framework of project H2MEMS. However, packaging and chip integration were specifically developed for the H2MEMS project, more, these chips had never been used to work in the air. This work was therefore very exploratory with regard to the H2MEMS project objectives. The detailed electrical and electroacoustic characterization results are presented in §3.5 and §3.6 respectively.

3.2 Topology of CMUTs array

In this part, the multi-scale topologies of CMUT arrays are discussed generically. To understand the topology of CMUT arrays, one should primarily know their multi-level scaling, starting from the smallest cell (µm) to the chip level (cm) representations. The geometries of each part have influence on the overall electroacoustic performances of the device.

3.2.1 Cell level representation

The CMUT cell has a structure similar to a parallel plate capacitor, as shown in figure 3.6. The structure looks relatively simple, which consists of two electrodes in parallel. The stationary electrode is located in the bottom and the mobile electrode in the top, separated by air or vacuum. The fixed electrode is electrically isolated from the substrate through an insulation layer. The bottom electrode is made of a heavily doped silicon layer or a conductive metal layer. The top electrode is a metal layer deposited on the membrane material. The mobile part refers to the membrane layer associated with the top electrode that is totally or partially metalized, based on the operating condition. In our case, a 50 % metallization ratio is used. Mostly, the membrane material is of bulk silicon in wafer-bonded CMUT and silicon nitride in surface micromachined CMUT. The different materials constituting various layers of CMUT are given in §3.4.

In our study, silicon nitride is used as membrane material, with a thickness of 450 nm. The CMUT cavity can be either sealed under vacuum or maintained at atmospheric pressure, depending on the targeted application. In our case, we used sealed cavities only. Non-sealed CMUT cavity requires a specific process step, which needs to add holes to evacuate air trapped in the cavity. The gap height (400 nm for our devices), thicknesses and dimensions of different layers are important to be optimized, because in case of sealing, the membrane undergoes a non-negligible deformation caused by atmospheric pressure that may produce non-functional CMUT cells (refer §3.3.1). In addition, they influence the device performances: the resonance frequency (f_r), the electromechanical coupling coefficients (k_t) and the collapse voltage (V_c), as shown in §3.3.2.

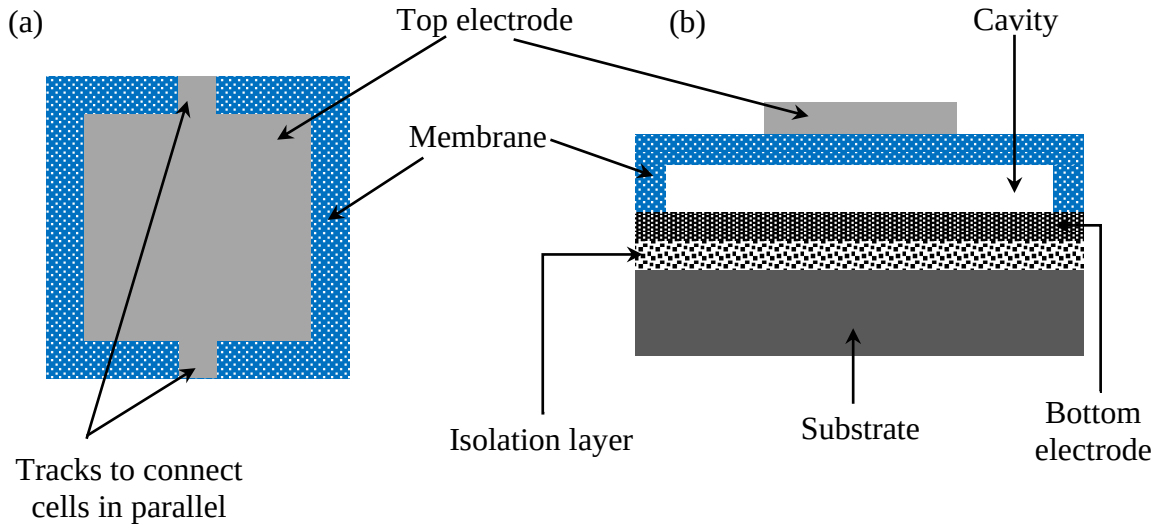


Figure 3.6: (a) Schematic of a square shaped CMUT cell and (b) cross-sectional view of a single CMUT cell.

Most commonly, CMUTs are of circular or square shape. The choice depends on the targeted performances and the expertise of the research group. GREMAN laboratory has proficiency in design and fabrication of rectangular and square shaped CMUT cells. These topologies are highly suitable, to fill a rectangular element array and obtain a high active surface ratio. In our case, CMUTs of different membrane sizes were fabricated (designed in the context of the PhD of A. Boulmé), in order to tune the active surface ratio and to investigate their impact on sensitivity. The specifications of those CMUT configurations are summarized in table 3.1. These chosen membrane sizes are explained in the §3.3.3.

Finally, the Parylene layer could be used to reinforce the protection from external environments and to avoid short circuits in fluid mediums, as demonstrated in [38]. Generally, for air applications, these layers are non-essential.

Table 3.1: Design parameters and material specifications of fabricated single CMUT cell.

Parameters	**Membrane**	**Electrode**	**Cavity**
Material	Silicon nitride	Aluminum	Vacuum
Thickness	400 nm	450 nm	250 nm
Dimension	37x37 µm² 37x32 µm² 32x32 µm² 32x27 µm² 27x27 µm²	22x22 µm²	
Young's modulus	220 GPa	68 GPa	
Poisson ratio	0.22	0.35	
Density	3300 kg/m^3	2700 kg/m^3	
Permittivity	7.5 ε_0		8.854 x 10^{-12}

3.2.2 Element level representation

The pressure generated by a single CMUT cell is insufficient for any application. In order to produce a large ultrasonic field intensity, it is necessary to connect several hundreds or thousands of CMUT cells electrically in parallel. Together, these whole populations of cells form a CMUT element. The organization of these cells depends on the final topology of transducers. For a rectangular element, like those used for medical imaging, the cells are arranged in several rows and columns, next to each other until the end of element length. Here, each emitter is defined by a width of 0.8 mm and length of 8 mm. Even if these values were fixed for the bone characterization in medical imaging, they were kept the same for our application, as they were suitable. Our aim is to use a "single element" transducer. Hence, we need to ensure the surface area is large enough compared to the acoustic wavelength. At 1 MHz, the acoustic wavelength is 330 µm, far lower compared to the element dimensions. In terms of electrical connections, all the CMUT cells are linked together and accessible by the metal pad

connected at the edge of the chip (see conducting pad in figure 3.7). The lower electrode (i.e. ground pad placed right after conducting pad), common to all CMUT cells of the element, is structured at the same level of top electrodes to eliminate the parasitic capacitances.

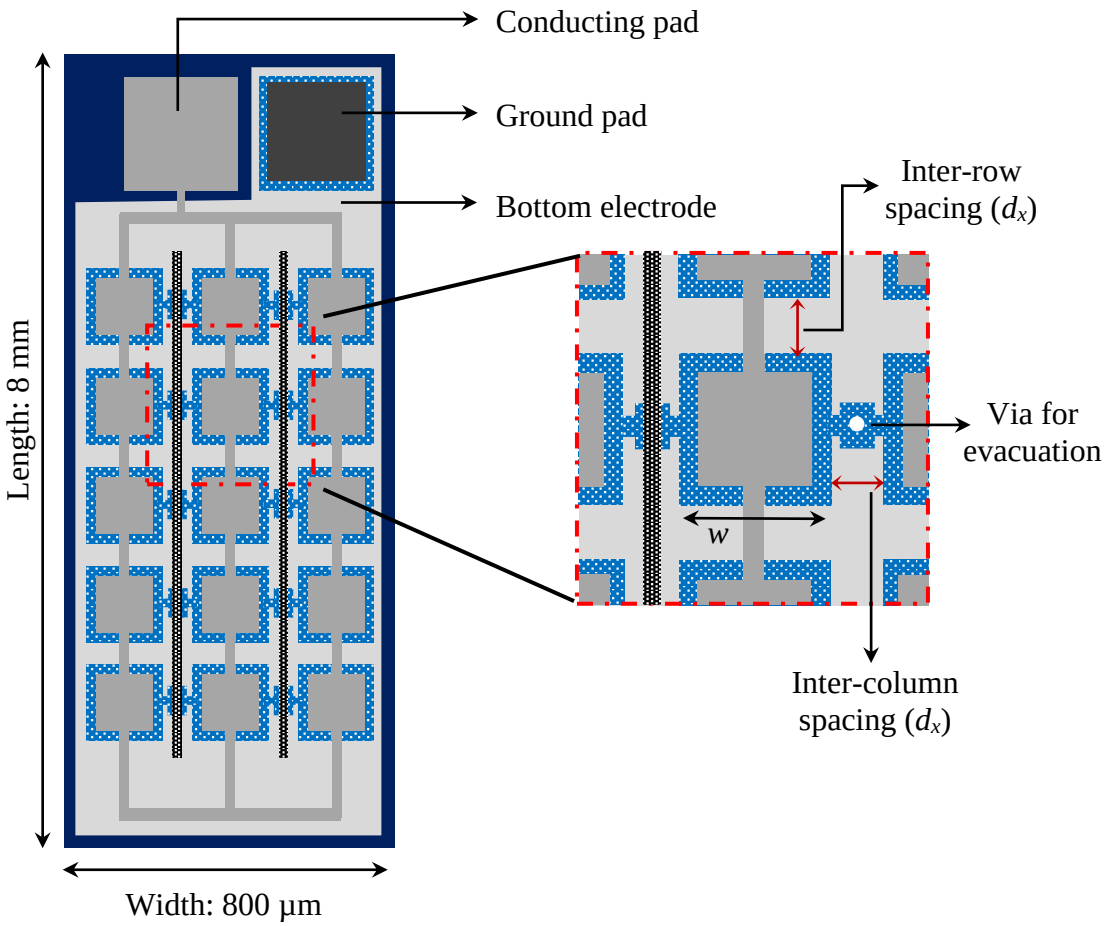


Figure 3.7: Schematic of single CMUT element containing several CMUT cells.

In some structures, all the elements in the chip are connected to a common ground and at times individually, depending on their requirements. In our case, the ground for each element is separated, which facilitates the characterization of a single element at a time. With the help of these connecting pads, the elements can be wedge bonded to a printed circuit board (PCB) for further electrical characterizations. In addition, the parameters like inter-membrane distances also have an influence on the response frequency of the element. These distances must be possibly minimum to obtain maximum active surface area. A sketch of CMUT layout is given in figure 3.7 (right), where w is the width of the CMUT, d_x is the CMUT-to-CMUT distance along *x-axis* and d_y along *y-axis*. The pitch values of d_x and d_y are fixed by the fabrication process. In our case, the pitch along *x-axis* (inter-column distance) is always greater than

y-axis (inter-row distance) because the via used to release the sacrificial layer is placed along *x-axis*, as shown in figure 3.7. For the device used here, the inter-row distance and the inter-column distance are 6 µm and 38 µm respectively. In addition, table 3.2 summarizes the element details of each configuration for different membrane sizes.

Table 3.2: Description of the element with various membrane sizes

Dimension (µm²)	Number of columns per element	Number of membranes per element	Element length (µm)	Element width (µm)	Pitch (µm)	Active surface ratio (%)
37x37	11	2046	7992	787	892	45
37x27	11	2662	7980	787	892	42
32x32	12	2532	8012	802	892	40
32x27	12	2904	7980	802	892	39
27x27	13	3146	7980	807	892	36

3.2.3 Chip level representation

The CMUT chip is made of several elements as shown in figure 3.8. The inter-element distance is the "*kerf*". The sum of the element width and the *kerf* gives the "*pitch*". In our device, the value of *kerf* and *pitch* are 10 µm and 892 µm respectively. From figure 3.8, the contact pads connected to the top and the bottom electrodes constituting the conducting point and the ground. It is possible to connect the number of elements in parallel to form an array of elements to obtain a higher field. In the targeted application, we use two elements that are positioned face to face, to perform time of flight measurement at low frequency mode (method IV detection) and single element for gas detection at resonance mode (method III detection).

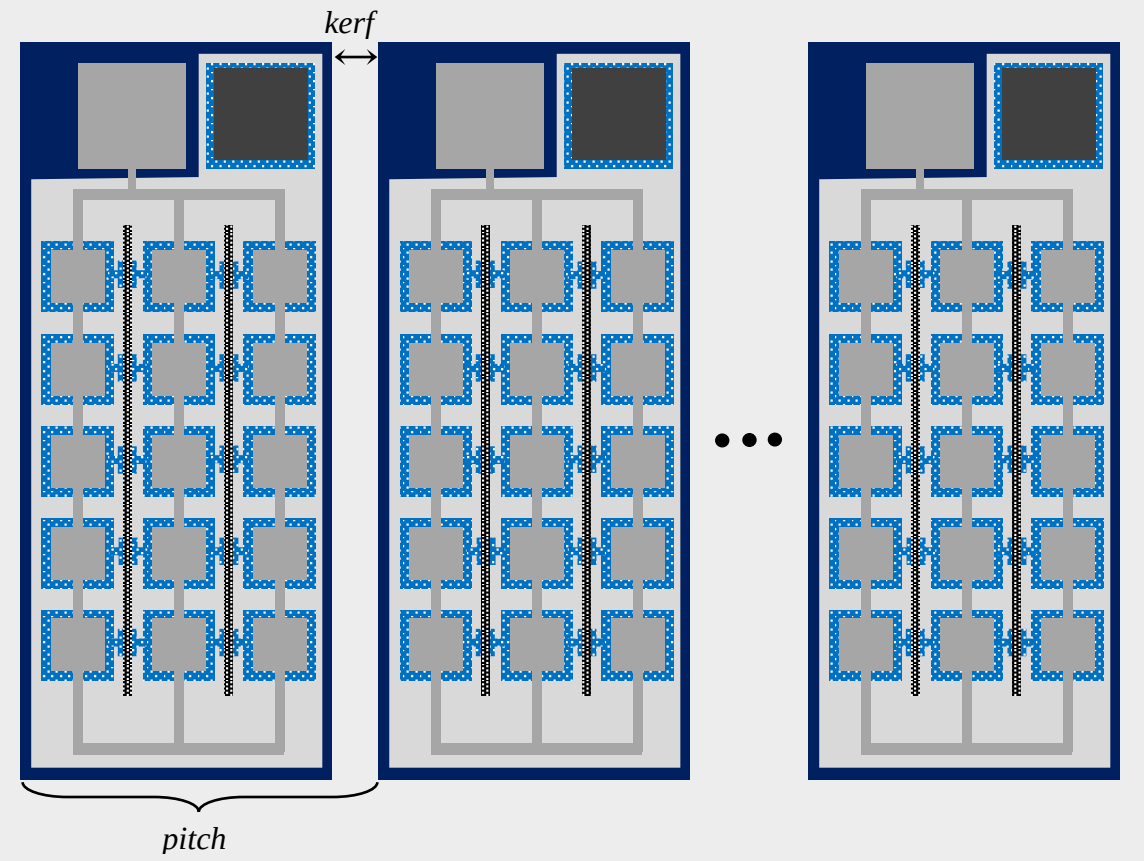


Figure 3.8: Chip level representation of CMUTs consisting of several available elements.

3.3 Fundamentals of CMUTs

Capacitive micromachined ultrasonic transducer working is based on electrostatic mechanism. Generally, the CMUTs can be operated in two modes: i) emission mode and ii) reception mode, as shown in figure 3.9. In emission mode, an AC voltage is applied between the top and the bottom electrode, which causes the membrane to deflect towards the bottom of the cavity. Due to this displacement, an acoustic pressure field is generated from the emitting transducer to its surrounding medium. Generally, a DC bias voltage is added to the emission to improve the transducer's sensitivity and electromechanical coupling coefficient. In the reception mode, only DC bias is applied to detect the variation in charges (ΔC), caused by the membrane deflection due to the incident acoustic pressure wave (from emission).

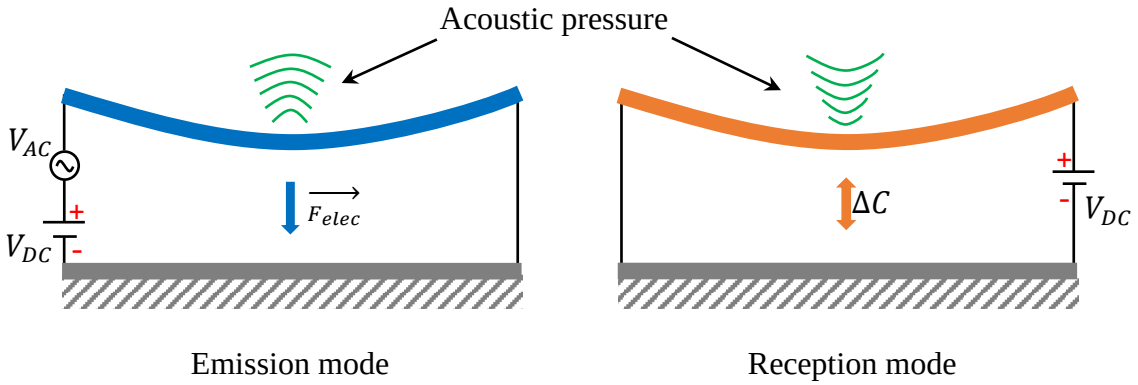


Figure 3.9: Schematic of CMUT cell in emission and reception modes.

In this part, the one-dimensional model of a single CMUT cell is illustrated (see figure 3.10). This method was largely used by the scientific community to understand the functionality of CMUT cell [47]. The corresponding lumped model with linear spring and parallel plate capacitor is shown in figure 3.10. It is assumed that the membrane restoring force is linear to its displacement. Likewise, given the small dimension of the CMUT membrane, its mass has been neglected.

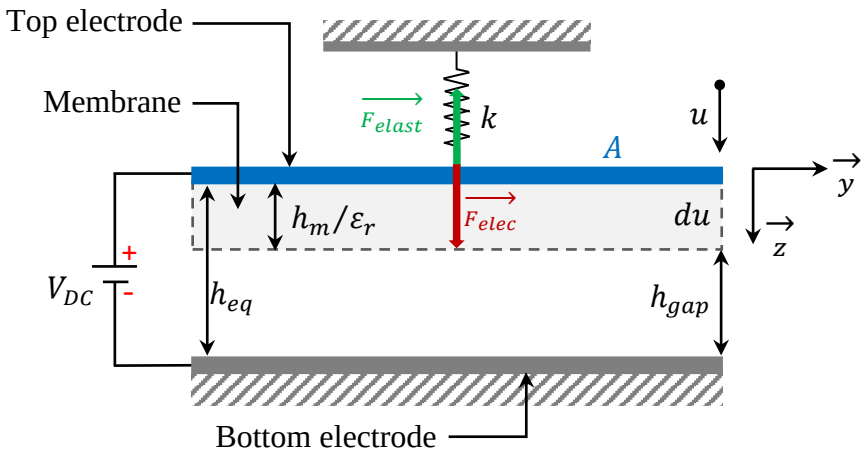


Figure 3.10: Schematic representation for 1-D equivalent of a single CMUT cell.

From figure 3.10, where V_{DC} is the continuous voltage across the top and bottom electrode, h_m the height of the membrane, ε_r the relative permittivity of the membrane material, h_{gap} the height of the vacuum cavity, h_{eq} the separation of top and bottom electrodes at rest, k the spring constant and A the area of membrane. The electrostatic force induced by the applied voltage across the CMUT and the restoring elastic force opposing the membrane displacement are given as $\overrightarrow{F_{elec}}$ and $\overrightarrow{F_{elast}}$ respectively.

The electrostatic force acting on the membrane at position *u*, as a function of capacitance is given by [5]:

$$\overrightarrow{F_{elec}}(u) = \frac{1}{2}\frac{\partial C}{\partial u}V_{DC}^2\vec{z} = \frac{1}{2}\frac{\varepsilon_0 A V_{DC}^2}{(h_{eq}-u)^2}\vec{z} \qquad \text{Eq. 3.1}$$

where, h_{eq} is expressed as:

$$h_{eq} = \left(\frac{h_m}{\varepsilon_r} + h_{gap}\right) \qquad \text{Eq. 3.2}$$

and the capacitance *C(u)* of the given model is written as:

$$C(u) = \frac{Q(u)}{V_{DC}} = \frac{\varepsilon_0 A}{(h_{eq}-u)} \qquad \text{Eq. 3.3}$$

Similarly, to derive the mechanical part, the elastic energy of the membrane/mobile electrode is considered as a simple mass-spring system using 1-D representation (figure 3.10). The mechanical force connecting the spring with stiffness *k*, at position *u* is given as:

$$\overrightarrow{F_{elast}}(u) = -ku\,\vec{z} \qquad \text{Eq. 3.4}$$

3.3.1 Static analysis with 1-D model

The aim of this study is to analyze the operating principle of CMUT cell in a static regime with respect to bias voltage (V_{DC}). For each step of bias voltage, the membrane position will displace and its corresponding change in charge is observed. At zero bias, the membrane rests at equilibrium (at its initial position). On increasing the polarization voltage, the h_{gap} decreases stably with minimum local potential. At one point, the membrane attains an unstable condition with high local potential (i.e. $h_{gap} = 0$), which is the collapsed state. The bias voltage at which the membrane stuck to its bottom electrode sweeping the whole gap height is referred as collapse voltage (V_c). At this stage, the electrostatic force becomes more prominent than the elastic restoring force. To release the membrane, it is necessary to gradually decrease the bias voltage, the event at which the release begins is called snapback, and the corresponding voltage is said to be snapback voltage (V_{sb}). This kind of behavior is common in all electrostatic MEMS, not exclusive to CMUTs.

To understand the static hysteresis cycle of the membrane displacement, the two important voltages (i.e. collapse and snapback) have to be observed. These voltages will define the excitation conditions of the system. To derive these two voltages analytically, the equilibrium position associated for each given polarization voltage has been calculated using Newton's second law of motion [5]:

$$F_{elec} + F_{elast} = 0 \Leftrightarrow u^3 - 2h_{eq}u^3 + h_{eq}^2 u - \frac{\varepsilon_0 A V_{DC}^2}{2k} = 0 \qquad \text{Eq. 3.5}$$

In addition, there are two other design possibilities to consider, either using unsealed cavities or sealed cavities. In case of unsealed CMUTs, they do not suffer due to atmospheric pressure effect, yet they are not suitable to observe large deflections, because the pressure inside (P_{in}) and the pressure outside (P_{out}) the cavity are equal, which makes it non-functional ($P_{in} - P_{out} = 0$). For sealed CMUTs, i.e. in our case, the collapse voltage is comparatively smaller than unsealed, due to the non-negligible curvature of the CMUT membrane while sealing. This causes the reduction in the gap height ($P_{in} - P_{out} \neq 0$). To demonstrate this, the simulation for real membrane displacement is shown in figure 3.11. This deflection occurs due to external atmospheric pressure (P_0) and residual mechanical stresses in the membrane (arising from process steps).

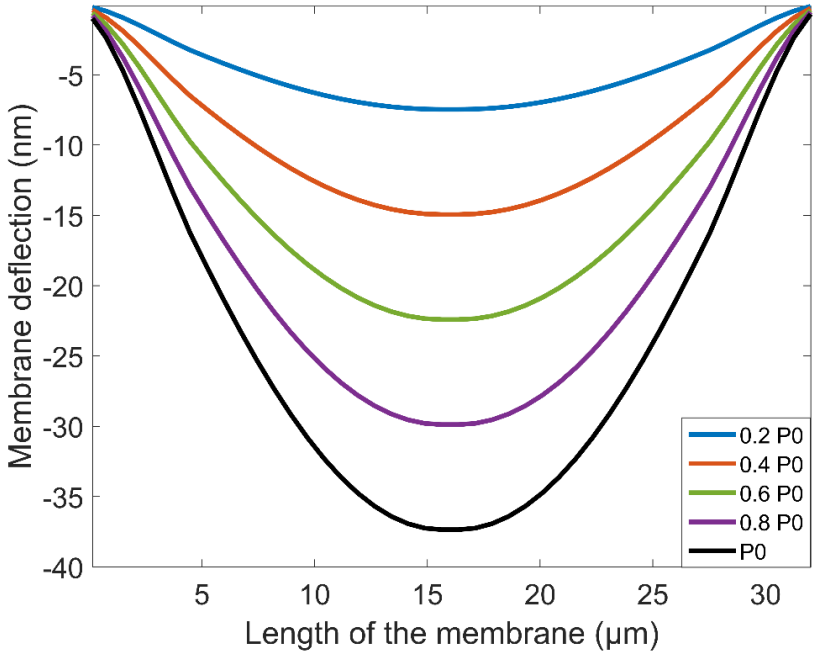


Figure 3.11: Computed static deflection of a CMUT cell experiencing different external acoustic pressure ranging from 0.2 P_0 to P_0. Simulation parameters are those given in table 3.1.

To mention, the 1-D model given in figure 3.10 is an illustration to highlight the parameters that govern the CMUT response. Therefore, the simulation results presented in this study do not concern CMUT 1-D model, but for real CMUT membranes. With this consideration, eq. 3.5 is rewritten by considering an external force (F_0) acting on the membrane causing static initial deflection (u_0) with an atmospheric pressure (P_0):

$$F_{elec} + F_{elast} + F_0 = 0 \Leftrightarrow u_0^3 - 2h_{eq}u_0^2 + h_{eq}^2 u_0 - \frac{\varepsilon_0 A V_{DC}^2}{2k} + P_0 A = 0 \qquad \text{Eq. 3.6}$$

Unlike electrostatic and elastic forces, the atmospheric pressure is independent of membrane position. Figure 3.11 shows the membrane displacement of a single CMUT cell undergoing various external acoustic pressures, ranging from 20 % to 100 % of P_0, where P_0 is the atmospheric pressure (10^5 Pa) with respect to eq. 3.6. Here in this modelling, we have taken a CMUT cell with specifications mentioned in table 3.1 for 32x32 µm² geometry, for which the initial deflection caused by atmospheric pressure is 38 nm. To derive the collapse voltage (V_c) without an external pressure, respecting eq. 3.5 is given below.

$$V_{DC} = V_c = \sqrt{\frac{8kh_{eq}^3}{27\varepsilon_0 A}} \qquad \text{Eq. 3.7}$$

In addition, the simulated static response without any external pressure for the range of applied voltage is shown in figure 3.12.

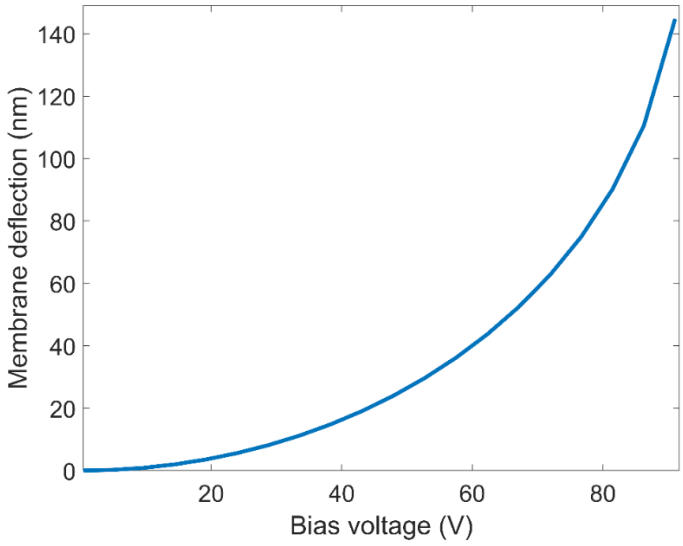


Figure 3.12: Simulated static displacement taken from the center of the membrane with respect to bias voltage (0-100 V) without external pressure, here the collapse voltage is 92 V. Simulation parameters are those given in table 3.1.

The membrane position at collapse (u_c) can be determined by calculating the double root of the third degree equation, i.e. eq. 3.5:

$$u_c = \frac{1}{3} h_{eq} \qquad \text{Eq. 3.8}$$

Similarly, the snapback voltage is calculated by considering the membrane released to the new initial state ($u = h_{gap}$), where electrostatic and elastic force become equilibrium again:

$$F_{elec}(u = h_{gap}) + F_{elast}(u = h_{gap}) = 0 \qquad \text{Eq. 3.9}$$

Therefore, the eq. 3.5 becomes:

$$h_{gap}^3 - 2h_{eq}h_{gap}^2 + h_{eq}^2 h_{gap} - \frac{\varepsilon_0 A V_{sb}^2}{2k} = 0 \qquad \text{Eq. 3.10}$$

On deducing, we get the mathematical expression of snapback voltage (V_{sb}):

$$V_{sb} = \frac{h_m}{\varepsilon_r}\sqrt{\frac{2kh_{gap}}{\varepsilon_0 A}} \qquad \text{Eq. 3.11}$$

3.3.2 1-D dynamic analysis without acoustic loading

The dynamic behavior of the membrane is studied when an alternative voltage (V_{AC}) is added to the bias voltage (V_{DC}). Therefore, the total membrane displacement is written as the sum of static (u_{DC}) and dynamic (u_{AC}) displacements created by the bias and the alternative voltages respectively. Here, we focus on understanding the dynamic behavior of the membrane at the stable equilibrium position produced by V_{DC}. Besides, the mechanical losses have been deliberately ignored. Therefore, in harmonic regime, we have:

$$\begin{cases} V = V_{DC} + V_{AC} & = V_{DC} + \tilde{V}_{AC} e^{j\omega t} \\ u = u_{DC} + u_{AC} & = u_{DC} + \tilde{u}_{AC} e^{j\omega t} \end{cases} \qquad \text{Eq. 3.12}$$

Recalling the Newton's second law of motion,

$$m\frac{\partial^2 u_{AC}}{\partial t^2} = \overrightarrow{F_{elec}}(u_{AC}, V_{AC}) + \overrightarrow{F_{elast}}(u_{AC}) \qquad \text{Eq. 3.13}$$

where *m* is the mass of the membrane. To simplify, it is considered that the excitation voltage is much lower than the bias voltage, i.e. $V_{AC} \ll V_{DC}$. Hence, the associated dynamic displacement is considered to be lower than the static displacement, which makes $u_{AC} \ll u_{DC}$. With these assumptions, the electrostatic force (F_{elec}) is linearized from its equilibrium position (u_{DC}, V_{DC}) using first order Taylor expansion:

$$\overrightarrow{F_{elec}}(u,V) = \overrightarrow{F_{elec}}(u_{DC},V_{DC}) + \frac{\partial \overrightarrow{F_{elec}}(u_{DC},V_{DC})}{\partial u} u_{AC} + \frac{\partial \overrightarrow{F_{elec}}(u_{DC},V_{DC})}{\partial V} V_{AC} \qquad \text{Eq. 3.14}$$

The electrostatic force induced by the dynamic component of the system is expressed as:

$$\begin{aligned} \overrightarrow{F_{elec}}(u_{AC},V_{AC}) &= \overrightarrow{F_{elec}}(u,V) - \overrightarrow{F_{elec}}(u_{DC},V_{DC}) \\ &= \frac{\partial \overrightarrow{F_{elec}}(u_{DC},V_{DC})}{\partial u} u_{AC} + \frac{\partial \overrightarrow{F_{elec}}(u_{DC},V_{DC})}{\partial V} V_{AC} \end{aligned} \qquad \text{Eq. 3.15}$$

On differentiating, we obtain:

$$\overrightarrow{F_{elec}}(u_{AC},V_{AC}) = \frac{\varepsilon_0 A V_{DC}^2}{\left(h_{eq} - u_{DC}\right)^3} u_{AC} + \frac{\varepsilon_0 A V_{DC}}{\left(h_{eq} - u_{DC}\right)^2} V_{AC} \qquad \text{Eq. 3.16}$$

Subsequently, by considering the excitation voltage (V_{AC}) as a harmonic signal, we can obtain the displacement (u_{AC}), which is purely harmonic. On reformulating the fundamental relation of the dynamics (eq. 3.13), we get:

$$m\omega^2 \tilde{u}_{AC} = \left(k - \frac{\varepsilon_0 A V_{DC}^2}{\left(h_{eq} - u_{DC}\right)^3}\right) \tilde{u}_{AC} - \left(\frac{\varepsilon_0 A V_{DC}}{\left(h_{eq} - u_{DC}\right)^2}\right) \tilde{V}_{AC} \qquad \text{Eq. 3.17}$$

From the above equation, two new quantities can be extracted, the equivalent stiffness (k_{soft}) and the electroacoustic transformation coefficient (φ).

$$k_{soft} = \left(k - \frac{\varepsilon_0 A V_{DC}^2}{\left(h_{eq} - u_{DC}\right)^3}\right) \qquad \text{Eq. 3.18}$$

$$\varphi = \frac{\varepsilon_0 A V_{DC}}{\left(h_{eq} - u_{DC}\right)^2} \qquad \text{Eq. 3.19}$$

The equivalent stiffness term reduces on increasing the polarization voltage, which is also called as the "softening effect". This occurrence is purely due to mechanical and electrostatic coupling. On substituting eq. 3.18 and eq. 3.19 in eq. 3.17, the dynamic displacement $(\tilde{u}_{AC})$ as a function of the excitation voltage $(\tilde{V}_{AC})$ can be derived.

$$\tilde{u}_{AC} = \frac{\varphi}{m\omega^2 - k_{soft}} \tilde{V}_{AC} \qquad \text{Eq. 3.20}$$

With the obtained dynamic displacement, one can derive several electrical quantities. Firstly, the dynamic charge $Q(u_{AC}, V_{AC})$ of the capacitor can be expressed as a function of the electroacoustic transformation coefficient (φ) and the static capacitance (C_0) obtained at the equilibrium position (u).

$$Q(u_{AC}, V_{AC}) = \varphi u_{AC} + C_0 V_{AC} \qquad \text{Eq. 3.21}$$

The electrical current $(\tilde{I})$ in harmonic regime at the electrode terminal derives from expression of the charge, given as:

$$\tilde{I} = j\omega\left(\varphi\tilde{u}_{AC} + C_0\tilde{V}_{AC}\right) \qquad \text{Eq. 3.22}$$

The electrical admittance (Y_{elec}) of the system with the obtained current $(\tilde{I})$ is expressed as:

$$Y_{elec} = j\omega\left(C_0 - \frac{\varphi^2}{m\omega^2 - k_{soft}}\right) = j\omega C(\omega) \qquad \text{Eq. 3.23}$$

$C(\omega)$ represents the equivalent capacitance of the CMUT, which takes charge accumulation from electrostatic effects and mechanical vibrations into account. From the expression of electrical admittance, one could define two electrical resonances: the resonance frequency (f_r) and the anti-resonance frequency (f_a), as shown in figure 3.13. The resonance frequency of the system corresponds to the frequency at which the electrical admittance tends toward infinity i.e. when input voltage $(\tilde{V})$ is zero.

$$f_r = \frac{1}{2\pi}\sqrt{\frac{k_{soft}}{m}} = \frac{1}{2\pi}\sqrt{\frac{k - \frac{\varepsilon_0 A V_{DC}^2}{\left(h_{eq} - u_{DC}\right)^3}}{m}} \qquad \text{Eq. 3.24}$$

In case of anti-resonance frequency, the electrical impedance tends toward infinity (when the input current ($\tilde{I}$) is zero).

$$f_a = \frac{1}{2\pi}\sqrt{\frac{k}{m}} \qquad \text{Eq. 3.25}$$

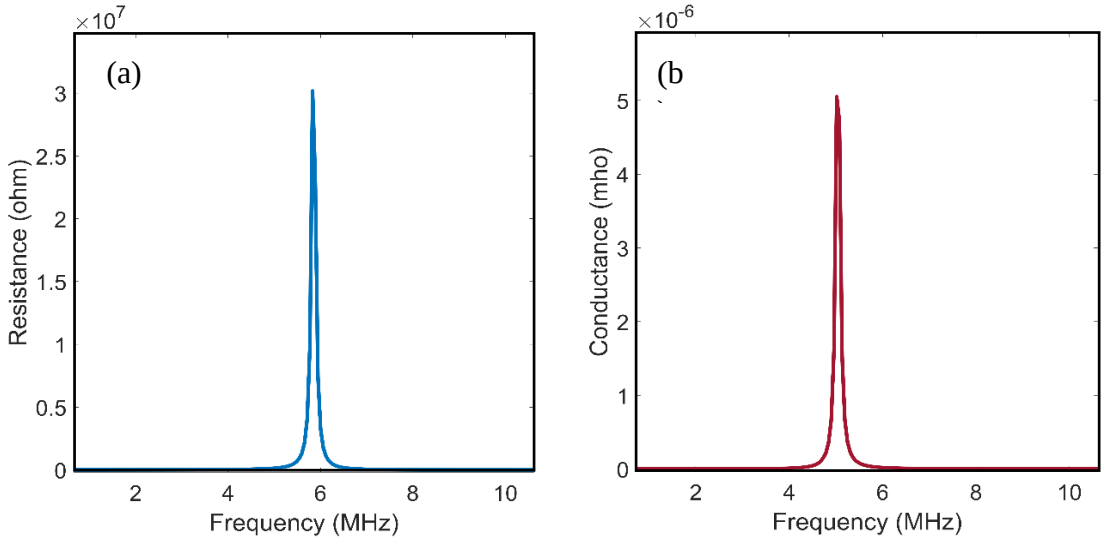


Figure 3.13: Simulated response of single CMUT cell (a) real part of the electrical impedance – the peak corresponds to the anti-resonance frequency (f_a). (b) Real part of the electrical admittance – the peak corresponds to the mechanical resonance frequency (f_r). Simulation parameters are those given in table 3.1.

To mention, the "softening effect" directly influences the resonance frequency of the system. However, in most cases, the CMUT membranes are uneven because of the non-negligible curvature (especially in sealed CMUTs), where f_a also depends on applied bias voltage (refer figure 3.14).

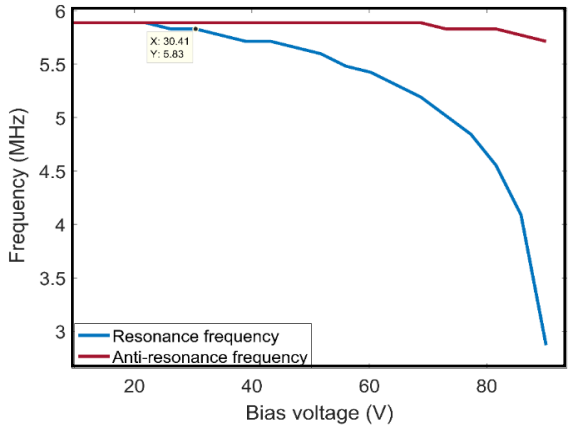


Figure 3.14: Evolution of the electrical resonance frequency (blue curve) and the anti-resonance frequency (marron curve) for the applied bias voltages. Simulation parameters are those given in table 3.1.

Then, the two other quantities of the system are high frequency (C_{HF}) and low frequency (C_{LF}) capacitances. These quantities limit the system behaviors, where C_{HF} corresponds to clamped capacitance and it tends towards static system capacitance (C_0), as said in eq. 3.26. The C_{LF} corresponds to the free vibration of the system, which is increased by the term φ^2/k_{soft}. This is represented in eq. 3.27. The simulated curves for these capacitances with respect to frequency component and bias voltage are displayed in figure 3.15.

$$C_{HF} = \lim_{\omega \to \infty} C(\omega) = C_0 = \frac{\varepsilon_0 A}{(h_{eq} - u_{DC})} \qquad \text{Eq. 3.26}$$

$$C_{LF} = \lim_{\omega \to \infty} C(\omega) = C_0 + \frac{\varphi^2}{k_{soft}} = \frac{\varepsilon_0 A}{(h_{eq} - 3u_{DC})} \qquad \text{Eq. 3.27}$$

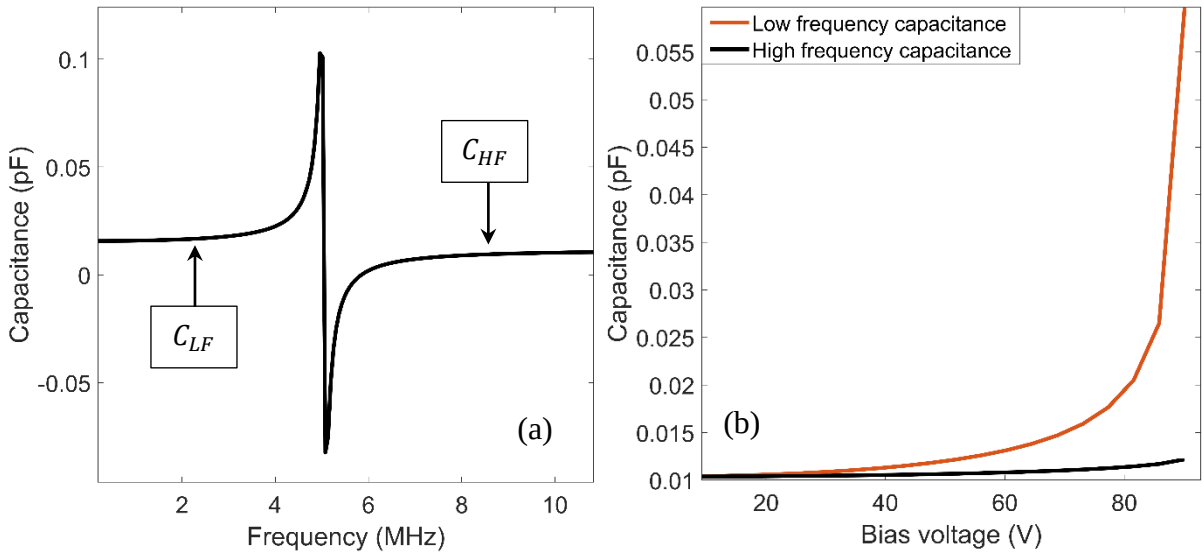


Figure 3.15: Simulated response of single CMUT cell with (a) its equivalent capacitance, where C_{HF} is observed after the resonance and C_{LF} at low frequency before resonance mode. (b) Evolution of the C_{HF} (black curve) and C_{LF} (orange curve) with respect to V_{DC}. Simulation parameters are those given in table 3.1.

Lastly, the electromechanical coupling coefficient (k_t) can also be determined. k_t is the ratio between mechanical energy to the total energy of the system, which is given as:

$$k_t^2 = \frac{mechanical\ energy}{mechanical\ energy + electrical\ energy} \qquad \text{Eq. 3.28}$$

k_t can be expressed in different ways; the commonly used one is with respect to resonance and anti-resonance frequencies or as a function of high frequency capacitance and low frequency capacitance.

The corresponding expression and the simulated figure are given in eq. 3.29 and figure 3.16.

$$k_t^2 = 1 - \left(\frac{f_r}{f_a}\right)^2 = 1 - \frac{C_{HF}}{C_{BF}} \qquad \text{Eq. 3.29}$$

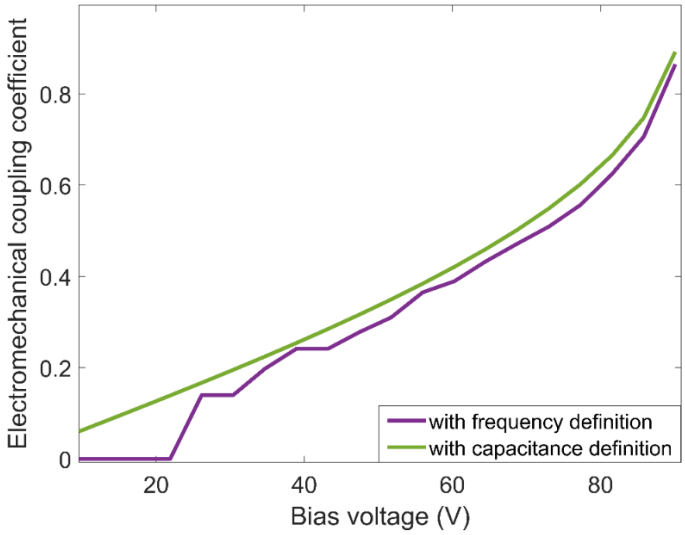


Figure 3.16: Evolution of the electromechanical coupling coefficient with respect to applied bias voltage for the values obtained from frequency definition (green curve) and with the capacitance definition (violet curve). Simulation parameters are those given in table 3.1.

From figure 3.16, both the curves are almost similar where the small discrepancy comes from the frequency resolution chosen for computing the electrical impedance curves.

3.3.3 Dynamic analysis in gas medium and CMUTs design

With 1-D analysis, only a single CMUT cell has been considered, whereas in reality we have the whole population of CMUT cells, as shown in figure 3.8. Therefore, the eq. 3.13 is reformulated on considering the radiated energy in the fluid:

$$m\omega^2 u_{AC} = \overrightarrow{F_{elec}}(u_{AC}, V_{AC}) + \overrightarrow{F_{elast}}(u_{AC}) + \overrightarrow{F_{rad}}(u_{AC}) \qquad \text{Eq. 3.30}$$

The radiation force $F_{rad}(u_{AC})$, writes as:

$$F_{rad} = Z_{rad} * \frac{\partial u_{AC}}{\partial t} \quad \text{Eq. 3.31}$$

where Z_{rad} is the radiation impedance of the CMUT, expressed as:

$$Z_{rad} = R_{rad} + iX_{rad} \quad \text{Eq. 3.32}$$

R_{rad} and X_{rad} are radiation resistance and reactance respectively. Z_{rad} changes at different rates depending on the acoustic medium properties and how the CMUTs are distributed over the surface of the transducer. In our case, the size of each transmitter is large enough (with population of CMUTs/emitter), hence, we could reasonably neglect the acoustic edge effects, and thus assume that the CMUTs are distributed periodically along the *x* and *y* axes, as shown in figure 3.7. As an illustration, figure 3.17 shows the radiation impedance of air-loaded CMUTs for square membrane (32x32 µm²) with 2D periodic distribution. Simulation results were obtained from models developed in the framework of A. Boulmé's PhD. The d_x and d_y pitch values are 38 µm and 6 µm respectively.

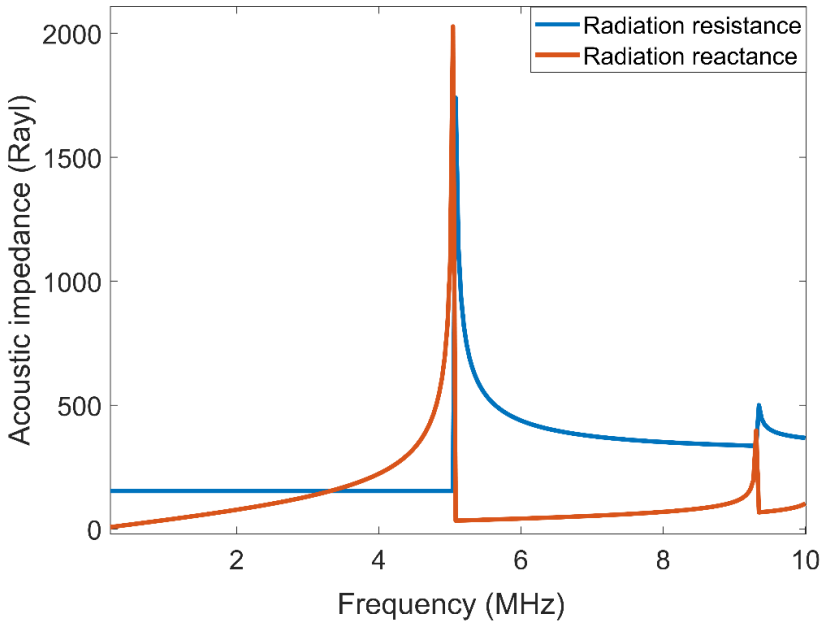


Figure 3.17: Computed acoustic radiation impedance of a CMUT with 2D periodic boundary conditions for 32x32 µm² membrane size. Simulation parameters are those given in table 3.1.

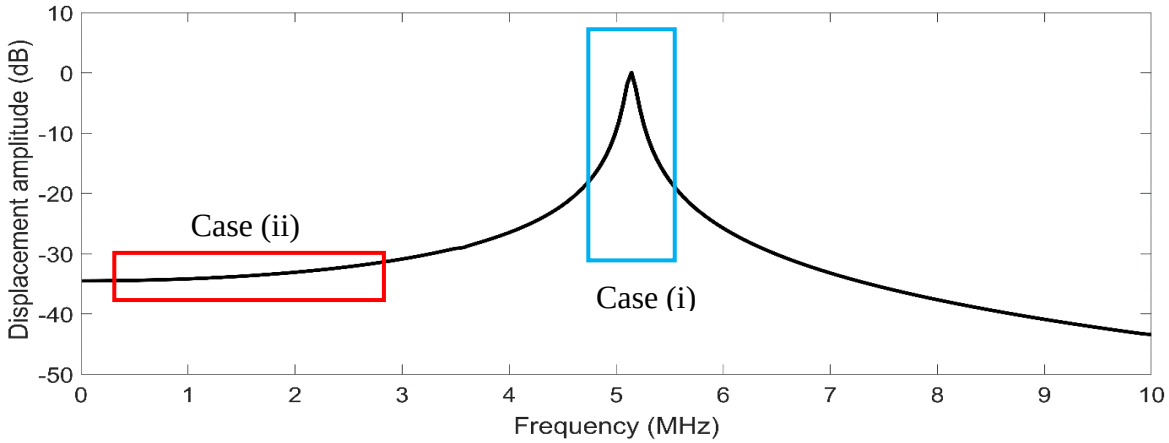


Figure 3.18: Computed frequency response of the spatial mean dynamic displacement of single CMUT cell. The mechanical resonance is close to 5 MHz. From very low frequency up to 3 MHz, the CMUT shows a flat response, with amplitude value 30 dB lower than the resonance peak.

Figure 3.18 shows the corresponding dynamic displacement of the CMUT, where the mechanical resonance is clearly observed because of very low air acoustic impedance (300 Rayl). It is worth to mention, the radiation impedance also remains low in gas media, thereby the CMUT behavior is similar with the one in air and shows a "high quality factor" at the resonance. Note, for water-loading conditions, the CMUT is strongly damped and shows very low quality factor.

From the frequency response of the CMUT given in figure 3.18, two working conditions can be considered. The first, is the resonance mode behavior (case (i), method III), which is used to detect variations of the acoustic impedance. And for the ToF method (case (ii), method IV), the CMUT works at the low frequency band (usually from 0.5 MHz to 3 MHz), showing a flat frequency response (typically a broad bandwidth response). Of course, in this frequency range, the transducer sensitivity is not optimized but it is suitable enough for our application.

For the resonance mode detection, the value of the resonance frequency is the sole design parameter of the CMUT. In our case, there is no requirement for the resonance frequency value. We just need to verify that the shift in resonance frequency is large enough to be measured, when gas properties are modified. As an illustration, in figure 3.19, the computed results of electrical admittance for varying gas concentration is exhibited. From this, it is obvious that the CMUT has the ability to detect change in very low concentration of hydrogen (H_2), i.e. below explosion limit, and there is a clear shift of f_r, greater than 100 Hz for 0 to 5 % of H_2 in nitrogen (N_2).

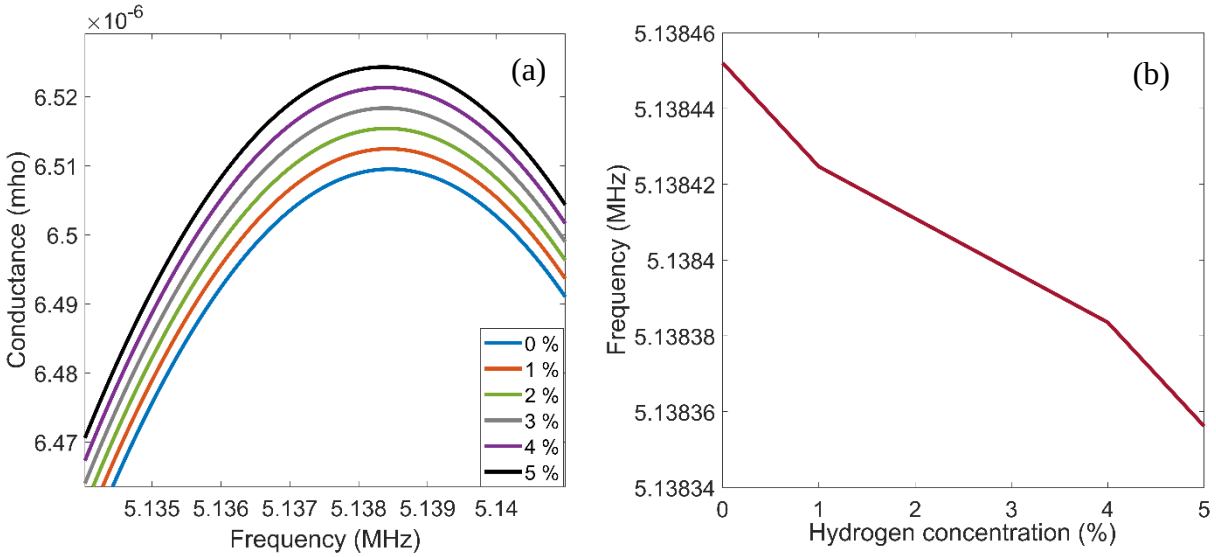


Figure 3.19: Simulated electrical admittance (Y_{elec}) in gas environment (a) evolution of conductance (real part of Y_{elec}) with respect to H_2 concentration and (b) shift in resonance frequency for varying concentration of H_2 in N_2.

For the ToF detection method, the CMUT has to be designed in order to optimize the radiated acoustic intensity (I_a). I_a writes:

$$I_a = \frac{1}{2} R_{rad} (v_0)^2 \qquad \text{Eq. 3.33}$$

where R_a is the radiation impedance (real part) and v_0 is the spatial mean acoustic velocity of the membrane. It is linked to the spatial mean dynamic displacement of the membrane, which can be approximated by $u_0/3$, where u_0 is the displacement taken at the center of the membrane. This factor is required since the membrane displacement is non-uniform [44], [48], this value was assessed from previous works of N. Sénégond.

One has:

$$I_a = \frac{1}{2} R_{rad} (v_0)^2 = \frac{1}{2} R_{rad} \left(2\pi f_0 \frac{u_0}{3}\right)^2 \qquad \text{Eq. 3.34}$$

where f_0 is the ultrasonic wave frequency.

To assess a value for the displacement amplitude, u_0, at the CMUT center, one considers the membrane is able to sweep the whole gap and reaches $h_{gap}/2$, if the membrane does not suffer from an initial deflection (see figure 3.20).

If the initial deflection (u_i) of the membrane caused by the atmospheric pressure is considered, then u_0 is written as:

$$u_0 = \frac{1}{2}(h_{gap} - u_i) \qquad \text{Eq. 2.34}$$

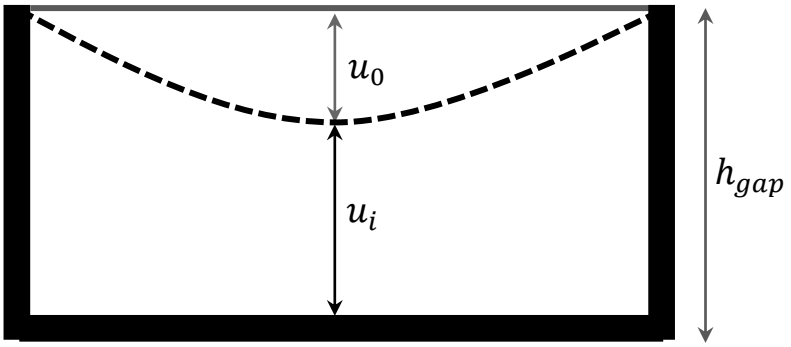


Figure 3.20: Initial displacement of the single CMUT membrane.

Therefore, to optimize the radiated acoustic intensity, one can either minimize the initial deflection (see figure 3.11) or increase the radiation impedance by increasing active surface ratio. On the basis of the theoretical design parameters mentioned in table 3.1, the output acoustic intensity was computed (at 1 MHz) for square CMUT membranes, with the spatial distribution shown in figure 3.7, for varying widths of CMUTs ranging from 10x10 µm² to 80x80 µm². Here, the active surface ratio of the CMUT cell is estimated using the expression $w^2/(w+d_x)(w+d_y)$ (see figure 3.7). Then, three gap values are used for simulation, namely, 400 nm, 300 nm and 250 nm. In which, 400 nm corresponds to a situation where the initial deflection is caused by the atmospheric pressure only. The two other cases consider a deflection occurring due to residual mechanical stresses in the membrane, in addition to the atmospheric pressure [4]. The gap value of 300 nm and 250 nm are simulated respecting the chosen membrane sizes.

The computed results for chosen gap values are shown in figure 3.21. From the graph, it is clear that the output acoustic intensity reaches a maximum for a given range of membrane sizes. As we know, smaller the membrane, lower the initial deflection and active surface ratio. Conversely, larger membrane favors higher active surface ratio at the expense of initial deflection (i.e. lower gap height). When the gap height decreases, the optimum size range slightly shifts to lower values. In order to anticipate the deflection caused by mechanical stresses, the gap height was considered as 250 nm. Based on these considerations, the CMUTs with square membrane configurations were chosen for fabrication. They are 27x27 µm, 32x32

µm and 37x37 µm respectively. These dimensions are chosen with respect to maximum output intensity, as shown in figure 3.21.

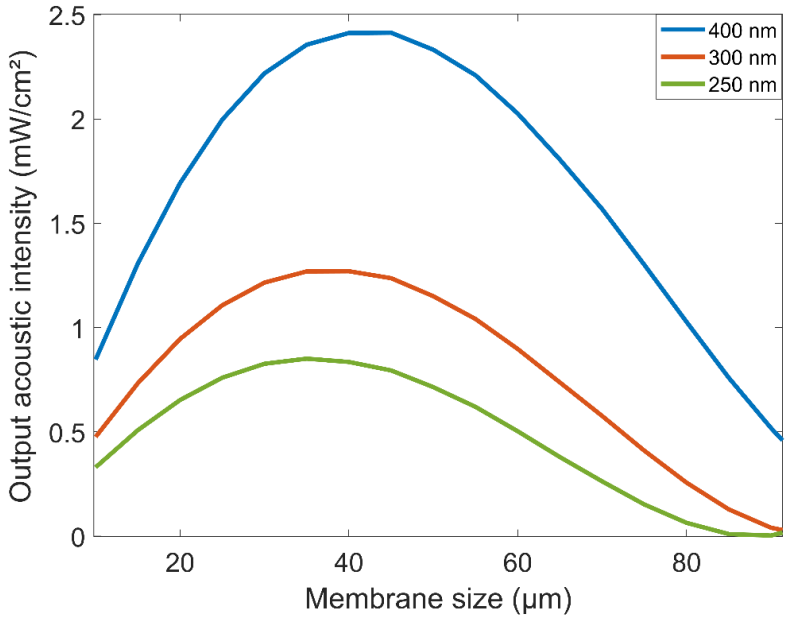


Figure 3.21: Computed acoustic intensity radiated in air for square CMUTs ranging from 10x10 µm² to 80x80 µm² membrane sizes. The curve with 250 nm assumes that the membrane was initially deflected with 150 nm deformation. Simulation parameters are those given in table 3.1.

Moreover, for exploratory purposes, rectangular CMUT with size of 32x27 µm² and 37x27 µm² were designed. To mention, these configurations were designed in the framework of A. Boulmé PhD, but for water-loading conditions. For air-loading conditions, the results are the same, since fluid acoustic impedance has no effect on the chosen CMUT sizes.

3.4 Fabrication and packaging of CMUTs

The capacitive micromachined ultrasonic transducers used for gas mixture analysis were originally developed for medical imaging and therapeutic purposes [43], [45], as explained in §3.1.2. These CMUTs were fabricated using standard surface micromachining technique, which was widely used by various groups over the last two decades [10], [14], [18], [19], [34], [49]. The main difference lies in the choice of materials, deposition techniques, shapes and dimensions of CMUTs that have been developed by our groups over two decades, which are disclosed in these references [20], [37], [38], [50], [51]. As explained earlier, the process used the results from the PhD of B. Belgacem [37], E. Jeanne [52] and S. Ngo [53].

The process flow is briefly shown in figure 3.22. An insulating layer (1.2 µm) of silicon dioxide is formed by thermal oxidation between the substrate and the bottom electrode in the first step of the process. Then, the bottom electrode is deposited using low-pressure chemical vapor deposition (LPCVD), i.e. 450 nm of heavily doped polysilicon (Poly-Si). After, deposition of sacrificial layer, i.e. 400 nm of phospho silicate glass (PSG), which determines the height of the CMUT cavity. This sacrificial layer has to be chosen with great care because it must have good uniformity and strong etching selectivity.

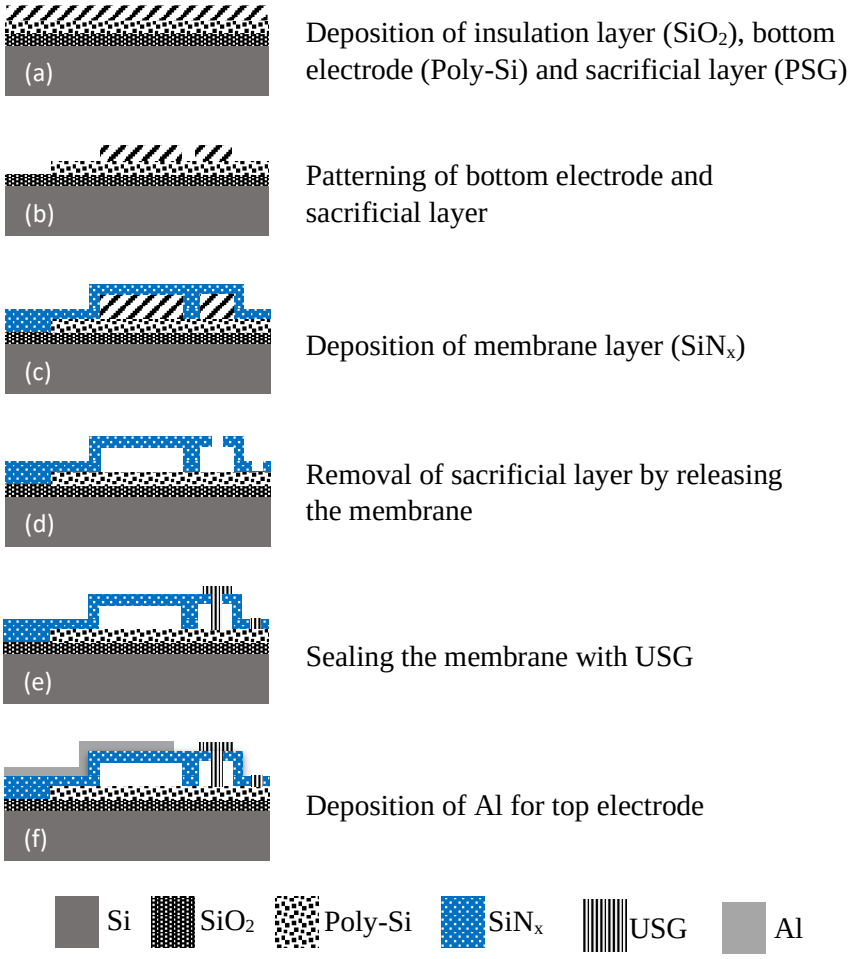


Figure 3.22: Process flow of surface micromachined CMUTs.

Step 2 comprises two photolithographic stages, one for patterning the sacrificial layer to define the membrane geometry and the other is to pattern the bottom electrode. Further, step 3 involves deposition of 400 nm of silicon nitride layer for CMUT membrane by LPCVD. In step 4, the membranes are released eventually by evacuating PSG by a chemical attack of buffered hydrofluoric acid. Then, the CMUT cavities are sealed using undoped silicon glass (USG) of 1.5 µm in step 5. Lastly, aluminum of 450 nm-thick is sputtered and patterned, which acts as

the top electrode. All fabricated CMUTs have the same metal compositions, gap height except membrane geometries.

After fabrication, the CMUT chips were diced to form an array of eight elements (refer figure 3.23.a). Next, they were packaged using specially designed printed circuit boards (PCBs). Then, the chips were glued on the PCBs using insulating epoxy adhesive (ALBEBOND 84-3J by Henkel). Later kept in the laboratory over an hour at 150 °C. Electrical connection between PCB and the chips was realized using wire-bonding technique, performed with aluminum wire of 25 µm diameter using K&S 4523AD manual wedge bonder. Next, the wires were encapsulated using epoxy NoSWEEP from Polysciences and kept in a laboratory oven for 2 hours at 165 °C to harden the resin (see figure 3.23.b). Finally, UFL connectors were soldered on the rear side of the PCB to facilitate the electrical connections for further characterizations, as shown in figure 3.23.c.

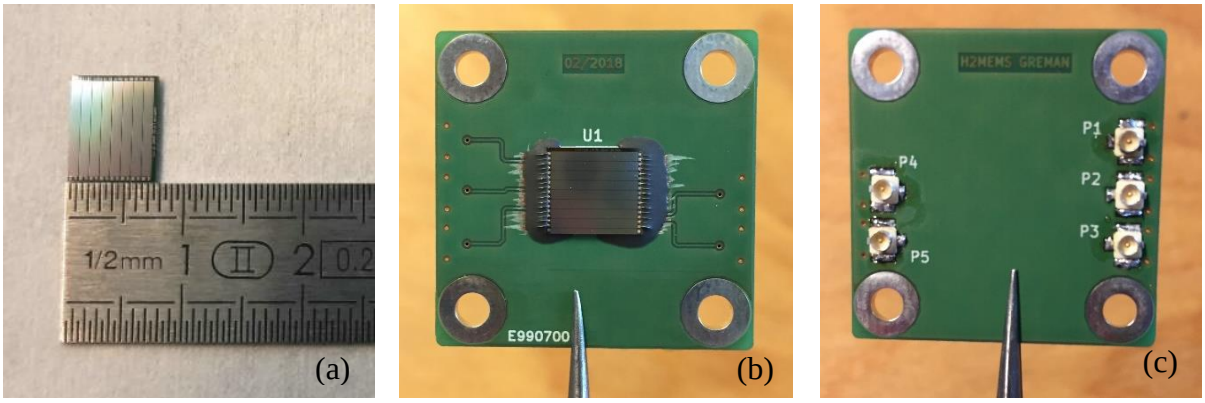


Figure 3.23: a) CMUT chip with an array of eight elements, b) front face of the fully functional prototype and (c) rear face with UFL connections.

The CMUT chips are made of eight available elements. For the ToF detection method, it was decided to electrically connect two elements in parallel to form an ultrasonic mono-element transducer. These emitter/receiver prototypes are of dimension 1.6x8 mm², consisting of approximately 2500 CMUTs per transducer. Among the eight elements, 6 are dedicated to ToF measurements. Then, the two others are connected individually and used for the resonance frequency detection method.

3.5 Characterizations of fabricated CMUTs

The CMUTs characterization is an important step, in order to verify the device functionalities and to derive their electromechanical properties. In general, there are several techniques used to characterize the device, such as laser Doppler vibrometry (LDV), impedancemetry, digital holography microscope (DHM), scanning electron microscopy (SEM), etc. In this section, both optical and electrical measurements are reported. Firstly, DHM measurements were carried out to understand the membrane behaviors at the cell scale. Afterwards, electrical impedance measurements were made to determine the electromechanical parameters of each element. Moreover, derived parameters such as collapse voltage and resonance peak position are used in resonance mode detection.

3.5.1 Digital holographic microscopy (DHM) measurements

DHM by LyncéeTec® records the time sequence of 3D topographies of the CMUT cells for a given excitation. The 3D images are generated by the principle of holography. This particular characterization tool is very interesting because it reconstructs the hologram using phase and intensity images for both in-plane and out-of-plane displacements.

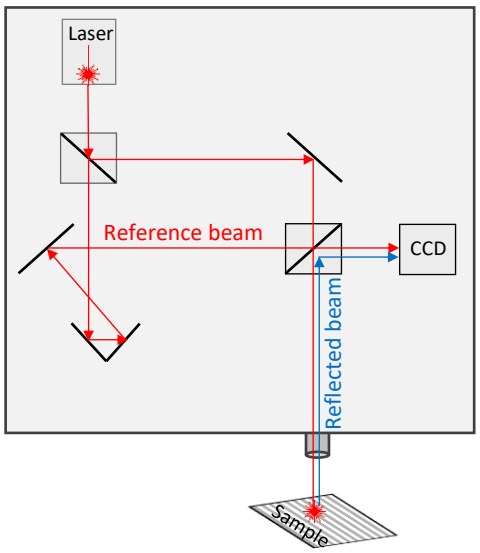


Figure 3.24: Principle of digital holographic microscopy.

To extract and construct the out-of-plane displacements, the interferometer needs a good reflectivity. Thanks to DHM's interferometric nature, the hologram produced by the interference wave front from the object with the reference wave is digitally recorded by the CCD camera (refer figure 3.24). Later, they are processed numerically with the sub-nanometer vertical resolutions [54]. This static measurement technique is insensitive to external vibration and has short acquisition time.

DHM characterization helps to extract various important parameters, such as initial displacement (at 0V) and membrane behavior/deflection for range of applied voltages. With these data, parameters like collapse voltage, snapback voltage and device homogeneity can be determined, on comparing with population of CMUT cells for each membrane geometry. As explained in §3.3.1 (see figure 3.11), the membrane curvature (i.e. initial displacement) caused during sealing the CMUTs due to atmospheric pressure and residual material stresses were non-negligible but an important parameter to be examined. This can be observed for all prototypes, to verify the device functionality, where the gap height should be greater than zero for any functional CMUTs (i.e. $h_{gap} > 0$).

To perform experiments, the element of interest is connected via UFL cable from the PCB to the source, as shown in figure 3.25.a. A MATLAB program developed by GREMAN is used to control the DC bias (MOTECH 0-250 V), which is connected through GPIB cable. The program also synchronizes the acquired data from DHM to their corresponding polarization voltages.

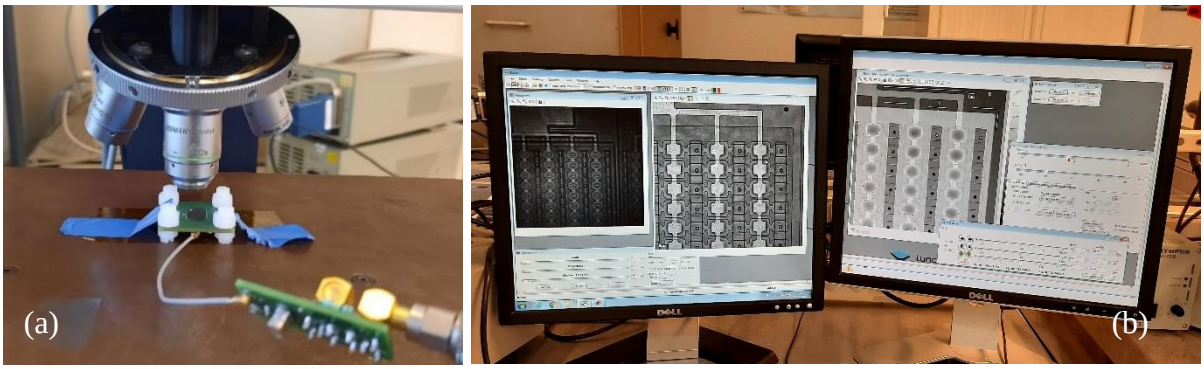


Figure 3.25: (a) Prototype placed under DHM (objective x20) which is physically connected to DC bias via UFL-UFL cable. (b) PC with active Koala software showing the generated hologram with the phase and intensity graphs for the connected CMUT element.

To characterize each prototype, a voltage cycle is applied from zero to maximum and vice versa. Later, with the acquired information, the output signal is reconstructed using the post-processing software (Koala).

CMUTs with different membrane sizes were characterized and their corresponding results are discussed below. Firstly, the static displacement evolution of a single CMUT cell is shown for arbitrarily chosen membrane geometry, here 32x32 µm². The corresponding results displaying initial displacement (at 0 V), collapse voltage (at V_c) and other membrane positions at various percentages of V_c are shown in figure 3.26.a. Based on the graph, it is clear that the membrane collapses when it reaches the bottom electrode where the capacitance is maximum. It also demonstrates that the membrane deflection is always towards the bottom for increasing bias voltage, thereby reducing the gap height until zero, i.e. $h_{gap} = 0$. Figure 3.26.b shows the classic collapse-snapback hysteresis curve for the range of applied voltages, which is 0-75 V in this case. To mention, the snapback always occurs after the collapse event, in the descending voltage cycle.

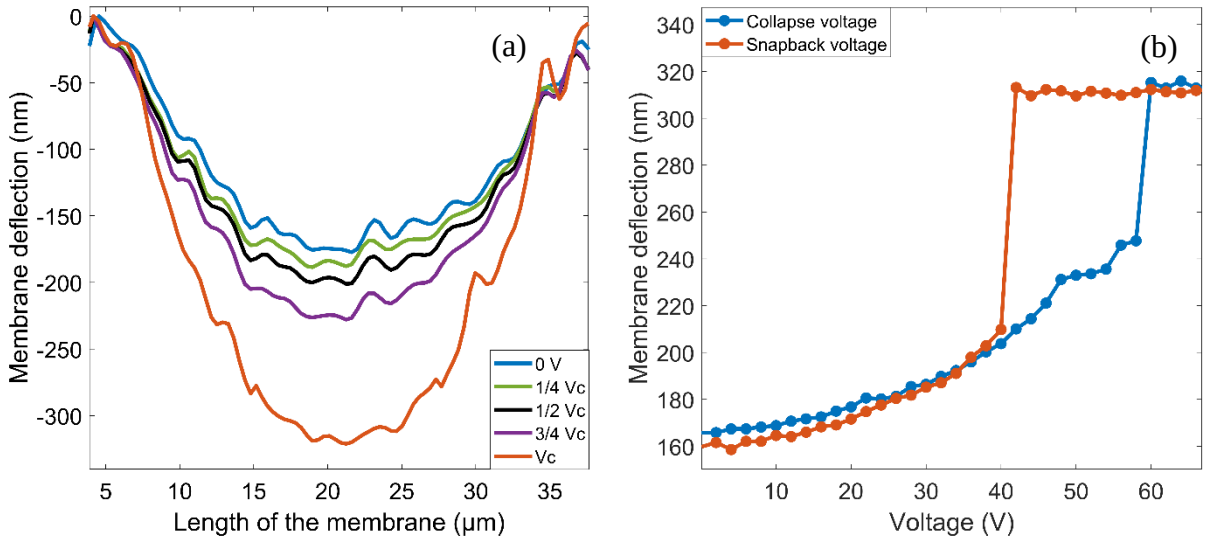


Figure 3.26: Experimental result of static membrane displacement of a single CMUT cell for varying percentages of collapse voltage for 32x32 µm² membrane geometry and (b) collapse-snapback hysteresis curve for the same.

In addition, the observed displacements at the extremities (at initial and at collapse positions) for various CMUT geometries are tabulated in table 3.3. These values give the idea about membrane sweeping. As an example, the biggest (37x37 µm²) and the smallest (27x27 µm²) of all membranes are compared at their extremities, shown in figure 3.27.

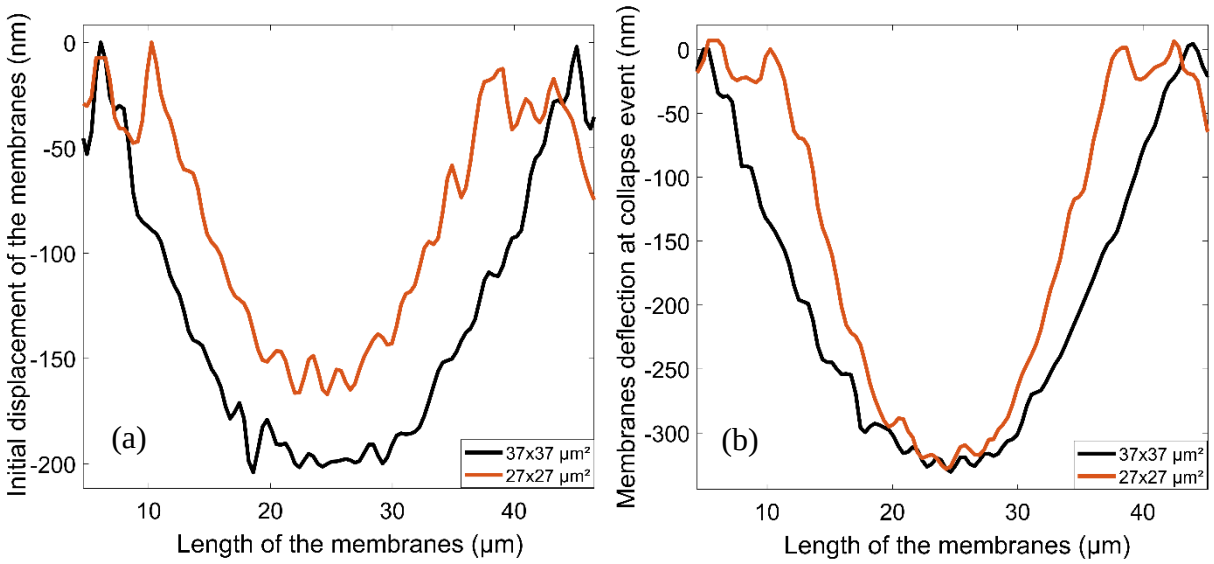


Figure 3.27: (a) Membrane deflection without polarization for the smallest (27x27 µm²) and largest (37x37 µm²) membrane geometries and (b) membrane deflection at collapse event of the same.

The figure 3.27.a, proves the statement mentioned in CMUT design (§3.3.3) that smaller the CMUT structure (27x27 µm²), lower the initial deflection and the active surface ratio and vice versa (37x37 µm²).

Table 3.3: Experimental values of static displacement for different sizes of membranes measured using DHM.

Parameters	**Values**				
Membrane geometry	37x37 µm²	37x27 µm²	32x32 µm²	32x27 µm²	27x27 µm²
Collapse voltage (V_c)	44 V	80 V	60 V	78 V	92 V
Initial deflection (at 0 V)	200 nm	165 nm	175 nm	140 nm	150 nm
Total amplitude swept by the membrane	125 nm	160 nm	150 nm	185 nm	175 nm
Membrane deflection at collapse	325 nm	325 nm	325 nm	325 nm	325 nm

3.5.2 Electrical impedance measurements

The electrical impedance measurements were performed to analyze the element level functionalities of the fabricated CMUTs. These measurements made it possible to extract most of their electrical and mechanical properties that play a vital role in the device operations. The experimental protocol has been developed within our laboratory and it was well explained in previous studies [36]. To perform characterizations, the CMUTs are connected to the 4294A1 probe through HP4294A precision impedance analyzer (by Keysight Technology-40 Hz to 110 MHz). Then, the analyzer reference signal is combined with the bias voltage by a RC-type decoupling circuit. Next, the bias voltage (0-250 V) is sourced and controlled by MOTECH DC power supply, which is connected to the decoupling circuit, as shown in figure 3.28.

Later, the CMUT prototype was enclosed in an EMC cage (electromagnetic compatibility) to protect the signal acquisition from external electromagnetic pollution. These measurements are conducted in air, without any acoustic coupling. Note that for detection based on resonance frequency monitoring, the protocol is the same except CMUT is loaded with the gas of interest.

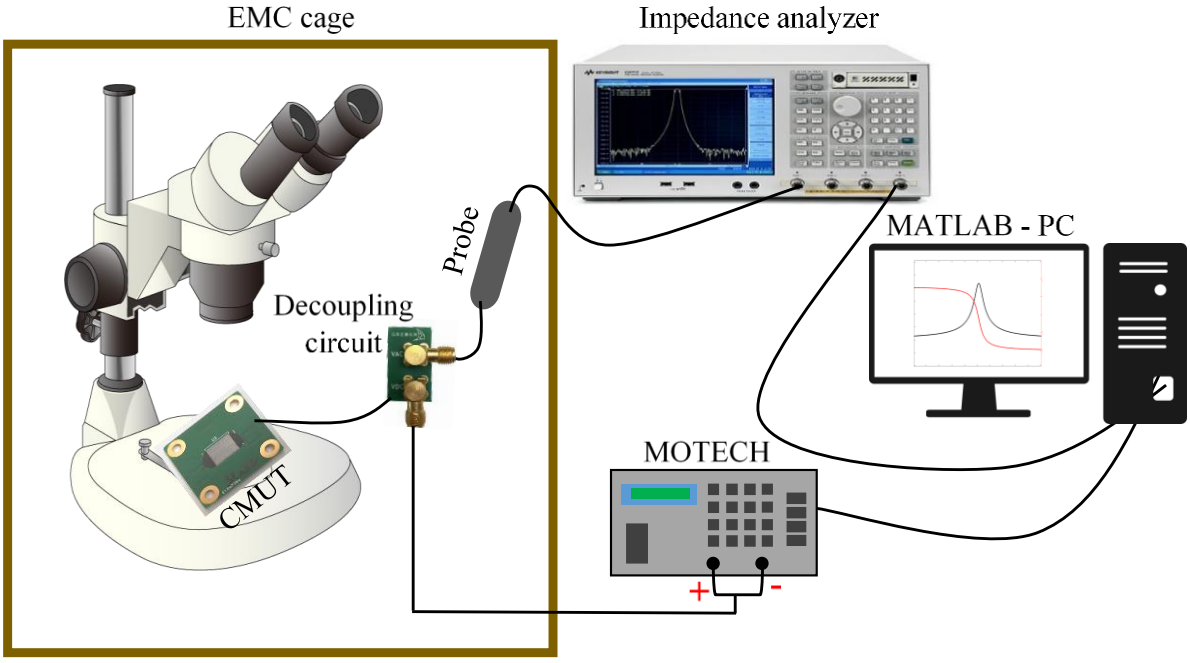


Figure 3.28: Experimental setup of electrical impedance measurement in air.

The measurements carried out for varying bias voltages from zero to maximum and vice versa, similar to the DHM measurements. A calibration procedure is executed before beginning the measurement with open, short and load (50 Ω) circuits. The V_{DC} sweeps automatically for a given set of values with the help of a developed MATLAB program. Here, the bias voltage is applied from 0 to 100 V with pitch of 2 V for the wide frequency range, i.e. 100 kHz-20 MHz, to complete preliminary characterization. With the obtained electrical impedance data as function of bias voltages and frequencies, one can extract their various electromechanical parameters, like:

- Resistance (R) and conductance (G) – the real part of electrical impedance and admittance from which anti-resonance frequency (f_a) and resonance frequency (f_r) are derived;
- Reactance (X) and susceptance (B) – the imaginary part of electrical impedance and admittance;
- Low frequency capacitance (C_{LF}) and high frequency capacitance (C_{HF});
- Electromechanical coupling coefficient (k_t) either by frequency definition or by capacitance definition.

In order to illustrate the proposed experimental protocol described above, one of the prototypes with 32x32 µm² geometry is arbitrarily chosen. Their results are exhibited in figure 3.29.

From figures 3.29.a and 3.29.b, the resonance and anti-resonance peaks for varying percent of collapse voltage are plotted. Here the f_r and f_a values vary with respect to polarization voltages due to the softening effect as explained in §3.3.2. In addition, the device homogeneity is exposed with the single resonance peak for each value of applied voltage, in both electrical impedance and admittance curves. Moreover, the figures 3.29.c and 3.29.d show the relevance in the measured responses with the simulation results specified in figures 3.14 and 3.15.b respectively.

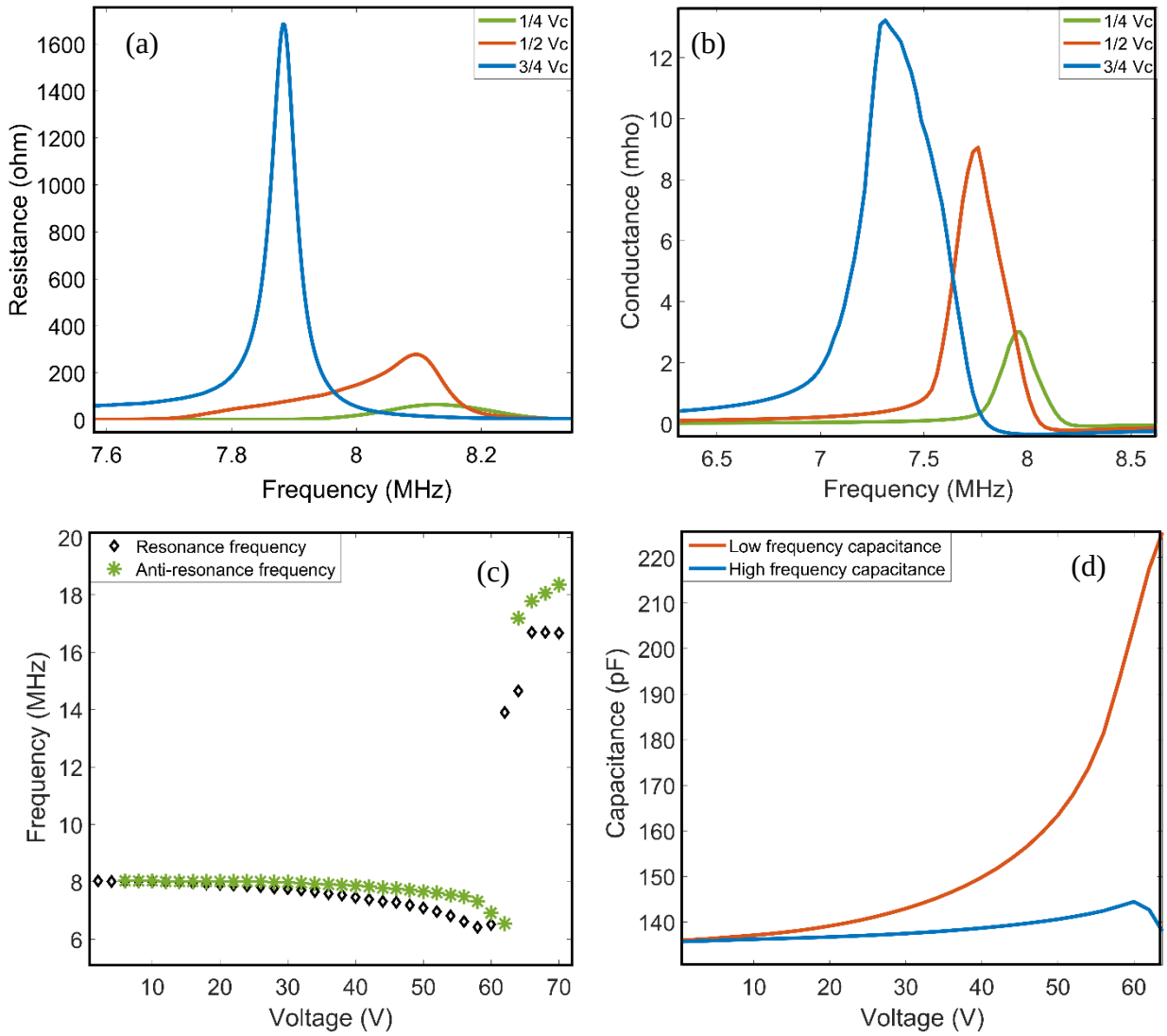


Figure 3.29: Measured electrical impedance of 32x32 µm² membrane geometry (a) real part of the impedance curve at three percentages of collapse voltages and (b) similarly, the real part of the admittance curve. (c) Variation of resonance and anti-resonance frequencies with respect to bias voltages and (d) likewise the variation of low and high frequency capacitances for applied voltages.

Figure 3.30 shows the experimental results corresponding to the range of CMUTs fabricated with various membrane geometries. The CMUT performances at bias voltage, i.e. 80% V_c are tabulated in table 3.4. From the displayed results, it is clear that the prototype with 32x32 µm² is best suited for resonance mode detection method, as it possesses higher quality factor (refer table 3.4) and better device homogeneity compared to others. It is worth mentioning an additional mode just before the fundamental resonance (see figure 3.30.a). It occurs probably due to partial metallization of membrane, i.e. 50% in our case. Additionally, the electrode's misalignment, or not being well-centered to the membrane, could also probably lead to this

degeneracy. Therefore, this can be solved in future by using 100 % metallization ratio of top electrode to the membrane layer.

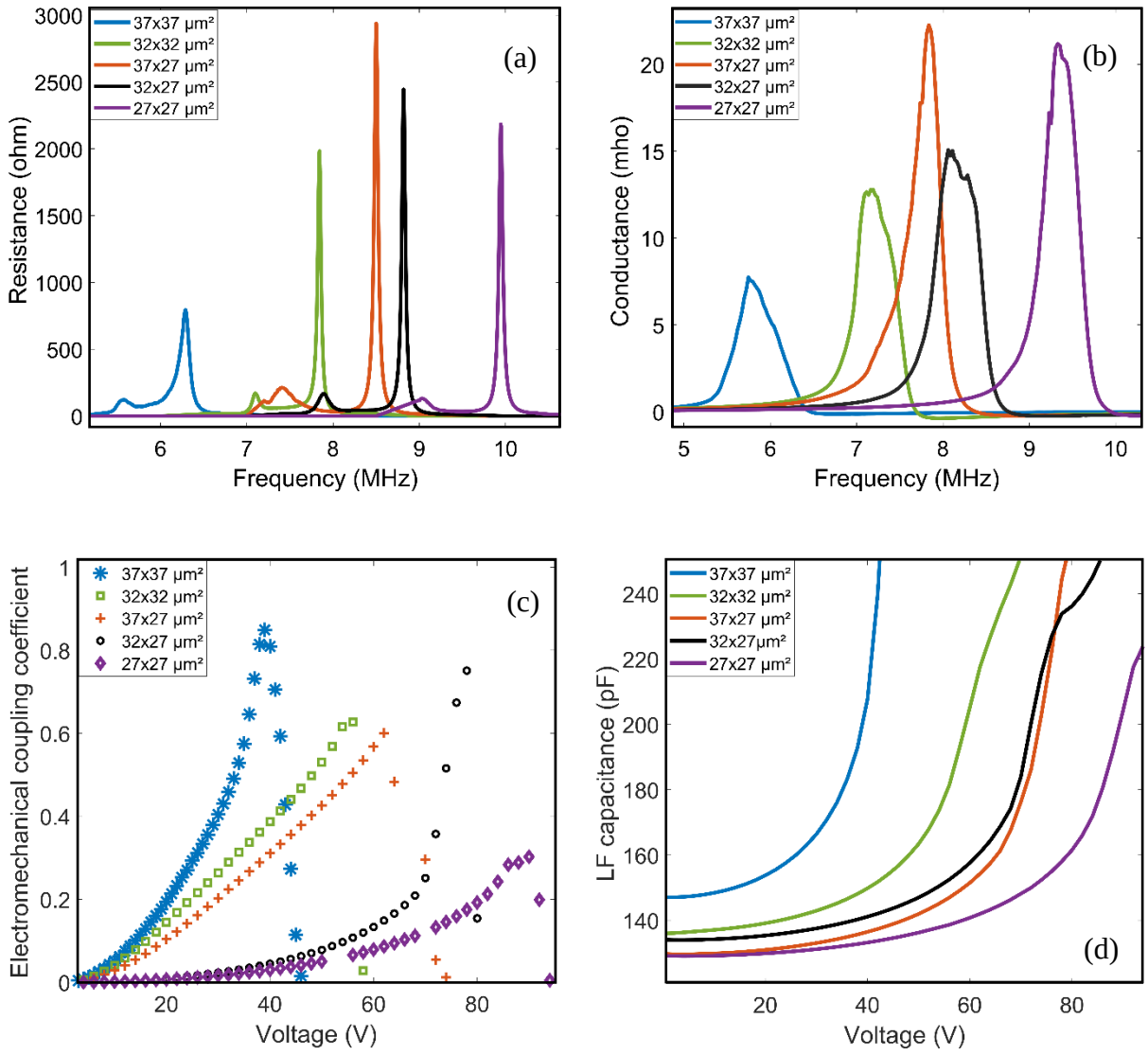


Figure 3.30: Experimental results for extracted electromechanical parameters of all fabricated membrane geometries in air through electrical impedance measurements. (a) Presents the real part of the impedances (i.e. anti-resonance frequencies) at their 80 % of collapse voltages and (b) exhibits the real part of the admittances (i.e. resonance frequencies) at their 80 % of collapse voltage. (c) Evolution of electromechanical coupling coefficient over applied range of bias voltages and (d) variation of low frequency capacitances with respect to applied bias voltages.

Table 3.4: The extracted electromechanical parameters from impedance measurements.

Parameters	**Values**				
Membrane size	37x37 µm²	37x27 µm²	32x32 µm²	32x27 µm²	27x27 µm²
Collapse voltage (V_c)	44 V	80 V	60 V	78 V	92 V
Resonance frequency at 80% of (V_c)	5.7 MHz	7.8 MHz	7.2 MHz	8.2 MHz	9.3 MHz
Electromechanical coupling coefficient at 80% of (V_c)	0.84	0.6	0.62	0.75	0.3
Quality factor (Q_G)	19	20	34	18	27
LF capacitance at (V_c)	294 pF	258 pF	205 pF	234 pF	218 pF
Active surface ratio	45 %	42 %	40 %	39 %	36 %

3.6 Electroacoustic characterizations of CMUTs in air

The ultrasound time of flight measurements were initially performed in air before testing in gas environments. These experimentations have been carried out in such a way that each aspect of device functionalities are considered. High attention was paid to retain the transducer with better sensitivity and faster response time, to make it more suitable for the targeted application. Firstly, the design and fabrication of measuring cell to perform time of flight (ToF) experiments will be presented. Later, in terms of optimization, the parameters like the emission frequencies (f_e), percentage of collapse voltage (% V_c) to bias the devices and alternating voltages for emission (V_{ac}) will be elaborately discussed.

3.6.1 Design and fabrication of the measuring cell

The main aim of designing this specific chamber is to master the binary gas mixture analysis using time of flight measurement. The cell is made of acrylic monomer material that withstands upto 160 °C. It is cubical in shape with outer dimension of 30x30x8 mm^3, as shown in figure 3.31 and fabricated using 3D printing. The height (h) of the cell determines distance (d) between emitter and receiver CMUTs. The measuring cell has openings in several faces; top

and bottom are for gas inlet and outlet that are made to fit M5-type screws. In addition, there is a circular cavity in the center connecting the front and rear face of the cell. These openings allow us to place emitter and receiver CMUTs face to face, in order to perform ToF measurements. The diameter of the cavity is 18 mm. The total volume of the cavity was kept minimum (i.e. < 3 mL) to reduce the filling time and to apply real time gas concentration commands. The cell was designed in such a way that the gas flow is always perpendicular to the ultrasound propagation.

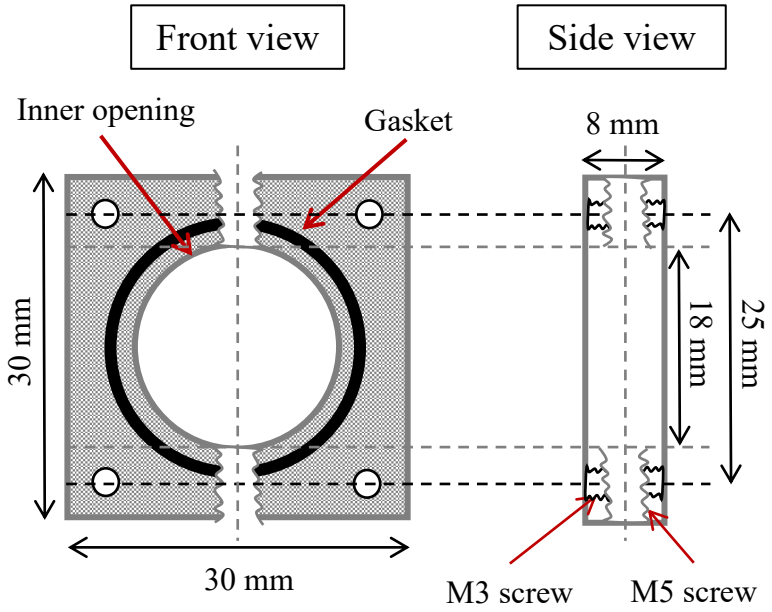


Figure 3.31: Schematic of the measuring cell.

From figure 3.32.b, the measuring cell combined with the CMUT prototypes makes it a complete gas sensor unit (excluding the electrical connections). In reality, the distance between the emitter and receiver are less than 8 mm due to the height of the CMUT chip (see eq. 3.35).

$$d = \left(h + 2 * e_{gasket}\right) - \left(2 * e_{element}\right) \qquad \text{Eq. 3.35}$$

where e_{gasket} and $e_{element}$ are the thickness of the gasket and CMUT chip respectively.

The emitter and receiver prototype are fitted to the chamber using four M3 screws. Also, two gaskets with outer diameter of 22 mm are placed between the PCB and the measuring cell in both the faces to avoid gas leakage, as shown in figure 3.32.a.

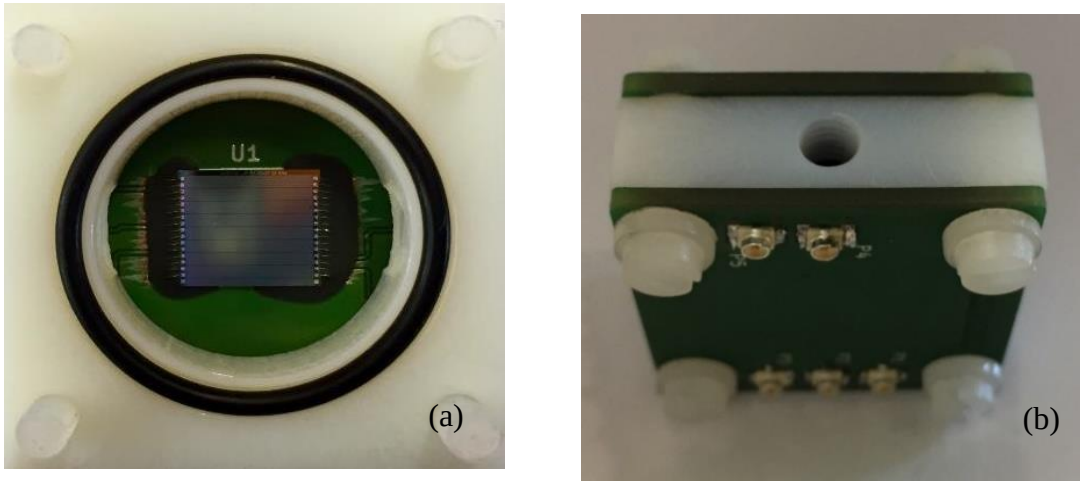


Figure 3.32: Fabricated measuring cell. (a) Inner view of the cell with emitter/receiver prototype and (b) completely packed gas sensor unit to perform time of flight measurement in air.

3.6.2 Experimental setup and preliminary results

The fabricated gas sensor unit is equipped with a specific workbench to conduct time of flight measurements in air. The schematic and the real time experimental setup are shown in figure 3.33. The emitter and the receiver are placed face to face, separated by distance ≈7 mm. The emission is connected to the wave generator to emit one period of sine pulse and to a DC power supply unit. The AC excitation system mentioned here was a home-made analogical emitter (same used for therapy imaging platform [26]). Then, the receiver was connected/enabled by DC power supply, as it has to receive the pulse echo. The received output echo is amplified using a type CA7/C charge amplifier (with 250 mV/pC) by Cooknell electronics ltd. Later, the output data is acquired by Picoscope 2000 series acquisition card (12 bits resolution and 20 MHz sampling frequency). Lastly, the resulting signals are displayed using PC Picoscope software installed in the computer to monitor current variations, as referred in figure 3.33.b.

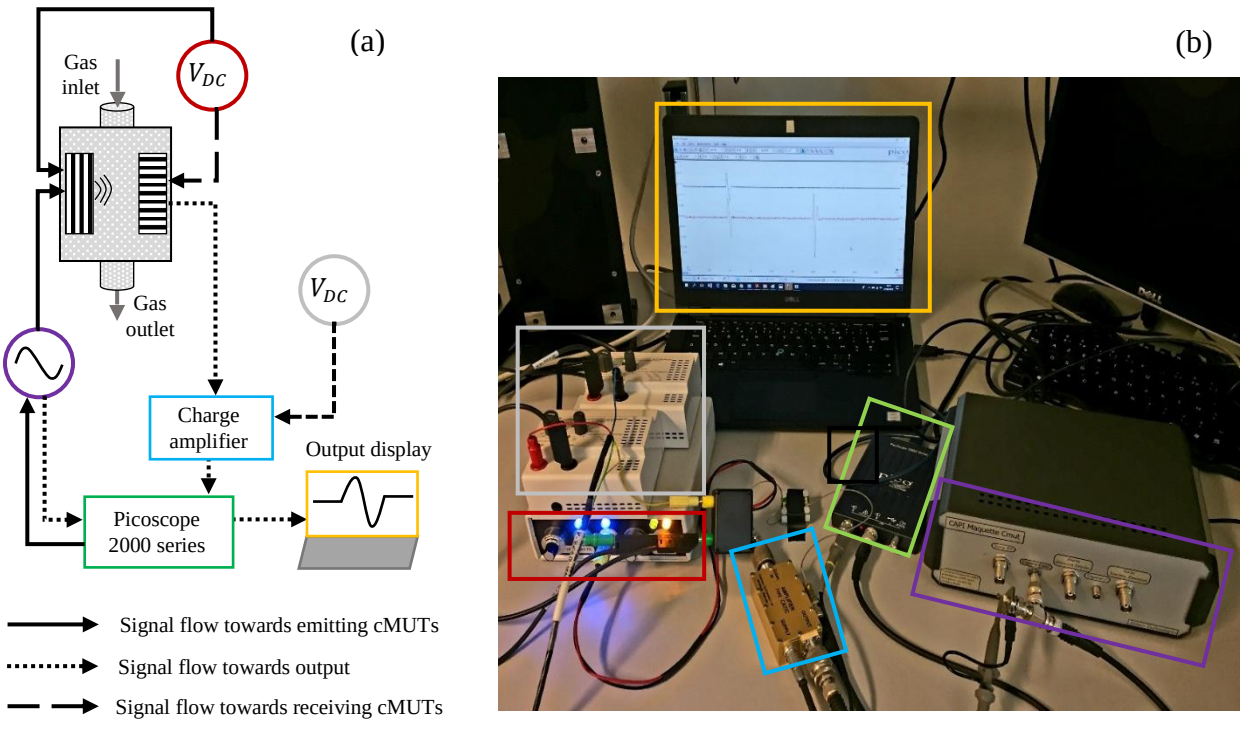


Figure 3.33: Experimental setup to perform time of flight measurement in air. (a) Schematic diagram and (b) real-time work bench.

According to ToF principle, CMUTs are made to work at quasi static regime, far low from their resonance frequencies. So the emission frequency (f_e) is maintained at 1 MHz (after which the attenuation in air is stronger). Then, the AC excitation (V_{ac}) of one period of sinusoidal signal with a 15 V_{ac} amplitude is used. Meanwhile, the bias voltage (V_{bias}) is maintained at 70 % of V_c for both emitter and receiver (refer table 3.5, to know V_{bias} corresponding to each membrane size). Also, the emitter and receiver belong to the same membrane geometry, in order to reduce device complexities.

To perform preliminary tests, the emission and the reception conditions are fixed (V_{ac}, V_{bias}) at the same conditions stated above, to compare different membrane geometries. The experiments are carried out at room temperature and in an air environment. The corresponding time domain and the frequency domain responses for the mentioned criterias are exhibited in figures 3.34 and 3.35 respectively. Table 3.5 exhibits the basic features of the acoustic pulse received for each membrane size.

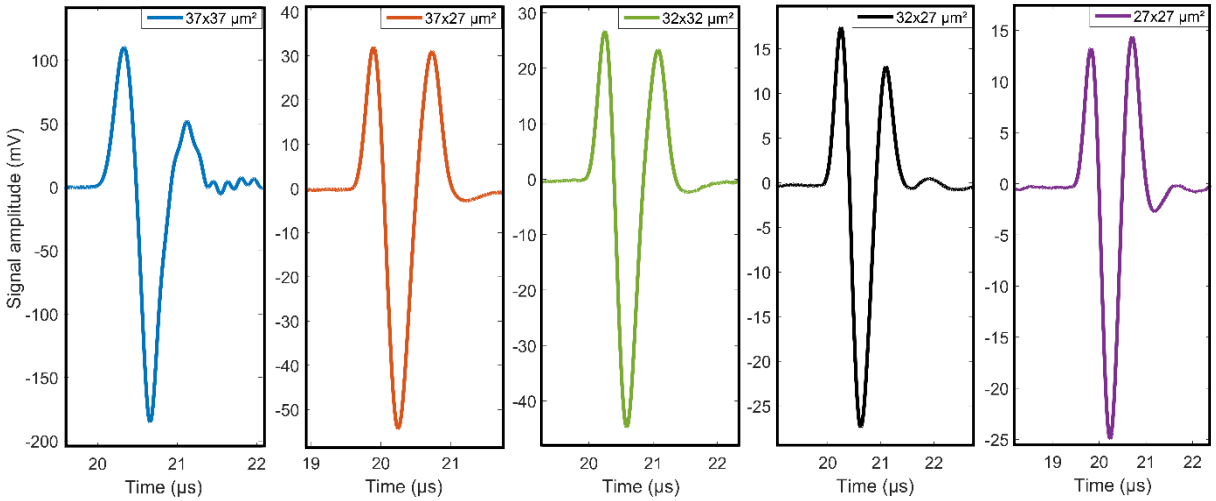


Figure 3.34: Received time domain responses of ToF echos for different membrane geometries at 47 V_{bias}, 15 V_{ac} and 1 MHz f_e.

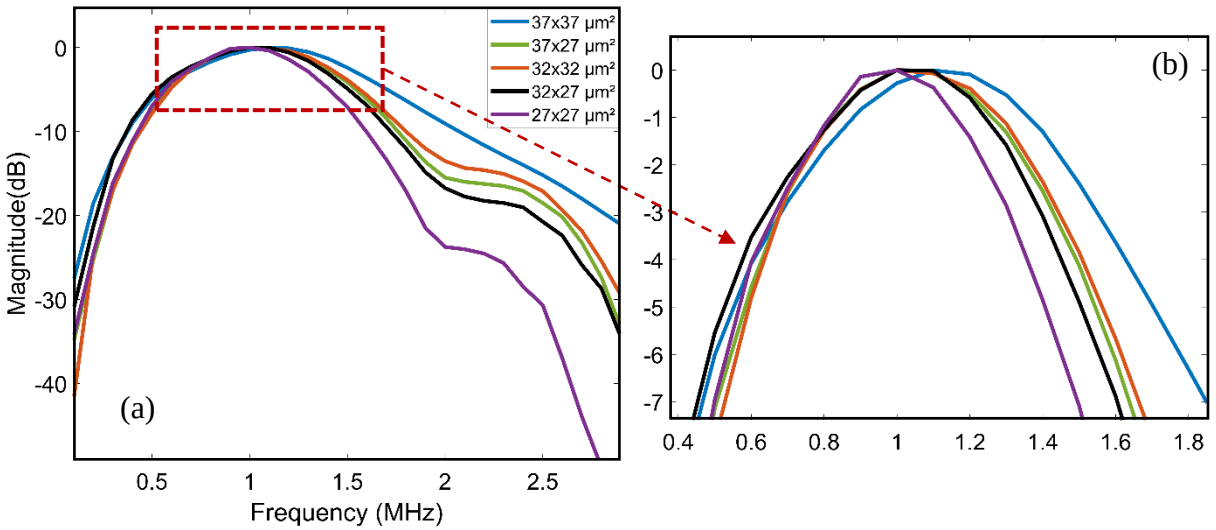


Figure 3.35: (a) Received frequency domain responses of ToF echos for different membrane geometries at 47 V_{bias}, 15 V_{ac} and 1 MHz f_e. (b) Focused view of spectral curves at 6 dB for the same.

From the results, it is clear that all the membrane geometries operate at low frequency and are capable of transmitting ultrasound at 1 MHz, as expected. They all show ≈100 % of -6 dB fractional bandwidth for the chosen working distance. These results validate the proof of concept for using CMUTs at quasi static regime, to emit and receive the ultrasound for gas detection measurement using time of flight technique. The CMUTs with the highest active surface ratio have the largest signal amplitude and wider bandwidth (e.g. 37x37 µm²), even if it shows the highest initial deflection. However, since initial deflection is more important, there is a high possibility that the CMUT membrane undergoes a collapse-snapback event

dynamically. This means that there is a trapping of additional charges each time the membrane touches the bottom of the cavity. In return, one has noticed a premature ageing caused by dielectric failure (electrical charges appear over time in the dielectric layer). The two prototypes for which the active surface ratio is the lowest (32x27 µm² and 27x27 µm²) show the smallest receiving amplitude. The last two prototypes (32x32 µm² and 37x27 µm²) have similar performances, i.e. a -6dB fractional bandwidth of 100 %.

Table 3.5: Extracted time and frequency domain information for various membrane geometries at fixed conditions.

Membrane size	70 % of collapse voltage	Signal amplitude of first ToF echo	-6 dB fractional bandwidth	Active surface ratio
37x37 µm²	31 V	295 mV	112 %	45 %
37x27 µm²	56 V	85 mV	98 %	42 %
32x32 µm²	42 V	72 mV	100 %	40 %
32x27 µm²	55 V	45 mV	102 %	39 %
27x27 µm²	65 V	40 mV	93 %	36 %

To complete these preliminary experiments, we have "pre-calibrated" the time of flight measurement to accurately determine the transmitter-receiver distance. To perform this experiment, the 32x32 µm² CMUT configurations were used for both emitter and receiver.

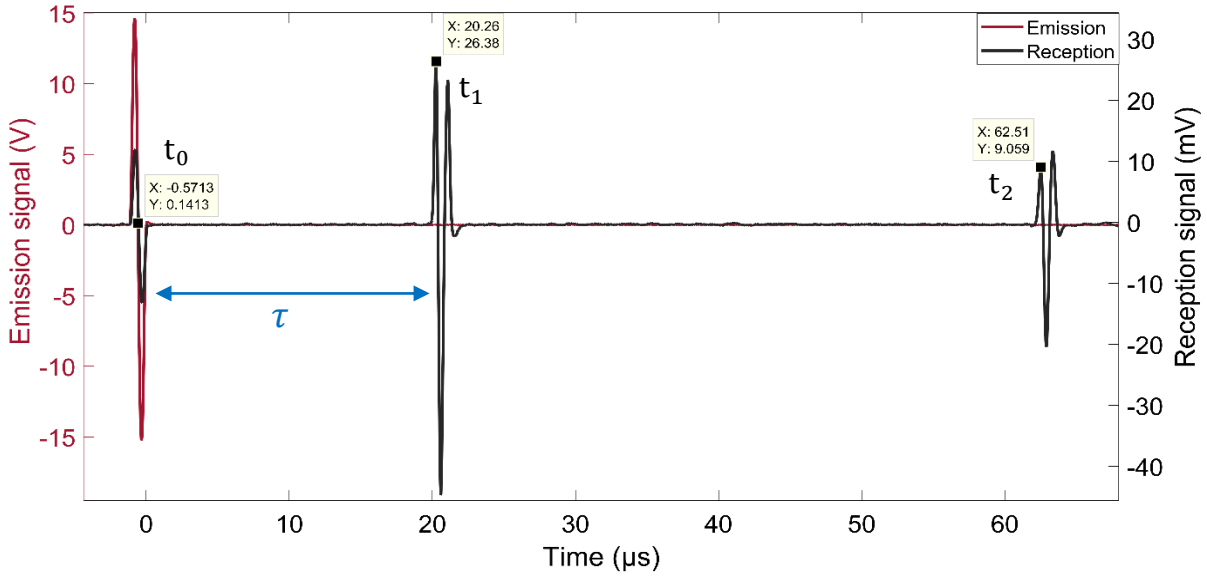


Figure 3.36: Time of flight in air using 32x32 µm² membrane at 42 V_{bias}, 15 V_{ac} and 1 MHz f_e.

With the aid of emission and reception signals shown in figure 3.36, one can find the distance with high precision using the simple sound velocity relation stated below:

$$d = c * \tau = c * (t_1 - t_0) \quad \text{Eq. 3.36}$$

where c is the velocity of sound in a medium (for air, c = 343 m/s at room temperature) and τ is the time of flight, which is the difference of time at position t_0 and t_1.

From figure 3.36, the obtained τ is 20.83 µs and by substituting this value in eq. 3.36, the calculated distance is 7.14 mm. In addition, one can predict the occurrence time of several echos with the eq. 3.36 by just adding a factor 'n', which is expressed as:

$$d = c * \tau * n \quad \text{Eq. 3.37}$$

where n refers to the number of travels between emitter and receiver. Namely, for the first echo n = 1, the second n = 3, the third n = 5 and so on. Moreover, τ can be deduced from the two consecutive echos at any position using the following relation:

$$\tau = \left(\frac{t_{m+1} - t_m}{2}\right) \quad \text{Eq. 3.38}$$

In our case from figure 3.36, t_m is t_1, t_{m+1} is t_2 and the relation is always divided by the factor of 2, on account to the difference in number of travels between these echos. These additional datas/echos help to attain high precision in gas detection and enables better gas discrimination.

3.6.3 Impact of V_{bias} and V_{ac} on time of flight performances

In this section, the device performances and behaviors with respect to the alternating (V_{ac}) and bias (V_{bias}) voltages are analyzed. These experiments are carried out at the same emission frequency, i.e. at 1 MHz, irrespective of V_{ac} and V_{bias}. The total applied emission voltage V_{tot} should not exceed 110 % of the collapse voltage V_c as expressed in eq. 3.39. This criterion is emphasized to attain stable working conditions and device safety.

$$V_{tot} = V_{bias} + V_{ac} \leq 110\ \%\ of\ V_C \quad \text{Eq. 3.39}$$

The previous expression is simplified as below for better understanding:

$$V_{xy} = V_{bias_y} + V_{ac_x} \qquad \text{Eq. 3.40}$$

where *x* denotes the amplitude of the sinusoidal pulse applied in the emission. It has two values; for *x*=1 and 2, the V_{ac} values are 20 V_{ac} and 15 V_{ac} respectively. *y* indicates the percentage of collapse voltage that ranges from 1 to 4. For *x*=1, V_{bias} varies from 40 % to 70 % of V_c and for *x*=2, it is from 50 % to 80 % of V_c. This is to keep the V_{tot} less than 110 % for varying V_{ac} values.

The CMUTs with different membrane geometries have been compared at V_{1y} and V_{2y} conditions as shown in figure 3.37.

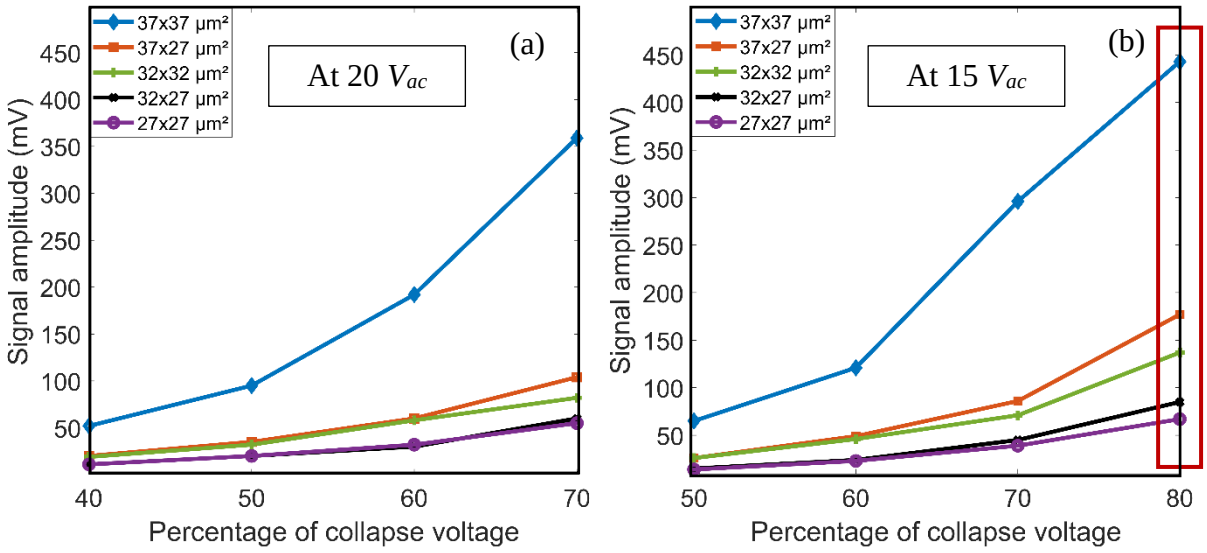


Figure 3.37: Comparison of signal amplitudes for different percent of applied collapse voltages with different V_{ac} for each membrane geometry (a) 20 V_{ac} and (b) 15 V_{ac}.

Both the graphs look almost similar, meaning that they have homogenous behaviors with minimal change in signal amplitudes for the membranes with low active surface ratio (27x27 µm²) and evident change for the membranes with high active surface ratio (37x37 µm²). In addition, the device performances were quite the same below, for conditions like $V_{bias} + V_{ac} < 100\ \%\ V_c$ in both the cases. Therefore, the spectral and the time domain responses for different V_{ac} with fixed V_{bias} are compared. This comparison is made to identify the impact of V_{ac} in terms of bandwidth. Because, from figure 3.37, we could clearly see that increase in V_{ac} increases the signal amplitude.

To carry out this comparison, two conditions from eq. 3.40 are taken, namely V_{14} and V_{24}. Also, the prototypes with same membrane geometries for emitter as well as receiver are chosen (here 32x32 µm²). The condition V_{14} corresponds to 70 % V_c (i.e. 42 V_{bias}) and 20 V_{ac}. Similarly, at condition V_{24}, its 80 % of V_c (47 V_{bias}) and 15 V_{ac} respectively. The corresponding frequency and time domain responses are shown in figure 3.38.

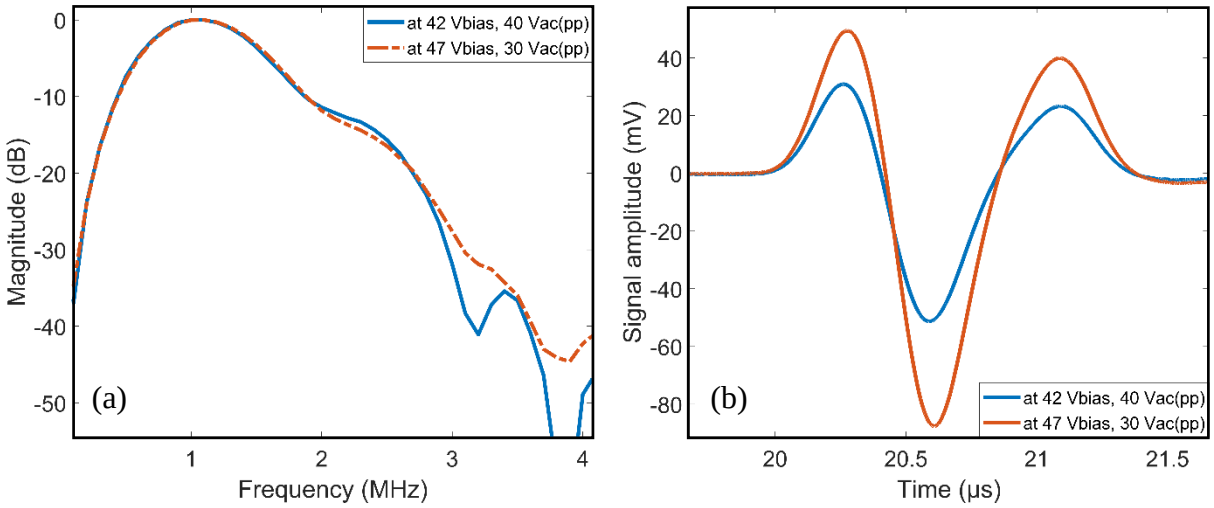


Figure 3.38: Comparison of (a) frequency domain responses and (b) time domain responses at V_{14} and V_{24} conditions at 1 MHz emission frequency.

To sum up, the condition V_{24} seems convincing enough for the targeted application because the bandwidth remains stable/same and has a distinguishable difference in signal amplitude at 80 % of V_c (refer figure 3.38.b). To mention, more than one prototype for each membrane size have been characterized and they all produced similar results corresponding to their membrane geometries.

As a partial conclusion, among all the prototypes, the 32x32 µm^2 configuration was retained for further experiments. This configuration has sufficient performance in terms of sensitivity and bandwidth for the intended application. Moreover, it was very stable over time. Of course, the 37x37 µm² configuration could also have been tested, but the premature ageing of this membrane geometry led us to secure 32x32 µm².

3.6.4 Comparison between different emission frequencies

Subsequently, after investigating the effect of V_{bias} and V_{ac}, the device performances with a range of emission frequencies were studied. So to investigate this aspect, prototypes with same membrane geometries are taken (here 32x32 µm²) and the emission frequencies are tuned from 0.5 MHz to 2 MHz at constant V_{bias} and V_{ac} (at V_{24} condition), where V_{tot} is kept at ≈110 % of V_c. The resulting time domain responses for the applied conditions are shown in figure 3.39.

From the response, it is clear that the emission frequencies play an important role in the duration of emitted time pulse ($\because f \propto 1/t$), lower the emission frequency, higher the pulse duration. In addition, the attenuation in air also limits the emission frequency. Therefore, this makes it more important to choose an optimal frequency.

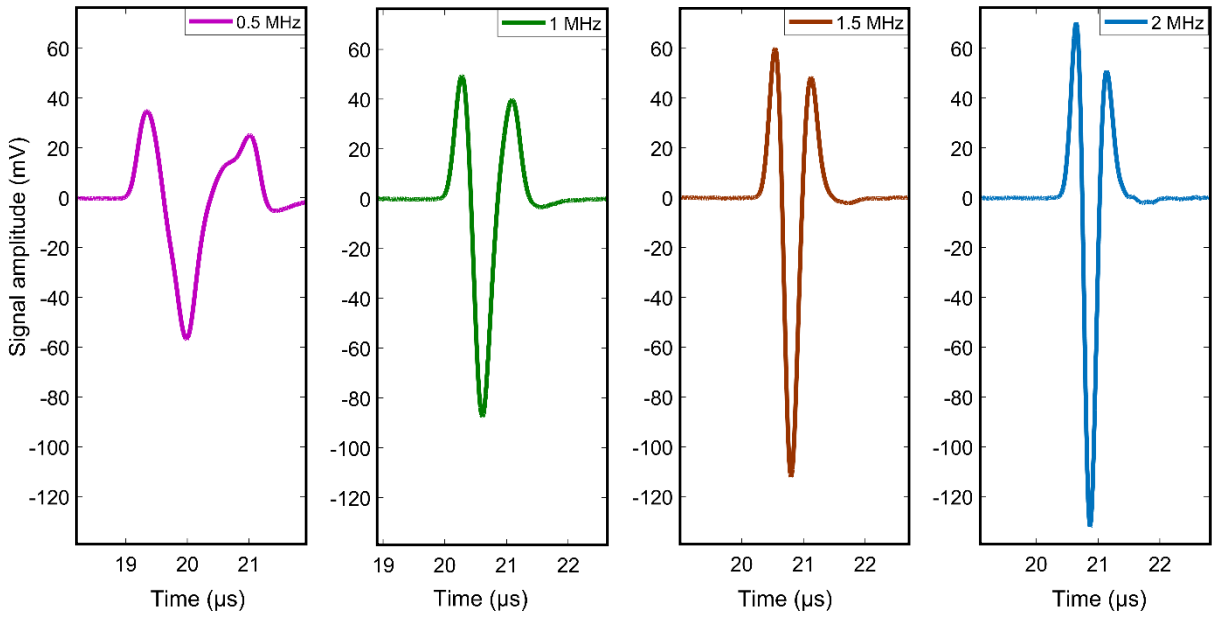


Figure 3.39: Time domain responses for different emission frequencies (0.5 MHz to 2 MHz) at 47 V_{bias} and 15 V_{ac}.

Figure 3.40.b shows frequency domain responses corresponding to the time domain curves shown in figure 3.39. Note that at 0.5 MHz and 1 MHz, the frequency components are well centered but the spectral contributions arising from intrinsic non-linear behavior of CMUTs are also observed. On the other hand, at 1.5 MHz and 2 MHz, there is gain in HF component but the attenuation in air is high. From the time and frequency domain response, one can clearly see that the device works well in a broad frequency range, i.e. 0.5-2 MHz, which opens path in

terms of gas discrimination. Notably, this work has been carried out by Iglesias *et al.* [55] [56]. In the current study, we chose to work at 1 MHz, as targeted.

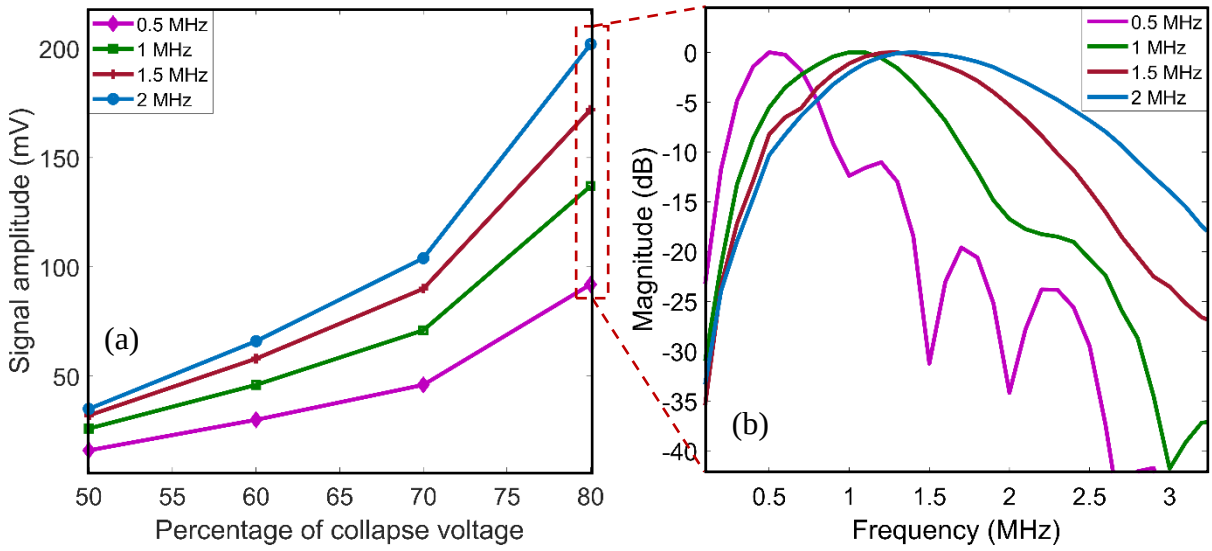


Figure 3.40: (a) Comparison of signal amplitude for different percent of applied collapse voltages for range of emission frequencies at V_{2y} conditions and (b) frequency domain responses for different emission frequencies (0.5 MHz to 2 MHz) at 47 V_{bias} and 15 V_{ac} conditions.

3.6.5 Detection of maximum working distances

This is a supplementary experiment done out of curiosity to assess maximum working distance of currently used prototypes, to unlock the usage for potential future applications. In order to perform these experiments, the emitter and receiver belonging to the same membrane geometries have been taken (here 32x32 µm²). The emission frequency is maintained at 1 MHz and the V_{bias} and V_{ac} were kept maximum that of 47 V and 20 V respectively. The emitter is fixed while the receiver moves vertically along the emitter axis from 5 mm to 250 mm, as shown in figure 3.41.a. The frequency domain responses at 5 mm, 100 mm and 220 mm are plotted in figure 3.41.b. The corresponding time domain responses are shown in figure 3.42.

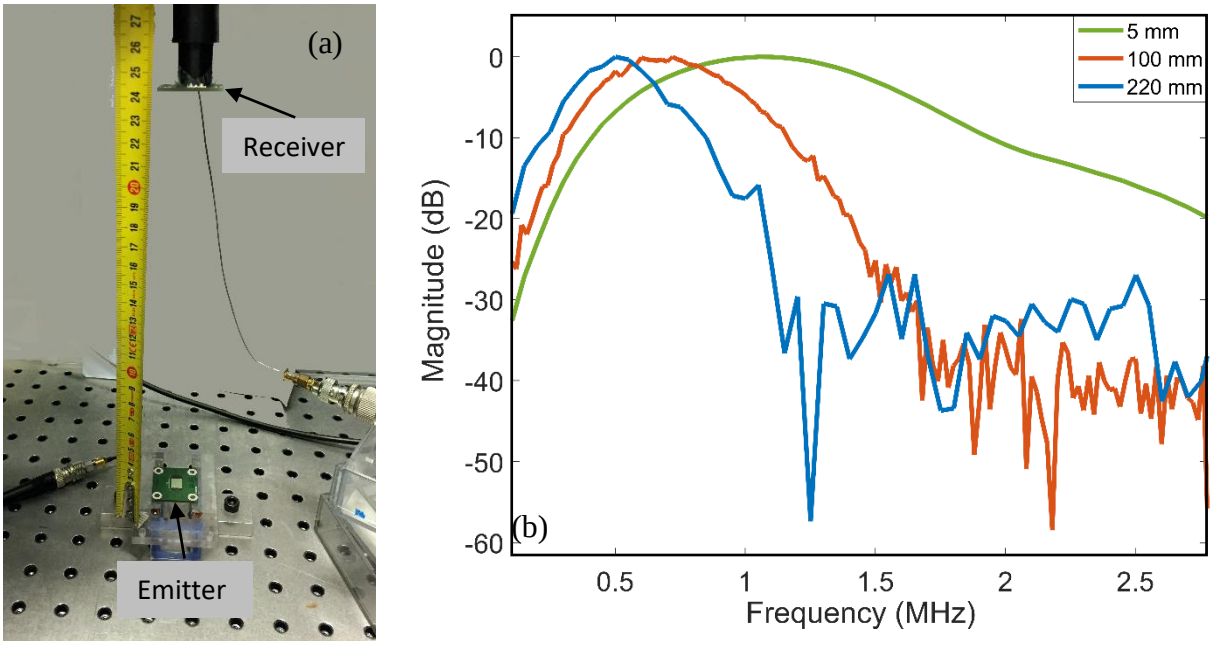


Figure 3.41: (a) Position of emitter and receiver prototype while performing maximum working distance measurements. (b) Frequency domain responses for various working distances (at 5 mm, 100 mm and 220 mm) at 1 MHz emission frequency, 47 V_{bias} and 20 V_{ac}.

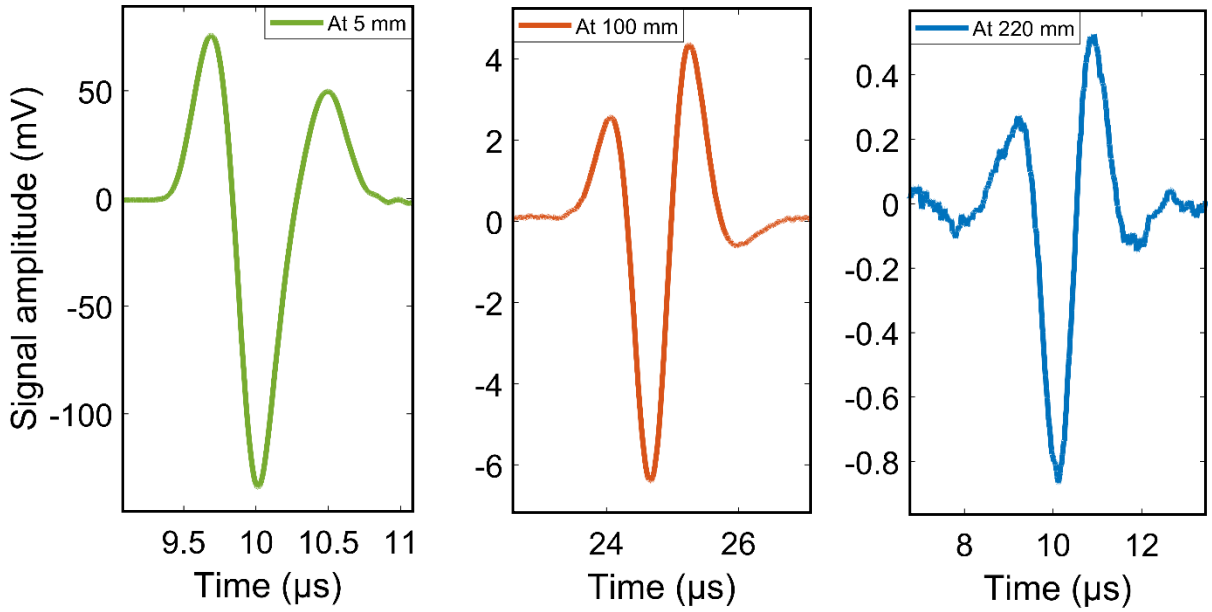


Figure 3.42: Time domain responses for various working distances (at 5 mm, 100 mm and 220 mm) at 1 MHz emission frequency, 47 V_{bias} and 20 V_{ac}.

From the spectrum observation, it is obvious that the bandwidth decreases with increase in distances. On the positive note, the received signal shows dynamic of 30 dB with the spectrum clearly centered at 1 MHz and shifts toward lower frequency on increasing the distance. This shift is caused by attenuation in air. The time domain representation reveals the limit of

detection, which is 220 mm for our device, beyond that the signal-to-noise ratio was not high enough. Even though these CMUTs are not specifically designed to work at large distances, their sensitivity can be increased through further optimizations, such as increasing number of transducers in emitter or receiver, by using specific V_{bias}, V_{ac} and emission frequency, etc., depending on the targeted application.

3.7 Binary gas mixture analyses

3.7.1 Time of flight model validation in gas mixture environments

The fully optimized gas sensor unit with specific V_{bias}, V_{ac} and f_e are fitted in the workbench dedicated to binary gas mixture analysis, as shown in schematic (see figure 3.43).

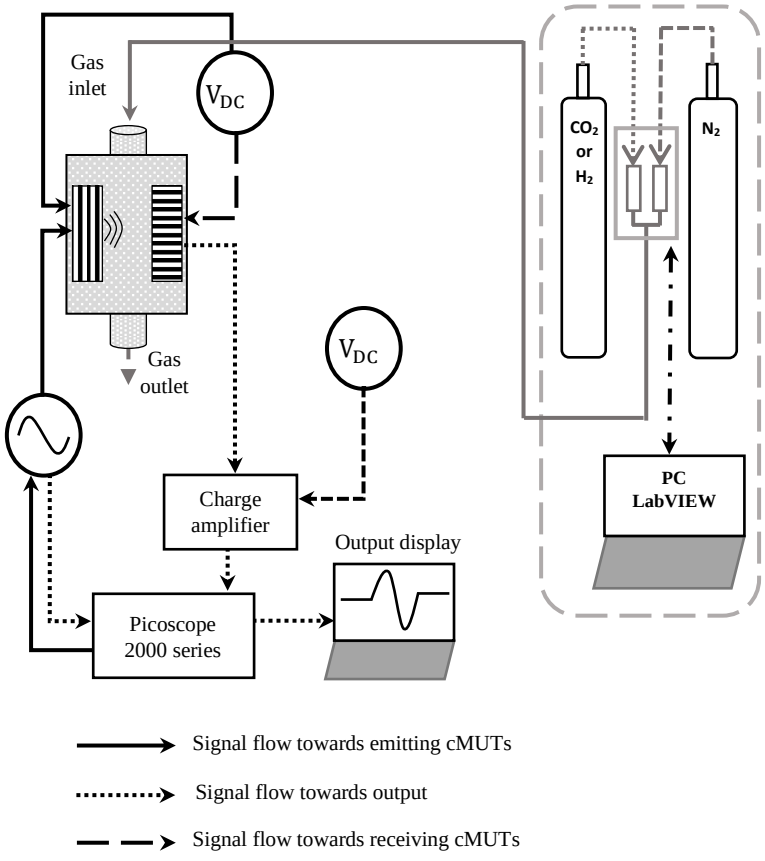


Figure 3.43: Schematic of time of flight measurement used by IMS laboratory to perform gas mixture analysis using our CMUT device.

The first set of binary gas analysis was conducted using carbon dioxide (CO_2) in nitrogen (N_2) for higher gas concentrations ranging from 0 % to 100 % with a step of 20 % at V_{24} condition, as shown in figure 3.44. Nitrogen is used as the reference gas because it has an acoustic velocity close to air at room temperature. Gas detection with CO_2 was chosen for preliminary testing due to safety reasons, as we used high gas concentrations at initial stages. The gas mixture compositions are controlled using a LabVIEW program through an electro-valve connected to various gas tanks allowing us to choose between binary gas mixtures of interest.

As explained previously, the time of flight varies/shifts depending on the velocity of sound (Δc). On introduction of CO_2, the sound velocity inside the gas sensor unit varies, resulting in the shift of ToF peak. The measured peak detections for relative change in time of flights for varying concentrations of CO_2 in N_2 is shown in figure 3.44. The gas concentration is switched for every five minutes by sending pure nitrogen to bring the system back to reference position.

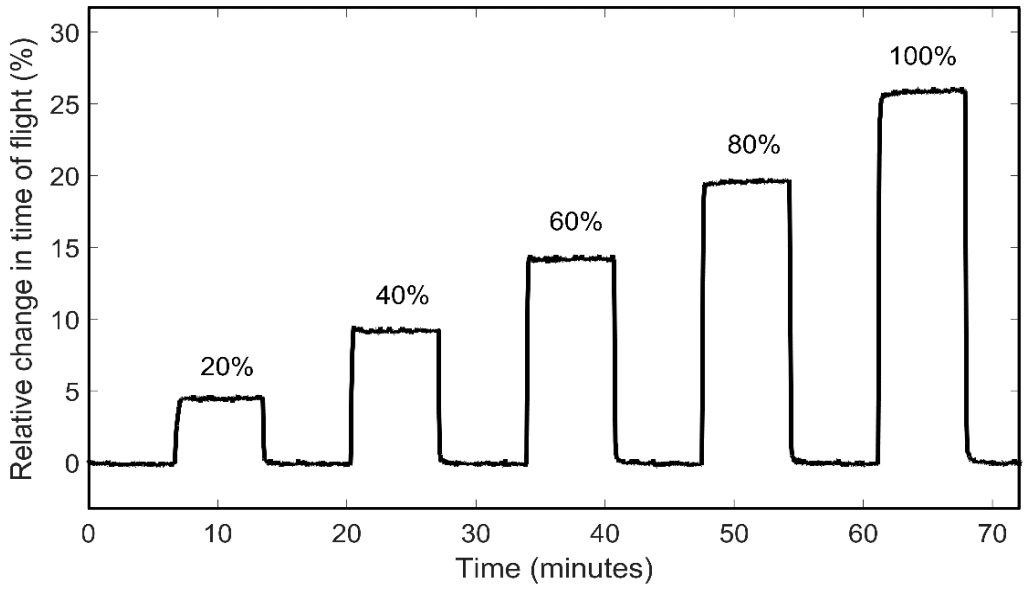


Figure 3.44: Experimental results of ToF in gas environment for higher gas concentrations (CO_2 in N_2 for 0 % to 100 % with step of 20 %) at 47 V_{bias}, 15 V_{ac} and 1 MHz f_e.

Following the positive results, the experiments were carried out for low concentrations of CO_2 in N_2 and H_2 in N_2. The measured peak detection for relative change in ToF for 1-4 % gas concentrations of CO_2 in N_2 and H_2 in N_2 are shown in figure 3.45, for 47 V_{bias}, 15 V_{ac} at 1 MHz emission frequency.

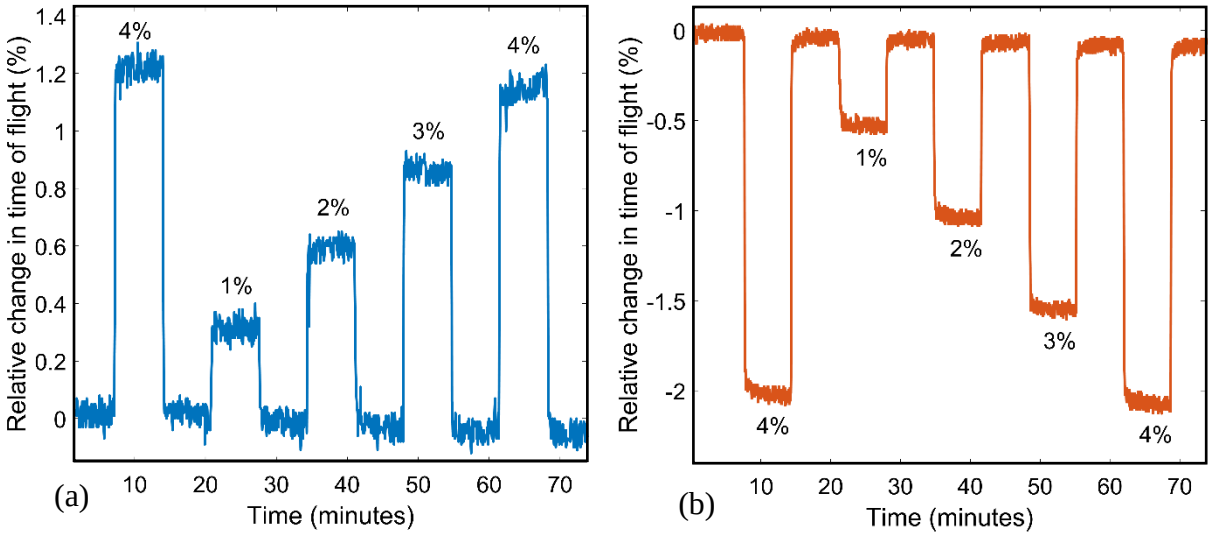


Figure 3.45: Experimental ToF results for gas concentrations less than 4 % of (a) CO_2 in N_2, (b) H_2 in N_2 at 47 V_{bias}, 15 V_{ac} and 1 MHz f_e.

In addition to this, the gas detection for very low gas concentrations (i.e. <1 %) have been conducted. These results provided the limit of detection (LOD) of the current system for the applied excitation conditions. The figure 3.46 demonstrates the LOD of 0.3 % and 0.15 % for CO_2 in N_2 and H_2 in N_2, respectively.

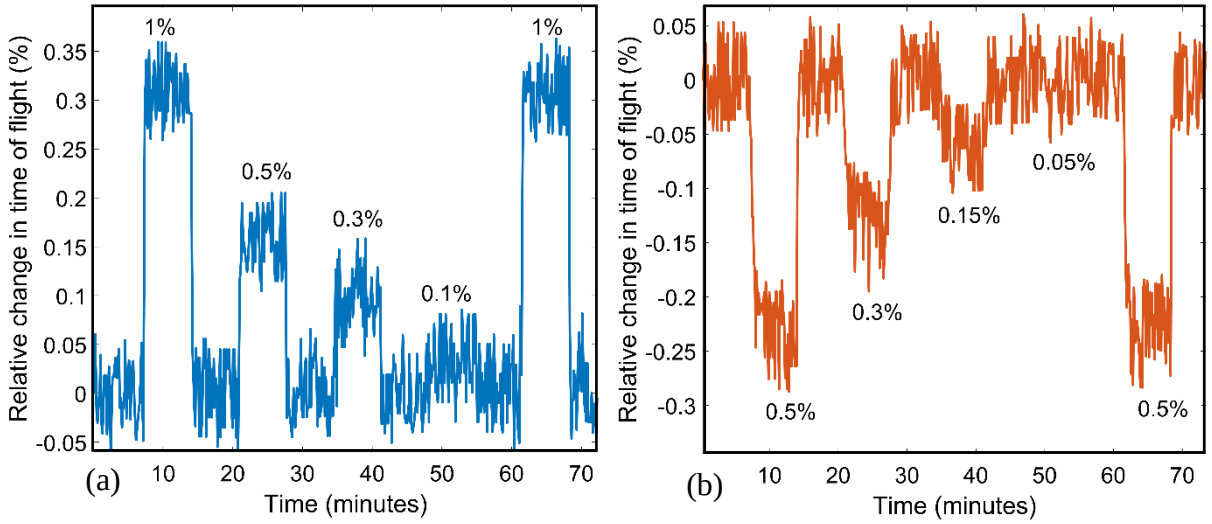


Figure 3.46: Experimental time of flight in gas environment for low concentrations of (a) CO_2 in N_2, (b) H_2 in N_2 at 47 V_{bias}, 15 V_{ac} and 1 MHz f_e.

To give an order of magnitude, the experimental results with expected first echo of ToF with the distance of 7.14 mm for pure gas concentrations are briefed in table 3.6. From the values, it is clear that the ToF difference between pure CO_2 and N_2 is 6 µs and pure H_2 and N_2 is -14.6 µs,

where the negative sign indicates the shift in opposite direction that can be evidenced from figure 3.46.b respectively. Along with that, the measured LOD is tabulated in table 3.6.

Table 3.6: Experimental ToF for pure gas concentrations.

Gas	Velocity (*c*) (m/s)	Expected ToF for pure gas at distance 7.14 mm	LOD
Carbon dioxide	267	26 µs	0.30 %
Nitrogen	349	20 µs	-
Hydrogen	1306	5.4 µs	0.15 %

3.7.2 Gas mixture analysis for CMUTs working at resonance mode

Finally, the gas mixture analysis based on resonance mode detection (method III) is presented (as supplementary). As explained earlier, here the relative change in gas concentration is identified by shift in resonance frequency, i.e. at admittance of the system. Similar to ToF results, first the gas analysis for concentration between 1 % and 4 % is displayed, as shown in figure 3.47. The presented results are carried out at 60 % of V_c (35 V_{bias}), where the best trade-off between sensitivity and noise is measured, as referred in [1].

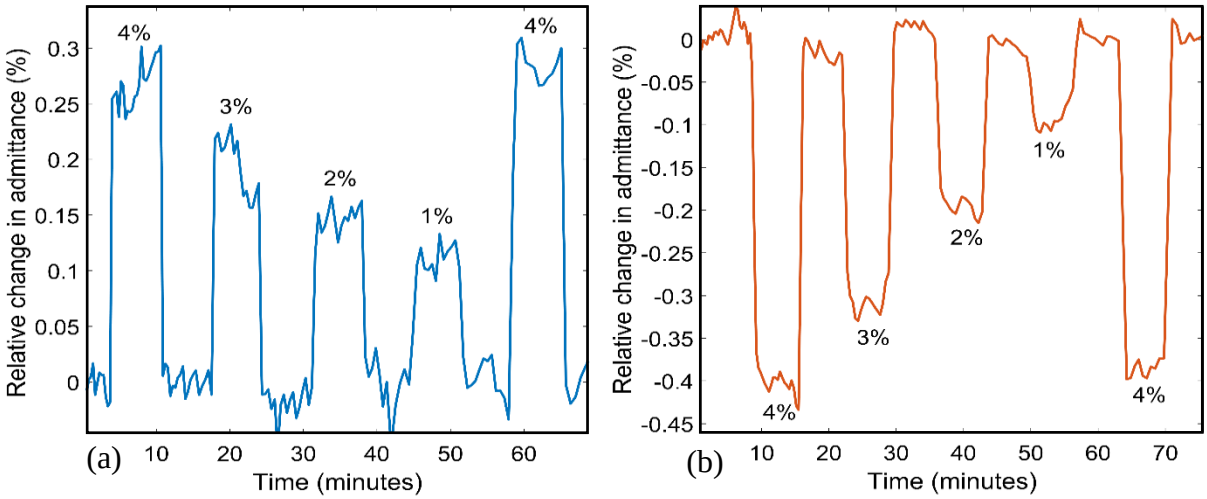


Figure 3.47: Measured relative change in admittance for change in gas concentrations of (a) CO_2 in N_2 and (b) H_2 in N_2 at 35 V_{bias} [1].

With these encouraging results, the measurement for LOD has been performed. The respective results are shown in figure 3.48. The measured LOD for very low concentration of CO_2 in N_2

and H_2 in N_2 are 0.25 % and 0.04 % respectively. Even though LOD is not upto the state-of-the-art sensitive coated gas sensors. This can be achieved by further optimizations in future devices, like increasing the quality factor (better CMUT-to-CMUT homogeneity) and suppressing the parasitic mode.

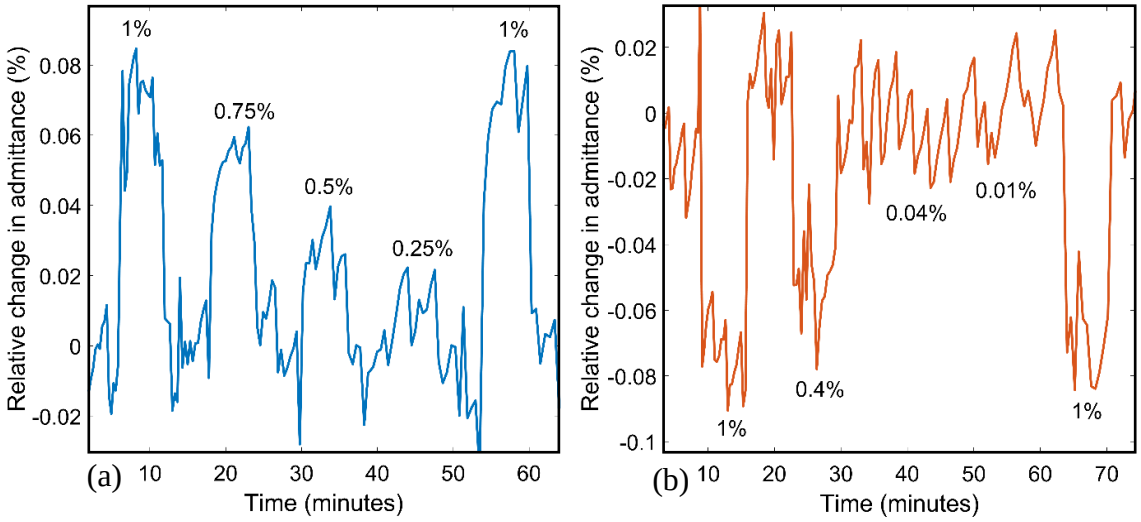


Figure 3.48: Measured relative change in admittance for change in very low gas concentration of (a) CO_2 in N_2 and (b) H_2 in N_2 at 35 V_{bias} [1].

To mention, Luis Iglesias (researcher at IMS laboratory, Bordeaux) has provided all the experimental datas regarding gas measurements. More detailed works are presented in his PhD [57].

Conclusion and perspectives

To summarize, a new approach for binary gas mixture monitoring without sensitive coating was designed, implemented and tested for the targeted application. The fabricated CMUTs with different membrane geometries, i.e. 37x37 µm², 37x27 µm², 32x32 µm², 32x27 µm² and 27x27 µm² are working well. They all have collapse voltages lower than 100 V with a range of resonance frequencies from 6 MHz to 10 MHz. All these prototypes are made to work at their low frequency regimes, like a microphone. The experimental electroacoustic characterization results in air show the developed CMUTs have tunable frequencies from 0.5 MHz to 2 MHz and have 6 dB fractional bandwidth ranging from 93 % to 112 % depending on the membrane geometries. Furthermore, the best excitation conditions are chosen to perform time of flight (ToF) measurements without risk of damaging the device, like ageing (refer §3.3.3 and §3.6.2).

The proposed system based on ToF technique has successfully measured the change in ultrasound velocities with respect to the change in gas mixture concentrations. The first experiments performed for higher concentrations of CO_2 in N_2 have paved the way with their remarkable shift in ToF. Therefore, the tests have been conducted for low (1-4 %) and very low (<1 %) gas concentrations. These results demonstrate a limit of detection of 0.30 % and 0.15 % for CO_2 in N_2 and H_2 in N_2 respectively, for method IV detection. These promising results makes our device suitable gas sensor with state-of-the-art detection technique (i.e. ToF).

Besides, the experimental results with resonance mode detection (method III) have also been discussed briefly. These measurements show the possibility of using the same device with multiple detection techniques. The presented results exhibit the limit of detection of 0.25 % and 0.04 % for CO_2 in N_2 and H_2 in N_2 respectively.

Finally, to conclude, the sensitivity for method III can be improved by increasing the device homogeneity and the quality factor. Similarly, for ToF (method IV), the active surface ratio is the key parameter, which also requires a better control of homogeneity. Therefore, we propose to increase the metallization ratio of the top electrode from 50 % to 100 %. Such configurations reduce the stress on the membrane and help to attain lower initial deflection. There have been few devices fabricated on this basis by our laboratory, which shows lower initial deflection and

membrane stress compared to partially metallized CMUTs. Therefore, the next set of CMUTs fabrication for gas detection will consider this specification.

References

[1] L. Iglesias *et al.*, "Proof of Concept and Preliminary Results of Gas Detection by Measuring the Admittance at the Resonance and Anti-resonance of an Uncoated CMUT," *Front. Mech. Eng.*, vol. 6, p. 14, Mar. 2020, doi: 10.3389/fmech.2020.00014.

[2] P. Shanmugam *et al.*, "Broad bandwidth air-coupled micromachined ultrasonic transducers for gas sensing," *Ultrasonics*, vol. 114, p. 106410, Jul. 2021, doi: 10.1016/j.ultras.2021.106410.

[3] M.-T. Boudjiet, "Microsystèmes durables de mesures de concentration d'hydrogène utilisant des micropoutres sans couche sensible," PhD dissertation, University of Bordeaux, 2015.

[4] N. Sénégond, "Approche temporelle de le simulation et de la caractérisation des transducteurs ultrasonores capacitifs micro-usinés," PhD dissertation, University of Tours, Tours, 2010.

[5] A. Boulmé, "Conception et caractérisation de sondes cmut large bande pour l'imagerie conventionnelle et l'évaluation du tissu osseux," PhD dissertation, University of Tours, 2013.

[6] F. V. Hunt, *Electroacoustics: the analysis of transduction, and its historical background*, 2. print. New York, NY: American Inst. of Physics, 1982.

[7] D. Hohm and G. Hess, "A subminiature condenser microphone with silicon nitride membrane and silicon back plate," *The Journal of the Acoustical Society of America*, vol. 85, no. 1, pp. 476–480, Jan. 1989, doi: 10.1121/1.397699.

[8] K. Suzuki *et al.*, "A silicon electrostatic ultrasonic transducer," *IEEE Trans. Ultrason., Ferroelect., Freq. Contr.*, vol. 36, no. 6, pp. 620–627, Nov. 1989, doi: 10.1109/58.39112.

[9] M. Rafiq and C. Wykes, "The performance of capacitive ultrasonic transducers using v-grooved backplates," *Meas. Sci. Technol.*, vol. 2, no. 2, pp. 168–174, Feb. 1991, doi: 10.1088/0957-0233/2/2/014.

[10] Haller and Khuri-Yakub, "A surface micromachined electrostatic ultrasonic air transducer," in *Proceedings of IEEE Ultrasonics Symposium ULTSYM-94*, Cannes, France, 1994, pp. 1241–1244 vol.2. doi: 10.1109/ULTSYM.1994.401810.

[11] M. I. Haller and B. T. Khuri-Yakub, "A surface micromachined electrostatic ultrasonic air transducer," *IEEE Trans. Ultrason., Ferroelect., Freq. Contr.*, vol. 43, no. 1, pp. 1–6, Jan. 1996, doi: 10.1109/58.484456.

[12] X. C. Jin *et al.*, "Micromachined capacitive transducer arrays for medical ultrasound imaging," in *1998 IEEE Ultrasonics Symposium. Proceedings (Cat. No. 98CH36102)*, Sendai, Japan, 1998, vol. 2, pp. 1877–1880. doi: 10.1109/ULTSYM.1998.765318.

[13] O. Oralkan *et al.*, "Initial pulse-echo imaging results with one-dimensional capacitive micromachined ultrasonic transducer arrays," in *2000 IEEE Ultrasonics Symposium. Proceedings. An International Symposium (Cat. No.00CH37121)*, San Juan, Puerto Rico, 2000, vol. 1, pp. 959–962. doi: 10.1109/ULTSYM.2000.922700.

[14] O. Oralkan *et al.*, "Capacitive micromachined ultrasonic transducers: next-generation arrays for acoustic imaging?," *IEEE Trans. Ultrason., Ferroelect., Freq. Contr.*, vol. 49, no. 11, pp. 1596–1610, Nov. 2002, doi: 10.1109/TUFFC.2002.1049742.

[15] O. Oralkan *et al.*, "Volumetric ultrasound imaging using 2-D CMUT arrays," *IEEE Trans. Ultrason., Ferroelect., Freq. Contr.*, vol. 50, no. 11, pp. 1581–1594, Nov. 2003, doi: 10.1109/TUFFC.2003.1251142.

[16] K. K. Park *et al.*, "Capacitive micromachined ultrasonic transducers for chemical detection in nitrogen," *Appl. Phys. Lett.*, vol. 91, no. 9, p. 094102, Aug. 2007, doi: 10.1063/1.2776348.

[17] P. Shanmugam *et al.*, "CMUT Based Air Coupled Transducers for Gas-Mixture Analysis," in *2018 IEEE International Ultrasonics Symposium (IUS)*, Kobe, Japan, Oct. 2018, pp. 1–4. doi: 10.1109/ULTSYM.2018.8579789.

[18] D. W. Schindel *et al.*, "The design and characterization of micromachined air-coupled capacitance transducers," *IEEE Trans. Ultrason., Ferroelect., Freq. Contr.*, vol. 42, no. 1, pp. 42–50, Jan. 1995, doi: 10.1109/58.368314.

[19] P. C. Eccardt *et al.*, "Micromachined transducers for ultrasound applications," in *1997 IEEE Ultrasonics Symposium Proceedings. An International Symposium (Cat. No.97CH36118)*, Toronto, Ont., Canada, 1997, vol. 2, pp. 1609–1618. doi: 10.1109/ULTSYM.1997.663304.

[20] L. Pizarro *et al.*, "Experimental investigation of electrostatic ultrasonic transducers with grooved backplates," in *1997 IEEE Ultrasonics Symposium Proceedings. An International Symposium (Cat. No.97CH36118)*, Toronto, Ont., Canada, 1997, vol. 2, pp. 1003–1006. doi: 10.1109/ULTSYM.1997.661750.

[21] Xuecheng Jin *et al.*, "Fabrication and characterization of surface micromachined capacitive ultrasonic immersion transducers," *J. Microelectromech. Syst.*, vol. 8, no. 1, pp. 100–114, Mar. 1999, doi: 10.1109/84.749409.

[22] E. Cianci *et al.*, "Micromachined capacitive ultrasonic transducers fabricated using silicon on insulator wafers," *Microelectronic Engineering*, vol. 61–62, pp. 1025–1029, Jul. 2002, doi: 10.1016/S0167-9317(02)00423-9.

[23] L. L. Liu *et al.*, "A novel method for fabricating capacitive micromachined ultrasonic transducers with ultra-thin membranes," in *IEEE Ultrasonics Symposium, 2004*, Montreal, Canada, 2004, vol. 1, pp. 497–500. doi: 10.1109/ULTSYM.2004.1417771.

[24] P. Gatta *et al.*, "P3R-3 Design and Characterization of Air Coupled Ultrasonic Transducers Based on MUMPs," in *2006 IEEE Ultrasonics Symposium*, Vancouver, BC, Canada, 2006, pp. 2373–2376. doi: 10.1109/ULTSYM.2006.603.

[25] B. T. Khuri-Yakub and Ö. Oralkan, "Capacitive micromachined ultrasonic transducers for medical imaging and therapy," *J. Micromech. Microeng.*, vol. 21, no. 5, p. 054004, May 2011, doi: 10.1088/0960-1317/21/5/054004.

[26] D. Gross *et al.*, "A cMUT probe for ultrasound-guided focused ultrasound targeted therapy," *IEEE Trans. Ultrason., Ferroelect., Freq. Contr.*, vol. 62, no. 6, pp. 1145–1160, Jun. 2015, doi: 10.1109/TUFFC.2014.006887.

[27] W. A. N'Djin *et al.*, "Capacitive Micromachined Ultrasound Transducers for Interstitial High-Intensity Ultrasound Therapies," *IEEE Trans. Ultrason., Ferroelect., Freq. Contr.*, vol. 64, no. 8, pp. 1245–1260, Aug. 2017, doi: 10.1109/TUFFC.2017.2707663.

[28] J. Lascaud *et al.*, "Investigation of ultrasonic absorption in the MHz frequency range by silicon substrates with a built-in porous silicon layer," *Ultrasonics*, vol. 96, pp. 196–202, Jul. 2019, doi: 10.1016/j.ultras.2019.01.006.

[29] B. T. Khuri-Yakub *et al.*, "6D-1 The Capacitive Micromachined Ultrasonic Transducer (CMUT) as a Chem/Bio Sensor," in *2007 IEEE Ultrasonics Symposium Proceedings*, New York, NY, Oct. 2007, pp. 472–475. doi: 10.1109/ULTSYM.2007.127.

[30] H. Toda and T. Kobayakawa, "High-speed gas concentration measurement using ultrasound," *Sensors and Actuators A: Physical*, vol. 144, no. 1, pp. 1–6, May 2008, doi: 10.1016/j.sna.2007.12.025.

[31] D. Barauskas *et al.*, "CMUT for high sensitivity greenhouse gas sensing," Oct. 2015, pp. 1–4. doi: 10.1109/ULTSYM.2015.0472.

[32] G. Bui *et al.*, "Two Capacitive Micro-Machined Ultrasonic Transducers for Wind Speed Measurement," *Sensors*, vol. 16, no. 6, p. 814, Jun. 2016, doi: 10.3390/s16060814.

[33] H. Carr and C. Wykes, "Diagnostic measurements in capacitive transducers," *Ultrasonics*, vol. 31, no. 1, pp. 13–20, Jan. 1993, doi: 10.1016/0041-624X(93)90028-X.

[34] L. Pizarro *et al.*, "Airborne ultrasonic electrostatic transducers with conductive grooved backplates: tailoring their centre frequency, sensitivity and bandwidth," *Ultrasonics*, vol. 37, no. 7, pp. 493–503, Nov. 1999, doi: 10.1016/S0041-624X(99)00033-5.

[35] J. Hietanen *et al.*, "Factors affecting the sensitivity of electrostatic ultrasonic transducers," *Meas. Sci. Technol.*, vol. 4, no. 10, pp. 1138–1142, Oct. 1993, doi: 10.1088/0957-0233/4/10/018.

[36] D. Certon *et al.*, "A finite difference model For cMUT devices," *IEEE Trans. Ultrason., Ferroelect., Freq. Contr.*, vol. 52, no. 12, pp. 2199–2210, Dec. 2005, doi: 10.1109/TUFFC.2005.1563263.

[37] B. Belgacem *et al.*, "Optimization of the fabrication of sealed capacitive transducers using surface micromachining," *J. Micromech. Microeng.*, vol. 14, no. 2, pp. 299–304, Feb. 2004, doi: 10.1088/0960-1317/14/2/019.

[38] E. Jeanne *et al.*, "Protection Layer Influence on Capacitive Micromachined Ultrasonic Transducers Performance," *MRS Proc.*, vol. 1052, pp. 1052-DD06-27, 2007, doi: 10.1557/PROC-1052-DD06-27.

[39] S. Ngo *et al.*, "Galvanically-Isolated Data Transmission Device," US20130135970A1, May 30, 2013 [Online]. Available: https://patents.google.com/patent/US20130135970A1/en.

[40] N. Senegond *et al.*, "Non-linear dynamic response of cMUTs population: modeling and characterization," in *2009 IEEE International Ultrasonics Symposium*, Rome, Sep. 2009, pp. 426–429. doi: 10.1109/ULTSYM.2009.5441558.

[41] N. Sénégond *et al.*, "High voltage time domain response of cMUT membrane: Laser interferometry measurements," *Physics Procedia*, vol. 3, no. 1, pp. 1011–1016, Jan. 2010, doi: 10.1016/j.phpro.2010.01.130.

[42] N. Senegond *et al.*, "Characterization of cMUT by Dynamic Holography Microscopy," in *2009 IEEE International Ultrasonics Symposium*, Rome, Sep. 2009, pp. 2205–2208. doi: 10.1109/ULTSYM.2009.5441729.

[43] D. Certon *et al.*, "Low frequency cMUT technology: Application to measurement of brain movement and assessment of bone quality," *IRBM*, vol. 34, no. 2, pp. 159–166, Apr. 2013, doi: 10.1016/j.irbm.2013.01.009.

[44] N. Senegond *et al.*, "Fast time-domain modeling of fluid-coupled cMUT cells: from the single cell to the 1-D linear array element," *IEEE Trans. Ultrason., Ferroelect., Freq. Contr.*, vol. 60, no. 7, pp. 1505–1518, Jul. 2013, doi: 10.1109/TUFFC.2013.2723.

[45] A. Boulmé *et al.*, "A capacitive micromachined ultrasonic transducer probe for assessment of cortical bone," *IEEE Transactions on Ultrasonics, Ferroelectrics, and Frequency Control*, vol. 61, no. 4, pp. 710–723, Apr. 2014, doi: 10.1109/TUFFC.2014.2959.

[46] D. Gross *et al.*, "Evaluation of an Ultrasound-Guided Focused Ultrasound CMUT Probe for Targeted Therapy Applications," *OJAppS*, vol. 08, no. 01, pp. 25–45, 2018, doi: 10.4236/ojapps.2018.81003.

[47] I. Ladabaum *et al.*, "Surface micromachined capacitive ultrasonic transducers," *IEEE Transactions on Ultrasonics, Ferroelectrics and Frequency Control*, vol. 45, no. 3, pp. 678–690, May 1998, doi: 10.1109/58.677612.

[48] E. Ventsel and T. Krauthammer, *Thin plates and shells: theory, analysis, and applications*. New York: Marcel Dekker, 2001.

[49] A. S. Erguri *et al.*, "Capacitive micromachined ultrasonic transducers: fabrication technology," *IEEE Transactions on Ultrasonics, Ferroelectrics and Frequency Control*, vol. 52, no. 12, pp. 2242–2258, Dec. 2005, doi: 10.1109/TUFFC.2005.1563267.

[50] F. Patat *et al.*, "A simple distributed model for cMUT [micromachined capacitive ultrasonic transducers]," in *IEEE Ultrasonics Symposium, 2004*, Montreal, Que., Canada, 2004, pp. 248-251 Vol.1. doi: 10.1109/ULTSYM.2004.1417713.

[51] O. Bou Matar *et al.*, "Characterization of airborne transducers by optical tomography," *Ultrasonics*, vol. 38, no. 1–8, pp. 787–793, Mar. 2000, doi: 10.1016/S0041-624X(99)00094-3.

[52] E. Jeanne, "Realisation et caracterisations electromecaniques de transducteurs ultrasonores capacitifs micro-usines," PhD dissertation, University of Tours, 2008.

[53] S. Ngo, "Dispositif acoustique pour l'isolation galvanique : le cmut, une voie innovante," PhD dissertation, University of Tours , 2013.

[54] J. Kühn *et al.*, "Axial sub-nanometer accuracy in digital holographic microscopy," *Meas. Sci. Technol.*, vol. 19, no. 7, p. 074007, Jul. 2008, doi: 10.1088/0957-0233/19/7/074007.

[55] L. Iglesias Hernandez *et al.*, "Discrimination of Binary Gas Mixture Using CMUT Based Sound Attenuation Spectrum Gas Sensor," *Meet. Abstr.*, vol. MA2021-01, no. 59, pp. 1592–1592, May 2021, doi: 10.1149/MA2021-01591592mtgabs.

[56] L. Iglesias Hernandez *et al.*, "Dispositif et procédé de détection d'hydrogène," FR2009222

[57] L. Iglesias, "Resonant Microsystems for Hydrogen Gas Detection without Functionalized Coating," PhD dissertation, University of Bordeaux, 2020.

General conclusion and perspectives

The goal of this study is to design, fabricate, test and validate a microsystem that is capable of detecting the presence of hydrogen in the radioactive environment. This aim has been achieved using the proposed micro resonant systems based on 3C-SiC-µCs (cubic polytype silicon carbide microcantilevers) and CMUTs (capacitive micromachined ultrasonic transducers). These developed hydrogen detectors have successfully measured the changes in gas mixture through changes in their physical properties, such as mass density and ultrasound velocity for targeted detection limit , i.e. less than 1 %.

The first part introduces the context and motivation for the study. Since the heart of the PhD is to develop a hydrogen detector, the range of hydrogen sensors working based on chemical and physical properties detection were discussed. Based on the comparative study, the chemical sensors have the best detection limits, however they suffer from fast aging and longer response times due to their sensitive coatings. In contrast, physical sensors are not affected by these drawbacks but still have higher detection limits, low selectivity, and high setup costs. The currently available chemical or physical sensors were therefore unsuitable for the targeted application. Thus, we proposed 3C-SiC-µCs and CMUTs based physical gas sensors.

The second part began with a general introduction to SiC and its material properties. Then, the design background was discussed in detail. Following that, the main section was presented, i.e. the systematic process flow of 3C-SiC-µCs fabrication. The material to be used for each layer and their dimensions, along with the difficulties encountered during the implementation of a few sub processes, were discussed in this section. Later, microcantilevers with various geometries, namely A0-iREC, A0-iSQR, A1-iREC, A1-iSQR, A3-i and A4-i, were packaged and taken for further characterizations. From the optical (laser Doppler vibrometry) and electrical (impedance) measurements, key parameters like resonance frequency (f_r) and quality factor (Q) were derived. Additionally, the obtained results show higher quality factors for cantilevers respecting Euler-Bernoulli's beam theory, which is $h \ll b \ll L$. We have also noticed that when $L = b/2$, the value of the quality factor was reduced by a factor of 2. However, these results may differ in gas analysis. Finally, to validate gas detection using electromagnetic actuation and induction detection (method I), a cantilever geometry was

chosen arbitrarily, here A0-iSQR. This microcantilever was square (500x500x10 µm^3) and has f_r and Q of 28.55 kHz and 357 respectively. At first, the gas detection was carried out for lower concentrations, i.e 1-4 % of hydrogen (H_2) in nitrogen (N_2) and carbon dioxide (CO_2) in N_2. After successfully detecting these concentrations, we measured very low gas concentrations, i.e. less than 1 %. Here, the changes in the gas concentrations were identified by a shift in resonance frequency. Their corresponding limit of detection (LOD) is tabulated in table 4.1. To mention, following electrical characterization, it was found that microcantilevers with method II detection were ineffective for the first set of measurements. It was caused by an open circuit within piezoresistors. Nevertheless, this can be solved by increasing the thickness of the detection metal layer in future fabrications, ensuring fully functional microcantilevers.

The second microsystem using silicon-nitride based surface-micromachined CMUTs was presented in the last part. First, the CMUT technology was outlined, then its topologies. Followed by explaining the fundamentals of CMUTs along with the design strategies. Thereafter, the chosen membrane sizes, namely 37x37 µm², 37x32 µm², 32x32 µm², 32x27 µm² and 27x27 µm², were packaged and characterized. Primarily, the optical (digital holographic microscopy, DHM) and electrical (impedance) measurements have been carried out. The characterization results provide information about the collapse voltage (V_c), resonance frequency, initial deflection, and complete gap height. Using this information, one can easily determine the electromechanical coupling coefficient, the quality factor, and the low and high frequency capacitances. Then, the electroacoustic characterizations were performed in air using time of flight (ToF) detection technique (method IV). This characterization allowed us to optimize excitation parameters, like the emission frequency (f_e), percentage of V_c used for the receiver and emitter (V_{bias}), and alternating voltage (V_{ac}). At the end of electrical and electroacoustic characterizations, 32x32 µm² geometry was chosen to conduct gas mixture analysis for both detection methods, which were method III and IV respectively. We chose this geometry in particular because it was homogenous, durable, needed a lower voltage, and had a 100 % fractional bandwidth. Later, the binary gas mixture analyses have been performed for low concentrations (1-4 %) and then at very low concentrations (less than 1 %) of H_2 in N_2 and CO_2 in N_2, using ToF technique, at 1 MHz f_e, 47 V_{bias} (70 % V_c), 15 V_{ac}. The obtained LOD for this method is tabulated in table 4.1. Similarly, the gas analysis has been carried out for method III detection with the same chosen parameters and geometry. Here, the changes in gas concentration were identified using shifts in resonance frequency, like SiC cantilevers.

The obtained LOD of H_2 in N_2 and CO_2 in N_2, for method I, III and IV detections are tabulated in table 4.1.

Table 4.1: Measured limit of detection for H_2 in N_2 and CO_2 in N_2 for various proposed detection methods.

Method of detection	Limit of detection	
	Hydrogen in nitrogen	Carbon dioxide in nitrogen
Resonance mode detection using 3C-SiC-µCs (Method I)	0.20 %	0.25 %
Resonance mode detection using CMUTs (Method III)	0.04 %	0.25 %
Time of flight detection using CMUTs (Method IV)	0.15 %	0.30 %

These promising results make our device a suitable gas sensor with state-of-the-art detection technique, i.e. uncoated CMUTs combined with ToF, in method IV and also with chosen material, 3C-SiC, in method I and II detections.

As mentioned earlier, method II microcantilevers do not function due to open circuits in detection metal gauges. But this could be resolved by increasing the thickness of the detection metal. On a positive note, the currently working 3C-SiC-µCs based on electromagnetic actuation and induction detection offer hope for next generation MEMS devices that are suitable for operating in extreme environments. Thus, depending on the method chosen, many other perspectives are possible. Below are some recommendations for future works:

- A surface micromachined CMUT gas sensor based on 3C-SiC also presents an attractive solution, as it can simultaneously measure gas density and ultrasound velocity, and also serves in radioactive environments. This reduces the risk of false alarm and opens a path to many other MEMS/NEMS applications, especially for sensors working in harsh environments and can be applied to all kinds of medical devices, because they are biocompatible.
- The presently used CMUTs can be further optimized by increasing the number of emitter/receiver CMUTs to increase the transmission field. In addition, the working distance measurement mentioned in §3.6.5 gives hope for other potential ToF applications, like proximity sensor, position sensors, etc. Further, the ability to use CMUTs as bimodal gas sensors, in combination with method III and IV detections simultaneously, opens doors for future applications like "electronic-nose".

- Subsequently, in terms of CMUTs design optimization, we propose a metallization ratio from 50 % to 100 % of the top electrode. This is to reduce the stress on the membrane layer and lower initial deflection.
- Both the microsystems, i.e. 3C-SiC-µCs and CMUTs gas detectors can be further optimized depending on different gas discrimination technique, such as peak detection in time domain, phase detection in frequency domain, attenuation measurement, etc., to achieve better sensitivity and LOD.

Scientific contributions

Peer Reviewed Articles

- **P. Shanmugam**, L. Iglesias, J.-F. Michaud, D. Alquier, L. Colin, I. Dufour and D. Certon, "Broad Bandwidth Air-Coupled Micromachined Ultrasonic Transducers for Gas Sensing". *Ultrasonics*, vol. 114, p. 106410, Jul. 2021, doi: 10.1016/j.ultras.2021.106410.
- L. Iglesias, **P. Shanmugam**, J.-F. Michaud, D. Alquier, D. Certon and I. Dufour, "Proof of Concept and Preliminary Results of Gas Detection by Measuring the Admittance at the Resonance and Antiresonance of an Uncoated CMUT", *Frontiers in Mechanical Engineering*, vol. 6, pp. 14, Mar. 2020, doi: 10.3389/fmech.2020.00014.

Patents

- **P. Shanmugam**, L. Iglesias Hernandez, D. Certon, J.-F. Michaud, L. Colin, I. Dufour. Dispositif et procédé d'identification d'une contamination gazeuse. FR n°2009223 (filed patent).
- **P. Shanmugam**, L. Iglesias Hernandez, D. Certon, J.-F. Michaud, L. Colin, I. Dufour. Dispositif et procédé de détection d'hydrogène. FR n°2009222 (filed patent).

Conference Proceedings

- **P. Shanmugam**, L. Iglesias, M. Portail, I. Dufour, D. Certon, D. Alquier and J.-F. Michaud, "A New Approach in the Field of Hydrogen Gas Sensing using MEMS based 3C-SiC-µCs", *Materials Science Forum*, 2022, Vol. 1062, pp. 593-597. Trans Tech Publications, Ltd. https://doi.org/10.4028/p-m048qs. Awarded as Best Poster at ECSCRM21.
- L. I. Hernandez, **P. Shanmugam**, J.-F. Michaud, D. Alquier, D. Certon and I. Dufour, "Hydrogen Selective Gas Sensor Based on Attenuation Measurement of Acoustic Wave

Using Uncoated CMUT", *2021 IEEE 34th International Conference on Micro Electro Mechanical Systems (MEMS)*, 2021, pp. 398-401, doi: 10.1109/MEMS51782.2021.9375432.

- L. I. Hernandez, **P. Shanmugam**, J.-F. Michaud, D. Alquier, D. Certon and I. Dufour, "CMUT Time of Flight Gas Sensor By Phase Shift Measurement", *2020 ECS-The Electrochemical Society*, vol. MA2020-01, doi: https://doi.org/10.1149/MA2020-01312323mtgabs.
- **P. Shanmugam**, L. Iglesias, J.-F. Michaud, I. Dufour, D. Alquier, L. Colin and D. Certon, "CMUT Based Air Coupled Transducers for Gas-Mixture Analysis", *2018 IEEE International Ultrasonics Symposium (IUS)*, pp. 1-4, Oct. 2018, doi: 10.1109/ULTSYM.2018.8579789.

Extended Summary

Conception, fabrication et caractérisation de microsystèmes résonnants pour la détection de l'hydrogène dans l'environnement radioactif

I. Introduction

L'hydrogène (H_2) est un gaz unique qui est hautement inflammable lorsqu'il est mélangé à une concentration de 4 à 75 % dans le volume d'air. Ce gaz incolore, inodore et sans saveur est indiscernable pour les organes sensoriels humains. En outre, c'est l'élément chimique le plus léger qu'il est donc difficile de contenir. Il est donc important de surveiller la concentration de H_2 dans l'air, étant donné la nature dangereuse et risquée de ce gaz. L'hydrogène étant largement utilisé dans les industries métallurgiques et dans de nombreuses applications spatiales, une surveillance rapide et précise devient essentielle pour améliorer le niveau de sécurité et éviter le risque d'explosion. La détection de la concentration d'hydrogène a une histoire de plus d'un siècle [1]. Néanmoins, il existe une demande continue pour des capteurs d'hydrogène rapide, précis et plus sensible pour surveiller et contrôler la concentration de gaz, ce qui est nécessaire pour de nombreuses applications industrielles. De plus, en parlant de leurs applications, on ne peut passer sous silence les nombreuses recherches en cours sur la production d'énergie à partir d'hydrogène. En effet, dans un avenir proche, il y aura un énorme besoin de surveillance de l'hydrogène dans la production, le transport et le stockage, que ce soit dans les pipelines, dans les stations de ravitaillement ou dans les véhicules automobiles [2].

Comme nous l'avons mentionné, les besoins en matière de production d'hydrogène sont en augmentation. Il est donc essentiel de surveiller le dégagement d'hydrogène pendant le stockage et/ou le retraitement des déchets nucléaires. À titre d'exemple, dans les mines de charbon, l'émission soudaine de niveaux importants de sulfure d'hydrogène (H_2S) présent dans les charbons et les couches rocheuses a provoqué des catastrophes imprévues. Il est donc crucial de surveiller ce type d'émission d'H_2S car elle provoque l'étincelle lors d'un accident et a un impact sérieux sur la santé humaine [3], [4]. De même, dans les centrales nucléaires, de l'hydrogène peut se former en raison du stockage des déchets radioactifs. Cela peut provenir soit du retraitement du plutonium par radiolyse de l'eau, soit d'une réaction avec des matériaux

métalliques parmi ces déchets, qui produisent de l'hydrogène par corrosion dans un environnement anoxique (corrosion par l'eau en l'absence d'oxygène) conduisant à une explosion. Pour donner des exemples, trois accidents causés par une explosion d'hydrogène ont été mentionnés, à savoir Three Mile Island (1979), Chernobyl (1986) et Fukushima Daiichi (2011) [5]–[7]. Pour cette raison, on peut facilement comprendre que la surveillance rapide et précise de ces types d'environnements difficiles est obligatoire.

II. Contexte, motivation et projet H2MEMS

Actuellement, l'énergie nucléaire est la source essentielle d'électricité dans de nombreux pays, notamment en France, où 67 % de l'électricité est produite par des centrales nucléaires, selon les données de 2020 [8], [9]. Même si la part de l'énergie nucléaire en France devrait diminuer de 50 % en 2035, il est essentiel de préserver les déchets moyennement actifs à longue durée de vie (MA-LL) et hautement radioactifs (HA) produits actuellement avec beaucoup de précautions pour éviter les catastrophes, comme expliqué dans l'introduction. C'est pourquoi, en France, l'Agence nationale pour la gestion des déchets radioactifs (ANDRA), a été créée en 1979 par le CEA (Commissariat à l'énergie atomique et aux énergies alternatives) pour gérer ces déchets radioactifs à long terme sur le territoire français.

L'ANDRA est devenue une agence publique autonome en 1991 sous la tutelle des ministères français de l'énergie, de l'environnement et de la recherche. Depuis lors, une série d'activités de recherche ont été menées pour gérer en toute sécurité les déchets radioactifs dangereux. Ainsi, en 2006, l'ANDRA a eu l'idée de construire un centre industriel de stockage géologique, appelé "projet Cigéo" (Centre industriel de stockage géologique). Ce centre de stockage géologique profond situé en Meuse/Haute-Marne, en France, est construit sous la surface de la terre (environ ≈500 m), afin de traiter et de stocker correctement les déchets radioactifs, comme le montre la figure 1. L'élimination des déchets aura lieu pendant 100 ans, puis l'installation sera scellée pour contenir les déchets radioactifs pendant une longue période sans intervention humaine.

L'objectif principal du projet H2MEMS est de développer des capteurs d'hydrogène gazeux pour la surveillance à long terme de son installation de stockage géologique profond. Dans ce type d'unité de stockage souterrain, la libération d'hydrogène est attendue en raison de la corrosion des métaux dans un environnement anoxique. Les composants structurels tels que les

cadres métalliques, des concentrés renforcés, les conteneurs de déchets ou la présence de grandes quantités de matériaux métalliques parmi ces déchets peuvent constituer un problème majeur. Cependant, l'hydrogène est inflammable à des concentrations de 4 à 75 % dans l'air. L'hydrogène peut également provoquer des explosions en présence d'éléments déclencheurs appelés énergie d'activation, comme les ultrasons, l'électricité statique, les chocs, etc. Par conséquent, il est important de surveiller régulièrement cet environnement. En outre, pour éviter l'accumulation de gaz, les installations souterraines et de surface seront ventilées pendant la période d'exploitation. Par conséquent, notre capteur d'hydrogène spécialement développé sera placé au niveau du système de ventilation pour la détection des gaz, ceci afin d'éviter le risque d'explosion et améliorer les mesures de sécurité.

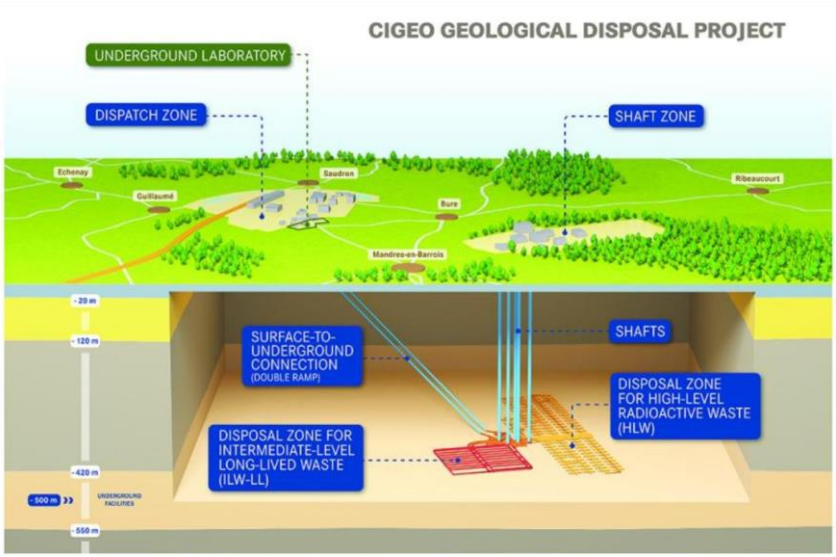


Figure 1: Schéma de l'installation de stockage radioactif en couche géologique profonde construite par l'ANDRA, dans le cadre du projet Cigéo [10].

Le projet H2MEMS est un projet de cinq ans impliquant quatre laboratoires en France. Ce sont: i) le laboratoire IMS (Intégration du Matériau au Système) à Bordeaux ; ii) le laboratoire CRHEA (Centre de Recherche sur l'Hétéro-Epitaxie et ses Applications) à Nice; iii) le LAAS-CNRS (Laboratoire d'analyse et d'architecture des systèmes) à Toulouse et iv) le laboratoire GREMAN (Groupe de Recherche en Matériaux, Microélectronique, Acoustique et Nanotechnologies) à Tours. Chaque laboratoire réalise une étape clé dans la création du dispositif. Le CRHEA fournit les épi-wafers pour la fabrication des microcantilevers 3C-SiC. Ensuite, le GREMAN fabrique les capteurs d'hydrogène avec l'électronique fournie par le LAAS et les caractérise dans un environnement aérien avant de les soumettre à des tests au gaz.

Enfin, IMS teste et valide les prototypes finaux dans un environnement de mélange gazeux. Pour mémoire, Pr. Isabelle Dufour, d'IMS, est la coordinatrice du projet.

III. Problème des capteurs chimiques et physiques actuellement utilisés

Les capteurs d'hydrogène sont largement utilisés dans de nombreuses industries pour des raisons de sécurité. Les exigences varient en fonction des applications. D'après la littérature, il est clair que l'histoire des capteurs d'hydrogène a été discutée pendant plus d'un siècle [1]. De nombreuses technologies ont été développées et démontrées, dont les principles sont présentées dans [2], [11]. Indépendamment de leur principe de fonctionnement, ces capteurs de gaz peuvent être classés en deux types en fonction de leur mécanisme de détection, à savoir les capteurs chimiques et physiques.

Tout d'abord, les capteurs chimiques sont toujours recouverts d'un polymère sensible, afin d'absorber le d'intérêt gaz. Ces capteurs sont très stables et très sensibles, mais leur temps de réponse est long. Cela est dû au processus d'absorption et de désorption chimique. Jusqu'à présent, de nombreux types de capteurs d'hydrogène ont été fabriqués et vendus dans le commerce, notamment des capteurs électrochimiques, catalytiques et à fibre optique. Néanmoins, aucun d'entre eux ne répond aux attentes en matière de survie dans un environnement difficile. D'après le tableau 1, les capteurs de type catalytique présentés ont besoin d'au moins 5-10 % d'oxygène pour fonctionner et n'ont aucune sélectivité vis-à-vis de l'hydrogène. En outre, il existe un risque d'empoisonnement dû à la contamination du catalyseur. Toutefois, ils ont une longue durée de vie et sont plus stables.

En termes de coût, les capteurs électrochimiques nécessitent un équipement électrique coûteux pour effectuer des mesures ampérométriques ou potentiométriques [2]. Les capteurs catalytiques et électrochimiques sont sensibles à d'autres gaz réducteurs, ce qui les rend peu fiables [12]. Dans le cas des capteurs à fibres optiques, ils utilisent des revêtements sensibles et des signaux lumineux pour la surveillance des gaz. Le problème réside dans le coût, la taille de la structure et la limite de détection. Si la précision est meilleure, alors il n'y a pas de détection multipoint et vice versa [13].

Tableau 1: Avantages et inconvénients des capteurs chimiques et physiques.

Type	Technologie		Avantages	Inconvénients
Chimiques	Catalytiq-ue	Pellistor Thermoélectrique	Robuste Facile à utiliser Température de fonctionnement élevée Stable Durable	Pas de sélectivité Nécessite de l'oxygène pour la détection Temps de réponse long Sensible à la température Besoin en énergie élevé Le catalyseur peut être inactif (ou) empoisonné par la contamination.
	Électrochi-mique	Ampérométrique Potentiométrique	Sensible Faible consommation d'énergie Ne nécessite pas de chauffage de l'élément Température de fonctionnement élevée	Non durable Coûteux Sensibilité croisée au CO Nécessite un étalonnage périodique
	Fibre optique	Micromiroir Champ évanescent	Haute sensibilité Structure simple Moins cher Surveillance à longue distance Faible temps de réponse	Complexité de la miniaturisation Convient uniquement à la mesure ponctuelle Faible stabilité mécanique
		SPR	Haute précision Sensible et réactif	Pas de détection multipoint Coûteux Structure complexe
		Interférences	Haute précision Bonne répétabilité Sensible	Grande structure Pas de compensation de température Ne peut pas travailler dans un environnement instable
		FBG	Détection multi-points Large gamme de mesures Favorable à la télédétection Insensible aux fluctuations d'intensité	Faible sensibilité Limite de détection élevée
Physiques	Conductivité thermique		Temps de réponse court Moins cher Stable Robuste Large plage de mesure	Pas de sélectivité Sensibilité croisée à l'hélium LOD élevé L'élément chauffant réagit avec le gaz
	LIDAR		Mesure à longue distance Haute sélectivité	Consommation d'énergie élevée Grande structure Limite de détection élevée Coûteux

Les capteurs physiques, eux, n'utilisent pas de revêtements sensibles comme les capteurs chimiques. Ils ont donc un temps de réponse court. Les capteurs physiques thermo-conducteurs sont plus stables, plus robustes, moins coûteux et ont une large plage de mesure, mais ils souffrent de problèmes de sensibilité croisée et ont une limite de détection élevée [14]. Les capteurs basés sur le lidar Raman sont très sélectifs vis-à-vis de l'hydrogène et peuvent surveiller de longues distances (plusieurs mètres). Par exemple, pour surveiller quotidiennement la qualité de l'air, les gaz ou la poussière sur les chantiers de construction [15]. Ces types de capteurs sont énormes et coûteux en raison du coût du laser et de l'analyseur de spectre et consomment beaucoup d'énergie [16]. Les avantages et inconvénients globaux des différentes techniques sont brièvement résumés dans le tableau 1.

IV. Notre approche de la détection de l'hydrogène gazeux

L'objectif de ce projet est de développer un microsystème pour surveiller la présence d'hydrogène dans les environnements radioactifs. Comme expliqué dans la section II, l'ANDRA a construit une installation de stockage en couche géologique profonde pour stocker les déchets radioactifs. Cette installation souterraine sera ventilée pendant la période d'exploitation et surveillée après sa fermeture, pour des raisons de sécurité. Malgré la haute sensibilité des capteurs chimiques, ils souffrent de certains inconvénients, tels qu'un temps de réponse élevé (dû à l'adsorption et à la désorption chimique), une faible fiabilité et l'irréversibilité, qui sont principalement liés à leurs revêtements sensibles. D'autre part, les capteurs physiques ont une grande sélectivité et un temps de réponse court, mais la limite de détection et le coût de l'installation sont élevés (par exemple, le lidar Raman). En outre, la plupart d'entre eux ne sont pas conçus pour fonctionner dans des environnements hostiles (voir section III).

L'application visée nécessite un capteur d'hydrogène de petite taille, robuste, durable et très réactif. Dans notre étude, nous proposons deux microsystèmes pour la surveillance de l'hydrogène, comme expliqué ci-dessous. Tous deux détectent les changements dans un mélange gazeux binaire en fonction de la variation des propriétés physiques, telles que la densité massique et la vitesse acoustique. Ces capteurs ne sont pas recouverts de matériaux sensibles pour absorber le gaz d'intérêt. Cela les rend très réactifs et durables.

IV.A Détection de gaz basée sur un micropoutre 3C-SiC

Les capteurs de gaz classiques sont fabriqués en silicium ou en céramique piézoélectrique. Les principaux inconvénients de ces systèmes classiques sont leur vieillissement, leur faible fiabilité et leur incapacité à survivre dans des environnements difficiles. C'est pourquoi le premier microsystème est fabriqué en utilisant du carbure de silicium (SiC). Ce matériau est avantageux par rapport aux matériaux classiques pour les raisons suivantes :

- Robuste et durable - grâce à ils impressionnantes propriétés mécaniques et physiques. C'est le matériau le plus adapté pour travailler dans un environnement hostile;
- Stabilité chimique - le SiC est inerte à la plupart des produits chimiques et résiste à tous les acides et solvants couramment utilisés lors de la microfabrication. Cela le rend presque universellement résistant à la corrosion;
- Énergie de seuil - en général, les semi-conducteurs génèrent des défauts lorsqu'ils sont exposés à un rayonnement extrême et ces défauts sont directement proportionnels à l'énergie de seuil du matériau. Dans le cas du SiC, l'énergie de seuil est plus élevée que celle du silicium, ce qui le rend plus adaptable aux environnements exposés aux rayonnements.

Plus de 250 polytypes de SiC existent et sont classés en fonction de leurs structures cristallines [17]. Parmi tous, ceux le dans notre étude, nous avons choisi de travailler avec le polytype cubique, c'est-à-dire le 3C-SiC. Cela nous permet de faire croître un film mince de 3C-SiC (100) par épitaxie sur un substrat Si (100) peu coûteux. Comme la technologie industrielle du silicium est bien développée, cela facilite l'intégration du dispositif et rend le capteur rentable.

La micropoutre en 3C-SiC fonctionne par actionnement électromagnétique. Ce capteur de gaz de type cantilever n'utilise pas de revêtement sensible et dispose de deux techniques de détection pour les analyses de mélanges gazeux binaires, à savoir: i) l'induction (méthode I) et ii) la piézo-résistance (méthode II). À noter que la conception avait déjà été validée par Boudjiet pour le mécanisme de détection piézo-résistive [18]. De plus, un deuxième ensemble de poutres a été produit avec le même actionnement mais avec un mécanisme de détection différent (i.e. induction). Dans les deux cas, le principe de fonctionnement est basé sur la loi de Laplace, où le courant induit $\left(\vec{I}(t)\right)$ dans le circuit, pour la tension appliquée (V_{act}), change la direction du

champ magnétique $(\vec{B})$, qui est imposé par l'aimant et exerce une force mécanique $(\vec{F}(t))$, comme le montrent les figures 2 et 3.

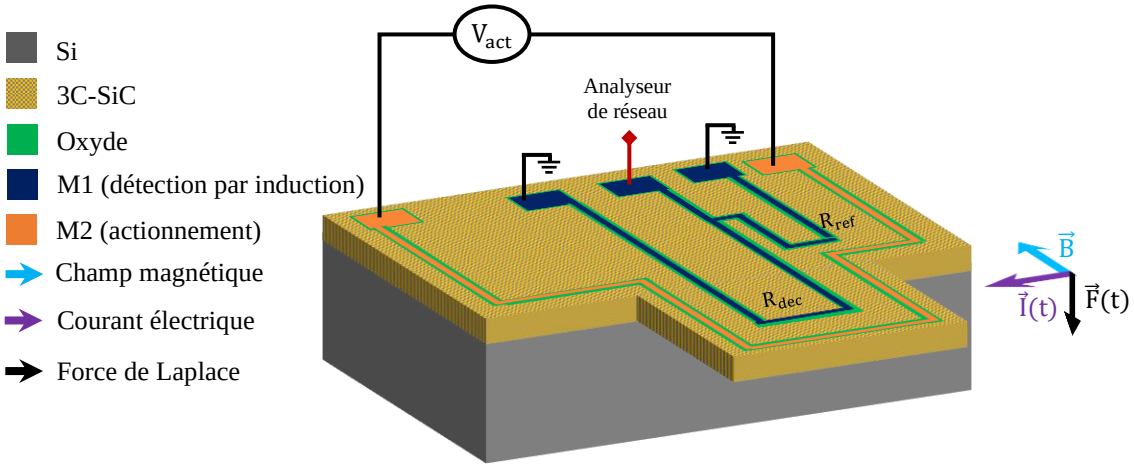


Figure 2: Micropoutre à base de 3C-SiC qui fonctionne par actionnement électromagnétique et détection par induction (méthode I).

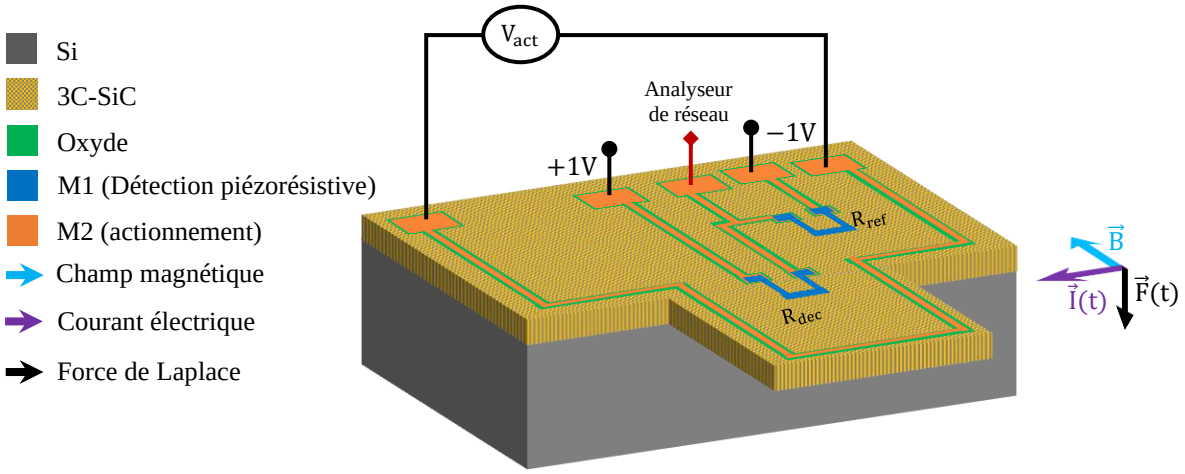


Figure 3: Micropoutre à base de 3C-SiC qui fonctionne par actionnement électromagnétique et détection piézorésistive (méthode II).

La détection par induction et la détection piézo-résistive sont toutes deux constituées de deux résistances, dont l'une se trouve sur la partie stable qui sert de référence (R_{ref}) et l'autre sur le cantilever pour détecter le changement de mouvement (R_{dec}). Le schéma de l'installation de mesure des gaz pour cette méthode est présenté à la figure 4. Ici, la détection est due à la modification du mélange gazeux est identifiée à l'aide du décalage de la fréquence de résonance. L'historique du choix des matériaux, leurs processus de fabrication complexes, les résultats de la caractérisation dans l'air pour vérifier la fonctionnalité du dispositif et la détection de l'hydrogène dans l'azote sont décrits dans cette étude.

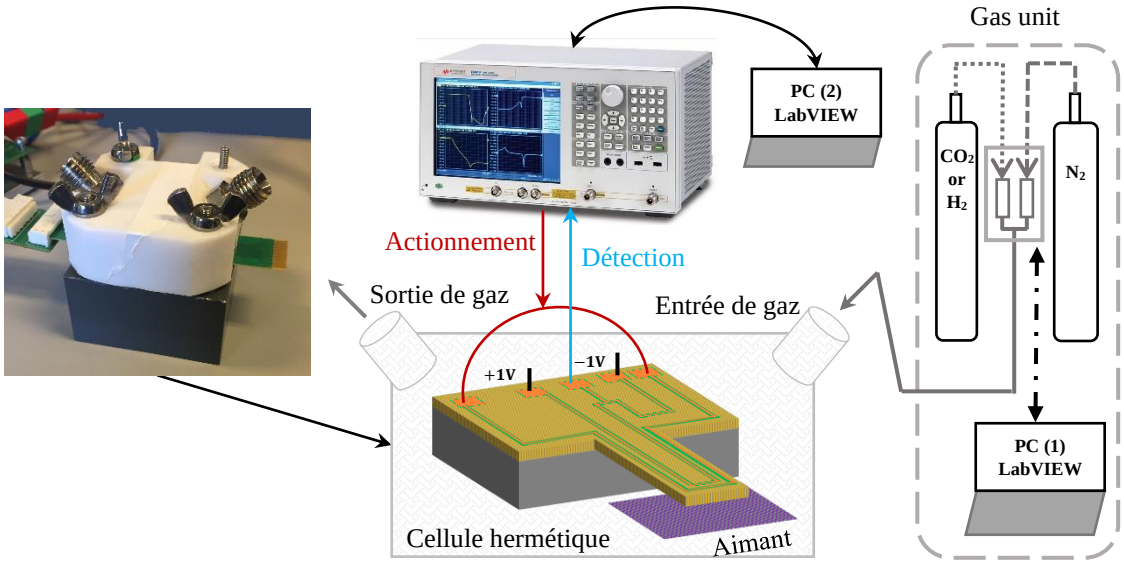


Figure 4: Schéma du protocole expérimental permettant de mesurer le décalage de la fréquence de résonance pour différentes concentrations de gaz présentes à l'intérieur de la cellule hermétique dans un environnement de mélange gazeux.

La première série d'analyses de gaz est réalisée avec de l'hydrogène (H_2) dans de l'azote (N_2) pour des concentrations de gaz allant de 1 % à 4 %. Ici, l'azote est utilisé comme gaz de référence. Le changement de la concentration de gaz est suivi pour son décalage relatif dans la fréquence de résonance, comme le montre la figure 5. La concentration de gaz est modifiée tous les 5 min avec passage à100 % d'azote, pour réinitialiser la mesure. Le résultat obtenu correspond à celui obtenu par Boudjiet *et al.* c'est-à-dire que la fréquence de résonance augmente avec l'augmentation de H_2 dans N_2, du fait que l'hydrogène est plus léger que l'azote [19].

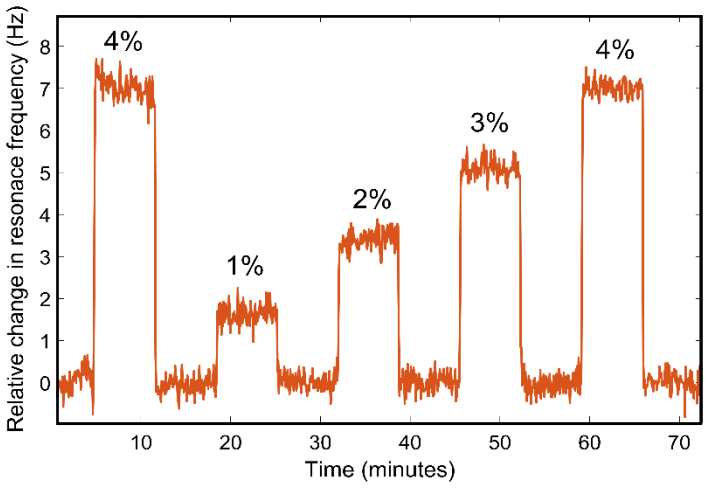


Figure 5: Déplacement relatif mesuré de la fréquence de résonance pour H_2 dans N_2 de A0-iSQR 3C-SiC-µC.

Par la suite, le dioxyde de carbone (CO_2) dans N_2 a également été testé pour les concentration de gaz déjà mentionnée, afin de vérifier que la mesure est due à la modification de la densité massique du gaz. D'après la figure 6, le décalage relatif de la fréquence diminue avec l'augmentation de la concentration du gaz. Ceci est dû au fait que le CO_2 est plus lourd que le N_2. Nos résultats valident le principe de détection proposé par Boudjiet *et al.* mais en utilisant des 3C-SiC-µCs, qui peuvent fonctionner dans des environnements difficiles.

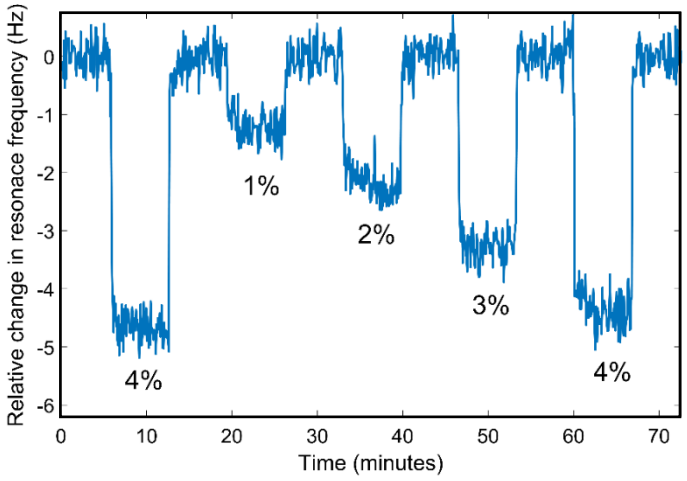


Figure 6: Déplacement relatif mesuré de la fréquence de résonance pour CO_2 dans N_2 de A0-iSQR 3C-SiC-µC.

Avant de réussir à mesurer des mélanges de gaz binaires, les expériences de limite de détection (LDD) sont évaluées avec de très faibles concentrations de gaz, c'est-à-dire de 0,2 % à 2 %. D'après la figure 7, les limites de détection pour H_2 dans N_2 et CO_2 dans N_2 sont de 0,2 % et 0,25 % respectivement.

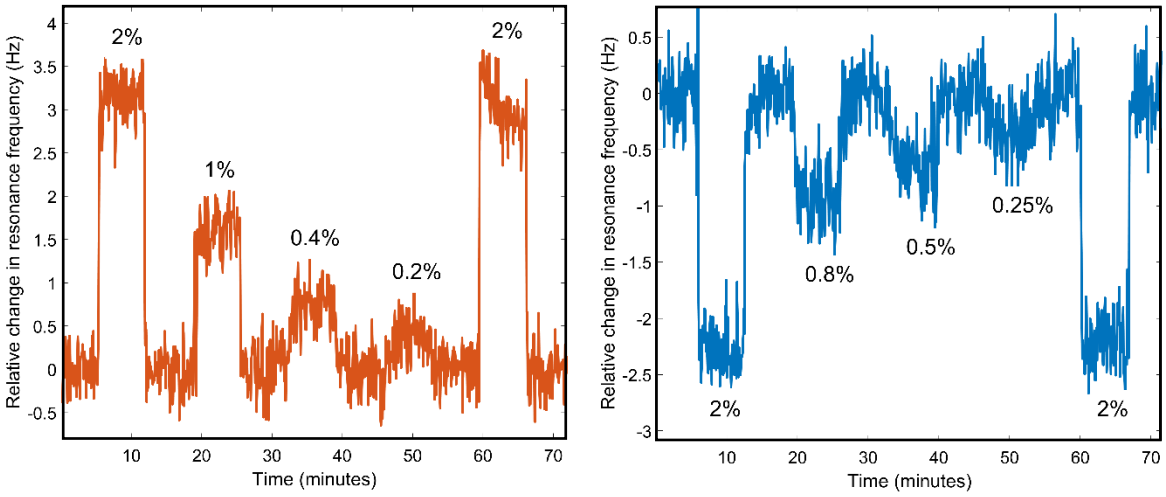


Figure 7: Mesure de la limite de détection pour la plus faible concentration de H_2 dans N_2 (à gauche) et de CO_2 dans N_2 (à droite).

IV.B Détection de gaz basée sur des transducteurs ultrasoniques micro-usinés capacitifs (CMUT)

Le deuxième système est un CMUT micro-usiné en surface qui fonctionne selon un mécanisme électrostatique. Ces CMUT ont été fabriqués pour des applications d'imagerie ultrasonore comme mentionné dans [20]. Plus tard, ils ont été utilisés dans des applications de détection de produits chimiques ou de gaz pour les raisons suivantes :

- Versatilité - peut être utilisé pour une gamme d'applications en modifiant quelques paramètres de conception;
- Évolutivité - la taille du dispositif peut être modifiée en fonction des besoins de l'application et les CMUT ne nécessitent pas d'énormes unités d'alimentation externes;
- Techniques de fabrication standard - les processus de micro-usinage de surface et de collage des plaquettes sont classiques pour les industries microélectroniques;
- Le parallélisme - améliore la résolution en contrôlant le bruit de fréquence par l'ajout de plusieurs micro-résonateurs homogènes en parallèle. Le parallélisme améliore la résolution en contrôlant le bruit de fréquence par l'ajout de multiples micro-résonateurs homogènes en parallèle.

Les CMUT utilisés dans notre étude fonctionnent selon deux techniques de détection. Premièrement, on utilise la surveillance de la variation du mélange gazeux en utilisant le décalage de la fréquence de résonance (méthode III). Ce mécanisme de détection est classiquement utilisé dans la plupart des applications de détection de gaz avec les CMUT. La figure 8 montre le schéma d'un seul prototype de CMUT placé dans une chambre à gaz pour l'analyse d'un mélange gazeux binaire. En outre, le graphique représente la technique de détection, c'est-à-dire le décalage de la fréquence de résonance (Δf_r) pour le changement de la concentration de gaz. Ce décalage est dû au changement de la propriété physique du gaz, c'est-à-dire la densité. Ici, les CMUT fonctionnent dans la gamme des hautes fréquences, en mode résonance.

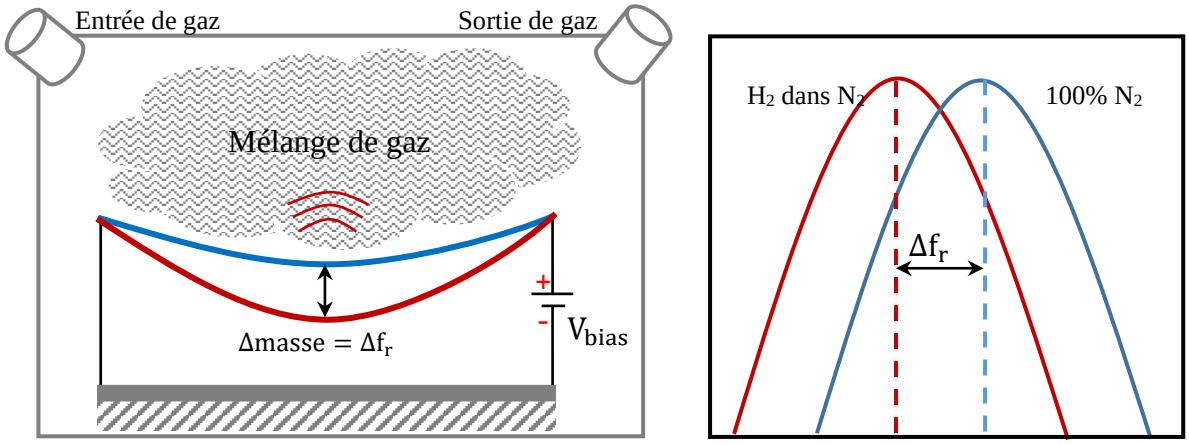


Figure 8: Schéma de la détection de gaz avec le mécanisme de la méthode III [21].

Comme expliqué précédemment, ici le changement relatif de la concentration de gaz est identifié par le déplacement de la fréquence de résonance, c'est-à-dire à l'admittance du système. La première analyse de gaz est effectuée pour une concentration comprise entre 1 % et 4 % pour deux mélanges de gaz: le dioxyde de carbone (CO_2) dans l'azote (N_2) et l'hydrogène (H_2) dans l'azote, comme le montre la figure 9. Les résultats présentés sont effectués à 60 % de tension de collpase (35 V_{bias}), où le meilleur compromis entre sensibilité et bruit est mesuré, comme indiqué dans [21].

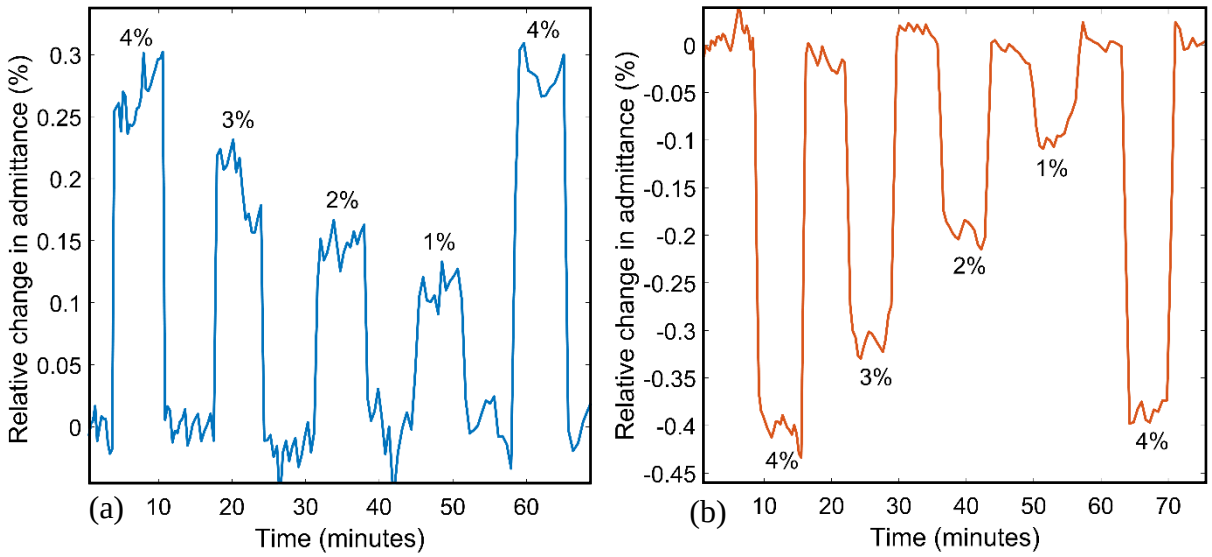


Figure 9: Changement relatif mesuré de l'admittance pour le changement des concentrations de gaz de (a) CO_2 dans N_2 et (b) H_2 dans N_2 à 35 V_{bias} [21].

Avec ces résultats encourageants, la mesure de la limite de détection (LDD) a été effectuée. Les résultats respectifs sont présentés dans la figure 10. La LDD mesurée pour de très faibles concentrations de CO_2 dans N_2 et de H_2 dans N_2 est de 0,25 % et 0,04 % respectivement. Même

si le LDD n'est pas aussi élevé que les capteurs de gaz à revêtement sensible dans l'état de l'art. Cela peut être atteint par des optimisations supplémentaires dans les futurs dispositifs.

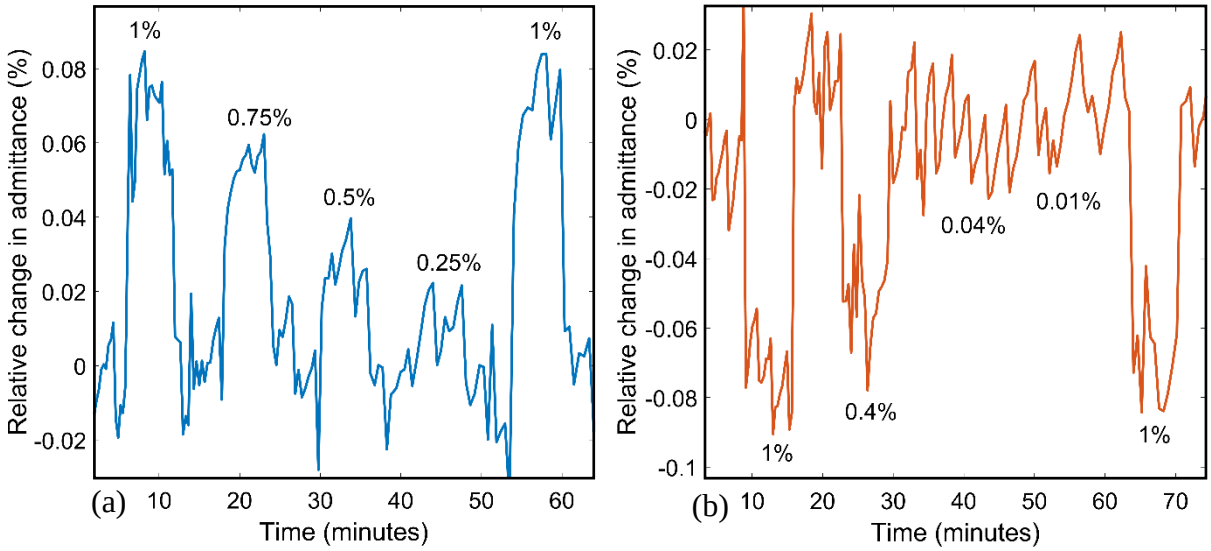


Figure 10: Variation relative mesurée de l'admittance pour une variation de la très faible concentration de gaz de (a) CO_2 dans N_2 et (b) H_2 dans N_2 à 35 V_{bias} [21].

Ensuite on s'est intéressé à, la variation de la concentration de gaz qui est détectée à l'aide de la technique du temps de vol (ToF) (méthode IV). En utilisant ce principe de détection, on peut surveiller la variation de la propriété acoustique du gaz, c'est-à-dire la vitesse des ultrasons. Contrairement à la troisième méthode, cette technique nécessite deux ensembles de CMUT, dont l'un sert d'émetteur et l'autre de récepteur, comme le montre la figure 11.

De plus, elle fonctionne à un régime quasi-statique, c'est-à-dire bien plus bas que sa fréquence de résonance, comme pour un microphone. Cela nous permet d'obtenir la bande passante la plus large et la réponse impulsionnelle la plus faible possible. Dans cette étude, l'optimisation du design, la création de prototypes, leurs caractérisations électroacoustiques dans des environnements d'air et de mélange gazeux sont étudiés de manière approfondie.

Comme expliqué précédemment, le temps de vol varie/décale en fonction de la vitesse du son (Δc). Lors de l'introduction de CO_2, la vitesse du son à l'intérieur de l'unité de détection de gaz varie, ce qui entraîne le décalage du pic de ToF.

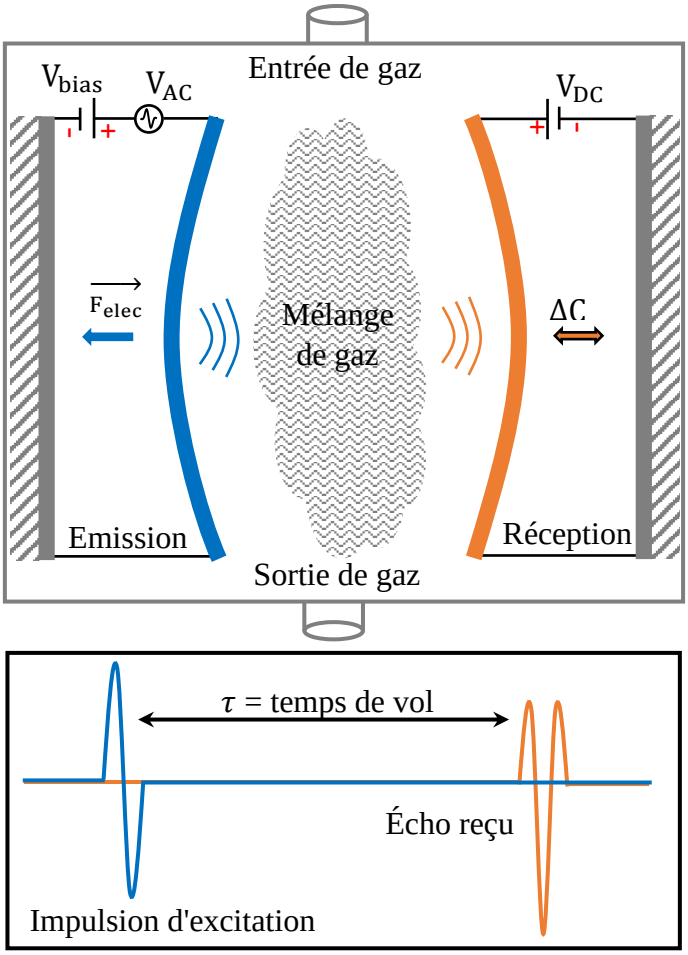


Figure 11: Schéma de la détection de gaz avec le mécanisme de la méthode IV [22].

Les expériences sont réalisées pour de faibles concentrations de CO_2 dans N_2 et de H_2 dans N_2. Les pics de détection mesurés pour la variation relative de la ToF pour des concentrations de gaz de 1 à 4 % de CO_2 dans N_2 et de H_2 dans N_2 sont présentés à la figure 12, pour 47 V_{bias} appliqué, 15 V_{ac} à la fréquence d'émission de 1 MHz.

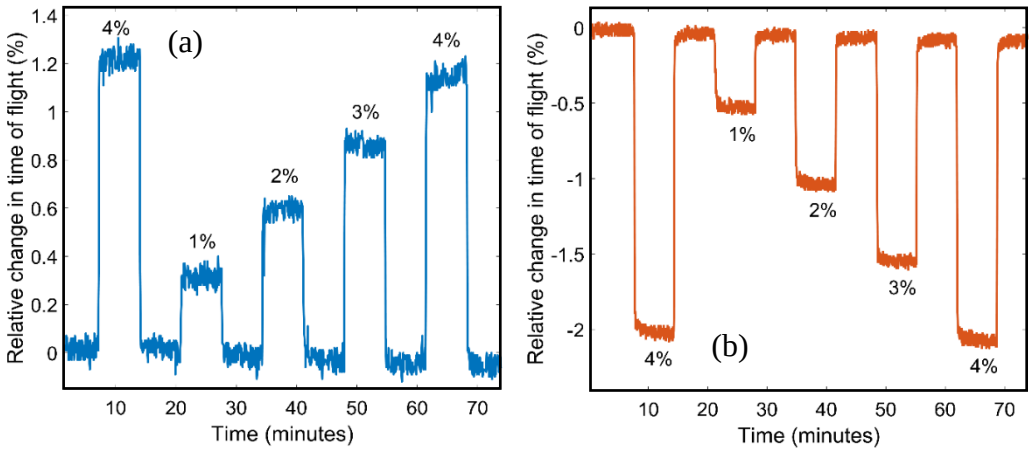


Figure 12: Résultats expérimentaux de la ToF pour des concentrations de gaz inférieures à 4 % de (a) CO_2 dans N_2, (b) H_2 dans N_2 à 47 V_{bias}, 15 V_{ac} et 1 MHz f_e [22].

En outre, la détection de gaz pour de très faibles concentrations de gaz (<1 %) a été réalisée. Ces résultats ont fourni la LDD du système actuel pour les conditions d'excitation appliquées. La figure 13 montre que la limite de détection est de 0,3 % et 0,15 % pour le CO_2 dans N_2 et le H_2 dans N_2 respectivement.

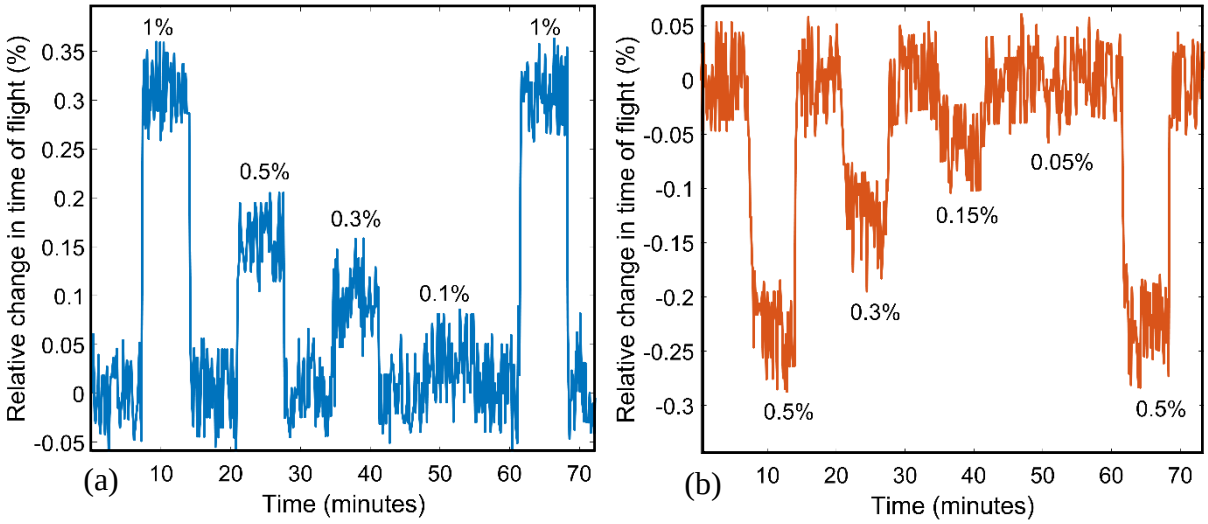


Figure 13: Temps de vol expérimental dans un environnement gazeux pour de faibles concentrations de (a) CO_2 dans N_2, (b) H_2 dans N_2 à 47 V_{bias}, 15 V_{ac} et 1 MHz f_e.

Pour donner un ordre de grandeur, les résultats expérimentaux avec le premier écho attendu de la ToF à la distance de 7,14 mm pour les concentrations de gaz purs sont présentés dans le tableau 2. D'après ces valeurs, il est clair que les différences de ToF entre le CO_2 pur et le N_2 sont de 6 µs et entre le H_2 pur et le N_2 sont de -14,6 µs, où le signe négatif indique le décalage dans la direction opposée qui peut être mis en évidence sur la figure 13.b respectivement. En outre, le tableau 2 présente le LDD mesuré.

Tableau 2: ToF expérimental pour des concentrations de gaz purs.

Gaz	Vélocité (c) (m/s)	ToF attendue pour un gaz pur à une distance de 7,14 mm	LDD
Dioxyde de carbone	267	26 µs	0,30 %
Azote	349	20 µs	-
Hydrogène	1306	5.4 µs	0,15 %

V. Conclusion

En résumé, les microsystèmes résonnants proposés, basés sur des micropoutres 3C-SiC (3C-SiC-µCs) et des transducteurs ultrasonores capacitifs micro-usinés (CMUTs), ont permis de mesurer avec succès la modification d'un mélange de gaz par le biais d'une modification de leurs propriétés physiques, à savoir la densité massique ou la vitesse des ultrasons.

Tout d'abord, la détection de gaz est réalisée à l'aide de 3C-SiC-µCs nouvellement conçus et fabriqués. Ces 3C-SiC-µCs détectent le changement dans le mélange de gaz dû au changement de leur propriété physique, c'est-à-dire le changement de la fréquence de résonance induite par la variation de la densité de masse du gaz.

Enfin, le système CMUTs proposé détecte le changement de concentration de gaz en utilisant le décalage de la fréquence de résonance dans la méthode III de détection. Puis, la surveillance du gaz à l'aide de la technique du temps de vol (ToF) est discutée, où les changements dans le mélange gazeux sont identifiés avec succès grace aux variations de vitesses des ultrasons. Tous ces microsystèmes mentionnés fonctionnent sans aucun revêtement chimique/sensible.

Dans tous les cas, c'est-à-dire par les méthodes I ,III et IV, les premières expériences ont été réalisées pour de faibles concentrations (1-4 %) de CO_2 dans N_2 et de H_2 dans N_2 avec des paramètres électriques optimisés obtenus par des caractérisations primaires du dispositif. Ces expériences ouvrent la voie à la réalisation de mesures à des concentrations de gaz très faibles (<1 %). Les résultats démontrent des limites de détection de 0,20 %, 0.04 % et 0.15 % pour H_2 dans N_2, pour les détections des méthode I, III et IV respectivement. Ces résultats prometteurs font de notre dispositif un capteur de gaz approprié avec une technique de détection de pointe (c.-à-d. ToF).

Tableau 3: Limite de détection mesurée pour H_2 dans N_2 et CO_2 dans N_2 pour les différentes méthodes de détection proposées.

Méthode de détection	Limite de détection	
	Hydrogène dans l'azote	Dioxyde de carbone dans l'azote
Méthode I	0,20 %	0,25 %
Méthode III	0,04 %	0,25 %
Méthode IV	0,15 %	0,30 %

Enfin, les micropoutres de la méthode II n'ont malheureusement pas permis de réaliser cette première série de mesures. Ceci est dû au circuit ouvert des piézo-résistances mentionnées dans la figure 3. Cependant, ce problème peut être résolu en augmentant l'épaisseur du film métallique (voir M1 sur la figure 3) afin de conserver des micropoutres entièrement fonctionnelles.

Par terminer sur une note positive, les 3C-SiC-µCs basés sur l'actionnement électromagnétique et la détection de l'induction, qui fonctionnent actuellement donnent de l'espoir pour la prochaine génération de dispositifs MEMS pour fonctionner dans des environnements extrêmes. Enfin, les CMUT à base de 3C-SiC constituent également une solution attrayante, car ils permettent de mesurer simultanément la variation de la densité de masse et la vitesse des ultrasons. Cela réduit le risque de fausse alarme et ouvre la voie à de nombreuses autres applications MEMS/NEMS dans divers domaines.

Références

[1] MAN Company, “Vorrichtung zur fortlaufenden Bestimmung des Wasserstoffgehaltes in Gasgemischen,” Patent DRP 165 349, 1904

[2] T. Hübert *et al.*, “Hydrogen sensors – A review,” *Sensors and Actuators B: Chemical*, vol. 157, no. 2, pp. 329–352, Oct. 2011, doi: 10.1016/j.snb.2011.04.070.

[3] S. K. Chaulya and G. M. Prasad, “Gas Sensors for Underground Mines and Hazardous Areas,” in *Sensing and Monitoring Technologies for Mines and Hazardous Areas*, Elsevier, 2016, pp. 161–212. doi: 10.1016/B978-0-12-803194-0.00003-9.

[4] Q. Deng *et al.*, “Research Advances of Prevention and Control of Hydrogen Sulfide in Coal Mines,” *The Scientific World Journal*, vol. 2019, pp. 1–15, Apr. 2019, doi: 10.1155/2019/8719260.

[5] “Three Mile Island Accident (1979).” https://www.world-nuclear.org/information-library/safety-and-security/safety-of-plants/three-mile-island-accident.aspx

[6] “Chernobyl Accident (1986).” https://www.world-nuclear.org/information-library/safety-and-security/safety-of-plants/chernobyl-accident.aspx

[7] “Fukushima Daiichi Accident (2011).” https://www.world-nuclear.org/information-library/safety-and-security/safety-of-plants/fukushima-daiichi-accident.aspx

[8] Hortense Goulard, “L’éolien, troisième source d’électricité en France en 2020,” *Les Echos*, Mar. 2021. [Online]. Available: https://www.lesechos.fr/industrie-services/energie-environnement/leolien-troisieme-source-delectricite-en-france-en-2020-1295128

[9] “World Nuclear Power Reactors & Uranium Requirements,” Jan. 2021. https://www.world-nuclear.org/information-library/facts-and-figures/world-nuclear-power-reactors-and-uranium-requireme.aspx

[10] “Project Cigéo.” https://www.andra.fr/cigeo

[11] P. S. Chauhan and S. Bhattacharya, “Hydrogen gas sensing methods, materials, and approach to achieve parts per billion level detection: A review,” *International Journal of Hydrogen Energy*, vol. 44, no. 47, pp. 26076–26099, Oct. 2019, doi: 10.1016/j.ijhydene.2019.08.052.

[12] W. J. Buttner *et al.*, “An overview of hydrogen safety sensors and requirements,” *International Journal of Hydrogen Energy*, vol. 36, no. 3, pp. 2462–2470, Feb. 2011, doi: 10.1016/j.ijhydene.2010.04.176.

[13] G. Wang *et al.*, “Fiber-Optic Hydrogen Sensors: A Review,” *IEEE Sensors J.*, pp. 1–1, 2020, doi: 10.1109/JSEN.2020.3029519.

[14] G. de Graaf and R. F. Wolffenbuttel, “Surface-micromachined thermal conductivity detectors for gas sensing,” in *2012 IEEE International Instrumentation and Measurement Technology Conference Proceedings*, Graz, Austria, May 2012, pp. 1861–1864. doi: 10.1109/I2MTC.2012.6229412.

[15] A. Liméry *et al.*, “Raman lidar for hydrogen gas concentration monitoring and future radioactive waste management,” *Opt. Express*, vol. 25, no. 24, p. 30636, Nov. 2017, doi: 10.1364/OE.25.030636.

[16] I. Asahi *et al.*, “Remote sensing of hydrogen gas concentration distribution by Raman lidar,” Kyoto, Japan, Nov. 2012, p. 85260X. doi: 10.1117/12.977348.

[17] T. L. Daulton, “Polytype Distribution in Circumstellar Silicon Carbide,” *Science*, vol. 296, no. 5574, pp. 1852–1855, Jun. 2002, doi: 10.1126/science.1071136.

[18] M.-T. Boudjiet, “Microsystèmes durables de mesures de concentration d’hydrogène utilisant des micropoutres sans couche sensible,” PhD dissertation, University of Bordeaux, 2015.

[19] M. T. Boudjiet *et al.*, “Preliminary results of the feasibility of hydrogen detection by the use of uncoated silicon microcantilever-based sensors,” *International Journal of Hydrogen Energy*, vol. 39, no. 35, pp. 20497–20502, Dec. 2014, doi: 10.1016/j.ijhydene.2014.03.228.

[20] A. Boulmé *et al.*, “A capacitive micromachined ultrasonic transducer probe for assessment of cortical bone,” *IEEE Transactions on Ultrasonics, Ferroelectrics, and Frequency Control*, vol. 61, no. 4, pp. 710–723, Apr. 2014, doi: 10.1109/TUFFC.2014.2959.

[21] L. Iglesias *et al.*, “Proof of Concept and Preliminary Results of Gas Detection by Measuring the Admittance at the Resonance and Anti-resonance of an Uncoated CMUT,” *Front. Mech. Eng.*, vol. 6, p. 14, Mar. 2020, doi: 10.3389/fmech.2020.00014.

[22] P. Shanmugam *et al.*, “Broad bandwidth air-coupled micromachined ultrasonic transducers for gas sensing,” *Ultrasonics*, vol. 114, p. 106410, Jul. 2021, doi: 10.1016/j.ultras.2021.106410.